



UNIVERSIDADE FEDERAL DO PARÁ  
INSTITUTO DE GEOCIÊNCIAS  
PROGRAMA DE PÓS-GRADUAÇÃO EM GEOFÍSICA

TESE DE DOUTORADO

# Post-imaging Analysis of Pressure Prediction in Productive Sedimentary Basins for Oil and Gas Exploration

WILDNEY WALLACY DA SILVA VIEIRA

BELÉM-PARÁ

2015

**WILDNEY WALLACY DA SILVA VIEIRA**

**Post-imaging Analysis of Pressure Prediction in  
Productive Sedimentary Basins for Oil and Gas  
Exploration**

Tese apresentada ao Programa de Pós-Graduação em Geofísica do Instituto de Geociências da Universidade Federal do Pará, em cumprimento às exigências para obtenção do título de Doutor em Geofísica.

Orientador: Lourenildo Willame Barbosa Leite

Dados Internacionais de Catalogação na Publicação (CIP)  
Biblioteca do Instituto de Geociências/SIBI/UFPa

---

Vieira, Wildney Wallacy da Silva, 1984-

Post-imaging analysis of pressure prediction in productive sedimentary basins for oil and gas exploration / Wildney Wallacy da Silva Vieira. – 2015

181 f. : il. ; 29 cm

Inclui bibliografias

Orientador: Lourenildo Willame Barbosa Leite

Tese (Doutorado) – Universidade Federal do Pará, Instituto de Geociências, Programa de Pós-Graduação em Geofísica, Belém, 2015.

1. Density. 2. Pressure. 3. Porosity. 4. Wave equations - Numerical solution. I. Título.

CDD 22. ed. 531.14

---

**WILDNEY WALLACY DA SILVA VIEIRA**

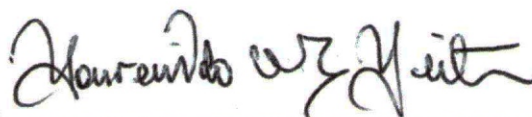
**Post-imaging Analysis of Pressure Prediction in Productive  
Sedimentary Basins for Oil and Gas Exploration**

Tese de Doutorado apresentada ao Programa de  
Pós-Graduação em Geofísica do Instituto de  
Geociências da Universidade Federal do Pará –  
UFPA, em cumprimento às exigências para  
obtenção do grau de Doutor em Geofísica.

Data de aprovação: 26/05/2015

Conceito: Excelente

Banca examinadora:



Prof. Dr. Lourenildo Williame Barbosa Leite - Orientador (UFPA)



Prof. Dr. José Jadsom Sampaio de Figueiredo - Membro (UFPA)



Prof. Dr. Amin Bassrei - Membro (UFBA)



Prof. Dr. João Carlos Ribeiro Cruz - Membro (UFPA)



Prof. Dr. Roberto Vizeu Lima Pinheiro - Membro (UFPA)

Dedico este trabalho à minha família.

# AGRADECIMENTOS

Ao orientador, Prof. Dr. Lourenildo W. B. Leite, por todo o conhecimento e experiência repassada ao longo destes anos de convivência, e por todo o apoio para que este trabalho pudesse ser realizado.

Aos professores da Banca Examinadora formada pelos Profs. Drs. José J. S. Figueiredo, Amin Bassrei, João Carlos Ribeiro Cruz, Roberto Vizeu Lima Pinheiro, pela participação e por todas as sugestões para melhoria do trabalho.

À Coordenação do CPGF pelo incentivo e apoio.

Em especial ao Prof. Boris Sibiryakov pela oportunidade de ter participado do projeto "*The Prediction of stresses and strains using P and S waves velocities in order to localize areas of small pressure in oil and gas productive layers as natural suction pumps*" coordenado pelo Prof. Lourenildo W. B. Leite, que faz parte do Programa Ciência sem Fronteiras com parceira entre a UFPA. O Prof. Boris Sibiryakov faz parte da Academia de Ciências da Rússia, Seção da Sibéria em Novosibirsk, e da Novosibirsk State University (NSU).

Os agradecimentos internacionais são também estendidos ao Prof. Dr. Egor Sibiryakov por ter participado do desenvolvimento dos trabalhos de pesquisa realizados e em andamento.

Ao CAPES pelo apoio financeiro da bolsa escolar durante os estudos.

Aos seguintes projetos que deram apoio ao desenvolvimento deste trabalho de pesquisa:

- Instituto Nacional de Ciência e Tecnologia - Geofísica do Petróleo (INCT-GP);
- Ciência Sem Fronteiras MEC/CAPES;
- Rede Cooperativa de Pesquisa Geofísica de Exploração (Rede 01 - Fase 5) da FINEP.

## RESUMO

Esta tese tem vários aspectos relacionados à modelagem de bacia sedimentar na exploração de óleo e gás, e com duas divisões gerais: estimativa de parâmetros, e predição de pressão. Para a estrutura do presente trabalho, o primeiro tópico está relacionada com a análise de velocidade e meios efetivos, onde se estima uma distribuição para a velocidade da onda P no tempo, seguido da transformação para a profundidade, e usar um modelo efetivo para a densidade e para a distribuição de velocidades da onda S. A razão para esta focalização inicialmente destas estimativas é porque eles representam a principal informação de base que se pode ter a partir do domínio sísmico, de onde os outros parâmetros sísmicos podem ser calculados, e que serve de base para a segunda parte deste trabalho. O segundo tópico está relacionado à cálculo de tensão, deformação e pressão na subsuperfície utilizando os dados das velocidades das ondas P e S e os modelos de densidade, com a finalidade de localizar áreas de altas e baixas pressões que atuam como bombas de sucção naturais para a mecânica da acumulação de óleo e gás em zonas produtivas e camadas reservatórios. Destacamos na segunda parte para a apresentação, chamar atenção para a sensibilidade do mapeamento de pressão em função da variação de velocidade e densidade. Classificamos a primeira divisão como dedicado ao processamento e imageamento sísmico convencional, e nomeamos a segunda divisão como predição de tensão-deformação-pressão pós-imageamento. Como o objetivo final da geofísica é obter imagens da subsuperfície sob diferentes propriedades, o cálculo de tensão só faz total sentido para o caso de dados reais, e isto faz com que os dados adquiridos seja obrigatoriamente em três componentes. Uma conclusão importante dos experimentos numéricos, mostramos que a pressão não tem um comportamento trivial, uma vez que pode diminuir com a profundidade e criar bombas naturais responsáveis pelo acúmulo de fluidos. A teoria de meios porosos baseia-se integralmente em geometria diferencial, porque esta disciplina matemática lida com propriedades geométricas coletivos para reservatórios reais. Mostrou-se que tais propriedades coletivas são, nomeadamente, a porosidade, a área da superfície específica, a curvatura média e a curvatura Gaussiana. Por exemplo, meios fraturados tem, como regra, uma pequena porosidade, mas área da superfície específica muito grande, o que cria a razão  $\gamma = v_S/v_P$  anômala e alta, e isto significa um coeficiente de Poisson,  $\sigma$ , negativo. Outra conclusão é relacionado ao cálculo da descontinuidade de pressão entre sólido e líquido, o que depende da estrutura de poros.

Palavras-chave: Sísmica de meios estruturados. Distribuição de velocidades P e S e densidade. Predição de pressão pós-imageamento. Modelagem de bacia.

# ABSTRACT

This thesis has several aspects related to the problem of basin modeling towards oil and gas exploration, and with two general divisions: parameter estimation, and pressure prediction. For the structure of this work, the first topic is related to velocity analysis and effective media, where estimated a distribution for the P wave velocity in time, the transformation to depth, and the use an effective model for the density and for the S wave velocity distributions. The reason for initially focusing on these estimations is because they represent one of the most basic information that one can have from the seismic domain, from where the other seismic parameters can be calculated, and from where the second part of this is totally based. The second topic is related to computing stress, strain and pressure distribution in the subsurface using the information from the P and S wave velocities and the density models, in order to localize areas of high and low pressures that act as natural suction pumps for the mechanics of oil and gas accumulation into productive zones and layers. We have highlighted this second part for the final work presentation, and call attention to the sensitivity of pressure mapping to the velocity and density variations. We also classify the first division as dedicated to the conventional seismic processing and imaging, and have called the second division as post-imaging stress-strain-pressure prediction. As for the final aim of geophysics is to create images of the subsurface under different properties, the stress calculation only makes total sense for real data, and this makes mandatory the acquired seismic data be three component. As an important conclusion from the numerical experiments, we show that pressure does not have a trivial behavior, since it can decrease with depth and create natural pumps that are responsible for accumulating fluids. The theory of porous media is based on integral geometry, because this mathematical discipline deals with collective geometrical properties for real reservoirs. It was shown that such collective properties are namely for porosity, specific surface, average curvature and Gaussian curvature. For example, cracked media has, as a rule, small porosity, but very large specific surface area that creates anomalous high  $\gamma = v_S/v_P$  ratio, what means a negative  $\sigma$  Poisson coefficient. Another conclusion is related to calculating discontinuity in pressure between solid and fluid, what depends on the structure of pore space.

Keywords: Seismic of structured. P and S velocity and density distribution. Post-imaging pressure prediction. Basin modeling.

## LIST OF ILLUSTRATIONS

Figure 2.1 – Element of the structured medium, where $l_0$ is an average distance between grains or porous. The problem is to create an equilibrium equation for an arbitrary element of the discrete medium. An equation of equilibrium exists for the surface $C$ , but does not for the surface $D$ .	27
Figure 2.2 – Another complex element of the structured medium, where $l_0$ is an average distance between grains or cracks. . . . .	27
Figure 2.3 – Plot of Eq. (2.11), real roots. The horizontal axis gives $\varepsilon = 2\pi \frac{l_0}{\lambda_B}$ ratio. Curve 1 shows the increasing wavenumber ratio $\frac{k_P(\omega)}{k_P(0)}$ ; therefore, $v_P$ decreases by increasing frequency. Curve 3 shows the same for S waves, $\frac{k_S(\omega)}{k_S(0)}$ , where $v_S$ decreases with increasing frequency. Curve 2 shows the increase of $\gamma = \frac{v_S}{v_P}$ ratio up to a negative Poisson coefficient $\sigma$ .	30
Figure 2.4 – Plot of Eq. (2.11), complex roots. The horizontal coordinates are $x = \text{Real}(kl_0)$ and $y = \text{Imag}(kl_0)$ . The vertical coordinate is $\varepsilon(x, y) = k_B l_0$ . If $k_B l_0 \ll 1$ , only real roots exist. . . . .	31
Figure 2.5 – Qualitative relation between stress ( $\sigma$ ) and strain ( $e = u_x$ ) showing the domains of linear elastic waves, and nonlinear Shock and Riemann waves. . . . .	32
Figure 2.6 – Qualitative plot of the function $\varphi(\xi)$ as a result of the inverse of Eq. (2.21) showing the attenuation with distance of an initial normalized sinusoidal causal pulse. The horizontal axis is divided in units 1 to 10, and the vertical axis normalized between -1.0 and +1.0. The nonlinear parameter is $\beta\varphi_0 = 0.1$ . The logarithmic decrement is nearly constant.	34
Figure 2.7 – Qualitative plot of the function $\varphi(\xi)$ as a result of the inverse of Eq. (2.21) showing the attenuation with distance of an initial normalized sinusoidal causal pulse. The horizontal axis is divided in units 1 to 10, and the vertical axis is normalized between -1.0 and +1.0. The nonlinear parameter is $\beta\varphi_0 = 0.5$ . The variation of the logarithmic decrement is now visible. . . . .	35
Figure 2.8 – Observed spectrum amplitude, $A(f_t)$ , of quasi-sinusoidal signals for an artificial laboratory sandstone model. The horizontal axis shows the frequency $f_t$ from 0 to 10.000 Hz, and the vertical axis shows the amplitude from 0 to 900 units. The data are according to Egorov and Mashinskii (2002). . . . .	35

Figure 2.9	– Plot of Eq. (2.31). The horizontal axis are porosity, $f$ , and the SSA parameter, $\sigma_0$ , and the vertical axis is the permeability, $\phi = \phi(f, \sigma_0)$ .	37
Figure 3.1	– Map of tectonic stress (represented by pressure $P$ ) of Jurassic reservoir, where the contour lines are overburden pressure $P = P_0(1 - \frac{4}{3}\gamma^2)$ (dark blue lines) drawn in an arbitrary scale, and superposed to the color scale. Orthogonal trajectories are probable fluid flow lines (red arrows). The pressure scale is in color and placed on the left side, and shows variations between 26-28 Megapascal (MPa), 1 MPa=10 atmospheres. The center of the map is dominated by a low pressure zone. The dots with numbers are producing boreholes. Heavy red lines are geological faults. Isolated circular enclaves correspond to local hydrodynamic systems. . . . .	46
Figure 3.2	– Map of intensity of tangent stress, $J = \gamma^2 P_0$ , as a measure of nonhydrostatic pattern (dark blue lines), where the high values are located around small stress zones. The lines are drawn in an arbitrary scale, and superposed to the color scale. The color pressure scale is on the left side and shows values between 15.3-16.0 in MPa. The dots with numbers are producing wells. Heavy red lines are geological faults. . .	47
Figure 3.3	– Map of calculated fracture inclinations $\phi(x, y, z)$ in producing bed. The color scale of the left shows a variation between 46 and 64 degrees with respect to the vertical (to the left and/or to the right). The blue areas shows roughly vertical fractures, and the brown areas show more Normal fractures with a more chaotic distribution. In the center of the map, we can describe more randomly inclined fractures (darker areas). The dots with numbers are producing wells. Heavy red lines are geological faults. . . . .	48
Figure 3.4	– Cross section of flow between infinite two plates. The length of dominant fracture is much larger than the crack opening. . . . .	53
Figure 3.5	– Stress nomenclature in cylindrical coordinates, and the representation of the borehole with liquid and solid around it. . . . .	54
Figure 3.6	– Plot of the Eq. (3.38) for the velocity flow as a function of porosity, $f$ , and SSA, $\sigma_0$ . . . . .	56
Figure 3.7	– A cube volume where the liquid has pressure is $P_\infty$ and in the solid is $P$ .	57
Figure 4.1	– Block perspective illustrating a sedimentary basin. It shows the Cartesian arbitrary system $(x, y, z)$ , the layer blocks limited by curved interfaces, a subtle reservoir volume limited above by the $S$ surface represented by $z = z_0(x, y)$ , and a flat free surface at $z = 0$ . . . . .	64

Figure 4.2 – Block diagram representing a reservoir volume $V$ limited above by the surface $S$ represented by $z = z_0(x, y)$ . The integration variable $\mathbf{y}$ and the $S$ surface reference point $\mathbf{x}$ are also shown. . . . .	68
Figure 4.3 – Topography of the anticline model according to Eq. (4.25) representing the $S$ surface separating the two media. The vertical axis indicates the surface position and amplitude $z_0(x, y)$ for $h = 10$ , $H = 3000$ , and $a = 1000$ . . . . .	70
Figure 4.4 – Normal overburden weight as pressure $P_0$ according to Eq. (4.3). . . . .	71
Figure 4.5 – Normal overburden weight as pressure discontinuity $\Delta P_0$ across the $S$ surface, and consistent with the results of Fig. 4.4. . . . .	71
Figure 4.6 – Cubic dilatation $\theta$ according to Eq. (4.12). The values in green are for the layer below the $S$ surface, and in blue for the layer above $S$ . . . . .	72
Figure 4.7 – This structure is a fluid attractor. Result for the dilatation pressure $P_\theta$ using Eq. (4.12) and $\theta$ as shown in Fig. 4.6. The blue color is for the medium above, and the red color is for the medium below the $S$ surface. . . . .	73
Figure 4.8 – Result for the dilatation pressure discontinuity $\Delta P_\theta = K_1\theta_1 - K_2\theta_2$ using the results in Fig. 4.7 to analyze the details of the pressure variation around the dome and rim. . . . .	73
Figure 4.9 – Difference between the overburden and the dilatation pressure discontinuities $\Delta P_{0\theta} = \Delta P_0 - \Delta P_\theta$ using the results as shown in Figs. 4.5 and 4.8. . . . .	74
Figure 4.10 – This structure is not a fluid attractor. The parameters have the inverse values of the ones for the case of Fig. 4.7: blue for $\gamma = 0.5$ below, and red for $\gamma = 0.577$ above the $S$ surface. . . . .	75
Figure 4.11 – Anticline surface topography according to Eq. (4.27). Case of a structure with steep slope angles. The color scale informs the ordinate $z(r)$ values. . . . .	77
Figure 4.12 – The vertical left axis gives the structural Gaussian anticline topography. The vertical right axis gives the pressure discontinuity $\Delta P_\theta$ versus radial distance from the dome central part. The green line shows a special oscillating pressure variation details, and an increase towards outside the dome. The right vertical axis had the sign changed for simplifying the reading. . . . .	77
Figure 5.1 – A physical particle, and the stress field representation, $\sigma_{ij}$ , where $\tau_{i,j}$ stands for the tangential components of $\sigma_{ij}$ . The letters $(\alpha, \beta, \gamma)$ are the rotation angles for the $(z', y', z')$ with respect to the $(x, y, z)$ system. The particle is referenced to the point $Q$ located at the origin of the Cartesian system. . . . .	82

Figure 5.2 – Old geological concept known as Heim’s rule for the stress variation in the crust. $S_V$ stands for the vertical stress, $S_H$ for the maximum horizontal stress, $S_h$ for the minimum horizontal stress, and where these quantities equalize as depth increases. This figure was redrawn based on Zang and Stephansson (2010). . . . .	87
Figure 5.3 – Geological description of the Marmousi according to Martin, Wiley and Marfurt (2006) with the oil and gas reservoir targets pointed to. We underlined the target in the bottom sequence related to the classical anticline structure. . . . .	89
Figure 5.4 – Velocity, $v_P(x, z)$ . . . . .	92
Figure 5.5 – Velocity, $v_S(x, z)$ . . . . .	93
Figure 5.6 – Density, $\rho(x, z)$ . . . . .	94
Figure 5.7 – P wave impedance, $I_P(x, z)$ . . . . .	95
Figure 5.8 – S wave impedance, $I_S(x, z)$ . . . . .	96
Figure 5.9 – P-S wave impedance contrast, $\Delta I_{PS}(x, z)$ . . . . .	97
Figure 5.10 – Normalized adimensional, $(A)$ , vertical impedance coefficient contrast, $R_{PS}(x, z) = \frac{I_P - I_S}{I_P + I_S}$ . . . . .	98
Figure 5.11 – Gamma, $\gamma(x, z)$ . . . . .	99
Figure 5.12 – Mu, $\mu(x, z)$ . . . . .	100
Figure 5.13 – Lambda, $\lambda(x, z)$ . . . . .	101
Figure 5.14 – Poisson, $\sigma(x, z)$ . . . . .	102
Figure 5.15 – Vertical pressure field, $P_z(x, z)$ . . . . .	104
Figure 5.16 – Horizontal pressure field, $P_x(x, z)$ . . . . .	105
Figure 5.17 – Hydrostatic pressure field, $P_H(x, z)$ . . . . .	106
Figure 5.18 – Horizontal deviatoric hydrostatic pressure field, $P_{XH} = \sigma_{xx} - P_H$ . . . . .	107
Figure 5.19 – Vertical deviatoric hydrostatic pressure field, $P_{ZH} = \sigma_{zz} - P_H$ . . . . .	108
Figure 5.20 – Tangential deviatoric pressure field, $P_T(x, z)$ . . . . .	109
Figure 5.21 – Horizontal/vertical stress ratio, $k_{xz}(x, z)$ . . . . .	110
Figure 5.22 – Horizontal/vertical stress ratio selected profile, $k_{xz}(z)$ . . . . .	111
Figure 5.23 – Vertical pressure discontinuities, $\Delta P(x, z)$ , across the interfaces. . . . .	112
Figure 5.24 – Vertical variation of the vertical pressure field, $\frac{\partial P_z(x, z)}{\partial z}$ , given in figure 5.15. . . . .	113
Figure 5.25 – Vertical variation of the horizontal pressure field, $\frac{\partial P_x(x, z)}{\partial z}$ , given in figure 5.16. . . . .	114
Figure 6.1 – The Cartesian system $(x, y, z)$ , the volume $V$ enclosed by the surface $S$ . (left) The fixed point $\mathbf{x}_0$ inside the volume $V$ , the integration point $\mathbf{x}_0$ , and the unit vectors $\vec{\mathbf{x}}$ , $\vec{\mathbf{y}}$ and $\vec{\mathbf{z}}$ . (center) The boundary conditions for the Laplace equation and the Dirichlet and Neumann problems. (right) The tangent unit vectors $\vec{\mathbf{e}}_{\mathbf{n}}$ , $\vec{\mathbf{e}}_{\varphi}$ and $\vec{\mathbf{e}}_{n\tau}$ . . . . .	120

Figure 6.2	– Geometry of grains with a contact surface (called platform by being flat), and force distribution around the surface. . . . .	134
Figure 6.3	– The clipped ball model with six flat contact areas (platforms) represented in Cartesian coordinates $(x, y, z)$ , and to be submitted to stress loading and boundary conditions. . . . .	136
Figure 6.4	– Discontinuity surface images of the clipped ball model with six flat areas of figure 6.3 in the $\theta$ and $\varphi$ cylindrical coordinates using the $I$ -Indicator function, with the conditions: $h_0 = 0.8$ ; $I = 1$ in the flat contact area; and $I = 0$ on the boundary part with the presence of fluid. The amplitude scale shows 1 and 0, and the six polygonal shapes of the flat contact area. On the two lateral parts $I = 1$ , and have an extended flat form. . . . .	137
Figure 6.5	– Amplitude of the coefficients of the linear system matrix $M_{ik}$ (6.33) to (6.37) versus $\theta$ and $\varphi$ for calculating the vector potential components $[F_n(\theta, \varphi)]$ , for $h_0 = 0.85$ and rigid contact. . . . .	140
Figure 6.6	– Dependence of the normal component of the vector potential components, $F_n$ , on the reliability and stability. This result says that it is a pleasant fact that the part of the surface bordered by the fluid, where the normal loading was well defined, did not change after the numerical calculations for the vector potential, $F_n$ . The values were: $h_0 = 0.85$ ; and the parameters $\theta$ and $\varphi$ : $0 \leq \theta \leq \pi$ , $0 \leq \varphi \leq 2\pi$ . . . .	140
Figure 6.7	– The normal component of the loading vector $p_n$ for $h_0 = 0.85$ , as a function of the $0 \leq \theta \leq \pi$ and $0 \leq \varphi \leq 2\pi$ parameters. The borders with fluid have loading $p_i$ equal to 1. On the platform boundaries, the normal loading and maximum modulus change rapidly. This result comes from a convolution with a modified stress tensor potential given by equation (6.45). . . . .	141
Figure 6.8	– Details of the normal component of the loading vector $p_n$ of figure 6.7 showing the upper platform for a narrow band of the parameters $\theta$ and $\varphi$ . . . . .	141
Figure A.1	– Physical illustration of the CRS model formed by one layer over a half-space separated by a curved interface. The velocity $v_0$ characterizes the upper layer involving the observation aperture. The emergence angle $\alpha_0$ is common to both N and NIP waves. $R_{\text{NIP}}$ is the NIP-wave radius and curvature $K_{\text{NIP}}$ , and $R_{\text{N}}$ is the N-wave radius and curvature $K_{\text{N}}$ . (MANN, 2002). . . . .	159
Figure A.2	– 3D perspective of the surfaces to be indirectly fit in the stack process: the CRS operator in green [Eq. (A.4)], and the simulated observed data in blue. (MANN, 2002). . . . .	159

Figure A.3 – Cube perspective of the coherence Semblance values calculated by Eq. (A.6) as function of the wavefield attributes $\alpha_0$ , $R_N$ and $R_{NIP}$ . (MAUCH, 1999). . . . .	161
Figure A.4 – 3D perspective of the time surface to be fit representing the forward model calculated by Eq. (A.4) showing the hyperbolic aspect along $h$ and $x_m$ . . . . .	162
Figure A.5 – 3D perspective of the time surface to be fit representing the synthetic data calculated by Eq. (A.4), where random noise was added to Fig. A.4, and still showing some hyperbolic aspect. The additive noise was calculated with 0.01% with respect to the maximum value of the travelttime. . . . .	162
Figure A.6 – Canonic representation of the optimization principle. . . . .	165
Figure A.7 – Price initial random misfit function. . . . .	172
Figure A.8 – Data resolution matrix decimated by 50 points. . . . .	173
Figure A.9 – Evolution of the objective minimization function calculated in 20 iterations showing the stabilization of the process before the tenth iteration. . . . .	175
Figure A.10 – Contour maps of the normalized derivative $(\alpha_0/t_0) * \partial t(x_m, h; \mathbf{m})/\partial \alpha_0$ . Figure positions: left, $t_0 = 0.25$ s; right, $t_0 = 5.00$ s. . . . .	176
Figure A.11 – Contour maps of the normalized derivative $(R_{NIP}/t_0) * \partial t(x_m, h; \mathbf{m})/\partial R_{NIP}$ . Figure positions: left, $t_0 = 0.25$ s; right, $t_0 = 5.00$ s. . . . .	177
Figure A.12 – Contour maps of the normalized derivative $(R_N/t_0) * \partial t(x_m, h; \mathbf{m})/\partial R_N$ . Fig. positions: left, $t_0 = 0.25$ s; right, $t_0 = 5.00$ s. . . . .	178
Figure A.13 – Contour maps of the normalized derivative $(v_0/t_0) * \partial t(x_m, h; \mathbf{m})/\partial v_0$ for the nominal values $v_0 = 1500$ m/s. Figure positions: top left, $t_0 = 0.50$ s; top right, $t_0 = 2.00$ s; bottom left, $t_0 = 4.00$ s; bottom right, $t_0 = 5.00$ s. From the experiments, the form varies very little after $t_0 = 2$ s. . . . .	179
Figure A.14 – Contour maps of the relative error calculated by Eq. (A.12) (left), and of the absolute error calculated by Eq. (A.13) (right), showing valleys of minimum around the nominal value at the center of figures. . . . .	180

## LIST OF TABLES

Table 5.1 – Input data and impedance . . . . .	89
Table 5.2 – Constitutive parameters . . . . .	89
Table 5.3 – Pressure fields . . . . .	90
Table 5.4 – Pressure field discontinuity . . . . .	90
Table 5.5 – Spatial derivatives . . . . .	90
Table 6.1 – Dependence of the average normal loading, $\bar{p}_n$ , (as effective pressure, $p_{eff}$ ) on the $h_0$ parameters, and on the type of boundary contact, with the condition that the pore pressure is equal to 1. From the table, the effective pressure is proportional to the pore pressure, as can be seen from the increasing negative values on both right columns with respect to the left column. . . . .	142
Table A.1 – Inversion values obtained by the CRSGM and GM optimization methods.	172
Table A.2 – Normalized Parameter Resolution matrix limited to 3 decimal places. Eq. (A.17). . . . .	173
Table A.3 – Normalized Unitary Parameter Covariance matrix limited to 3 decimal places. Eq. (A.19). . . . .	174

# SUMMARY

<b>1</b>	<b>INTRODUCTION . . . . .</b>	<b>17</b>
<b>2</b>	<b>MODEL OF THE STRUCTURED CONTINUUM, AND THE RE- LATION BETWEEN SPECIFIC SURFACE AREA, POROSITY AND PERMEABILITY . . . . .</b>	<b>25</b>
<b>2.1</b>	<b>Introduction . . . . .</b>	<b>25</b>
<b>2.2</b>	<b>Methodology . . . . .</b>	<b>26</b>
2.2.1	Equation of motion for structured media . . . . .	26
2.2.2	Condition for a negative poisson coefficient . . . . .	29
2.2.3	The long wave approach. Equations of motion as Korteweg-De-Vries and Boussinesq types . . . . .	31
2.2.4	Porous media with viscous liquid . . . . .	36
<b>2.3</b>	<b>Conclusions . . . . .</b>	<b>40</b>
<b>3</b>	<b>BEHAVIOR OF STRESSES AND HYDRODYNAMICS FROM MUL- TICOMPONENT SEISMIC DATA . . . . .</b>	<b>41</b>
<b>3.1</b>	<b>Introduction . . . . .</b>	<b>41</b>
<b>3.2</b>	<b>Methodology . . . . .</b>	<b>42</b>
3.2.1	Physical-mathematical theory . . . . .	48
3.2.2	Pressure discontinuity between rock skeleton and fluid . . . . .	49
3.2.3	Percolation and permeability near borehole . . . . .	51
3.2.4	Volume dissipative forces by viscosity . . . . .	52
3.2.5	Stresses in solid near borehole . . . . .	53
3.2.6	Equation of equilibrium and fluid velocity . . . . .	55
3.2.7	Estimation of pressure in liquid far from borehole . . . . .	57
<b>3.3</b>	<b>Conclusions . . . . .</b>	<b>58</b>
<b>4</b>	<b>LOCAL LOW PRESSURE AREAS IN ANTICLINE STRUCTURES</b>	<b>61</b>
<b>4.1</b>	<b>Introduction . . . . .</b>	<b>61</b>
<b>4.2</b>	<b>Methodology . . . . .</b>	<b>63</b>
4.2.1	The role of slope angles and curvatures . . . . .	63
4.2.2	Contribution of the poisson integral to displacements . . . . .	68
4.2.3	Contribution of the poisson integral to stresses . . . . .	69
4.2.4	Test example: anticline structure with low slope angles . . . . .	70
4.2.5	Test example: anticline structure with high slope angles . . . . .	75
<b>4.3</b>	<b>Conclusions . . . . .</b>	<b>78</b>

<b>5</b>	<b>SUBSURFACE STRESS PREDICTION USING SEISMIC DATA FOR OIL AND GAS EXPLORATION</b>	<b>79</b>
<b>5.1</b>	<b>Introduction</b>	<b>79</b>
<b>5.2</b>	<b>Methodology</b>	<b>81</b>
5.2.1	The stress and strain tensor fields	81
5.2.2	Stress states	82
5.2.3	Isotropic media	83
5.2.4	Scalar pressure field	86
<b>5.3</b>	<b>Results</b>	<b>88</b>
<b>5.4</b>	<b>Conclusions</b>	<b>115</b>
<b>6</b>	<b>A NEW METHOD FOR THE SOLUTION OF THE ELASTO-DYNAMIC PROBLEM</b>	<b>117</b>
<b>6.1</b>	<b>Introduction</b>	<b>117</b>
<b>6.2</b>	<b>Method</b>	<b>118</b>
6.2.1	Basic equatinos	119
6.2.2	Fundamental solution of the first kind	120
6.2.3	Fundamental solution of the second kind	122
<b>6.3</b>	<b>Delta loading source</b>	<b>124</b>
<b>6.4</b>	<b>Normal and radial components from finite analogs</b>	<b>126</b>
<b>6.5</b>	<b>The new tensor</b>	<b>128</b>
6.5.1	Boundary conditions and the mixed type elastic problem	129
6.5.2	Appropriate rotation of axes and libraries	130
6.5.3	The static mixed bvp	132
6.5.4	An integral criterion for accuracy	133
<b>6.6</b>	<b>Effective pressure, rigid and slip contacts</b>	<b>134</b>
6.6.1	Numerical example	135
6.6.2	Assigning the surface	135
6.6.3	Adjusting the numerical analog	138
<b>6.7</b>	<b>Results</b>	<b>139</b>
<b>6.8</b>	<b>Conclusions</b>	<b>143</b>
<b>7</b>	<b>GENERAL CONCLUSIONS</b>	<b>145</b>
	<b>Bibliography</b>	<b>148</b>
	<b>APPENDIX</b>	<b>153</b>
	<b>APPENDIX A – SENSITIVITY, RESOLUTION AND AMBIGUITY OF THE CRS STACK OPERATOR</b>	<b>154</b>

# 1 INTRODUCTION

This research work has been developed in topics of seismic exploration for oil and gas, and it is composed of methodologies directly related to the projects in development in the Institution, specially related to the Graduate Program in Geophysics (CPGF).

Our aim is to develop methods and techniques that can be useful for extending, or to locate, a drilling zone that can be oil and gas productive. As a result of this plan, we concentrate on conclusions related to post-migration models, in order to apply methods of stress prediction in sedimentary basins, and define low and high pressure zones that can act as fluid suction pumps for accumulating hydrocarbons (ALLEN; ALLEN, 2013).

We divided the research topics in three main parts aiming at sedimentary basin analysis, as the general objectives, and they are:

1. velocity analysis, where we intended to develop methods to obtain the velocity distribution in subsurface;
2. stack and migration (time and depth) processing using a velocity distribution model, followed by geometrical interpretation of lineament and structures;
3. prediction of stress, deformation and pressure variation in the subsurface as a post-migration process.

The first effort in this research work was towards the estimation of a velocity distribution (root mean square velocity, time and depth interval velocities) for real, based on synthetic data testing, and mainly for the P-wave mode, since we lack of S-wave mode information at the time of this completion (HARDAGE et al., 2011).

The second part of the research work was under the subject of prediction of stresses and strains using P and S waves velocities in order to localize areas of small pressure in oil and gas productive layers as natural suction pumps, as a post-migration process, where we modeled real structures based on geological knowledge of productive reservoirs (anticlines, fault and stratigraphic zones) (ZOBACK, 2007).

A great effort in this second part of the research work has been under the subject "*The Prediction of stresses and strains using P and S waves velocities in order to localize areas of small pressure in oil and gas productive layers as natural suction pumps*", that is a project in the Science Without Borders, having Prof. Boris Sibiryakov as PVE in the CPGF.

Back to the first part, it is more related to conventional seismic investigations, where we look for obtaining information on the P and S wave velocity distribution and density

distribution, and also on the configuration of seismic boundaries, where the subsurface is characterized by porous sedimentary media (BROWN, 2011).

The main selected research work for presenting in this thesis has been the following publications, that compose the chapters. Each chapter is individualized, but the topics are interrelated to give a harmony to the work towards basin analysis from the point of view of seismic information, where we include modeling, inversion, imaging and post-stack pressure prediction.

Therefore, each chapter represent specific research work published as articles.

- Chapter 2: (SIBIRYAKOV; LEITE; VIEIRA, 2013b).

Title: Model of the Structured Continuum, and the Relation Between Specific Surface Area, Porosity and Permeability.

Authors: Sibiryakov, E. P.; Leite, L. W. B.; Vieira, W. W. S.

Published: Brazilian Geophysical Journal, volume 31, number 4, 2013.

Presentation :

This chapter treats a new theory for structured (also called porous, fractured, or blocked) media that contains several degrees of freedom, and it is contrary to the Cauchy and Poisson classical seismic theory of the continuum. This fact is clear because elementary blocks (grains) may transfer the motion by contact interaction, by rotation, and by group of physical particles instead of a mathematical particle.

Therefore, the energy content is not only contained within the first spatial derivatives (strains), but the potential energy content is within the second (curvatures) and other higher order spatial derivatives. As a result, the equation of motion of porous media should contain higher order spatial derivatives, and may even contain infinite order spatial derivatives.

Congress Presentation: (SIBIRYAKOV; LEITE; VIEIRA, 2013a).

Title: Model of structured continuum and relation between specific surface, porosity and permeability.

Authors: Sibiryakov, E. P.; Leite, L. W. B.; Vieira, W. W. S.

Publisher: Thirteenth International Congress of The Brazilian Geophysical Society.

- Chapter 3: (SIBIRYAKOV; LEITE; VIEIRA, 2015).

Title: Behavior Of Stresses And Hydrodynamics From Multicomponent Seismic Data.

Authors: Sibiryakov, E. P.; Leite, L. W. B.; Vieira, W. W. S.

Submitted: Brazilian Geophysical Journal.

Situation: Approved for publication.

Presentation :

A method for fluid-stress modeling of 3D seismic, and drilling data, provided new information on the stress conditions, and on the hydrodynamics of the U11 layer of the Upper Jurassic sandstone reservoir in the Arigol field, Western Siberia, Russia. It is proposed to detect and outline oil fields, and divide them into isolated traps, marked by low sedimentary overburden pressure, and fluid-trapping properties based on correlation between the structural pattern and mapped stress.

A different systematic approach, that implies on the use of 3D component seismic data, on  $v_P$  and  $v_S$  velocities, on density  $\rho$ , for stress modeling of reservoirs, to detect the areas of low overburden pressure  $P(x, y, z)$ , and vertical inclination of fractures (faults),  $\varphi(x, y, z)$ , caused by the nonhydrostatic behavior of stress.

Symposium Presentation: (VIEIRA; LEITE; SIBIRYAKOV, 2014).

Title: Stress Prediction and Hydrodynamics from Multicomponent Seismic Data.

Authors: Vieira, W. W. S.; Leite, L. W. B.; Sibiryakov, E. P.

Publisher: VI Brazilian Symposium on geophysics.

- Chapter 4: (SIBIRYAKOV et al., 2013).

Title: Local Low Pressure Areas In Anticline Structures.

Authors: Sibiryakov, E. P.; Leite, L. W. B.; Sibiryakov, E.; Vieira, W. W. S.

Submitted: Brazilian Geophysical Journal.

Situation: Approved for publication.

Presentation :

This chapter treats the case of localizing low pressures zones in sedimentary basins for oil and gas exploration, and for this aim it is necessary to know P and S wave velocities for medium. Strictly speaking, we need to know the rock densities for all layers, and as an addition there are many correlation tables between seismic velocities and densities.

Besides, density is a parameter admitted to change slowly with depth to the top of the target interface. P wave velocities are considered a conventional asset, and S wave velocities can be obtained from special field survey, in particular from converted P-S waves registered by VSP technology, and by petrophysical measurements. The described theory deals with stress prediction in the subsurface, and takes in consideration the constitutive parameters (density and Lamé's), and the geometry of the reservoir target surface. The model does not separate the different contributions (porosity, fluids) to the rock velocities controlled by the constitutive parameters.

As a result of this study, it is not a necessary condition that an anticline be a potential structure for oil and gas accumulation. This role can be played by horizontal structures if there is a positive  $\gamma = \frac{v_S}{v_P}$  ratio discontinuity, or a negative discontinuity

of the Poisson,  $\sigma$ , ratio across the horizontal boundary. These conditions are responsible for producing a pressure discontinuity, such that beneath the boundary there will be a sufficiently lower pressure zone than above the boundary. In this case, the lower horizontal boundary is said to be an attractor surface for fluids of the any kind; in the opposite case, this boundary does not have fluid attractor properties. Congress Presentation: (LEITE; SIBIRYAKOV; VIEIRA, 2015).

Title: Stress Prediction and Hydrodynamics from Multicomponent Seismic Data.

Authors: Leite, L. W. B.; Sibiryakov, E. P.; Vieira, W. W. S.;

Submitted: Fourteenth International Congress of The Brazilian Geophysical Society.

- Chapter 5: (SIBIRYAKOV et al., 2014).

Title: Subsurface Stress Prediction Using Seismic Data For Oil And Gas Exploration.

Authors: Sibiryakov, E. P.; Leite, L. W. B.; Sibiryakov, E.; Vieira, W. W. S.

Submitted: Brazilian Geophysical Journal, September, 2014.

Situation: Under analysis.

Presentation :

This chapter is related to a major research study that has for objective the prediction of stress in sedimentary basins, as a contribution to geological and engineering methods and techniques for oil and gas exploration.

Such an attractive and important scientific theme is based on the knowledge of the compressional ( $v_P$ ) and shear ( $v_S$ ) wave velocities and the densities ( $\rho$ ) distributions, in order to localize low pressures zones in sedimentary basins.

It is rather usual to think and accept that pressure increases continuously with depth, and we show here that this is not the case. The vertical and horizontal pressure variations act as natural pumps that pushes fluids from high to low pressure areas. The major physical parameter for this phenomena is played by the  $\gamma = \frac{v_S}{v_P}$  ratio discontinuity along interfaces.

Most of the seismic exploration is based on the acoustical wave equation, what results in a knowledge of the compressional wave velocity model. To obtain the shear wave velocity information it is necessary a 3D component sensor survey, and density log information can also be incorporated. Shear wave velocities can also be obtained from VSP technology, and by petrophysical measurements.

Regression models for seismic velocities and densities that can also be incorporated in this prediction.

As a result of the  $\gamma$  ratio behavior, an anticline is not necessarily the only structural condition for a potential area for oil and gas accumulation. A trap can be present as a horizontal structure if there is a positive  $\gamma$  ratio discontinuity, or a negative discontinuity of the Poisson  $\sigma$  ratio across the horizontal boundary.

These physical conditions are responsible for producing a pressure discontinuity, such that there will be a sufficiently lower pressure zone underneath than above the boundary. In this case, the lower horizontal boundary is said to be a fluid attractor surface. In the opposite physical conditions, this boundary does not have fluid attraction properties. For the theory developed and implemented here, the example presented here is the 2D Marmousi subsurface model for simpler and direct visualization, but the theory accounts for a 3D case.

Congress Presentation: (VIEIRA; SIBIRYAKOV; LEITE, 2015).

Title: Pressure variation prediction using seismic data for oil and gas exploration.

Authors: Vieira, W. W. S.; Sibiryakov, E. P.; Leite, L. W. B.;

Submitted: Fourteenth International Congress of The Brazilian Geophysical Society.

- Chapter 6: (SIBIRYAKOV et al., 2015a).

Title: A new method for the solution of the elasto-dynamic problem.

Authors: Sibiryakov, E. P.; Leite, L. W. B.; Sibiryakov, E.; Vieira, W. W. S.

Situation: To be submitted to the EAGE Latin America Journal.

Presentation:

We present here a new computer technology for solving three-dimensional problems of elastic stationary oscillations. The method can be used not only for applications in oil and gas exploration, but also for modeling buried structures and structural components such as foundations, tunnels, trenches, cavities, etc.

The basis of this method is the construction of the integral equations kernels as a response to an analog Delta loading, or to its derivatives.

The finiteness of the kernels gives the possibility to increase accuracy in many orders, and to solve the elastic problem in the case of discontinuity of the normal surface vector.

As an example, we show that the variation of characteristics of the static stress state under the influence of pore pressure depends essentially on the contact geometry, and a little on the type of boundary condition at the contact.

Other selected research work developed and related directly to this thesis has been the following publications:

- Appendix A (LEITE; VIEIRA, 2013).

Title: Sensitivity, Resolution And Ambiguity Of The CRS Stack Operator.

Authors: Leite, L. W. B.; Vieira, W. W. S.

Published: Brazilian Geophysical Journal, volume 31, number 4, 2013.

Presentation:

This paper describes an investigation about the sensitivity and ambiguity of the CRS stack operator parameters  $(v_0, R_{\text{NIP}}, R_N, \alpha_0)$ , and their resolution in terms of statistical properties of the solution of a nonlinear multi-parametric optimization problem for surface fitting between the forward model and a synthetic data, in the least-square sense.

The sensitivity method is borrowed from dynamic system analysis and synthesis, and the definitions are based on the Miller-Murray model.

The results are analyzed in terms of the CRS attributes search strategies during the stack process.

The investigation principle is to combine global and local optimization methods to reach a minimum of the object function of minimization, where the problem matrix has a better linear relation to the parameters. A first search for a minimum is performed with a controlled random search method, followed by a gradient method for the last steps for the optimization to calculate the data and parameter resolution and covariance matrices, and any further model statistical properties.

The sensitivity functions are represented by the columns of the optimization problem matrix, and they in general exhibit a linear behavior instead of a convex form; as a result, this linear behavior establish the necessity of a good starting point for the optimized multi-parametric attributes search.

The following article is a scientific production, it has been inserted in this Thesis, but it is related to the general division of the research work:

- (LEITE; MANN; VIEIRA, 2014).

Title : Processing and Imaging of Marine Seismic Data from the Jequitinhonha Basin (Bahia, Brazil)

Authors : Leite, L. W. B.; Mann, J.; Vieira, W. W. S.

Submitted: Brazilian Geophysical Journal, July, 2014.

Situation: Under analysis.

Presentation:

The present case study results from a consistent processing and imaging of marine seismic data from a set collected over the East Brazilian Atlantic.

Our general aims are first, to subsidize geological interpreters with plausible sub-surface images for petroleum exploration; second, to verify published schematic geological interpretation for these basins by underlying the sediment/basement contact, from where sub-vertical faults are projected through the basin followed by folded structures. The data driven results can be used to trace the reflector boundaries in the time sections, submitted to time-to-depth axis transformation,

and used as a first model for further basin studies of pressure prediction as natural pumps for oil and gas accumulation.

The applied fundamental techniques are mainly based on the data-driven common reflection surface stack, where we show the improvement of the signal-to-noise ratio, the continuity of the reflection events, and that time migration collapses the diffractions.

The CRS migration strongly collapsed the diffractions allowing some subsurface structures be more evident.

The free surface and some shallow multiples can be clearly traced for further processing aiming at their elimination.

The interpretation lines are meant to show the geometry of reflectors, and to help in comparing with the results of other sections. We could trace the presence of subvertical fault system starting from the lower basement, and up through the sedimentary sequence.

Another work under present development and directly related to this thesis is the following research topic:

- (SIBIRYAKOV et al., 2015b).

Title : Numerical applications of the new method for the solution of the elasto-dynamic problem for asymmetrical reservoirs.

Authors : Sibiryakov, E. P.; Leite, L. W. B.; Sibiryakov, E.; Vieira, W. W. S.

Situation: To be submitted to the EAGE Latin America Journal.

Presentation:

In this work we applied a new computer technology for solving three-dimensional problems of elastic stationary oscillations for the prediction of deformation, stress and pressure distributions in sedimentary basin for oil and gas exploration.

The basis of this method is the solution of the elasto-dynamic differential equation system to a system of integral equations of Fredholm type, as a response to an analog delta loading or to its spacial derivatives.

The method shows advantages due to the finiteness and smoothness of the integral kernel, that makes it possible to solve the elastic problem for surfaces, where the normal vector can be a point of discontinuity.

The application of this novel method is on a classical synthetic seismic model where there is control on the physical parameters.

A rock reservoir is limited above and below by a contact surface, and it can be assymetrical and steep, and is naturally characterized as a low pressure zone.

---

The idea is to complement the work-study under way, with the theory and application of the numerical method for the modeling of assymetrical and steep surfaces.

As a last subject for this introduction, are the perspective for a continuation under the line of sedimentary basin modeling based on seismic information, together as a post-stack methodology, where we include the velocity analysis and effective media, petrophysics, stack, migration, geological interpretation, geometry of the reflectors, target reservoir, stress, deformation and pressure variation, under tectonic and thermal history.

## 2 MODEL OF THE STRUCTURED CONTINUUM, AND THE RELATION BETWEEN SPECIFIC SUR- FACE AREA, POROSITY AND PERMEABILITY

Contrary to the Cauchy and Poisson classical seismic theory of the continuum, the new theory for structured (also called porous, fractured, or blocked) media must contain several degrees of freedom. This fact is evident because elementary blocks (grains) may transfer the motion by contact interaction, by rotation, and by group of particles. Therefore, the energy content is not only contained within the first spatial derivatives (strains), but the potential energy content is within the second (curvatures) and other higher order spatial derivatives. Thus, the equation of motion of porous media should contain higher order spatial derivatives, and may even contain infinite order spatial derivatives.

### 2.1 Introduction

This chapter introduces a major project aiming to predict the stresses and strains using P and S wave velocities to localize small pressure areas in oil and gas productive layers as natural suction pumps. The project is divided into different relative independent parts.

The first part, for stress prediction, is related to conventional seismic investigations to obtain information on the P and S wave velocities, and also the configuration of seismic boundaries.

The second part will predict the stress and strain in the geological structures using the information obtained in the first part. Additionally, the nontrivial behavior of pressure will be predicted, because pressure can increase and decrease in depth, and create what we call natural pumps that is the mechanism to push fluids towards the low pressure zones. Predicting these natural pumps is a major aim of this project.

The third element of stress prediction is related to predicting the discontinuity in pressure between solids and fluids, which depends on pore space structure; the present study falls within this third piece.

To begin predicting the stress and strain for real geological structures, we need to know the P and S velocities and the seismic boundary configuration, which is a separate classical seismic problem. In the present description, we focus on isotropic models, but the equations are more complicated for anisotropic situations.

The data acquired must contain three components. From land-observed data, we

can use S waves from horizontal vibroseis with VSP technology. From marine observed data, we can use AVO technology to look for converted P-S-P waves. In certain cases, we can use petrophysical measurements of borehole data.

The first discussions on the topic of pore space and integral geometry were presented by Sibiryakov (2002) and Sibiryakov and Prilous (2007). The theory of porous media is based on integral geometry because this mathematical discipline addresses collective geometrical properties of real collectors (reservoirs). Santalo (1953) showed that these collective properties correspond to porosity, specific surface area (SSA) parameter, average curvature and Gaussian curvature. For example, porous and cracked media generally have a small porosity, but very large SSA parameter, which creates anomalous high  $\gamma = \frac{v_S}{v_P}$  ratios, and which results in negative Poisson coefficient,  $\sigma = \frac{1-2\gamma^2}{2-2\gamma^2}$ .

The popular tubular pore space model has very high cross-sectional curvature,  $K_1$ , and very small longitudinal curvature,  $K_2$ . Therefore, the Gaussian curvature  $K_G = \sqrt{K_1 K_2}$  is much less than average curvature  $K_A = \frac{K_1 + K_2}{2}$ . In granular media,  $K_G$  and  $K_A$  are similar (SMIRNOV, 1964).

## 2.2 Methodology

### 2.2.1 Equation of motion for structured media

The new structured continuum model contains an internal geometry of a micro-inhomogeneous medium described mainly by porosity and the SSA parameter. By structured continuum model, we mean a media formed by grains and/or by blocks, limited by cracks and/or porous containing fluids (gas, water, oil), as depicted in Figs. 2.1 and 2.2.

The porosity,  $f$ , is described as a fraction of the empty volume space,  $V_E$ , to the total volume,  $V_T$ , of the material including the solid and empty space:  $f = \frac{v_E}{v_T}$ . The empty space may contain gas and liquid.

The SSA parameter is the ratio between the real surface of pores (and cracks) and the volume of the specimen,  $\sigma_0 = \frac{S}{V_T} [\text{cm}^{-1}]$ , and this quantity is used to solve petrophysical and chemical problems; the SSA is measured from mercury (Hg), and from gas absorption methods. Examples of geometrical figures, for instance, from a tetrahedron to a sphere provide decaying values of the form  $\sigma_0 \propto \frac{1}{a}$ , where  $a$  is the solid parameter, such as radius or length of a regular side (MAVKO; MUKERJI; DVORKIN, 1999).

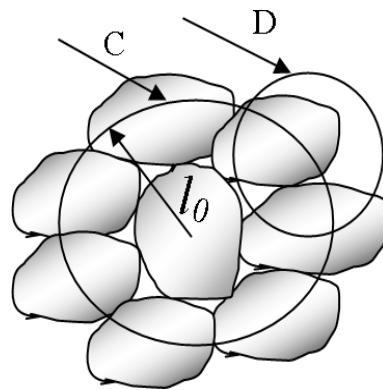
Fig. 2.1 shows a volume element of a structured body, where  $l_0$  is the average distance between grains (or the distance between pores). A theorem of Integral Geometry

relates the SSA parameter  $\sigma_0$  to  $l_0$  by the formula, Sibiryakov (2002),

$$\sigma_0 l_0 = 4(1 - f). \tag{2.1}$$

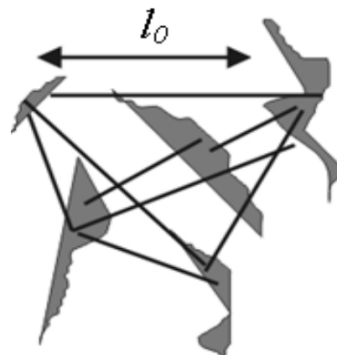
This same Eq. (2.1) applies to Fig. 2.2 that presents a different situation, where a volume element of a structured body is characterized by cracks, and also by the SSA parameter  $\sigma_0$ , and by the arithmetic average distance,  $l_0$ , between the grains (or the distance between the cracks). In grainular media, we have negative curvature for the grains, but positive curvature for the pore space. In cracked media, we generally find zero curvature for the boundary porous/solid. Positive solid curvature for cavernous pores gives a large pressure jump between solid and liquid (LANDAU; LIFSCHITZ, 1961).

Figure 2.1 – Element of the structured medium, where  $l_0$  is an average distance between grains or porous. The problem is to create an equilibrium equation for an arbitrary element of the discrete medium. An equation of equilibrium exists for the surface  $C$ , but does not for the surface  $D$ .



Source: From autor

Figure 2.2 – Another complex element of the structured medium, where  $l_0$  is an average distance between grains or cracks.



Source: From autor

In Eq. (2.1),  $f$  is the porosity; therefore, given a sample with the SSA  $\sigma_0$ , there is automatically an average size  $l_0$  for the microstructure. The distinction between the classical and structured continuum should be clear in Figs. 2.1 and 2.2. In the volume bounded by the surface  $C$ , there is an equation of equilibrium because all forces cancel, while there is no equation of equilibrium in the volume bounded by surface  $D$  because all forces are concentrated on one side of the grain, and the other side contains no forces.

The objective here is to create a new spatial model for wave propagation in structured media characterized by porosity, permeability, and specific surface area.

We consider some finite body volume, where surface forces are applied on a sphere of radius  $l_0$ , while the inertial forces are applied in the structure center. It is not possible to make an elementary volume approach zero, making the points of the surface to coincide to the point in the center, and the inertial forces are similar to the classical continuum; we must consider a finite volume as a representative body volume, and the inertial forces at different positions on the surface.

The main feature of this approach is to fill all space, including pores and cracks, with a force field. This approach provides a continuous image of a real, complicated medium. The natural laws must apply to continuous image of the medium, and not to the real image. The one-dimensional space operator for field translation from point  $x$  to point  $x \pm l_0$  is given by the symbolic equation, Maslov (1973),

$$u(x \pm l_0) = u(x)e^{\pm l_0 D_x}. \quad (2.2)$$

This form applies to any field, and here  $u(x, y, z, t)$  stands for particle displacement, and  $\dot{u}(x, y, z, t) = \frac{d}{dt}u(x, y, z, t)$  for particle velocity.

From formula (2.2), the one dimensional field translation operator,  $D_x = \frac{\partial}{\partial x}$ , can be rewritten for 3D space as follows, Sibiryakov and Prilous (2007),

$$P(D_x, D_y, D_z) = \frac{\sinh(l_0\sqrt{\Delta})}{l_0\sqrt{\Delta}} = E + \frac{l_0^2}{3!}\Delta + \frac{l_0^4}{5!}\Delta\Delta + \dots, \quad (2.3)$$

where  $E$  is the unit operator,  $\Delta$  is the Laplace operator, and  $\frac{\partial^2}{\partial x^2} + \frac{\partial^2}{\partial y^2} + \frac{\partial^2}{\partial z^2} = \Delta$ . The operator  $P$  is also represented by the special symbolic averaging operator given by:

$$P(D_x, D_y, D_z) = \frac{1}{4\pi} \int_0^{2\pi} \int_0^\pi e^{l_0(D_x \sin\theta \cos\phi + D_y \sin\theta \sin\phi + D_z \cos\theta)} \sin\theta d\theta d\phi \quad (2.4)$$

In a classical continuum, we apply the impulse conservation law,  $F_i = m\ddot{u}_i$ , to any element of the medium, or under the form  $F_i = \frac{\partial \sigma_{ik}}{\partial x_k} = \rho \frac{\partial^2}{\partial t^2} u_i$  where  $m$  stands for mass, and  $\rho$  for density.

In the present case, we need to fill all pore space by a force field, and we write the infinite order equation of motion as:

$$P \left( \frac{\partial \sigma_{ik}}{\partial x_k} \right) = \left( E + \frac{l_0^2}{3!}\Delta + \frac{l_0^4}{5!}\Delta\Delta + \dots \right) \frac{\partial \sigma_{ik}}{\partial x_k} = \rho \frac{\partial^2}{\partial t^2} u_i. \quad (2.5)$$

Instead of real stress, which may change from a large value (in the grain) down to zero (in the pore space), we use the image of real stress. Namely, we use a continuous field constructed by applying the  $P$  operator to the real complicated force field. For this continuous image of real stress,  $P(\sigma_{ik})$ , we can apply the conservation law of physical impulse. In a classical model of the continuum, the operation  $P = E$  comes from nature itself. The constructed model (2.5) of the continuum requires some mathematical operations to create the continuum medium.

Considering the one-dimensional case for simplicity and extracting results considering plane waves, stationary motion,  $u(x, y, z, t) \rightarrow u(x, \omega = k_B v_B; l_0)$ , we have a simpler infinite order equation of motion in the form, Sibiryakov and Prilous (2007),

$$\left( E + \frac{l_0^2}{3!} \frac{\partial^2}{\partial x^2} + \frac{l_0^4}{5!} \frac{\partial^4}{\partial x^4} + \dots \right) u_{xx} + k_B^2 u(x, k_B; l_0) = 0, \quad (2.6)$$

where  $k_B = \omega/v_B$  stands for both P and S waves. Considering only one term, we write Eq. (2.6) as:

$$u_{xx} + k_B^2 u = 0. \quad (2.7)$$

Considering only two terms, we write Eq. (2.6) as:

$$u_{xx} + \frac{l_0^2}{3!} u_{xxxx} + k_B^2 u = 0. \quad (2.8)$$

We can examine a solution of the equation of motion (2.6) in the stationary form,

$$u(x, y, z, t) = U(x, y, z) e^{i\omega t}. \quad (2.9)$$

For one dimensional case,  $U(x, y, z)$  has the form  $U(x)$ , and:

$$U(x) = A(k) e^{ikx} = A \left( \frac{\omega}{v} \right) e^{i \frac{\omega}{v} x}. \quad (2.10)$$

We are not applying the Fourier transform, but are examining discrete values of the temporal radial frequency ( $\omega$ ), and of the wavenumbers ( $k_x, k_y, k_z$ ).

### 2.2.2 Condition for a negative poisson coefficient

Substituting representation (2.10) into Eq. (2.6), we obtain the dispersion equation for the unknown wavelength  $k = \frac{2\pi}{\lambda}$ ,

$$\frac{\text{sen}(kl_0)}{kl_0} = \left( \frac{k_B}{k} \right)^2, \quad (2.11)$$

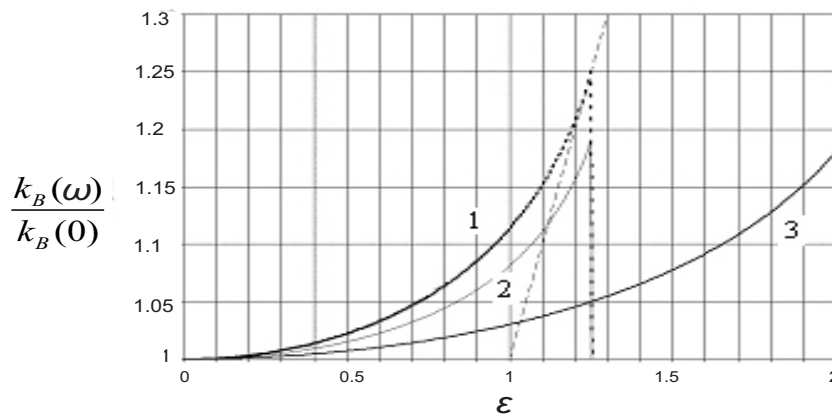
where  $k_B = \frac{\omega}{v_B}$  ( $v$  is velocity and  $\omega = 2\pi f$ ) is the wavenumber of the usual P or S waves. Eq. (2.11) is a transcendental equation with respect to the unknown  $k$ . For the condition  $l_0 \rightarrow 0$ ,  $k \rightarrow k_B$ , we have the usual wave velocities infinite small structures. In the case

that  $l_0$  is not very small, then  $k < k_B$ , the dispersion velocity  $v = \frac{\omega}{k}$  is greater than  $v_B$ , and the  $v_P$  and  $v_S$  velocities are decreasing due to structure.

Numerically examining Eq. (2.11) shows that the P-wave velocity decreases more rapidly than the S-wave velocity. Therefore, the ratio  $\gamma = \frac{v_S}{v_P}$  may be greater than  $\frac{1}{\sqrt{2}}$ . For the classical continuum model,  $\gamma = \sqrt{\frac{\mu}{\lambda+2\mu}}$ , and if  $\lambda = 0$ , the  $\gamma = \sqrt{\frac{1}{2}} \approx 0.705$ , where  $(\lambda, \mu)$  are the Lamè parameters. Now, if we measure  $\gamma > 0.705$ , we must have  $\lambda < 0$ . As a result, the Poisson coefficient  $\sigma = \frac{1}{2} \frac{\lambda}{\lambda+\mu}$  is negative because  $\lambda < 0$ , and for small values the denominator is positive. Experimental observations of this strange result were first published by Gregory (1976). The negative Poisson coefficient is due to a dispersion phenomenon in structured media. The real Poisson coefficient measured in statics, instead of wave propagation, does not produce such a strange result.

Fig. 2.3 shows the relation between the P and S wavenumbers,  $\frac{k_B(\omega)}{k_B(0)}$ , versus the ratio  $\varepsilon = 2\pi \frac{l_0}{\lambda_B}$ . It is clear that the P wavenumber (curve 1) increases faster than the S wavenumber (curve 3), which means that the P-wave velocity decreases faster than the S-wave velocity. The ratio  $\gamma = \frac{v_S}{v_P}$  increases from 1 to 1.25, from low to high frequencies.

Figure 2.3 – Plot of Eq. (2.11), real roots. The horizontal axis gives  $\varepsilon = 2\pi \frac{l_0}{\lambda_B}$  ratio. Curve 1 shows the increasing wavenumber ratio  $\frac{k_P(\omega)}{k_P(0)}$ ; therefore,  $v_P$  decreases by increasing frequency. Curve 3 shows the same for S waves,  $\frac{k_S(\omega)}{k_S(0)}$ , where  $v_S$  decreases with increasing frequency. Curve 2 shows the increase of  $\gamma = \frac{v_S}{v_P}$  ratio up to a negative Poisson coefficient  $\sigma$ .



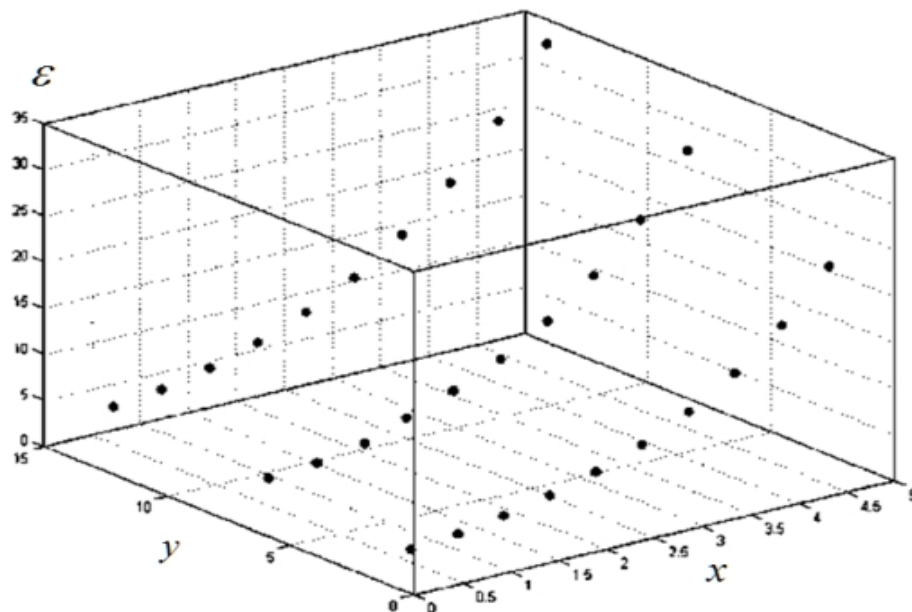
Source: From autor

Fig. 2.4 shows the real and imaginary parts of the roots of the dispersion Eq. (2.11) as a function of  $\varepsilon = 2\pi \frac{l_0}{\lambda_B}$ . The roots of Eq. (2.11) are obtained for  $kl_0 = n\pi$ , ( $n$  integer), and very large  $k$  with a velocity that is very small. The interpretation of this figure is that if  $\varepsilon \ll x$ , then there is a wave with abnormally small velocities less than  $v_S$ . Additionally, velocities are discrete in porous media, while velocities are continuous in classic media.

This situation is analogous in quantum mechanics (the discrete points represent a discrete spectrum of eigenvalues).

Clearly, Eq. (2.6) contains derivatives of infinite order, and this circumstance is due to the several degrees of freedom for structured bodies. For  $l_0 \rightarrow 0$ , we have the usual equations of motion for a classical continuum space model.

Figure 2.4 – Plot of Eq. (2.11), complex roots. The horizontal coordinates are  $x = \text{Real}(kl_0)$  and  $y = \text{Imag}(kl_0)$ . The vertical coordinate is  $\varepsilon(x, y) = k_B l_0$ . If  $k_B l_0 \ll 1$ , only real roots exist.



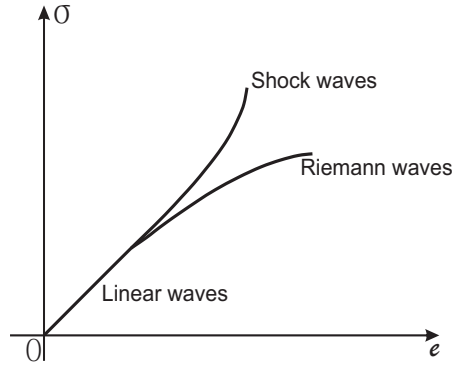
Source: From autor

### 2.2.3 The long wave approach. Equations of motion as Korteweg-De-Vries and Boussinesq types

For small  $l_0$  values compared to wavelength, it is possible to reduce the equation of motion (2.6) of an infinite order to an equation of the fourth order by neglecting the terms containing values of order  $l_0^4$  and above. In this case, we can consider some nonlinear relations between stress and strain.

Fig. 2.5 depicts a general case of linear and nonlinear stress-strain relation, and Savarensky (1975) and White (1983), among other authors, present more general cases of the stress-strain nonlinear behavior in solids. Sibiriyakov (1974) describes the two solutions for one dimensional nonlinear equation of motion. Fig. 2.5 does not show the stress and strain complexities of the loading and unloading process; therefore the area of the hysteresis loop representing dissipative energy is not present.

Figure 2.5 – Qualitative relation between stress ( $\sigma$ ) and strain ( $e = u_x$ ) showing the domains of linear elastic waves, and nonlinear Shock and Riemann waves.



Source: From autor

For the nonlinear case, the reduction of stress can take place by the increase in deformation for rocks and subsurface. Therefore, shock waves are absent in such a media, and the nonlinear waves are the Riemann waves (ZELDOVICH; RAIZER, 1966).

The reduced equation of motion (2.6) takes the following form:

$$\frac{\partial}{\partial x_k} \left( E + \frac{l_0^2}{3!} \Delta \right) \sigma_{ik} = \rho \ddot{u}_i \quad (2.12)$$

Furthermore, we consider the 1D case, and use the nonlinear relation between stress and strain given by:

$$\sigma_{xx} = (\lambda + 2\mu)(u_x - bu_x^2), \quad (2.13)$$

where  $b$  is a given constant. We can write the corresponding Eq. (2.12) in the form:

$$u_{xx}(1 - 2bu_x) + \frac{l_0^3}{3!} u_{xxxx} = \frac{1}{c^2} \ddot{u}_i. \quad (2.14)$$

By changing of variables,  $\xi = ct - x$  and  $\eta = ct + x$ , the equation of motion (2.14) reduces to a type similar to the Korteweg-de-Vries, (KdV)-equation, Dazin and Johnson (1989):

$$u_\eta - 2buu_\xi + \frac{l_0^2}{3!} u_{\xi\xi\xi} = 0. \quad (2.15)$$

The classical KdV-equation has another sign in the nonlinear term, and Eq. (2.15) thus has no solutions of the soliton type, and the role of the nonlinear term will be presented below. If the nonlinear term is absent, Eq. (2.15) is similar to the Boussinesq type, i.e.:

$$u_{xx} + \frac{l_0^3}{3!} u_{xxxx} = \frac{1}{c^2} \ddot{u}_i, \quad (2.16)$$

where the second term in the left is the dispersion term.

Now, we look at the solution of the Eq. (2.14) in the wave form given by:

$$u(t, x) = cTF \left( \frac{t - \alpha \frac{x}{c}}{T} \right), \quad (2.17)$$

where  $T$  is a characteristic time of the pulse,  $c$  is a given constant value, and  $\alpha$  is greater than unity. Changing variables as  $\xi = \frac{t - \alpha \frac{x}{c}}{T}$ , and assuming that  $F'(\xi) = \frac{\partial F(\xi)}{\partial \xi} = \varphi(\xi)$ , we can write the ordinary nonlinear Eq. (2.14) in the form:

$$\varphi'' + \frac{3!(\alpha - 1)}{l_0^2 \alpha^4} \varphi = -\frac{3!2b}{l_0^2 \alpha} \varphi^2. \quad (2.18)$$

To analyze Eq. (2.18), consider that the following quantities can be valid:

$$\frac{3!(\alpha^2 - 1)(cT)^2}{l_0^2 \alpha^4} = 1, \quad \delta = \frac{l_0}{cT}, \quad \alpha = 1 + \frac{1}{2}\delta^2. \quad (2.19)$$

Therefore, the value of  $\varphi(\xi)$  is represented by the product  $\varphi = \varphi_0 \bar{\varphi}$ , where the constant  $\varphi_0$  is equal to the characteristic value of strain; an example value, is the elastic limit of shear deformation. With the assumptions considered above, a simpler equation is obtained for the variable  $\bar{\varphi}$ . Ignoring the bar over  $\bar{\varphi}$ , we have a nonlinear equation for (2.18):

$$\varphi'' + \varphi + \beta \varphi_0 \varphi^2 = 0, \quad (2.20)$$

where  $\beta = \frac{3!2b}{\alpha \delta^2}$ . Therefore, in spite of  $\varphi_0$  being very small, and  $\beta$  being large, the product  $\beta \varphi_0$  is not very small. Additionally,  $\alpha \approx 1$ , and  $\delta$  is a very small value for the small structure size compared to the wavelength. Hence, the dispersion phenomena in micro-inhomogeneous media increase the nonlinear effects, and a form of the solution of Eq. 2.20 is shown in Figs. 2.6 and 2.7.

The rigorous solution of Eq. (2.20) is given by the following in implicit elliptical integral form:

$$\xi = \frac{t - \alpha \frac{x}{c}}{T} = \int_0^{\varphi(\xi)} \frac{dp}{\sqrt{1 - p^2 - \beta \varphi_0 p^3}}. \quad (2.21)$$

This solution for  $\beta \varphi_0 \rightarrow 0$  tends to the usual sinusoidal function, and is written as:

$$\int_0^{\varphi} \frac{dp}{\sqrt{1 - p^2 - \beta \varphi_0 p^3}} = \frac{t - \alpha \frac{x}{c}}{T} \approx \arcsin(\varphi(\xi)), \quad (2.22)$$

from where, for  $\beta \varphi_0 = 0$ ,

$$\varphi(\xi) = \sin\left(\frac{t - \alpha \frac{x}{c}}{T}\right), \quad (2.23)$$

corresponds to a consistent sinusoidal solution.

A more common exact solution of Eq. (2.20) takes a form:

$$\frac{t - \alpha \frac{x}{c}}{T} = \int_0^{\varphi} \frac{dp}{\sqrt{C_1 + Cp + 1 - p^2 - \beta \varphi_0 p^3}}, \quad (2.24)$$

where  $C_1$  and  $C$  are arbitrary constants, and the integral (2.24) describes a wider class of phenomena than the integral (2.21).

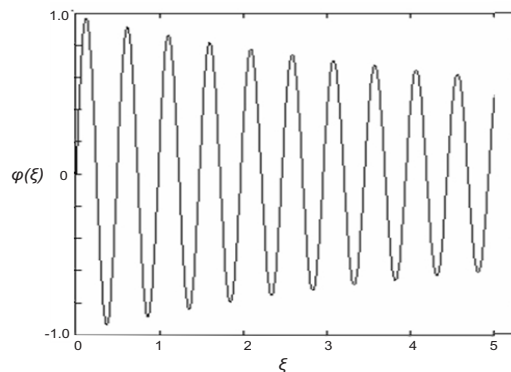
We can linearize Eq. (2.20) using, instead of function  $\varphi^2$ , the good approximation  $\varphi^2 = \varphi\varphi_0 = \varphi(\xi)\cos(\xi)$ , in which the  $\cos(\xi)$  term is the solution of the linear equation found when  $\beta\varphi_0 \rightarrow 0$ . In other words, we can write  $\varphi^2 \approx \varphi\cos(\xi)$ , and  $\xi = \frac{t-\alpha\frac{x}{c}}{T}$ . As a result, we can linearize Eq. (2.20) to a form of Mathieu's equation that describes the parametric resonance of mechanical excitation and oscillation given by:

$$\varphi'' + \left(1 + \frac{\varphi_0}{\delta^2} \cos(\xi)\right) \varphi = 0. \quad (2.25)$$

This equation contains both, stable and unstable solutions. The instabilities contain attenuation and increasing vibrations as catastrophes. The role of the parameter  $\varphi_0$  is not for its small value, but is more significant under the ratio  $\frac{\varphi_0}{\delta^2}$ .

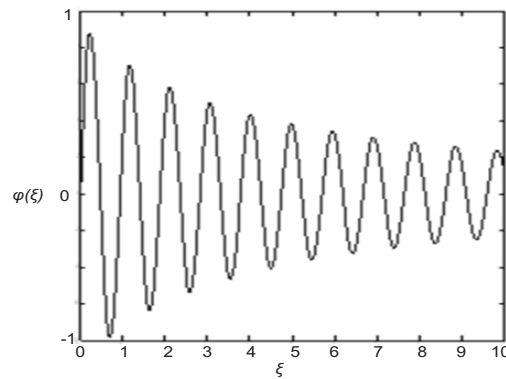
The attenuation of a sinusoidal pulse with distance due to nonlinearity is shown in Figs. 2.6 and 2.7. The nonlinearity parameter is not very small due to the large factor  $\frac{1}{\delta^2}$ . These figures show how the attenuation of a sinusoidal pulse should appear. When the nonlinear parameter is equal to zero, i.e.,  $\beta\varphi_0 = 0$ , attenuation is absent; if  $\beta\varphi_0 = 0.1$ , a small attenuation occurs with almost constant logarithmic decrement; for larger nonlinear parameter, say  $\beta\varphi_0 = 0.5$ , sufficient attenuation occurs without of constant decrement. Eq. (2.25) also contains increasing solutions, but we deal only with damping vibrations in this paper.

Figure 2.6 – Qualitative plot of the function  $\varphi(\xi)$  as a result of the inverse of Eq. (2.21) showing the attenuation with distance of an initial normalized sinusoidal causal pulse. The horizontal axis is divided in units 1 to 10, and the vertical axis normalized between -1.0 and +1.0. The nonlinear parameter is  $\beta\varphi_0 = 0.1$ . The logarithmic decrement is nearly constant.



Source: From autor

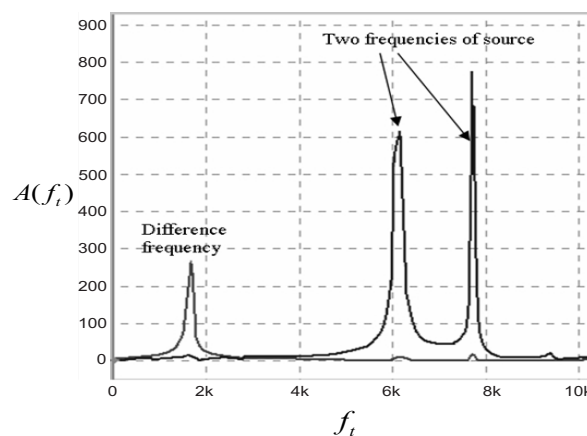
Figure 2.7 – Qualitative plot of the function  $\varphi(\xi)$  as a result of the inverse of Eq. (2.21) showing the attenuation with distance of an initial normalized sinusoidal causal pulse. The horizontal axis is divided in units 1 to 10, and the vertical axis is normalized between -1.0 and +1.0. The nonlinear parameter is  $\beta\varphi_0 = 0.5$ . The variation of the logarithmic decrement is now visible.



Source: From autor

The authors (EGOROV; MASHINSKII, 2002) realized a laboratory experiment with an artificial sample of dry sandstone (general properties: length, 1 m; diameter, 0.76 m; porosity, 0.3; and density  $2 \text{ g/cm}^3$ ) subjected to simultaneous excitation by two vibroseis with frequencies 6100 Hz and 7720 Hz. The signal spectrum was observed at the round surface of the cylindrical sample, and the source was placed at the flat end of the cylinder. The result of the experiment is shown in Fig. 2.8.

Figure 2.8 – Observed spectrum amplitude,  $A(f_t)$ , of quasi-sinusoidal signals for an artificial laboratory sandstone model. The horizontal axis shows the frequency  $f_t$  from 0 to 10.000 Hz, and the vertical axis shows the amplitude from 0 to 900 units. The data are according to Egorov and Mashinskii (2002).



Source: From autor

The receivers registered also the difference frequency of 1620 Hz at a distance of 75 cm from the source. It is interesting that the amplitude of the difference frequency is extremely high; i.e., it reached the order of 30% percent of initial signal (EGOROV; MASHINSKII, 2002). The classical approach related to the second-order equations of motion predicts this effect, which is proportional to the square of strain. The dispersion phenomena in porous media sharply strengthen nonlinear processes, so even weak fluctuations are accompanied by appreciable nonlinear effects. (MASHINSKII; EGOROV, 2011).

## 2.2.4 Porous media with viscous liquid

Let us suppose that at the gravity center (i.e., at the point  $\mathbf{x} = (x, y, z)$ ) the particle velocity is  $\dot{u}_i(\mathbf{x})$  (see Fig. 2.1). The average distance from point  $\mathbf{x}$  to the grain boundary is  $fl_0$ , and the velocity on the grain boundary is therefore represented by a Taylor series in the form:

$$\dot{u}_i(\mathbf{x}+fl_0) = \dot{u}_i(\mathbf{x})+fl_0 \left( \frac{\partial \dot{u}_i}{\partial x} \cos(r, x) + \frac{\partial \dot{u}_i}{\partial y} \cos(r, y) + \frac{\partial \dot{u}_i}{\partial z} \cos(r, z) \right) + O((fl_0)^2). \quad (2.26)$$

This expansion is bounded by the first order term with respect to  $fl_0$ , and the total sum in the right side is equal to zero. Therefore, there is no displacement between grain and viscous fluid on the boundary of the grain.

We can consider that the derivatives act on the contact skeleton-fluid with accuracy up to small values in the second order, and the center of gravity,  $\mathbf{x}$ , is in the pore. The relation between the radial and normal derivatives of the particle velocity, with components  $(x, y, z)$ , as in Eq. (2.26), is given by:

$$\frac{\partial \dot{u}_i}{\partial r} = \frac{\partial \dot{u}_i}{\partial n} \cos(r, n). \quad (2.27)$$

The average value of  $\cos(r, n)$  in three-dimensional space is 0.5. The relation between the particle velocity and the derivative of the particle velocity is given by the following:

$$\dot{u}_i = -\frac{1}{2}fl_0 \frac{\partial \dot{u}_i}{\partial n}, \quad (2.28)$$

for the sum in Eq. (2.26) to be null.

The surface force,  $F_{S_i}$ , of viscous friction is proportional to the viscosity,  $\eta$ , and to the derivative of the particle velocity,  $\dot{u}$ , with respect to the normal,  $n$ , to the surface that separates matrix and fluid:

$$F_{S_i} = \eta \frac{\partial \dot{u}_i}{\partial n} = -2 \frac{\eta}{fl_0} \dot{u}_i. \quad (2.29)$$

The volume force of viscous friction is a product of the surface force to the SSA parameter of the pore space, i.e.:

$$F_i = \sigma_0 \eta \frac{\partial \dot{u}_i}{\partial n} = -2 \frac{\sigma_0 \eta}{fl_0} \dot{u}_i = 8 \frac{\eta(1-f)}{fl_0^2} \dot{u}_i. \quad (2.30)$$

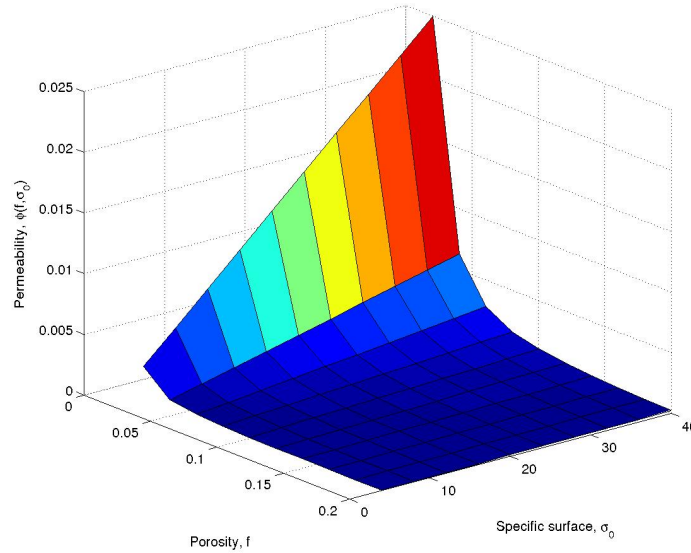
In formula (2.30), the factor  $\frac{1}{2f}\sigma_0^2$  plays the role of inverse permeability, which means that the permeability  $\phi$  is a geometric parameter, and we have the equality:

$$\phi(f, \sigma_0) = 2\frac{f}{\sigma_0^2}. \quad (2.31)$$

This formula is shown in Fig. 2.9, from which we learn that  $\sigma_0$  diminishes the permeability very quickly.

This approach shows that it is unnecessary to use Darcy's law for wave physics or percolation (BIOT, 1962).

Figure 2.9 – Plot of Eq. (2.31). The horizontal axis are porosity,  $f$ , and the SSA parameter,  $\sigma_0$ , and the vertical axis is the permeability,  $\phi = \phi(f, \sigma_0)$ .



Source: From autor

In the structured continuum model, the forces created by internal stresses act via the  $P$ -operator. The Eq. (2.6) of motion is of infinite order, because many internal waves with different velocities exists in micro-inhomogeneous bodies. The Cauchy-Poisson hypothesis is that  $P = E$ , which means that any property is an average for any arbitrary small volume. In reality, it is not possible to use arbitrary small volumes, because the representative volume must contain some elementary structures (grains), and they have internal motions, rotations, etc. If  $l_0 \Rightarrow 0$ , we have the classical standard equation of motion, and  $P = E$ .

Considering one dimensional case, in the classical continuum ( $P = E$ ) model we obtain the wave equation:

$$u_{xx} = \frac{1}{c^2}\ddot{u}. \quad (2.32)$$

And with viscous friction included we obtain the Telegraph equation:

$$u_{xx} = \frac{1}{c^2}\ddot{u} + \frac{\beta}{f}\dot{u}, \quad (2.33)$$

where we have added the dissipative forces in the second term on the right of Eq. (2.32), based on the Eq. (2.30). Here,  $\beta$  can be summarized as  $\beta = \sigma_0^2 \frac{\eta}{M}$ , where  $M = \rho c^2$ . Therefore,  $\beta = \beta_P = \sigma_0^2 \frac{\eta}{\lambda+2\mu} [TL^{-2}]$  is a property of the stress relaxation time for the P waves, and  $\beta = \beta_S = \sigma_0^2 \frac{\eta}{\mu}$  for the S waves, where we can see that  $\beta_S$  is larger than  $\beta_P$ . The quantities  $\lambda$  and  $\mu$  are the Lamè parameters, and  $\eta$  the viscosity.

For the solution of Eq. (2.33), we separate the amplitude and time components in the form:

$$u(x, t) = U(x)e^{i\omega t}. \quad (2.34)$$

Substituting (2.34) into (2.33), we obtain the differential equation for the amplitudes given by:

$$U'' + \left( \frac{\omega^2}{c^2} - i \frac{\beta\omega}{f} \right) U = 0. \quad (2.35)$$

For the solution of (2.35) we find that:

$$U = U_0 e^{mx}, \quad \text{and} \quad m = \pm \sqrt{\frac{\omega^2}{c^2} - i \frac{\beta\omega}{f}}. \quad (2.36)$$

Therefore, Eq. (2.34) has now the form:

$$u(x, t) = U_0 e^{i\omega(t \pm \frac{x}{c} \sqrt{1 - i \frac{c^2\beta}{f\omega}})}. \quad (2.37)$$

Let's analyze two conditions for binomial expansion of the square root in the exponent of (2.37). The first is for  $\frac{\omega\beta}{f} \ll 1$ , then:

$$\sqrt{1 - i \frac{c^2\beta}{f\omega}} \approx 1 - i \frac{c^2\beta}{2f\omega}. \quad (2.38)$$

The attenuation is the imaginary part of the exponent and, from (2.37) and (2.38), it is given by:

$$e^{i\omega \frac{x}{c} (i \frac{c^2\beta}{f\omega})} = e^{-x \frac{c\beta}{f}}, \quad (2.39)$$

that does not depend on  $\omega$  frequency. The second is for the opposite situation,  $\frac{\omega\beta}{f} \gg 1$ , where we have the attenuation in the form:

$$e^{-x \frac{\beta\omega}{\sqrt{f\omega}}} = e^{-x\beta\sqrt{\omega}} \quad (2.40)$$

which gives the attenuation proportional to the square root of the  $\omega$  frequency.

For porous media, the viscous friction creates velocities only by the fluctuation of particles, and the friction forces therefore act by the  $P - E$  operator (SIBIRYAKOV;

PRILOUS; KOPEYKIN, 2011). The equation of motion in this porous and viscous media can be represented in the form:

$$P \left( \frac{\partial \sigma_{ik}}{\partial x_k} \right) - i \frac{\beta \omega}{2f} (P - E)U + k_B^2 U = 0, \quad k_B = \frac{\omega}{v_{P,S}}, \quad (2.41)$$

where  $U = U(x, y, z, \omega)$ . The corresponding dispersion equation is given by:

$$\frac{\text{sen}(kl_0)}{kl_0} \left( k^2 - i \frac{\beta \omega}{2f} \right) + i \frac{\beta \omega}{2f} = k_B^2. \quad (2.42)$$

The case  $l_0 \rightarrow 0$ ,  $k^2 \rightarrow k_B^2$ , means that in classical continuum media, with infinitely small structure size, the viscous friction is absent.

Continuing examining the dispersion Eq. (2.42), then for small values of  $l_0$  we have the expansion:

$$\frac{\text{sen}(kl_0)}{kl_0} = 1 - \frac{(kl_0)^2}{3!} + \dots, \quad (2.43)$$

and we can now write Eq. (2.42) as:

$$k^2 - i \frac{\beta \omega}{3!2f} (kl_0)^2 = k_B^2. \quad (2.44)$$

Using the relations  $\sigma_0 l_0 = 4(1 - f)$  and  $\beta = \sigma_0^2 \frac{\eta}{\rho c^2}$ , we can write (2.44) in the form:

$$k^2 \left( 1 - i \frac{4\eta(1-f)^2}{3f} \omega \right) = k_B^2. \quad (2.45)$$

Then, we can write:

$$k \sqrt{\left( 1 - i \frac{4\eta(1-f)^2}{3f} \omega \right)} = k_B. \quad (2.46)$$

For small ratios  $\frac{\eta \omega}{\rho c^2} \ll 1$ , we have that:

$$k \left( 1 - i \frac{2}{3} \frac{4\eta(1-f)^2}{3f} \omega \right) \approx k_B. \quad (2.47)$$

Now, we need an approximation for the wavenumber  $k$  in terms of  $k_B$ , and:

$$k \approx \frac{k_B}{\left( 1 - i \frac{2}{3} \frac{4\eta(1-f)^2}{3f} \omega \right)}, \quad (2.48)$$

after an expansion,

$$k \approx k_B \left( 1 + i \frac{2}{3} \frac{\eta(1-f)^2}{\rho c^2 f} \omega \right), \quad (2.49)$$

where the structure parameters  $(f, \eta, \rho, c)$  and  $\omega$  are present in the complex part.

## 2.3 Conclusions

Presently, fluid percolation theory based on Darcy's law ignores stress-strain state in solids. Additionally, this percolation theory contains porosity, but does not contain the SSA parameter that creates forces to stop percolation.

We need to predict the stress-strain in solids, and pressure discontinuity between phases; and this discontinuity depends on the structure of pore space, and not only on porosity.

It is unnecessary to use Darcy's law for determining permeability, because permeability is only a geometric property of porous medium. The permeability value is directly proportional to porosity, and is inversely proportional to the square of the SSA parameter for a specimen. In a submitted paper, Sibiryakov, Leite and Vieira (2013b), we show that the fluid velocity ( $\dot{u}_0$ ) into a borehole is approximated by  $\dot{u}_0 = K f \eta \sigma_0^{-2}$ , where  $K$  is a constant,  $f$  is porosity,  $\eta$  is the viscosity, and  $\sigma_0$  the SSA parameter. In this equation,  $\eta$  is usually included into  $K$ , leaving  $f \sigma_0^{-2}$  playing the role of permeability.

Porosity and the SSA parameter enable using alternative methods to measure the permeability.

The equation of motion for long wavelengths compared to the specimen structure does not result in the wave equation, but in the telegraph equation that describes the propagation and diffusion of waves.

### 3 BEHAVIOR OF STRESSES AND HYDRODYNAMICS FROM MULTICOMPONENT SEISMIC DATA

A method for fluid-stress modeling of 3D seismic, and drilling data, provided new information on the stress conditions, and on the hydrodynamics of the U11 layer of the Upper Jurassic sandstone reservoir in the Arigol field, Western Siberia, Russia. It is proposed to detect and outline oil fields, and divide them into isolated traps, marked by low sedimentary overburden pressure, and fluid-trapping properties based on correlation between the structural pattern and mapped stress. A different systematic approach, that implies on the use of 3D component seismic data, on  $v_P$  and  $v_S$  velocities, on density  $\rho$ , for stress modeling of reservoirs, to detect the areas of low overburden pressure  $P(x, y, z)$ , and vertical inclination of fractures (faults),  $\varphi(x, y, z)$ , caused by the nonhydrostatic behavior of stress.

#### 3.1 Introduction

In the new fluid-stress model, contour lines of anomalous overburden pressure ( $P$ ) are used as hydrodynamic barriers for hydrocarbon migration, and the geometry of fluid flow lines (horizontal pressure gradients) corresponds to barriers between traps.

The areas of detected fluid-stress traps depend on the choice of the boundary values of constant overburden pressure and its horizontal gradients. It is proposed to map fluid-stress traps, and to predict their sizes in a way similar to that for structural-depositional and structural-stratigraphic traps.

Deep drilling within the hydrodynamic screened traps should be undertaken, if they fall into the most contrasting and unexplored low pressure ( $P$ ) anomalies, aiming at to estimate the fluid-stress properties of the section.

Unlike the traditional methods of hydrodynamic modeling, the new method is based on 3D component seismic exploration data ( $v_P, v_S, \rho$ ). Stress, shear waves, porosity, specific surface, 3D hydrodynamic pressure modeling of buried oil and gas traps have received much attention recently.

This modeling is based primarily on downhole logging followed by the estimation of porosity and permeability with implications on the inner borehole space. In this approach, seismic data are used as supplementary information to specify the structural framework, and to find relationships between the seismic image and the hydrodynamic parameters of hydrocarbon reservoirs.

This chapter is part of a study about computing stresses and strains using P and S

wave velocities in order to localize areas of small pressure in oil and gas productive layers as natural sucking pumps, and it is divided in different relative independent parts.

The first part concerns conventional seismic investigations in order to obtain information about P and S wave velocities, and also the seismic boundary configurations. The second part concerns calculating stress and strain in the geological structures using the information obtained in the first part, and also the nontrivial behavior of pressure, since it can decrease with depth, and create natural pumps which accumulates fluids, that is a major aim for calculating these natural pumps. And the third is concerned with calculating discontinuity in pressure between solid and fluid, what depends on the structure of the pore space.

In order to start to predict stress and strain for real geological structures, we need to know P and S velocities, densities, and the seismic boundaries configuration. This is a separate classical problem of seismic investigations. We restrict our present description to isotropic models, and for anisotropic cases the equations are more complicated.

It is mandatory that the acquired data be three component. From land observed data, we can use S waves from horizontal vibroseis, together with VSP technology. From marine observed data, we can use AVO technology looking for converted P-S-P waves. In special cases, we can use petrophysical measurements of borehole data.

The first appearances on pore space and integral geometry were presented by Sibiriyakov (2002) and Sibiriyakov and Prilous (2007). The theory of porous media is based on integral geometry because such mathematical discipline deals with collective geometrical properties of real reservoirs. It was shown by Santalo (1953) that such collective properties are namely for porosity, specific surface, average curvature and Gaussian curvature. For example, cracked media has, as a rule, small porosity, but very large specific surface area that creates anomalous high  $\gamma = \frac{v_S}{v_P}$  ratio, what means a negative Poisson coefficient,  $\sigma = \frac{1-2\gamma^2}{2-2\gamma^2}$ .

The popular model of tubular pore space has a very high crosssectional curvature,  $K_1$ , and a very small longitudinal curvature,  $K_2$ . This means that the Gaussian curvature  $K_G = \sqrt{K_1 K_2}$  is much less than average curvature  $K_A = \frac{K_1 + K_2}{2}$ . In granular media,  $K_G$  and  $K_A$  are close to each other (SMIRNOV, 1964).

## 3.2 Methodology

The general subject of the paper is a model for the calculation of fluid velocity prediction into borehole. This important study would be impossible without the prediction of stresses in the petroleum (oil and gas) producing layer. After stress prediction, we must predict discontinuity of pressure between the solid and liquid phases in order to calculate

fluid pressure far from well, and then calculate the velocity of fluid into borehole.

The first research paper published on this subject was Sibiriakov et al. (2004), where percolating process was not considered. Besides, there was no words about optimal coordinates for well positioning. In the present work we continue with this study, and show all steps from common stress prediction, based on multicomponent seismic, to fluid velocity prediction using laboratory measurements of the pore space structure.

The state of elastic layered media is described in the general case by six (three normal and three tangential) stress tensor components. Complex stress behavior of buried traps is modeled on the basis of P and S layer velocities, and of the bulk density of reservoir and cap rocks. Overburden pressure and tangential stress intensity (the measure of nonhydrostatic behavior of stress) are other key parameters, the so-called scalar invariants of stress tensor. Overburden pressure is one third of the sum of vertical and horizontal stresses; if they are equal, the overburden pressure is simply the weight of the overlying (SIBIRYAKOV, 2004).

Stress is nonhydrostatic even in horizontal layered media subject to only vertical gravity compactation without horizontal displacement. Vertical stress is defined as equal to the weight of the overburden in the form:  $\sigma_{zz} = P_z = P_0$ . The correspondent horizontal stress is sufficiently lower than  $P_z$ , and given by:  $\sigma_{xx} = P_x = P_0(1 - 2\gamma^2)$ , ( $\sigma_{xx} = \sigma_{yy}$  in this case, and applied in this paper example), where  $\gamma = \frac{v_s}{v_p}$  (SIBIRYAKOV et al., 2004).

Pressure is always a scalar quantity, and the simplest case for overburden pressure is  $P = \frac{1}{3}(\sigma_{xx} + \sigma_{yy} + \sigma_{zz}) = P_0(1 - \frac{4}{3}\gamma^2)$ , which is sufficiently less than the overlying weight  $P_z$ .

Structural effects complicate stress modeling, since in the general case the equilibrium equations should be integrated with the boundary conditions of loading continuity, displacement on layer boundaries, and zero stress on the free Earth's surface. However, overburden pressure depends on velocity ratio ( $\gamma$ ) and rock density.

Note that overburden pressure breaks at layer boundaries if the velocity ratio  $\gamma$  has a jump. In the simplest case of layered media, the jump of overburden pressure at layer boundaries is  $\Delta P = \frac{4}{3}P_0(\gamma_1^2 - \gamma_2^2)$ . Therefore, overburden pressure drops jumpwise with depth, if the underlying ( $\gamma_2$ ) velocity ratio is higher than the overlying ( $\gamma_1$ ) one. This idea would appear strange to geologists, but it is a fact related to the nonelementary behavior of stress in solids.

The behavior of continuous vertical stress at layer boundaries is rather simple, whereas horizontal stress behaves in a complex way and changes jumpwise, which causes the nonelementary behavior of overburden pressure as the sum of vertical and horizontal stresses. As a result, low-pressure zones favorable for accumulation of fluids can arise even in the absence of anticlines. The presence of an anticline complicates the drop of

overburden pressure, as rocks slide down the fold limbs produce additional horizontal extension, but this is not a necessary condition for the emergence of a favorable setting for fluid accumulation.

The intensity of tangential stress is a measure of mechanic instability, and it is the parameter responsible for the failure of the solid rock skeleton and fracturing. In simple layered media, tangential stress, scalar invariant,  $P_T = J = \frac{1}{2}(\sigma_{zz} - \sigma_{xx})$ , also depends on velocity ratio, and it is shown to be given by  $J = \gamma^2 P_z$ . Obviously, tangential stress increases with depth and rock weight, which should cause fracturing and failure. Tangential stress breaks at layer boundaries if velocity ratio  $\gamma$  differ in the different layers, and this discontinuity occurs also in the general case when tangential stress shows complex dependence on wave velocities and boundary geometry. The proportions between individual components of tangential stress and their intensities controls the inclination of fractures. Note that the above considerations concern primarily the present stress field. This is especially important in calculating fluid flow into boreholes, as the underground hydrodynamics is apparently controlled uniquely by the actual rock stress.

The key stress parameters of a section discontinuity (namely, overburden pressure, normal components of horizontal stress, intensity of tangential stress), for horizontal and nonhorizontal boundaries, depend on the velocity ratio (Poisson's ratio) change at these boundaries. Therefore, multicomponent P and S wave seismic surveys are indispensable in studies of stress conditions of oil and gas traps. It does not mean that experiments should include both P and S surveys, but multicomponent VSP, multicomponent modifications of ultrasonic logging, or laboratory measurements of samples, can be used.

In addition, maps of stratigraphic surfaces, if they include the above stress parameters listed, should give two sets of data: one for the layer below, and the other for the layer above the mapped surface. Only three stress components are continuous in the general case, and the other three show jumpwise changes at layer boundaries.

Computing stress components implies integration of equations of equilibrium, that is a system that reflects the fact that the stress-induced 3D forces are equal to the gravity force (weight, overload, overload weight,  $mgz$ , mass  $\times$  acceleration  $\times$  thickness, stress dimension), whereas the horizontal forces cancel each other and their sum is zero.

The system of equations includes six unknown stresses and only three equations of equilibrium. Thus, it is not closed in the general case, but it can be made closed using an elastic model of stress-strain relationship. This is justified by relative simplicity of the model, and by the possibility to measure the elastic constants using P, S and PS waves. The closed system of partial derivative equations can be transformed into a system of integral singular equations. Methods for the transformation of these singular systems into regular ones were suggested by Kupradze (1963) and Parton and Perlin (1985), and they imply in the use of conjugate operators of fundamental solutions. Sibiryakov and Zaikin

(1994) have applied this method for 2D applications to stress modeling in seismic sections in East and West Siberia.

However, direct extrapolation of the method for 3D problems complicates the computation. It can be simplified in view of the fact that many geological structures in West Siberia are quite shallow dipping; i.e., one tangential stress component is small relative to the two others. Sibiryakov and Zaikin (1994) used a particular solution to inhomogeneous equilibrium equations as Poisson-type integrals where the integration is made over the structure volume. The effect of 3D structures on stress is more local than of 2D ones, as it decreases in inverse proportion to the square distance from the structure.

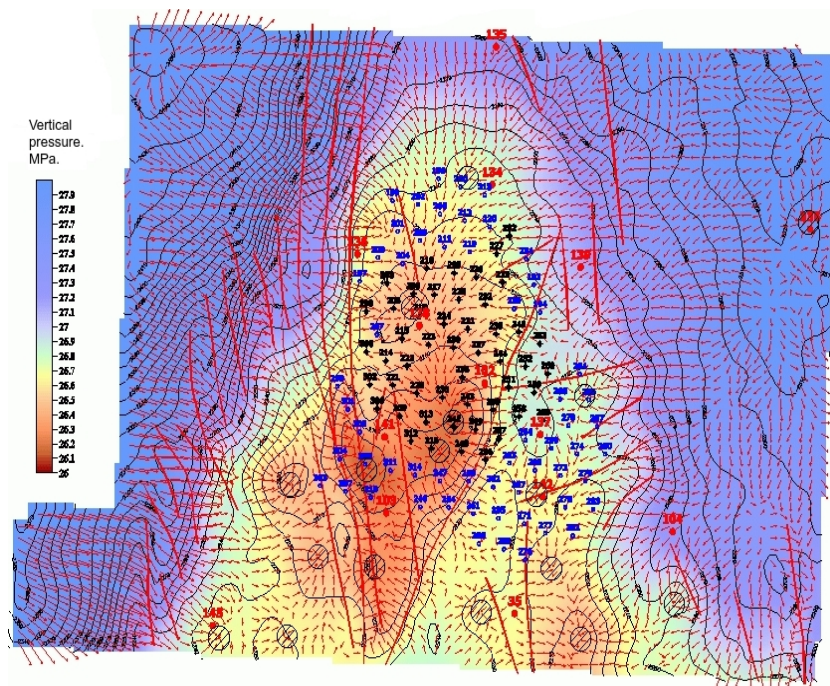
We propose here a new method to calculate Poisson-type curvature integrals that are reduced to a succession of 2D quadratures followed by common 1D integration. Stress is defined by velocity discontinuity and the effect of structure geometry.

As an example from the Arigol field, the local high (Vakh pattern holes) contribution due geometry is 20% of the total effects. Therefore, the overburden pressure in the producing bed, and in the layers below and above, is controlled mainly by the velocity ratio. The area has hundreds of wells, and the overburden stress was estimated using density logs. The distribution of layer P wave velocities was obtained by CMP stacks and VSP data from three boreholes. The greatest difficulty was in the estimation of velocity ratio, since there was no direct P or S velocity measurements made. Nevertheless, petrophysical data used ultrasonic measurements of the Jurassic sandstones, and allowed to find that the  $\gamma$  ratio for the producing bed ranges between 0.577 and 0.550. Velocity ratio for other layers were inferred from density-velocity relationships.

It is obviously expected that if the  $\gamma$  ratio is higher in the producing bed, its overburden pressure is lower than in the overlying. Indeed, the pressure deficit in the producing bed is about 50 atmospheres in the average (SIBIRIAKOV et al., 2004).

Figure 3.1 shows overburden pressure on the roof of a Jurassic reservoir. First, the pressures are about 30% lower than in the overlying layer. Second, the pressure in the producing bed shows about to 5 MPa drop at the transition to the overlying layer. The layer fluid pressure differs from the mapped overburden pressure.

Figure 3.1 – Map of tectonic stress (represented by pressure  $P$ ) of Jurassic reservoir, where the contour lines are overburden pressure  $P = P_0(1 - \frac{4}{3}\gamma^2)$  (dark blue lines) drawn in an arbitrary scale, and superposed to the color scale. Orthogonal trajectories are probable fluid flow lines (red arrows). The pressure scale is in color and placed on the left side, and shows variations between 26-28 Megapascal (MPa), 1 MPa=10 atmospheres. The center of the map is dominated by a low pressure zone. The dots with numbers are producing boreholes. Heavy red lines are geological faults. Isolated circular enclaves correspond to local hydrodynamic systems.



Source: From autor

The pressure discontinuity between the rock skeleton and the fluid is controlled by the structure of the pore space and by the skeleton-fluid compressibility ratio. However, the orthogonal trajectories, to the shown contour lines of overburden pressure, coincide with fluid flow lines, if the pore space structure in the producing bed remains invariable (SIBIRIAKOV et al., 2004).

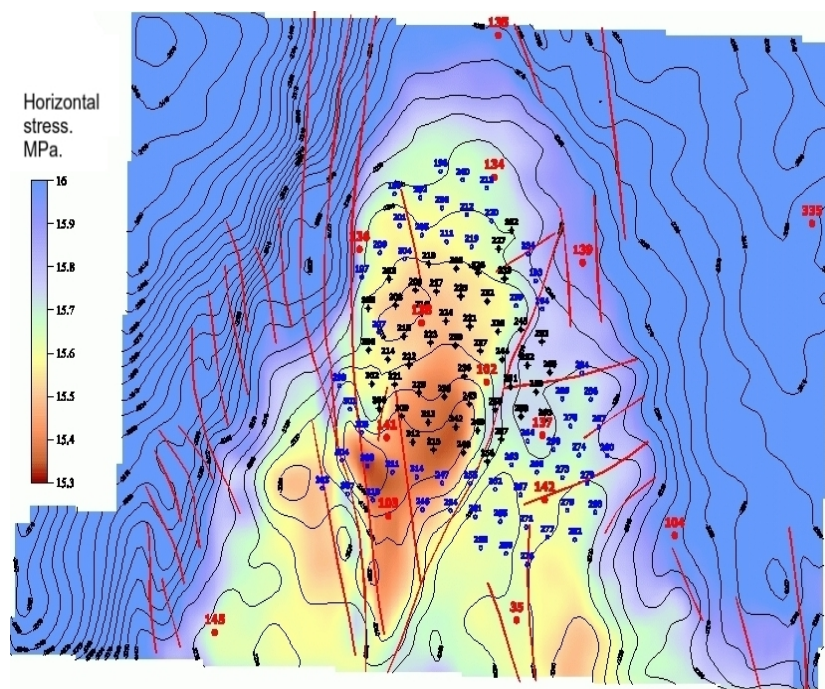
Examining the probable flow lines and calculated points of discharge in Figure 3.1, the local enclaves of these lines may account for depth variations of the oil-water contact (OWC). Therefore, orthogonal to pressure isolines on the surface of the producing bed are the probable fluid flow lines, and the sinks point to fluid and gas discharge. This fact should be taken into consideration as an additional criterion in the selection of new exploratory drilling sites.

Still referring to Figure 3.1, the overburden pressure and intensity of tangential stress estimated on the basis of velocity ratio  $\gamma$  were assumed constant over the reservoir,

and the flow lines are thus tentative. Almost all lines converge toward the top of the structure. The points of local discharge, to the right and left of the main borehole complex, are prominent even in this generalized model. More detailed information from S-wave data may provide a basis for higher-resolution map of local discharge in the producing bed.

Figure 3.2 shows the map of tangential stress intensity for the same surface of Figure 3.1, where the region of lowest pressure almost coincides with faults within the region of minimum tangential stress, which indicates a certain stability of the structure as a whole. High tangential stresses cluster near a fault, which appears as a rather realistic result.

Figure 3.2 – Map of intensity of tangent stress,  $J = \gamma^2 P_0$ , as a measure of nonhydrostatic pattern (dark blue lines), where the high values are located around small stress zones. The lines are drawn in an arbitrary scale, and superposed to the color scale. The color pressure scale is on the left side and shows values between 15.3-16.0 in MPa. The dots with numbers are producing wells. Heavy red lines are geological faults.



Source: From autor

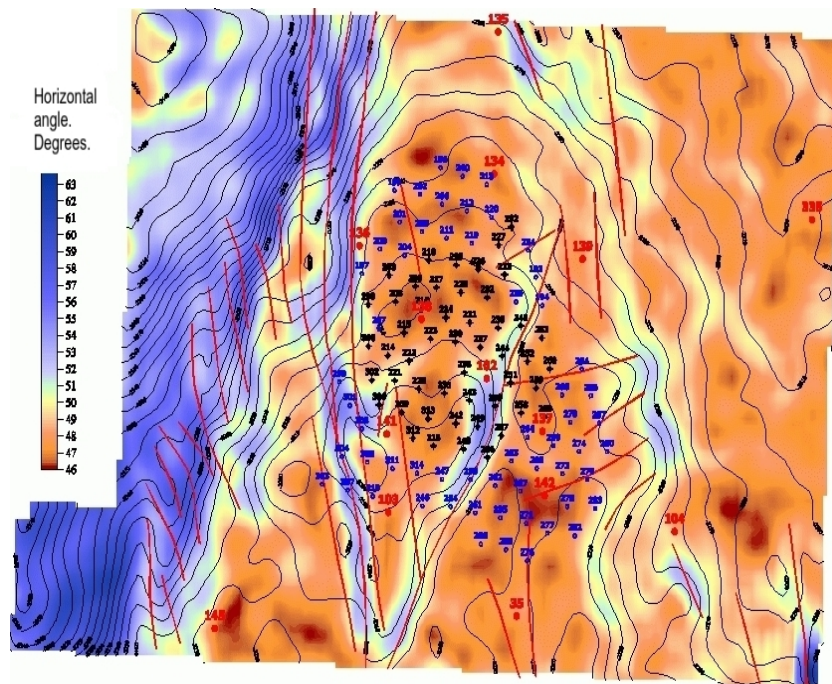
Maximum tangential stresses do not always coincide with faults detected by geological methods; possibly, because not all faults may be associated with the present-day stresses. This regularity can be used in age discrimination of faults.

Figure 3.3 shows calculated fracture inclinations,  $\phi(x, y, z)$ , around the structure. The fracture planes are inclined about 45 degrees with respect to the vertical, which may correspond to either randomly oriented fractures or to anisotropic medium with rhombic symmetry. However, fractures change their inclinations near faults to roughly vertical

inclinations, thus producing another preferred inclination. This result can be checked by shear-wave splitting techniques in multi component VSP.

The vertical inclination of fractures, called  $\phi(x, y, z)$ , are obtained from the rotation of the stress system to give the stress diagonal matrix, where the diagonal elements are the main stresses, and where  $\sigma_{xx} \approx \sigma_{yy}$  (NOVACKY, 1970).

Figure 3.3 – Map of calculated fracture inclinations  $\phi(x, y, z)$  in producing bed. The color scale of the left shows a variation between 46 and 64 degrees with respect to the vertical (to the left and/or to the right). The blue areas shows roughly vertical fractures, and the brown areas show more Normal fractures with a more chaotic distribution. In the center of the map, we can describe more randomly inclined fractures (darker areas). The dots with numbers are producing wells. Heavy red lines are geological faults.



Source: From autor

### 3.2.1 Physical-mathematical theory

We now follow with the physical-mathematical theory necessary to give a basement, and explain the results presented in Figures 3.1, 3.2 and 3.3, and we divided it into sections.

We start with the system of equations of equilibrium used to estimate stresses as given below, where two differential equations are homogeneous and one nonhomogeneous (SIBIRYAKOV; PRILOUS, 2007):

$$\frac{\partial \sigma_{xx}}{\partial x} + \frac{\partial \sigma_{xy}}{\partial y} + \frac{\partial \sigma_{xz}}{\partial z} = 0, \quad (3.1)$$

$$\frac{\partial \sigma_{yx}}{\partial x} + \frac{\partial \sigma_{yy}}{\partial y} + \frac{\partial \sigma_{yz}}{\partial z} = 0, \quad (3.2)$$

$$\frac{\partial \sigma_{zx}}{\partial x} + \frac{\partial \sigma_{zy}}{\partial y} + \frac{\partial \sigma_{zz}}{\partial z} = \rho g. \quad (3.3)$$

The first two Eqs. (3.1) and (3.2) correspond to full cancellation of horizontal 3D forces produced by inner stresses, and the last one means that vertical 3D forces are simply equal to the normalized gravity force.

The common solution of this system is to obtain the displacement components, and it is given by the sum of the fundamental solution,  $u_k^F$ , obtained for the complete homogeneous system, and of particular solution,  $u_k^P$ , given by the above nonhomogeneous system, in the form:  $u_k = u_k^F + u_k^P$ . To obtain this solution, it is used boundary integral methods. The result is a type of Poisson's integral, which illustrates the participation of additional displacement and stress, represented by volume  $V$ , due to more or less complex geometry of geological structures. The fundamental solution of the system of Eqs. (3.1), (3.2) and (3.3) is given by Novacky (1970) in the form:

$$u_k(\mathbf{x}) = \frac{g}{v_S^2} \int_V \Gamma_{kz}(\mathbf{x}, \mathbf{y}) dV_y. \quad (3.4)$$

The additional displacement  $u_k(\mathbf{x})$ , due to structure deformation, is the integral of the fundamental solution,  $\Gamma_{kz}(\mathbf{x}, \mathbf{y})$ , over the structure volume  $V$  of the equilibrium equation. It depends on the square S-wave velocity, and  $z$  in  $\Gamma_{kz}$  relates to the vertical component, as in the gravity  $g$ . The integration covers all the volume represented by the  $\mathbf{y}$  coordinate.

### 3.2.2 Pressure discontinuity between rock skeleton and fluid

Consider a fluid-filled reservoir, and let  $u_n$  be the normal displacement of a grain skeleton. Applying the Gauss theorem, we obtain:

$$\iint_S u_n ds = \iiint_V \text{Div } \vec{u} dV = fV \frac{P_0}{\rho_0 c^2}, \quad (3.5)$$

where  $S$  is the grain surface,  $V$  the total volume,  $fV$  is the pore space volume,  $P_0$  is the fluid pressure, and  $\rho_0 c^2$  is the fluid inverse compressibility (noncompressibility). Also,

$$\iint_S u_n ds = \langle u_n \rangle S, \quad (3.6)$$

where  $\langle u_n \rangle$  is the mean normal displacement, and by substituting this formula in Eq. (3.5) gives:

$$\frac{P_0}{\rho_0 c^2} = \frac{1}{f} \frac{\langle u_n \rangle}{r_0} \sigma_0 r_0, \quad (3.7)$$

where  $\sigma_0 = \frac{S_P}{V_T}$  is the Specific Surface Area (SSA) ( $S_P$  is the total empty porous, and  $V_T$  is the total volume of sample), and  $r_0$  is the mean grain radius.

In a solid grain, the relation:

$$\Delta(u_i + x_i e) = 0 \quad (3.8)$$

is a rigorous relationship, where  $\Delta$  is the Laplace operator,  $u_i$  is the displacement in grain, and  $e$  is the dilatation of the grain material. By definition, pressure is given by the dilation times the bulk module, as:

$$P = e(\lambda + \frac{2}{3}\mu). \quad (3.9)$$

Eq. (3.8) means, that the sum  $u_i + x_i e$  is a harmonic vector. As its mean value is zero in the grain center, we can assume this harmonic function to be zero in the grain material, and make a relationship between displacement,  $u_i$ , and dilatation,  $e$ ; in other words,  $u_i = -x_i e$ , and also for the average value in the form:

$$\langle u_n \rangle = - \langle e \rangle r_0. \quad (3.10)$$

Eq. (3.10) relates normal displacement in liquid and dilatation in solid.

Substituting the relations (3.10) and (3.9) into Eq. (3.7), we can write in explicit form the pressure discontinuity,  $\frac{P_0}{P}$ , between solid and liquid in the form:

$$\frac{P_0}{P} = \frac{\sigma_0 r_0}{f} \frac{\rho_0 c^2}{\lambda + \frac{2}{3}\mu}. \quad (3.11)$$

Eq. (3.11) shows that the pressure gradient in solid,  $\nabla P$ , perfectly coincides with the fluid flow lines if the pore structure,  $\nabla P_0$ , and it remains invariable in the producing layer, if the structure of the pore space (porosity and specific surface) are constant in this layer.

The pressure discontinuity depends on the ratio of two nondimensional parameters of the pore structure; to be specific, the product of the SSA ( $\sigma_0$ ) by the mean grain radius ( $r_0$ ) and inverse porosity ( $f^{-1}$ ). Yet, Eq. (3.11) contains small factors in the numerator and in the denominator which may lead to the instability of the estimation, especially in the case of a gas-saturated fluid.

Compressibility decreases abruptly at low gas contents, and viscosity varies slowly. Therefore, gas saturation of liquids is not necessarily favorable to oil production, but reduces the pressure gradient which is not always canceled by the respective fluid viscosity decrease.

According to Eq. (3.10), the problem of calculating fluid flow into a borehole is reduced to the integration of Poisson's equation:

$$\Delta u_i = \frac{1}{\eta} \frac{\sigma_0 r_0}{f} \frac{\rho_0 c^2}{\lambda + \frac{2}{3}\mu} \text{Grad}_i P, \quad (3.12)$$

where  $\text{Grad}_i = \nabla_i = \frac{\partial}{\partial x_i}$ , ( $i = x, y, z$ ), and  $\eta$  the fluid viscosity. Boundary conditions for this equation (conditions of viscous adhesion) require the velocities of particles be zero over the entire complex surface of pores. The problem of integration of Eq. (3.12) and flow rate estimation requires calculating of stress and, and also the knowledge of two parameters of the pore space and fluid compressibility.

The methods of integration for Eq. (3.12) are straightforward, even in the case of an arbitrarily complex pore structure; permeability is unnecessary as it appears in a complex way as a result of phase interaction and the pore structure. In a particular case of noninteracting fractures, modeled by rectilinear segments with constant crack opening, Eq. (3.12) can be easily integrated to yield the equation for flow rate in the form:

$$\dot{u}_i = \frac{\delta^2}{12\eta} \frac{\sigma_0 r_0}{f} \frac{\rho_0 c^2}{\lambda + \frac{2}{3}\mu} \text{Grad}_i P = K \text{Grad}_i P, \quad (3.13)$$

where  $\delta$  is the mean crack opening, and  $\delta^2$  represents permeability for this particular pore structure. Thus, the pressure difference between the skeleton and the fluid depends on the geometry of the pore space (mainly on its SSA), and on the hydrodynamic properties (compressibility and viscosity) of the fluid. The problem of the pore pressure estimation cannot be solved separately from the problem of general stress calculation. Eq. (3.13) plays the role of Darcy's law for the specific model now in focus.

### 3.2.3 Percolation and permeability near borehole

Sibiriyakov (2002) described that the estimation of stresses and strains in oil-gas structure requires the integration of equations of equilibrium of the kind:

$$\frac{\partial \sigma_{ik}}{\partial x_k} = \rho g, \quad (i, j, k = 1, 2, 3; \text{ or } x, y, z), \quad (3.14)$$

for every layer.

For elastic rock deformation, the equation of equilibrium derived from Eqs. (3.1), (3.2), and (3.3) for the condition of Hooke's law, in closed form is given by:

$$(\lambda + \mu) \text{Grad}_i \text{Div} \vec{u} + \mu \Delta u_i = \rho g_i, \quad (3.15)$$

where  $g_i$ , ( $i = x, y, z$ ),  $g_z = g$ ,  $g_x = g_y = 0$  (LANDAU, 1988). The Lamé parameters  $\lambda$  and  $\mu$  are determined from P and S wave velocities.

For boundary conditions, we can write the stress for the inside of any layer as an expression of the form:

$$\sigma_{ik} n_k^+(S_m) = \sigma_{ik} n_k^-(S_m), \quad u_i^+(S_m) = u_i^-(S_m), \quad (3.16)$$

where  $S_m$  stands for a surface numbered  $m$ , and  $n^+$  and  $n^-$  points to outside or to the inside of the surface  $S_m$ .

On the free surface of Earth we have the evident stress boundary conditions in the form:

$$\sigma_{ik}n_k^+(S_0) = 0, \quad (3.17)$$

where the summation over the repeated index is implicit.

Besides conditions in Eqs.(3.16) and (3.17), there are some conditions for the lateral surfaces that bounds the oil-gas structure. For the usual case, these conditions depend on the geological structures, but often these conditions are not sufficient, especially if the horizontal dimension of the structure is larger than the vertical dimension. Sometimes it is possible to use as boundary conditions the normal field of stresses without the effect of the structure.

The second part Eq. (3.16) becomes evident, because the fluid pressure equals the normal stress in solid matrix, and not the pressure in solid, because the lateral stresses are not equal to the normal stress.

To calculate a discontinuity of pressure between liquid and solid, it is necessary to integrate the equation of equilibrium in a small volume of the producing layer with boundary conditions on the pore space like:

$$\sigma_{ik}n_k^+(S) = P_\infty(S), \quad u_i^+(S) = u_i^-(S). \quad (3.18)$$

In the above equation,  $P_\infty = \text{constant}$  is the pressure in the fluid. On the external boundaries of an elementary volume (edges of cube, for example) we require the same displacements like in the edges of elastic cube without the pore space. These conditions gives the constant value  $P_\infty$ , which is in equilibrium state with respect to the stresses in the solid. We have no doubt that this pressure depends on the structure of the pore space, but first of all on the SSA of the pore space.

The first step to attack the percolation and permeability is to calculate the stress for the entire area. The second part is to calculate the stress near the borehole. And the third step is to calculate the stress discontinuity between solid and liquid. As a result, we obtain the estimation of fluid flow as a function of the common stress-strain condition on the structure of the pore space, and on the fluid viscosity.

### 3.2.4 Volume dissipative forces by viscosity

The tangential surface force,  $F_{S\tau}$ , due to viscosity is given by the expression  $F_{S\tau} = \sigma_0 \frac{\partial u_\tau}{\partial n}$ , while the tangential volume force,  $F_{V\tau}$ , due to the same effect is given by:

$$F_{V\tau} = \sigma_0 \eta \frac{\partial u_\tau}{\partial n}, \quad (3.19)$$

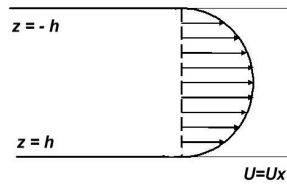
where  $\sigma_0$  is the SSA,  $\eta$  is the viscosity,  $\dot{u}$  is the particle velocity, and  $n$  and  $\tau$  are the normal and tangent directions of liquid-grain contact. For cracks sufficiently long compared to

their opening, it would be convenient to use a simpler problem from the Navier-Stokes equation; namely, the solution of the problem about flowing between two infinite plates in the form (LANDAU, 1988):

$$\frac{\partial p}{\partial x} = \eta \frac{\partial^2 u_\tau}{\partial z^2}. \quad (3.20)$$

In this equation  $p$  is pressure in liquid, and  $u_\tau = u_x = u_x(z)$  for the particular case of Figure 3.4, where  $u_y = u_z = 0$ , and it represents a layout of the physical process of the flow, showing the sticking at the boundaries.

Figure 3.4 – Cross section of flow between infinite two plates. The length of dominant fracture is much larger than the crack opening.



Source: From autor

The solution of Eq. (3.20) takes the form:

$$\frac{\partial p}{\partial x} = P = \text{constant}, \quad \dot{u}_x = \frac{P}{2\eta}(h^2 - z^2). \quad (3.21)$$

In the above equations,  $h$  is the crack opening. Hence, the surface force due to viscosity is given by the formula:

$$\eta \frac{\partial p}{\partial x} = -hP. \quad (3.22)$$

And the volume force acting in any point of the continuum is:

$$\sigma_0 \eta \frac{\partial p}{\partial x} = -\sigma_0 hP = -\frac{2\sigma_0}{h} \eta \langle u_x \rangle. \quad (3.23)$$

In the above equation  $\langle u_x \rangle$  is the average particle velocity between two planes. It means, that the Navier-Stokes equation contains an additional term that describes the volume dissipative force against the fluid velocity, namely:

$$\langle F_\tau \rangle = -k^2 \dot{u}_r, \quad (k^2 = 2 \frac{\sigma_0}{h} = \frac{\sigma_0^2}{f}), \quad (3.24)$$

where  $f$  is porosity.

### 3.2.5 Stresses in solid near borehole

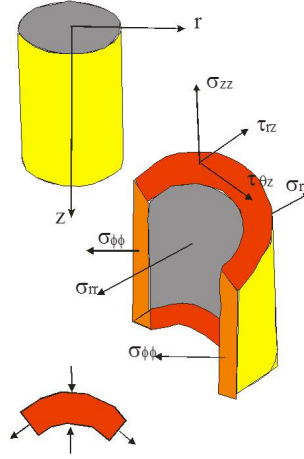
For the solid near borehole the equations of equilibrium in cylindrical coordinates are:

$$\frac{\partial \sigma_{zz}}{\partial z} + \frac{\partial \tau_{rz}}{\partial z} + \frac{\tau_{rz}}{r} = \rho g \quad (3.25)$$

$$\frac{\partial \sigma_{rr}}{\partial r} + \frac{\sigma_{rr} - \sigma_{\varphi\varphi}}{r} + \frac{\partial \tau_{rz}}{\partial z} = 0. \quad (3.26)$$

The correspondent pattern of stresses are shown in Figure 3.5.

Figure 3.5 – Stress nomenclature in cylindrical coordinates, and the representation of the borehole with liquid and solid around it.



Source: From autor

The above equations have very simple solutions, because for very large layer thickness in comparison to the radius of the borehole, the tangent stress  $\tau_{rz}$  is equal to zero in all volume of rocks near the borehole.

There is an already known formula for the deformation ( $e$ ) of an elastic medium of density  $\rho$ , with a cylindrical cavity of radius  $r_0$ , and saturated by a liquid of density  $\rho_0$ , given by:

$$e_{\varphi\varphi}(r_0) = \frac{u_r(r_0)}{r_0} = \rho g z \left( \frac{\sigma}{1 - \sigma} - \frac{\rho_0}{\rho} \right). \quad (3.27)$$

In the above formula,  $\sigma$  is the Poisson ratio,  $u_r$  is the radial displacement, and  $g$  the gravity. Besides that, considering that there is planar incompressibility (no change in density with respect to the  $z$  coordinate, compression along  $z$ , dilation along  $(x, y)$  axis, dilation along  $z$  axis, compression along  $(x, y)$  axis) in solid, we write for the deformation that:

$$e_{rr} + e_{\varphi\varphi} = 0. \quad (3.28)$$

The respective solutions of Eqs. (3.25) and (3.26) for the elastic stresses near borehole is given by the formulas (SIBIRYAKOV, 1993):

$$\sigma_{rr} = (1 - 2\gamma^2)P_0 - \left(\frac{r_0}{r}\right)^2 P_0 \eta, \quad (3.29)$$

$$\sigma_{\varphi\varphi} = (1 - 2\gamma^2)P_0 + \left(\frac{r_0}{r}\right)^2 P_0 \eta. \quad (3.30)$$

In Eqs. (3.29) and (3.30),  $\gamma = \frac{v_s}{v_p}$ ,  $P_0$  is the weight of overburden rocks, and  $\eta = 1 - 2\gamma^2 - \frac{\rho_0}{\rho}$ .

### 3.2.6 Equation of equilibrium and fluid velocity

The equation of equilibrium with dissipative force around the borehole has the following form:

$$\Delta \dot{u}_r - k^2 \dot{u}_r - \frac{1}{\eta} \frac{\partial p}{\partial r} = 0, \quad (3.31)$$

where  $\dot{u}_r$  is the particle fluid velocity in the borehole. The normalized components are: the first term ( $\Delta \dot{u}_r$ ) the volume force, the second ( $-k^2 \dot{u}_r$ ) is the volume dissipative force, and the third ( $-\frac{1}{\eta} \frac{\partial p}{\partial r}$ ) the volume force due to pressure.

Let us try to find a solution for the above Eq. (3.31), considering that there is planar incompressibility for the liquid and for the solid, and that there is a linear relationship with respect to the vertical  $z$  coordinate, like in Eq. (3.25). It means that there is a term  $\frac{\partial^2 \dot{u}}{\partial z^2} = 0$  in the Laplace operator, such that this operator simplifies to the form:

$$\Delta \dot{u}_r = \frac{\partial^2 \dot{u}_r}{\partial r^2} + \frac{1}{r} \frac{\partial \dot{u}_r}{\partial r}. \quad (3.32)$$

With the assumption of planar (not in volume) incompressibility, there is additional conditions for Eq. (3.32) in the forms:

$$\frac{\partial \dot{u}_r}{\partial r} + \frac{\dot{u}_r}{r} = 0, \quad \dot{u}_r = \frac{C(r)}{r^2}, \quad (3.33)$$

where  $C(z)$  is an arbitrary function. Besides that, we can write Eq. (3.32) in the form:

$$\frac{\partial^2 \dot{u}_r}{\partial r^2} + \frac{1}{r} \frac{\partial \dot{u}_r}{\partial r} = \frac{\partial}{\partial r} \left( \frac{\partial \dot{u}_r}{\partial r} + \frac{\dot{u}_r}{r} \right) + \frac{\dot{u}_r}{r^2} = \frac{\dot{u}_r}{r^2}. \quad (3.34)$$

Substituting Eq. (3.34) in Eq. (3.32) gives a simpler expression for Eq. (3.31) in the form:

$$\frac{\partial p(r)}{\partial r} = \eta \left( \frac{C(z)}{r^3} - k^2 \dot{u}_r \right). \quad (3.35)$$

Integrating the above equation with respect to  $r$ , with inferior limit  $r$  and superior  $R$ , follows that:

$$p(r) = P_\infty - \eta \left( \frac{C(z)}{2r^2} - k^2 C(z) \ln \frac{R}{r} \right). \quad (3.36)$$

To take into account, that on the borehole surface  $r = r_0$ ,  $p \rightarrow P_0$ ,  $R \gg r_0$ , and  $p(R) = P_\infty$  we get:

$$p(r_0) = P_0 = P_\infty - \eta \left( \frac{\dot{u}_0}{2r_0} + k^2 \dot{u}_0 r_0 \ln \frac{R}{r_0} \right). \quad (3.37)$$

In the above equation,  $R$  is the horizontal range of producing layer,  $P_\infty$  is the pressure in liquid outside the borehole (very far from it, and inside the reservatory), and  $P_0$  is the pressure in borehole liquid.

From Eq. (3.37), we obtain the fluid velocity,  $\dot{u}_0(r_0)$ , into borehole in the form, and in its approximations:

$$\dot{u}_0(r_0) = \frac{P_\infty - P_0}{\eta} \frac{2r_0}{1 + 2k^2 r_0^2 \ln \frac{R}{r_0}} \approx \frac{P_\infty - P_0}{\eta} \frac{1}{r_0 \ln \frac{R}{r_0}} \frac{f}{\sigma_0^2} = K \frac{f}{\sigma_0^2}, \quad (3.38)$$

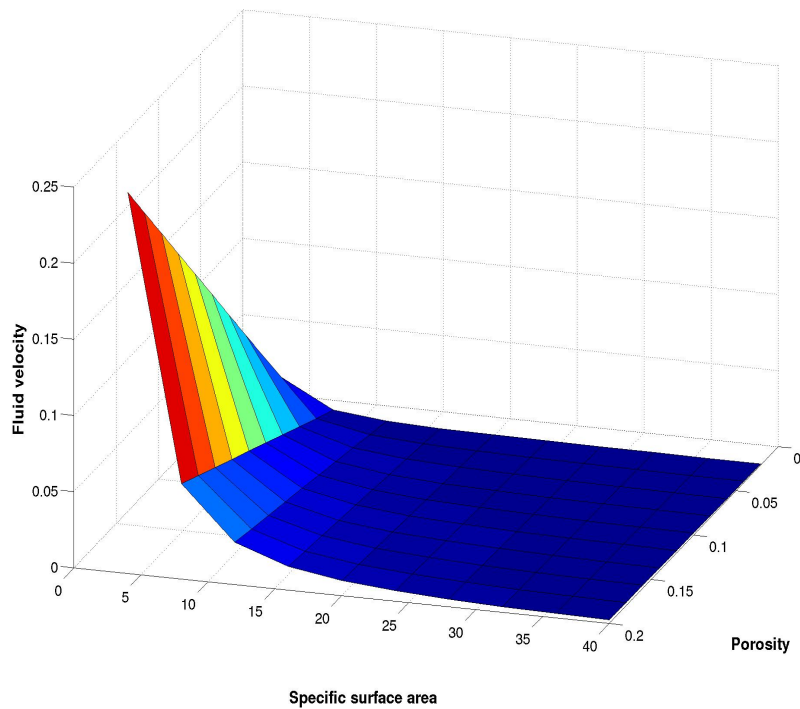
where

$$K = \frac{P_\infty - P_0}{\eta} \frac{1}{r_0 \ln \frac{R}{r_0}}.$$

We simplified to the last form to emphasize the dependence of  $\dot{u}_0(r_0)$  on  $f$ ,  $\sigma_0$ , and its ratio  $\frac{f}{\sigma_0^2}$ , with  $K$  representing a constant term. Figure 3.6 shows the plot of  $\dot{u}_0(r_0)$  versus  $\sigma_0$  and  $f$ , where the quantity  $\frac{f}{\sigma_0^2}$  plays the role of permeability.

Also, for positive pressure contrast,  $+|P_\infty - P_0|$ , the flow is from layer reservoir to borehole, and when negative,  $-|P_\infty - P_0|$ , from borehole to layer reservoir.

Figure 3.6 – Plot of the Eq. (3.38) for the velocity flow as a function of porosity,  $f$ , and SSA,  $\sigma_0$ .



Source: From autor

Due to large SSA parameter, the velocity is almost of zero flow in spite of sufficient porosity. It is interesting to mention that there is no necessity to use Darcy's law. Besides that, Eq. (3.38) does not contain the permeability coefficient,  $k$ . However, there is empiric relation between the SSA,  $\sigma_0$ , the porosity,  $f$ , and the permeability,  $k$ , namely (SIBIRYAKOV; PRILOUS, 2007):

$$k = \frac{D_p^2 f^3}{150(1-f)^2}, \quad D_p = \frac{6}{\sigma_0}, \quad (3.39)$$

where  $S_E$  is the total area of the porous space, and  $V_T$  is the total volume of the sample, and  $\sigma_0 = \frac{S_E}{V_T}$ . The Eq. (3.39) can be rewritten as:

$$\sigma_0 = \frac{\sqrt{6}}{5} \frac{f^{\frac{3}{2}}}{(1-f)\sqrt{k}}. \quad (3.40)$$

In spite of that, the percolation process depends on the porosity and on the SSA only. The hydrofracture effect is due to very small SSA for several large fractures compare to a lot of small fractures. Permeability plays the role of inverse square of the SSA.

### 3.2.7 Estimation of pressure in liquid far from borehole

The value  $P_\infty$  contained in Eq. (3.38) can be determine by solving of a problem about discontinuity between pressures of solid and liquid. The common stress-strain condition is given by integration of the equation of equilibrium Eq. (3.14), rewritten below:

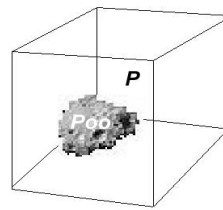
$$\frac{\partial \sigma_{ik}}{\partial x_k} = \rho g_i \quad (3.41)$$

Let us take into account usual boundary conditions like continuity of force and displacement vectors. The configuration of boundaries and elastic properties are obtained by multiwave seismic.

The pressure is always a scalar. In liquid, the pressure,  $P_0$ , is defined as the normal stress in solid represented by  $\sigma_{nn}$ . The pressure in solid,  $P_S$ , is defined as the average of normal ( $\sigma_{nn}$ ) and tangential stresses ( $\sigma_{\tau_i}$ ), in the form:  $P_S = \frac{1}{3}(\sigma_{nn} + \sigma_{\tau_1} + \sigma_{\tau_2})$ .

For simply common stress conditions with the vertical component equal to the weight of rocks, and the horizontal components containing a factor of the type  $\frac{\sigma}{1-\sigma}$ , ( $\sigma$  is the Poisson coefficient), it is possible to formulate the following problem related to Figure 3.7.

Figure 3.7 – A cube volume where the liquid has pressure is  $P_\infty$  and in the solid is  $P$ .



Source: From autor

The elementary cube is submitted to vertical displacement  $u_0$ , while horizontal displacements are equal to zero. Inside the cube there is a liquid with constant pressure  $P_\infty$ . On the boundary solid-liquid the average normal displacement is given by the formula:

$$\langle u_n \rangle = \frac{P_\infty f}{\rho_0 c_0^2 \sigma_0}. \quad (3.42)$$

Under the condition of fluid incompressibility, then for the average tangent ( $u_S$ ) displacement on the boundary solid-liquid it can be shown that:

$$\left\langle \frac{\partial u_S}{\partial n} \right\rangle = - \frac{\langle u_n \rangle}{\pi l_0}. \quad (3.43)$$

with  $l_0$  as a dominant distance between cracks. This result comes from differential geometry, and the quantities  $\left\langle \frac{\partial u_S}{\partial n} \right\rangle$  and  $\frac{\langle u_n \rangle}{\pi l_0}$  have opposite sign due to physical counter action at the boundary solid-liquid.

The relation between  $\sigma_0$ ,  $l_0$  and  $f$  is described by Sibiryakov and Prilous (2007), and it has a simply form given by:

$$\sigma_0 l_0 = 4(1 - f) \quad (3.44)$$

The simplification of boundary conditions as in Eqs. (3.42) and (3.43) gives the possibility to determine all stresses and displacements as a function of the unknown constant  $P_\infty$ . On the vertical sides of the cube there are displacements equal to constant value, but on the other side it is equal to zero. The usual boundary condition; to be specific, equality between normal force in solid and unknown pressure  $P_\infty$  in liquid, gives a functional equation for determining the value  $P_\infty$  as an inverse problem, namely:

$$\left\langle \lambda \theta(P_\infty) + 2\mu e_{nn}(P_\infty) \right\rangle = P_\infty, \quad (3.45)$$

for given  $\theta(P_\infty)$  and  $e_{nn}(P_\infty)$  functionals, with  $\lambda$  and  $\mu$  as Lamé parameters of the solid material.

### 3.3 Conclusions

We described the main steps for the estimation of complex stress behavior in a given structural-velocity model of a medium, and calculation of the storage capacity of buried traps. The first results of mathematical modeling and geological interpretation of the obtained fluid-stress maps are associated with the formation of a new step in applied geodynamics, namely fluid-stress modeling of oil and gas traps.

The basic principles of this modeling are as follows. The relationship between overburden pressure, which is a scalar function  $P(x, y, z)$ , and rock stress (six components in the 3D model ( $\sigma_{xx}, \sigma_{yy}, \sigma_{zz}, \sigma_{xy}, \sigma_{xz}, \sigma_{yz}$ )) is a fairly complex function in a general case. However, it is obvious that fluids accumulate in closed sites of porous reservoirs where the overburden pressure is minimum.

Under these assumptions, detected regions are a sort of fluid-stress traps in which hydrocarbons can accumulate rather by influence of stress ( $\sigma = \text{constant}$ ) than by structural ( $z = \text{constant}$ ) factors.

Maps of horizontal gradients of overburden pressure are especially informative for the detection and outlying these traps, and they reveal: convergent (inflow) and divergent (outflow) pressure gradients; isolated inflow regions in the detected trap separated by the geometry of outflow lines (fluid-stress barriers); and possible fluid-stress traps in structural and nonstructural conditions.

There is no possibility to use the Biot parameters, and the reason is that we have seismic waves velocities and densities of rocks, what gives a possibility to calculate Lamé's constants for the integration of equilibrium equations.

The construction of the maps of Figures 3.1 and 3.3 used log data, core samples and 3D seismic data image of the Upper Jurassic sandstone reservoir of the Arigol field, that contains numerous sites of lithological replacement and faulting. Geological prospecting surveys show different depths of oil-water contact (OWC), what contradict the accepted arch-layer model for the reservoir.

The paradoxical behavior of the OWC depths finds a sound explanation within the limits of a fluid-stress model, since the single Upper Jurassic reservoir was subdivided by us into nine fluid-stress traps on the basis of correlation of the overburden pressure and its horizontal gradients (see Figure 3.2).

Comparison of the maps of intensity of tangential stresses  $J(x, y, z) = \frac{1}{2}(\sigma_{zz} - \sigma_{xx}) = \gamma^2 \sigma_{zz}$  and of inclinations  $\phi(x, y, z)$  of stress-produced fractures (see Figures 3.2 and 3.3) leads to the following conclusions:

- faults detected from 3D seismic data correspond to local anomalies of tangential stresses;
- the observed mismatch can be related to the difference between the present-day stress and the past stress along the faults;
- different OWC depths in boreholes with numbers 124, 136, 139 can be caused by their position in different fluid-stress zones.

At this point, an interesting question arises of how to separate tangential stress (all stress out the orthogonal plane) in rock matrix from their natural fractures, since seismic data do not allow seeing in this centimeters scale (sub-seismic data). The answer is related to the scalar  $J(x, y, z)$  that is responsible to produce cracks, if it is sufficiently large, and we can only calculate the probabilistic orientation of cracks.

Note that the method of fluid-stress modeling has some limitation as quantitative estimates of stresses are, both in oil-saturated and water-saturated, as well as dry rocks. Therefore, it must always be integrated with other methods of seismic-geological modeling. At present, the fluid percolation theory based on Darcy's law says that we can ignore

stress-strain state in solids; besides, percolation theory contains porosity, and does not contain SSA that creates forces to stop percolation.

We need predict stress-strain in solid, and pressure discontinuity between phases, what depends on the structure of the pore space, and not only on porosity. Therefore, it is not necessary to use Darcy's law for determining the permeability, since it is only a geometric property of porous medium. Permeability value is directly proportional to porosity, and inversely proportional to the square of the specific surface for a specimen.

Porosity and SSA give a possibility to use alternative methods for measuring permeability.

The velocity of fluid into a borehole depends on common stress-strain conditions of the producing layer, on the structure of the pore space (SSA and porosity) and on the viscosity of the fluid.

The solution shows that the main factor of oil production is the specific surface area of porous and cracks. The solution does not contain the permeability; instead, there is the inverse square of the SSA that plays the role of permeability.

The hydrofracture effect is due to a very small SSA for several large fractures, in comparison to a lot of small fractures.

## 4 LOCAL LOW PRESSURE AREAS IN ANTICLINE STRUCTURES

In order to localize low pressures zones in sedimentary basins for oil and gas exploration, it is necessary to know P and S wave velocities for medium. Strictly speaking, we need to know the rock densities for all layers, and in addition there are many correlation tables between seismic velocities and densities; besides, density is a parameter admitted to change slowly with depth to the top of the target interface.

P wave velocities are considered a conventional asset, and S wave velocities can be obtained from special field survey, in particular from converted P-S waves registered by VSP technology, and by petrophysical measurements.

The theory in this paper deals with stress prediction in the subsurface, and takes in consideration the constitutive parameters (density and Lamé's), and the geometry of the reservoir target surface. The model does not separate the different contributions (porosity, fluids) to the rock velocities controlled by the constitutive parameters.

It is not a necessary condition that an anticline be a potential structure for oil and gas accumulation. This role can be played by horizontal structures if there is a positive  $\gamma = \frac{v_S}{v_P}$  ratio discontinuity, or a negative discontinuity of the Poisson,  $\sigma$ , ratio across the horizontal boundary. These conditions are responsible for producing a pressure discontinuity, such that beneath the boundary there will be a sufficiently lower pressure zone than above the boundary. In this case, the lower horizontal boundary is said to be an attractor surface for fluids of the any kind; in the opposite case, this boundary does not have fluid attractor properties.

### 4.1 Introduction

The anticline structure can be a very useful trap, especially if it has a negative discontinuity in the  $\gamma = \frac{v_S}{v_P}$  ratio. In this case, exists also an additional horizontal stretching due to the negative curvature of the anticline structure. It is interesting, that the effects of slope and curvature are in opposite directions; the slopes produce an additional compression, while the average curvature produces a horizontal stretching.

If there is an anticline structure with a positive discontinuity in the  $\gamma$  ratio, it can be a compensational effect. The additional pressure due to the  $\gamma$  discontinuity, and the additional stretching due to the average curvature may eliminate each other. In this case, the anticline structure is not a fluid attractor.

The present paper is part of a major project under the theme prediction of stresses

and strains using P and S wave velocities in order to localize areas of low pressure in oil and gas productive layers as natural suction pumps. This project is structured in different and independent parts, and as a result the paper Sibiriyakov, Leite and Vieira (2013b) is already accepted for publication, and another by Sibiriyakov, Leite and Vieira (2015) has been submitted and is under review.

The first part of the project is related to conventional seismic investigations in order to obtain the distribution of the P and S wave velocities, and also to obtain the configuration of seismic boundaries in sedimentary basins. The second part is related to the prediction of stress and strain in the geological structures, and also to the prediction of the nontrivial behavior of pressure, since it can decrease with depth and create natural pumps that accumulate fluids. The third part is related to the prediction of discontinuity in pressure between solid and fluid, what depends on the structure of pore space.

In the present description we restrict our attention to isotropic models, and for anisotropic situations the equations are more complicated, there are more control parameters, and the data needs more processing. Every layer forming the geological 3D structure model has constant elastic parameters.

It is mandatory that the acquired data be three components, otherwise it is necessary to apply special processing to obtain the S wave information from P-S phase conversion. S waves can be used from land data obtained with horizontal vibroseis and VSP technology, and from marine data using AVO technology looking for converted P-S-P waves. In special cases, we can use petrophysical measurements of borehole samples for  $v_P$  and  $v_S$  and density  $\rho$ .

The first published appearances about pore space and integral geometry were presented by Sibiriyakov (2002) and Sibiriyakov and Prilous (2007). The theory of porous media is based on integral geometry, because such mathematical discipline deals with collective geometrical properties of real reservoirs. It has been shown by Santalo (1953) that such collective properties are namely for porosity, specific surface area, Average curvature and Gaussian curvature (SMIRNOV, 1964). For example, cracked media have as a rule small porosity, but very large specific surface area, what creates anomalous high  $\gamma$  ratio, and it means that the Poisson coefficient,  $\sigma = \frac{1-2\gamma^2}{2-2\gamma^2}$ , can be negative, and this discussion can be seen in Sibiriyakov, Leite and Vieira (2013b) and Sibiriyakov and Sibiriyakov (2010).

## 4.2 Methodology

### 4.2.1 The role of slope angles and curvatures

In order to predict the stress-strain state in geological structures we need to integrate the elastic equations of equilibrium. The boundary conditions are for continuity of forces and displacements. The equilibrium equations contain the elastic parameters; that is, the  $v_P$  and  $v_S$  velocities, and the rock densities.

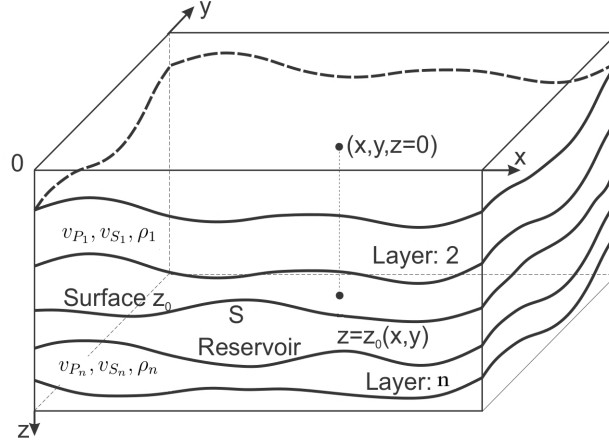
It should be clear that these parameters and the boundary configuration have to be obtained from the seismic processing and imaging. It means that we need to have detailed velocity analysis from previous investigations. As for the special case of the shear wave velocity distribution, results of exploration with special explosion and horizontal vibroseis can be used.

The stresses in geological structures represent a very complicate subject in a six dimensional space, because there are in the usual case six components of the stress tensor in any point of the medium.

The present work is dedicated to the solution of a simpler problem: the pressure prediction in the vicinity of geologic structural boundaries. The scalar invariant pressure is very important, and it is the simplest characteristic of stress-strain condition. This paper answers a question about the boundary attraction for fluids, or the condition of a boundary not being a fluid attraction.

Figure 4.1 represents a model for a sedimentary basin, where we aim at a reservoir volume limited on the top by a  $S$  surface, where the layers above it are responsible for the overload weight that causes the stress field in the underground rocks. The stress pattern varies according to the  $\gamma$  ratio, that can present important discontinuities across the interfaces. Therefore, the aim is the  $S$  surface where the stress discontinuity will varie according to its topographic form, and this effect measured by the spatial slopes and curvatures of the reference  $S$  surface. The physical aspects of this theory does not take geological faulting and lithological variations in the rock volume, and only the bending of the formations (above and below the  $S$  interface) that defines the anticline structure. For geological representations, special block drawings for reservoir representations are found, for instance, in Chopra and Marfurt (2007).

Figure 4.1 – Block perspective illustrating a sedimentary basin. It shows the Cartesian arbitrary system  $(x, y, z)$ , the layer blocks limited by curved interfaces, a subtle reservoir volume limited above by the  $S$  surface represented by  $z = z_0(x, y)$ , and a flat free surface at  $z = 0$ .



Source: From autor

In the usual case, a geological structure represents a very complicate problem for the solution of the equilibrium equations, which are given by (KUPRADZE, 1963; NOVACKY, 1970):

$$\begin{cases} \frac{\partial \sigma_{xx}}{\partial x} + \frac{\partial \sigma_{yx}}{\partial y} + \frac{\partial \sigma_{zx}}{\partial z} = 0 \\ \frac{\partial \sigma_{xy}}{\partial x} + \frac{\partial \sigma_{yy}}{\partial y} + \frac{\partial \sigma_{zy}}{\partial z} = 0 \\ \frac{\partial \sigma_{xz}}{\partial x} + \frac{\partial \sigma_{yz}}{\partial y} + \frac{\partial \sigma_{zz}}{\partial z} = \rho g \end{cases} ; \quad (4.1)$$

where the symbology and units are:  $\sigma$  [ $N/m^2$ ] for stress,  $\rho$  [ $kg/m^3$ ] for density, and  $g$  [ $m/s^2$ ] for gravity acceleration. The spatial variables  $(x, y, z)$  stand for the Cartesian system of coordinates, with  $z$  pointing positive downwards inside the underground. Physically, the system of Eqs. (4.1) means that: (1st) the sum of the stress variation along the vertical axis is given by the weight of the overburden column; (2nd) the sum of the stress variation along the horizontal  $x$ -axis is chosen to be null; and (3rd) the sum of the stress variation along the  $y$ -axis is also chosen to be null. The gravity acceleration,  $g = g(z)$ , is considered constant in the underground volume in consideration, and also  $g = g_z$  when it is needed a convenient notation.

The total solution of the system of Eqs. (4.1),  $u^{(T)} = u^{(C)} + u^{(P)}$ , is given by the complementary solution,  $u^{(C)}$ , of the three homogeneous equations, added to the particular solution,  $u^{(P)}$ , of the inhomogeneous system obtained via Green's function and convolution (ROACH, 1986).

The particular solution for the displacement component  $u_k(\mathbf{x})$ , ( $k = x, y, z$ ), is

given by the Poisson integral with respect to the structural volume  $V$  as:

$$u_k(\mathbf{x}) = g \frac{1}{v_S^2} \int_V \Gamma_{kz}(\mathbf{x}, \mathbf{y}) dV_{\mathbf{y}}. \quad (4.2)$$

It is interesting that this integral depends mainly on the shear velocity  $v_S$  [ $LT^{-1}$ ].  $\Gamma_{kz}(\mathbf{x}, \mathbf{y})$  [ $L^{-1}$ ] is the Green tensor for the system of Eqs. (4.1) (fundamental solution, where in the third equation  $\rho g$  is replaced by  $\rho g \delta(x) \delta(y) \delta(z)$ ), and it is given by Kupradze (1963).

For the solution represented by Eq. (4.2), and others in the sequel based on this formulation (see, for instance, Eqs. (4.17) and (4.31)), once the displacement field,  $u_k(\mathbf{x})$ , is known, then the deformation, stress, and pressure fields can be calculated. But, we demonstrate ahead for simple models that the contribution of the particular solution in Eq. (4.2) is small and, as a result, the complementary solution is more important.

The system of Eqs. (4.1) with the particular solution in Eq. (4.2), and a possible general complementary solution, establish a very complicate problem. To obtain a complementary solution,  $u^{(C)}$ , is already a special problem by itself.

However, we can obtain an elegant complementary solution to system of Eqs. (4.1) by considering a plausible model described by simple geometric relations for the  $S$  surface,  $z = z_0(x, y)$ , and by the overburden weight components  $P_k = \rho g z n_k$ , [ $N/m^2$ ], in the form:

$$P_x(S) = \rho g z_0(x, y) n_x; \quad P_y(S) = \rho g z_0(x, y) n_y; \quad P_z(S) = \rho g z_0(x, y); \quad (4.3)$$

where  $n_i = \cos(n, x_i)$  is the direction cosine between the surface normal vector,  $\vec{n}$ , and the arbitrary  $(x, y, z)$  Cartesian system. The stress expressions for Eqs. (4.3) (with  $\sigma$  for normal and  $\tau$  tangential stress components) on the interface  $S$  are written as:

$$\begin{cases} P_x(S) = \sigma_{xx} n_x + \tau_{yx} n_y + \tau_{zx} n_z |_{S} = \rho g z_0(x, y) n_x \\ P_y(S) = \sigma_{yy} n_y + \tau_{xy} n_x + \tau_{zy} n_z |_{S} = \rho g z_0(x, y) n_y \\ P_z(S) = \sigma_{zz} n_z + \tau_{xz} n_x + \tau_{yz} n_y |_{S} = \rho g z_0(x, y) \end{cases} \quad (4.4)$$

We can now consider that the rock displacements on the boundary  $z = z_0(x, y)$  to be related with the vertical displacement by the formulas:

$$u_x = u_z \cos(\rho g, x); \quad u_y = u_z \cos(\rho g, y); \quad \cos(\rho g, z) = 1. \quad (4.5)$$

On the boundary, represented by the surface  $z = z_0(x, y)$ , the vertical strain is given by the relation:

$$e_{zz} = \frac{\partial u_z}{\partial z} = \frac{\rho g z(x, y)}{\lambda + 2\mu}; \quad (4.6)$$

that comes from Eqs. (4.1) considering a flat structure. Under integration, Eq. (4.6) gives the displacement,

$$u_z(z_0(x, y)) = \int_0^{z_0} \frac{\rho g z(x, y)}{\lambda + 2\mu} dz = \frac{\rho g z_0^2(x, y)}{2(\lambda + 2\mu)}. \quad (4.7)$$

In the above equation, the quantities  $\rho$  and  $g$  are allowed to varie as a function of  $z(x, y)$ ; but, the solution in the right hand consider them constant with  $z(x, y)$ .

The horizontal strain,  $e_{xx} = \frac{\partial u_x}{\partial x} = u_{x,x}$ , with Eq. (4.5), using the convenient symbology, is expressed by:

$$e_{xx} = \frac{\partial}{\partial x} u_z(x, y) \cos(n, x); \quad (4.8)$$

with the result under derivation by parts,

$$e_{xx} = u_{z,x} \frac{z_{0,x}}{\sqrt{1 + z_{0,x}^2 + z_{0,y}^2}} - u_z \frac{z_{0,xx}}{\sqrt{1 + z_{0,x}^2 + z_{0,y}^2}} \left( 1 - \frac{z_{0,x}^2}{1 + z_{0,x}^2 + z_{0,y}^2} \right). \quad (4.9)$$

For the above Eq. (4.9),

$$u_{z,x}(x, y) = \frac{\rho g}{\lambda + 2\mu} z_0(x, y) \frac{\partial z_0(x, y)}{\partial x}. \quad (4.10)$$

Eq. (4.9), with Eq. (4.7), can be rewritten in the following form:

$$e_{xx}(z_0(x, y)) = \frac{\rho g z_0}{\lambda + 2\mu} \frac{z_{0,x}^2}{\sqrt{1 + z_{0,x}^2 + z_{0,y}^2}} - \frac{\rho g z_0^2}{2(\lambda + 2\mu)} \frac{z_{0,xx}}{\sqrt{1 + z_{0,x}^2 + z_{0,y}^2}} \left( 1 - \frac{z_{0,x}^2}{1 + z_{0,x}^2 + z_{0,y}^2} \right). \quad (4.11)$$

The total dilatation ( $\theta = \nabla \cdot \vec{u}$ ) (vertical compression and horizontal decompression) on the boundary  $z = z_0(x, y)$  takes the result:

$$\theta(z_0(x, y)) = \frac{g z_0}{v_P^2} \left[ 1 + \frac{z_{0,x}^2 + z_{0,y}^2}{\sqrt{1 + z_{0,x}^2 + z_{0,y}^2}} \right] - \frac{g z_0^2}{2v_P^2} [z_{0,xx}\varphi_1(x, y) + z_{0,yy}\varphi_2(x, y)]; \quad (4.12)$$

where,

$$\varphi_1(x, y) = \frac{1 + z_{0,y}^2}{(1 + z_{0,x}^2 + z_{0,y}^2)^{3/2}}; \quad \text{and} \quad \varphi_2(x, y) = \frac{1 + z_{0,x}^2}{(1 + z_{0,x}^2 + z_{0,y}^2)^{3/2}}. \quad (4.13)$$

The quantity named Pressure  $P$  is defined as the average of the normal stresses; that is:

$$P = \frac{1}{3} (\sigma_{xx} + \sigma_{yy} + \sigma_{zz}); \quad (4.14)$$

and it is the first invariant of the stress tensor. Using the generalized Hooke's law for isotropic medium:

$$\sigma_{ij} = \lambda \theta \delta_{ij} + 2\mu e_{ij}; \quad (4.15)$$

the pressure in Eq. (4.14) is now directly related to the dilatation, and we specify it in the form,

$$P_\theta = \left( \lambda + \frac{2}{3}\mu \right) \theta = K\theta, \quad (4.16)$$

where  $K = \lambda + \frac{2}{3}\mu$  stands for the pressure module.

Some observations about the dilatation Eq. (4.12) are now important.

First, that Eq. (4.12) depends on  $v_P$ , and on the first and second order space derivatives of the surface  $z = z_0(x, y)$ . The first derivative terms,  $(z_{0,x}(x, y), z_{0,y}(x, y))$ , are slope angles. The second derivative terms,  $(z_{0,xx}(x, y), z_{0,yy}(x, y))$ , relate to the surface general curvature (SMIRNOV, 1964).

Second, in the case that the P wave velocity does not change across the boundary (this is very rare situation), the dilatation has a continuous value. But, in the usual case the P wave has a discontinuity across the boundary and, as given above, the pressure is given by the product of pressure module ( $K$ ) to the dilatation ( $\theta$ ), that can also change across the boundary (SIBIRIAKOV et al., 2004).

Third, the first term of the Eq. (4.12) contains the square of the first derivative, which means that, for not very large angles, the slope effect results in the increase of pressure due to the structure. However, the curvature effect is more interesting.

Fourth, for negative curvature (anticline structure) there is a decrease in pressure, and this effect increases with depth due to the  $z_0^2(x, y)$  factor in the second term of Eq. (4.12), instead of in the first term where there is the factor  $z_0(x, y)$ .

Fifth, and continuing, the sign of the second derivative is negative, and the curvature is also of a negative value. This means, the anticline structure produces a low pressure zone, which is a favorable condition for fluid accumulation.

For positive curvature (sincline structure), we have the opposite effect.

Sixth, consider the ideal case of a spherical arc; then, the value of the second term in Eq. (4.12) may have the value of the first term. This means that the negative curvature produces a planar stretching near the top and shortening near the rim.

Seventh, the first term in Eq. (4.12) is related to the slope angles, with a positive contribution to the dilatation. This means that this term produces an increase in compression as a function of the increase in the amplitude of the anticline structure.

The question that we raise now is: When is it possible that the simple representations in Eq. (4.5) is sufficiently accurate to diminish the pressure field in the vicinity of the anticline dome?

It should also be clear that the contributions of the Poisson integral in Eq. (4.2) to the displacement and stress fields are small, in comparison to the fields due to elementary geometrical and physical properties of structures (tangent and vertical forces, and displacements along the structure boundary).

### 4.2.2 Contribution of the poisson integral to displacements

We can represent the contribution of the Poisson integral Eq. (4.2) to the displacement field as the difference of two integrals in the form:

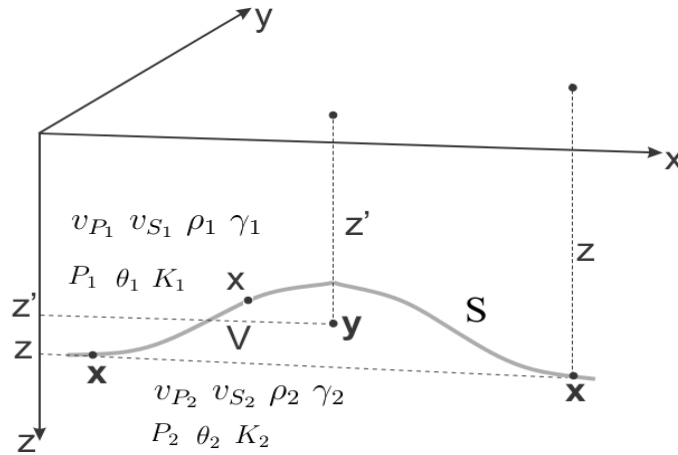
$$\Delta u_k(\mathbf{x}) = g \left( \frac{1}{v_S^{(+)2}} - \frac{1}{v_S^{(-)2}} \right) \int_V \Gamma_{kz}(\mathbf{x}, \mathbf{y}) dV_{\mathbf{y}}, \quad (4.17)$$

where  $v_S^{(+)}$  (above) and  $v_S^{(-)}$  (below) are seismic wave velocities across the structure  $S$  boundary. The integrand is the Green tensor given by:

$$\Gamma_{kz}(\mathbf{x}, \mathbf{y}) = \frac{1}{8\pi} \left[ (1 + \gamma^2) \delta_{kz} + (1 - \gamma^2) \frac{(\mathbf{x}_k - \mathbf{y}_k)(z - z')}{r^2(\mathbf{x}, \mathbf{y})} \right] \frac{1}{r(\mathbf{x}, \mathbf{y})}, \quad (4.18)$$

where  $\mathbf{y} = (x', y', z')$  is the integration variable throughout the volume  $V$ . The two integrals in Eq. (4.17) are interpreted as material substitution: the first integral relates to the material which is eliminated from the structure, and the second to the material which is occupied by the real structure. Fig. 4.2 illustrates the coordinate system, the geometry of the reservoir volume  $V$ , the integration variable  $\mathbf{y}$  in the volume  $V$ , and the reference point  $\mathbf{x}$  along the  $S$  surface.

Figure 4.2 – Block diagram representing a reservoir volume  $V$  limited above by the surface  $S$  represented by  $z = z_0(x, y)$ . The integration variable  $\mathbf{y}$  and the  $S$  surface reference point  $\mathbf{x}$  are also shown.



Source: From autor

The quantity  $r$  is the geometrical distance between the  $\mathbf{x}$  and  $\mathbf{y}$  points. The contribution in Eq. (4.17) vanishes if the velocities  $v_S^{(+)}$  and  $v_S^{(-)}$  are equal. On the other hand, the displacement field due to the elementary method expressed by Eqs. (4.6) and (4.7) is given by:

$$u_z^0 = \frac{\rho g z_0^2}{2(\lambda + 2\mu)} = \frac{g z_0^2}{2v_P^2}. \quad (4.19)$$

Let us consider a simple but important structure model represented by a spherical body characterized by the volume  $V = \pi R^2 h$ , where  $R$  is the average radius of the structure, and  $h$  is the amplitude. The result for the integral in Eq. (4.17) gives a simple and good numerical condition for an estimation method (formulas of the type in Eq. (4.12)), that is given by:

$$\frac{Rh}{8} \frac{\Delta v_S}{v_S} \ll 4\gamma^2 z_0^2; \quad (4.20)$$

where  $\Delta v_S = v_S^{(+)} - v_S^{(-)}$ . Considering that the  $\gamma$  ratio be about  $\gamma^2 \approx 0.25$ , then the numerical condition in Eq. (4.20) simplifies to:

$$\frac{h}{R} \frac{\Delta v_S}{v_S} \ll 8 \left( \frac{z_0}{R} \right)^2. \quad (4.21)$$

This interesting result says that for small value of  $h$  with respect to  $R$ , the Eq. (4.21) is true, specially for large  $z_0$ , and it establishes that a spherical segment represents well an anticline structure.

### 4.2.3 Contribution of the poisson integral to stresses

For estimating forces  $P_k$ , ( $k = x, y, z$ ), at the  $S$  boundary from stresses  $\sigma_{ki}$ , such that  $P_k = \sigma_{ki} n_i$ , there is an analogous equation to the one for displacement in Eq. (4.17), which is given by:

$$P_k(\mathbf{x}) = \frac{1}{4\pi} \rho g z \int_V P \Gamma_{kz}(\mathbf{x}, \mathbf{y}) dV_{\mathbf{y}} = -\frac{1}{4\pi} \rho g z \int_V \left\{ \left[ a \delta_{kz} + b \frac{(\mathbf{x}_k - \mathbf{y}_k)(z' - z)}{r^2} \right] \frac{\partial}{\partial n} \left( \frac{1}{r} \right) + a \left[ \cos(n, \mathbf{x}_k) \frac{z' - z}{r^3} - \cos(n, z) \frac{\mathbf{x}_k - \mathbf{y}_k}{r^3} \right] \right\} dV_{\mathbf{y}}; \quad (4.22)$$

where  $a = \frac{1}{2\pi} \frac{\mu}{\lambda + 2\mu}$ ,  $b = \frac{3}{2\pi} \frac{\lambda + \mu}{\lambda + 2\mu}$ , and  $P$  under the integral stands for a general operator for the concentrated forces in the integration point  $\mathbf{y}$ ; that means, placed at in the Green function  $\Gamma_{kz}$ , that includes differentiation, multiplication, summation and convolution to construct the force field (KUPRADZE, 1963). Comparing  $\Gamma_{kz}$  in Eq. (4.17) with  $P\Gamma_{kz}$  in Eq. (4.22) above, the  $P[L^{-1}]$  operator stands for the directional derivative  $\frac{\partial}{\partial n} = n_k \frac{\partial}{\partial x_k}$  with respect to the normal to the  $S$  surface (see Fig. 4.2).

Considering the structure to be a spherical segment, as done for obtaining the result in Eq. (4.20) followed by Eq. (4.21) above, the estimation of stresses for this simple model gives the numerical condition:

$$\frac{\rho g V}{2\pi R^2} (\gamma_1^2 - \gamma_2^2) \ll \rho g z_0. \quad (4.23)$$

Or, in another simplified form, as:

$$\frac{h}{2} (\gamma_1^2 - \gamma_2^2) \ll z_0. \quad (4.24)$$

The estimations in Eqs. (4.24) and (4.21) mean that the simple spherical model offer a good method for stress estimation, if the depth  $z_0$  to the structure is much larger than its amplitude  $h$ ; this is a usual situation in most oil deposits.

#### 4.2.4 Test example: anticline structure with low slope angles

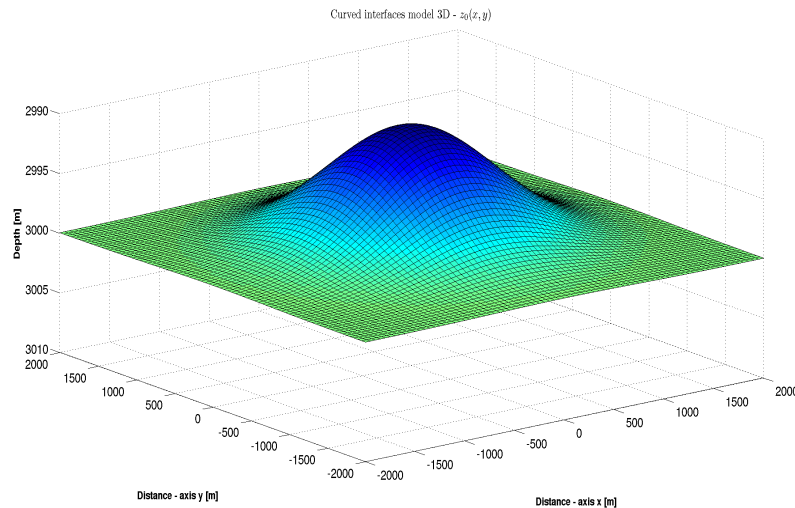
Figure 4.3 shows the case of an anticline structure modeled by a Gaussian surface defined by:

$$z_0(x, y) = H - he^{-\left(\frac{x^2+y^2}{a^2}\right)}, \quad (4.25)$$

where  $H$  is the depth to the rim of the structure,  $a$  the average radius, and  $h$  is the amplitude of the Gaussian dome.

For calculating the pressure across the model surface, the parameters for the two media are defined as:  $v_P$  above is 3000 m/s, and 3200 m/s below;  $\gamma = v_S/v_P$  above is 0.5, and 0.577 below; the density is  $\rho = 3000 \text{ kg/m}^3$  above and below; and the gravity value was taken as  $g = 9.8 \text{ m/s}^2$ . The figures that follow are the results obtained with these parameter values.

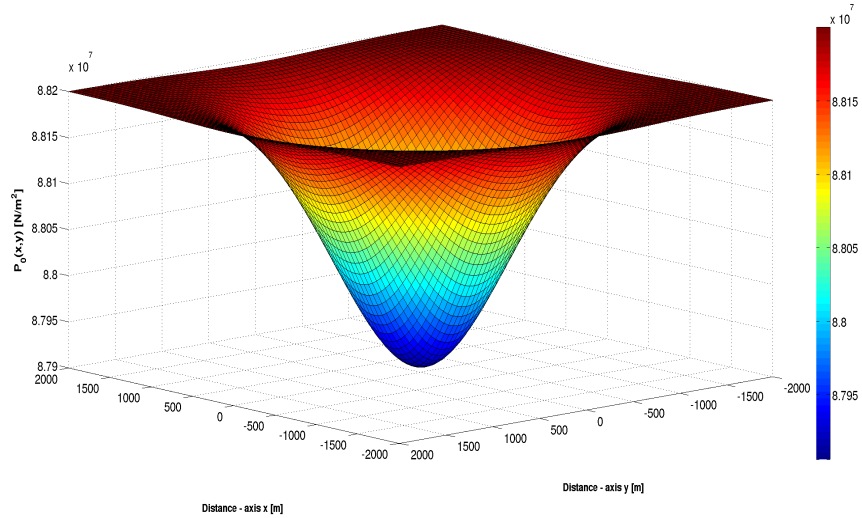
Figure 4.3 – Topography of the anticline model according to Eq. (4.25) representing the  $S$  surface separating the two media. The vertical axis indicates the surface position and amplitude  $z_0(x, y)$  for  $h = 10$ ,  $H = 3000$ , and  $a = 1000$ .



Source: From autor

Figure 4.4 shows the elementary overburden pressure field  $P_0 = P_z(S) = \rho g z_0$  behavior above the  $S$  surface, and with a consistent low around the dome.

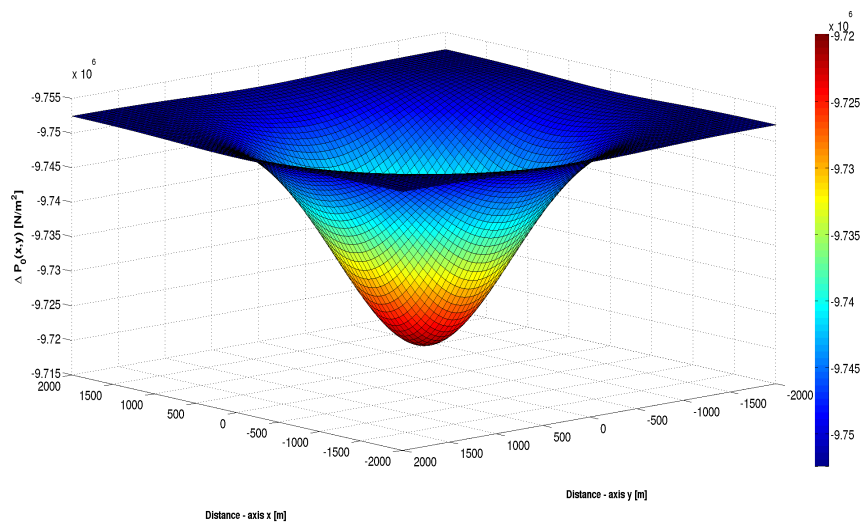
Figure 4.4 – Normal overburden weight as pressure  $P_0$  according to Eq. (4.3).



Source: From autor

Figure 4.5 shows the overburden weight pressure discontinuity  $\Delta P_0 = \frac{4}{3}P_0(\gamma_1^2 - \gamma_2^2)$  form across the  $S$  surface, and with a consistent low around the dome as expected for the given parameters.

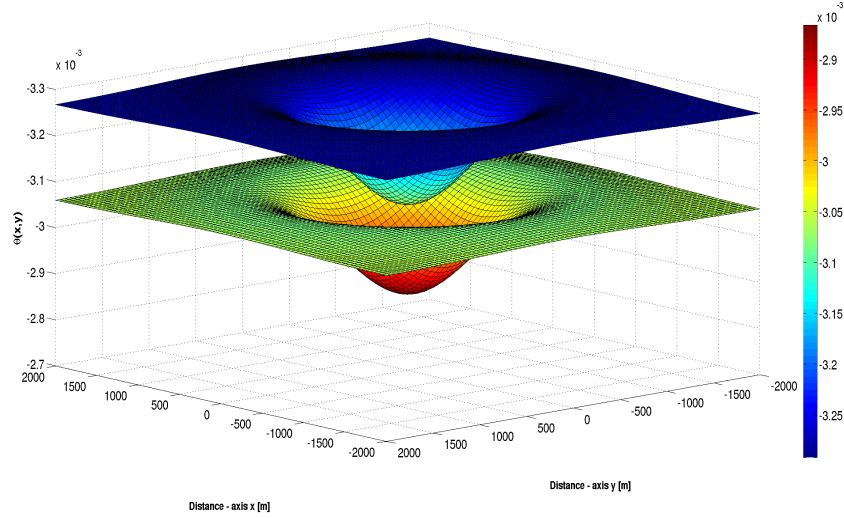
Figure 4.5 – Normal overburden weight as pressure discontinuity  $\Delta P_0$  across the  $S$  surface, and consistent with the results of Fig. 4.4.



Source: From autor

Figure 4.6 shows the cubic dilatation  $\theta$  calculated with Eq. (4.12), where the red color is for the medium above, and the green color for the medium below the  $S$  surface. The figure shows a consistent form for the dilatation with respect to the specified model.

Figure 4.6 – Cubic dilatation  $\theta$  according to Eq. (4.12). The values in green are for the layer below the  $S$  surface, and in blue for the layer above  $S$ .



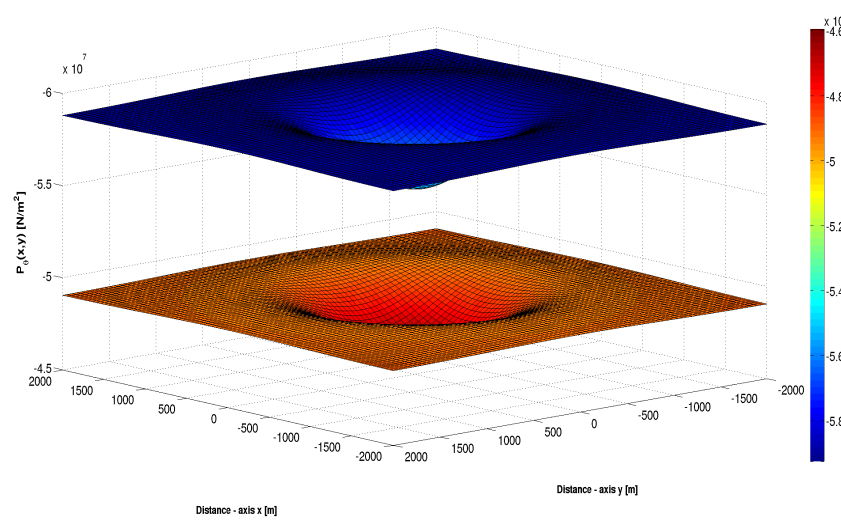
Source: From autor

Figure 4.7 shows the distribution of the dilatation pressure  $P_\theta$ , where is clear a low area around and under the dome. This distribution is calculated by  $P_\theta = (\lambda + \frac{2}{3}\mu)\theta = P_\theta(z_0)$  using Eq. (4.12) referenced to the  $S$  surface  $z_0(x, y)$ . The pressure immediately above the  $S$  surface (blue color) is given by  $P_\theta^{(+)} = P_\theta - \frac{1}{2}\Delta P_\theta$ , and immediately below (red color) by  $P_\theta^{(-)} = P_\theta + \frac{1}{2}\Delta P_\theta$ .

The pressure unit used is  $N/m^2 = 1\text{Pascal (Pa)}$ , which is equivalent to  $1\text{Pa} = 9.8692 \times 10^{-6}\text{atm (atmosphere)}$ .

It is interesting to observe that the pressure below the  $S$  surface (blue color) is sufficiently less than the pressure above (red color) by about  $1.0 \times 10^7 [N/m^2]$  (about 200 atmospheres). The main role in pressure decrease is played by the negative curvature of the anticline arc, and by the negative discontinuity of the  $\gamma$  parameter. This structure acts as an attractor for fluids. Besides, we can see a pressure increase near the periphery of the structure, and this means that around the periphery of an anticline there is a border for fluid migration to below, or to above, the anticline  $S$  surface.

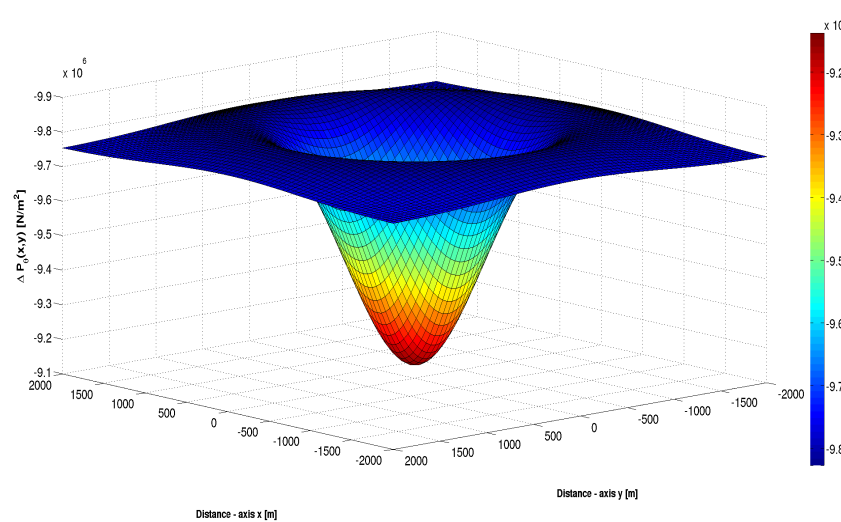
Figure 4.7 – This structure is a fluid attractor. Result for the dilatation pressure  $P_\theta$  using Eq. (4.12) and  $\theta$  as shown in Fig. 4.6. The blue color is for the medium above, and the red color is for the medium below the  $S$  surface.



Source: From autor

Figure 4.8 shows the pressure discontinuity  $\Delta P_\theta$  across the  $S$  surface, where is clear a low pressure area around and under the dome. This is a convenient figure to see the nuance and details for the analysis of fluid migration around the dome and rim of the structure. Fluids should migrate from a high to low a pressure zone, but we still have to consider the petroleum geology principles to form a complete analysis of the migration process as, for instance, the source and sealing rocks, and structural attitudes.

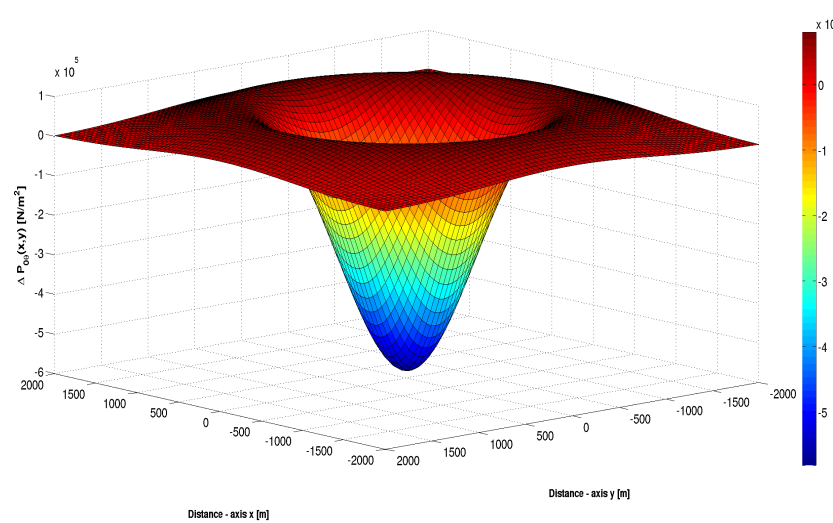
Figure 4.8 – Result for the dilatation pressure discontinuity  $\Delta P_\theta = K_1\theta_1 - K_2\theta_2$  using the results in Fig. 4.7 to analyze the details of the pressure variation around the dome and rim.



Source: From autor

Figure 4.9 shows the difference between the pressure discontinuities as calculated by the two related models: overburden minus dilatation pressures, and given by  $\Delta P_{0\theta} = \Delta P_0 - \Delta P_\theta$ , using results as shown in Figs. 4.5 and 4.8. The rim area shows the expected value around zero, and the dome presents a discrepancy between these two models, but by only around 0.1 atm, what represents a good approximation considering a discontinuity of 200 atm for  $\Delta P_0$  and  $\Delta P_\theta$ .

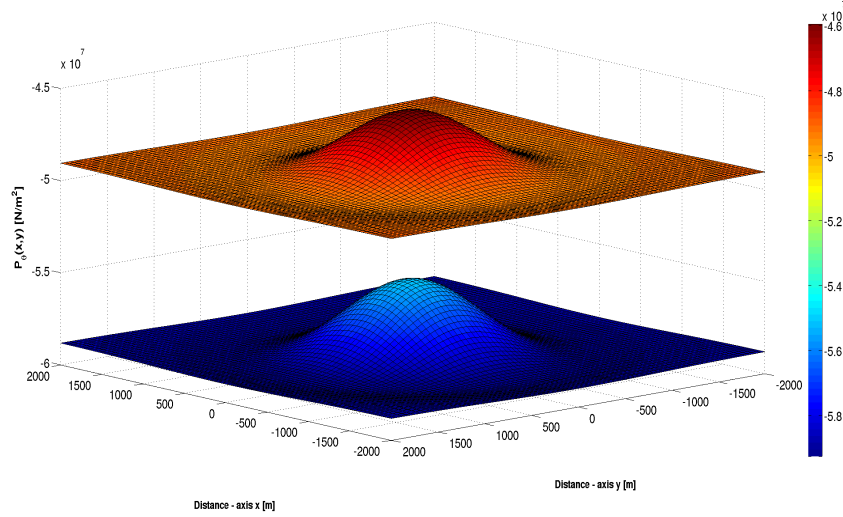
Figure 4.9 – Difference between the overburden and the dilatation pressure discontinuities  $\Delta P_{0\theta} = \Delta P_0 - \Delta P_\theta$  using the results as shown in Figs. 4.5 and 4.8.



Source: From autor

For the case of Fig. 4.10, we inverted the physical conditions through the parameters of the anticline; that is,  $\gamma = 0.577$  above, and  $\gamma = 0.5$  below the  $S$  surface. The result gives another picture, as the inverse of the Fig. 4.7; that is, the pressure below the  $S$  surface is larger than above by about  $1.0 \times 10^7 [\text{N/m}^2]$  (about 200 atmospheres), and the vicinity of the structure is not a fluid attractor.

Figure 4.10 – This structure is not a fluid attractor. The parameters have the inverse values of the ones for the case of Fig. 4.7: blue for  $\gamma = 0.5$  below, and red for  $\gamma = 0.577$  above the  $S$  surface.



Source: From autor

#### 4.2.5 Test example: anticline structure with high slope angles

We treat now an application of the modified boundary integral equation method as described by Sibiryakov (2006) for the case of pressure prediction for arbitrary structural forms. In the development of the theory, it is established continuity of the displacement vector  $\mathbf{u}$ , and of the force vector  $\mathbf{P}$  across the boundary surface.

The method corresponds to the solution of the inhomogeneous elastic static equation, considering a model formed by homogeneous layers (the  $\lambda$ ,  $\mu$ , and  $\rho$  parameters are constant in every layer), which is given by:

$$\mu\Delta\mathbf{u}_i + (\lambda + \mu)\text{grad}_i\text{div}\mathbf{u} = -\rho g\mathbf{e}_z, \quad (4.26)$$

where the  $\mathbf{e}_z$  is the unit vector for the  $z$  axis.

We consider a boundary surface  $S$ , as shown in Fig. 4.11, represented by the parametrical form:

$$\begin{cases} x &= r \cos \varphi \\ y &= r \sin \varphi \\ z(r) &= H + h \exp(-\alpha r^2) \end{cases}, \quad (4.27)$$

that separates two different media, one above and one below. The distance parameter  $r$  changes from 0 to 1 km with a step of  $1/200$ ,  $\varphi$  from 0 to  $2\pi$  with a step of  $\pi/100$ , the rim at  $H = -0.5$  km, the height of the dome  $h = 0.25$  km, and the dispersion factor as  $\alpha = 10$ . The upper boundary (free surface) is the plane represented by  $z = 0$ . The parameters of

the upper layer are simplified to  $\lambda^{(+)} = \mu^{(+)} = \rho^{(+)} = g^{(+)} = 1$ . The lower medium has also the same parameters, but  $\lambda^{(-)} = 0.8$ .

The problem is divided in two steps; the first deals with the particular solution, and the second with the complementary solution of Eq. (4.26).

**Step 1:** The particular solution of the inhomogeneous Eq. (4.26), without satisfying boundary conditions, are specified by the following simple expressions. For above the  $S$  surface by:

$$\mathbf{u}^{(+)} = \left( 0, 0, -\frac{\rho^{(+)}gz^2}{2(\lambda^{(+)} + 2\mu^{(+)})} \right) \quad \text{at } z \in (-z_0, 0). \quad (4.28)$$

And for below the  $S$  surface by:

$$\mathbf{u}^{(-)} = \left( 0, 0, -\frac{\rho^{(-)}g(z-z_0)^2}{2(\lambda^{(-)} + 2\mu^{(-)})} - \frac{\rho^{(+)}gz z_0}{(\lambda^{(-)} + 2\mu^{(-)})} + \frac{\rho^{(+)}gz_0^2}{(\lambda^{(-)} + 2\mu^{(-)})} - \frac{\rho^{(+)}gz_0^2}{2(\lambda^{(+)} + 2\mu^{(+)})} \right) \quad \text{at } z \in (-\infty, -z_0). \quad (4.29)$$

**Step 2:** The complementary solution of the homogeneous Eq. (4.26) adds to the particular solutions in Eqs. (4.28) and (4.29), and satisfies the boundary conditions on the structure surface and on the free flat surface. Therefore, the starting form is:

$$\mu\Delta\mathbf{u}_i + (\lambda + \mu)\text{grad}_i\text{div}\mathbf{u} = 0, \quad (4.30)$$

with the solution for the displacement component,  $u_i$ , given by

$$u_i(\mathbf{x}) = \frac{1}{2\pi} \int M_{ik}(\mathbf{x}, \mathbf{y}) F_k(\mathbf{y}) dS_{\mathbf{y}}. \quad (4.31)$$

The force component operator,  $P_i(M_{ik}) = P_i$ , obtained from solution in Eq. (4.31), satisfies the Fredholm integral equation of the second kind:

$$P_i(\mathbf{x}) = F_i(\mathbf{x}) - \frac{1}{2\pi} \int P_{ik}(\mathbf{x}, \mathbf{y}) F_k(\mathbf{y}) dS_{\mathbf{y}}. \quad (4.32)$$

The algorithm for calculating the tensor kernels  $M_{ik}(\mathbf{x}, \mathbf{y})$  and  $P_{ik}(\mathbf{x}, \mathbf{y})$ , from where the vector function  $F_i(\mathbf{y})$  is obtained, was published in Sibiryakov (2006) where, for the possibility of the tensor calculations, it is necessary to solve a linear algebraic system, where one part is formed by Fredholm equations of the first kind, and the other part by Fredholm equations of the second kind.

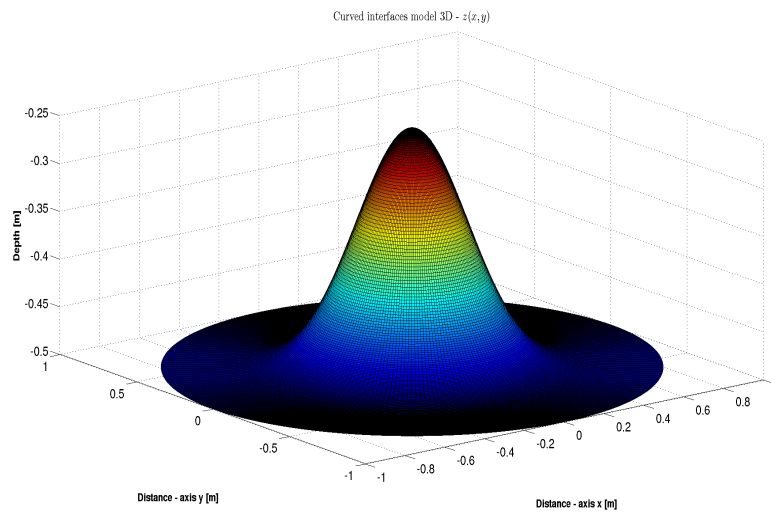
For large slope angles (more than 45 degrees), the tangent increases fast, and the approximate Eqs. (4.11) and (4.12) are no longer valid.

Figure 4.11 shows the topography of the anticline structure, that varies with radial distance from the center of the structure. The pressure around this structure is calculated using numerical accurate methods of boundary integral equations, and the details of this method is discussed in the paper by Sibiryakov (2006). This method is used to calculate

pressure for any surface geometrical form; but, for the present example we used a Gaussian dome characterized by steep side slopes.

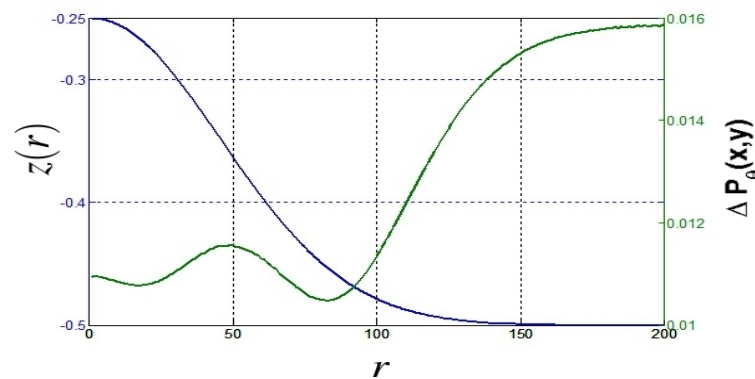
Figure 4.12 represents further calculations over the case of Fig. 4.11 to show details of the pressure variation, where the values outside the dome are approximately as given by Eqs. (4.11) and (4.12). But, here we call attention to fact of the predictive oscillating behavior of pressure around the sides of the structure, that can be important for the analysis of fluid migration.

Figure 4.11 – Anticline surface topography according to Eq. (4.27). Case of a structure with step slope angles. The color scale informs the ordinate  $z(r)$  values.



Source: From autor

Figure 4.12 – The vertical left axis gives the structural Gaussian anticline topography. The vertical right axis gives the pressure discontinuity  $\Delta P_\theta$  versus radial distance from the dome central part. The green line shows a special oscillating pressure variation details, and an increase towards outside the dome. The right vertical axis had the sign changed for simplifying the reading.



Source: From autor

### 4.3 Conclusions

Zones of low pressure exist not only in anticline structures; but, they can also be present in horizontal layers if the  $\gamma$  ratio is smaller in the layer above than in the layer below with respect to the structure surface. The search for such zones requires the knowledge of both P and S seismic velocity distributions, which can be determined by seismic processing, VSP and laboratory measurements.

The local decrease of pressure near the dome of an anticline structure depends on the discontinuity of the physical parameters across the structural surface, and on the geometrical parameters (slope angle and curvature). The quantity physically affected is the stress field, and the constitutive parameters (density, Lamé's, and if needed the porosity, specific surface area, etc) are admitted constant for the volume rock under the static condition. The volume rocks that form the anticline extend laterally to a horizontal attitude with the same constitutive parameter values.

The negative discontinuity of pressure causes the decrease of pressure below the structure surface, which turns it an attractor for fluid accumulation.

The positive discontinuity of pressure causes an increase of pressure below the structure surface, and as a result this structure is not an attractor feature for fluid accumulation.

The role of structural curvature is to increase its effect on the pressure value as a function of depth of the structure; that means, as the depth increases the role of the curvature also increases.

Figures 4.9 and 4.12 serve also as a numerical sensitivity analysis of the model considering the effect of the anticline dome to the pressure discontinuity across the target interface, that may serve as a natural suction pump for fluids (gas, water and oil) in the migration process.

## 5 SUBSURFACE STRESS PREDICTION USING SEISMIC DATA FOR OIL AND GAS EXPLORATION

The present chapter is part of a major research study that has for objective the prediction of stress in sedimentary basins, as a contribution to geological and engineering methods and techniques for oil and gas exploration.

Such an attractive and important scientific theme is based on the knowledge of the compressional ( $v_P$ ) and shear ( $v_S$ ) wave velocities and the densities ( $\rho$ ) distributions, in order to localize low pressures zones in sedimentary basins.

It is rather usual to think and accept that pressure increases continuously with depth, and we show here that this is not the case. The vertical and horizontal pressure variations act as natural pumps that pushes fluids from high to low pressure areas. The major physical parameter for this phenomena is played by the  $\gamma = \frac{v_S}{v_P}$  ratio discontinuity along interfaces.

Most of the seismic exploration is based on the acoustical wave equation, what results in a knowledge of the compressional wave velocity model. To obtain the shear wave velocity information it is necessary a 3D component sensor survey, and density log information can also be incorporated. Shear wave velocities can also be obtained from VSP technology, and by petrophysical measurements. There are tables and regression models for seismic velocities and densities that can also be incorporated in this prediction.

As a result of the  $\gamma$  ratio behavior, an anticline is not necessarily the only structural condition for a potential area for oil and gas accumulation. A trap can be present as a horizontal structure if there is a positive  $\gamma$  ratio discontinuity, or a negative discontinuity of the Poisson  $\sigma$  ratio across the horizontal boundary. These physical conditions are responsible for producing a pressure discontinuity, such that there will be a sufficiently lower pressure zone underneath than above the boundary. In this case, the lower horizontal boundary is said to be a fluid attractor surface. In the opposite physical conditions, this boundary does not have fluid attraction properties.

For the theory developed and implemented here, the example presented here is the 2D Marmousi subsurface model for simpler and direct visualization, but the theory accounts for a 3D case.

### 5.1 Introduction

This paper is a continuation of a major study for the prediction of subsurface stress and strain using P and S wave velocities ( $v_P(\mathbf{x})$ ,  $v_S(\mathbf{x})$ ) and density ( $\rho(\mathbf{x})$ ) to localize

areas of pressure discontinuity, that act as natural suction pumps in oil and gas productive layers. As a result of these studies, Sibiryakov, Leite and Vieira (2015) and Sibiryakov, Leite and Vieira (2013b) are submitted and accepted papers for publication, and they deal with different aspects of the research studies.

The main question here raised is: How sensitive is the pressure prediction calculus to variations of velocity and density distribution models?

The answer to this inquiry could be theoretically given by sensitivity analysis of the problem's differential equation system, or in a more practical way by numerical experiments. We chose this later route based on migration methodology, where testing is performed with smoothed versions of the input data.

To develop the theory for stress-strain prediction for practical application in oil and gas exploration, the first part has to be related to conventional seismic investigations to obtain the P and S wave velocities and densities model. Also, the configuration of seismic boundaries in the sedimentary basins can be necessary. With these informations, the second part follows with the prediction of stress and strain, and of the nontrivial behavior of pressure. As a third part, is the continuation of the prediction of pressure discontinuity between solid and fluid, that depends on the structure of the pore space.

The present description considers only isotropic models, and the theory also says that it is mandatory the knowledge of  $v_P(\mathbf{x})$ ,  $v_S(\mathbf{x})$  and  $\rho(\mathbf{x})$ . For anisotropic situations the equations are more complicated, more control parameters, and the data needs more processing. Since we have discretized the model in uniform 3D grid, the layer cells forming the 3D geological structure have constant elastic parameters.

The data needed for pressure prediction can be 3C (three component sensors) to obtain P and S (SH and SV) wave modes, and density log information can also be incorporated. Also S wave velocities can also be obtained from VSP technology, and by petrophysical measurements (BIONDI, 2010; GALPERIN, 1985; HARDAGE et al., 2011).

The theory is based on the static stress-strain equations, where the overload gravity weight is responsible for the strain and stress effects in the subsurface. Therefore, organizing this problem calls for Hooke's generalized law of linear elasticity.

Another approach is to take into consideration the layer interface curvature, and to model this case as a confined plate (SIBIRYAKOV et al., 2013), what becomes a more complex problem. For instance, the anticline structure can be a very useful trap, especially if it has a negative discontinuity (lower minus upper parameter) in the  $\gamma = \frac{v_S}{v_P}$  ratio. In this case, exists also an additional horizontal stretching due to the negative curvature of the anticline structure. It is interesting, that the effects of the structure slope and curvature are in opposite directions; the slopes produce an additional compression, while the average surface curvature (SMIRNOV, 1964) produces a horizontal stretching.

If there is an anticline structure with a positive discontinuity in the  $\gamma$  ratio, it can be a compensational effect. The additional pressure due to the  $\gamma$  discontinuity, and the additional stretching due to the average curvature may eliminate each other. In this case, the anticline structure is not a fluid attractor.

Basin studies aiming at oil and gas exploration contain many theoretical aspects of engineering, geology, geochemistry and geophysics, in order to characterize the reservoirs (HANTSCHHEL; KAUEAUF, 2009). Ameer (2003) presents a special bibliography for methods and theories on crustal stress studies, and also Zang and Stephansson (2010) is here used as a systematic reference. But, it should be clear that here we are developing a specific data driven method that is based on  $v_P(\mathbf{x})$ ,  $v_S(\mathbf{x})$  and  $\rho(\mathbf{x})$  knowledge, where we want to map low pressure zones important to locate a successful drilling zone for oil and gas exploration.

## 5.2 Methodology

### 5.2.1 The stress and strain tensor fields

The stress ( $\sigma = \sigma(x, y, z)$ ) and strain ( $\epsilon = \epsilon(x, y, z)$ ) elastic fields are related by the generalized Hooke's law, and described as tensors, functions of the space coordinates, and they are represented by nine components. Figures 5.1 illustrates these quantities for an arbitrary Cartesian reference coordinate system  $(x, y, z)$ , where any other desired plane,  $(x', y', z')$ , can be drawn to to have stress and strain calculated. Therefore, for the general anisotropic media the stress ( $\sigma$ ) and strain ( $\epsilon$ ) tensors obey the spatial coordinate rotation relation given by:

$$\sigma_{ij} = \sum_{k,l} a_{ijkl} \sigma'_{kl}, \quad (5.1)$$

and

$$\epsilon_{ij} = \sum_{k,l} b_{ijkl} \epsilon'_{kl}, \quad (5.2)$$

where the coefficients  $a_{ijkl}$  and  $b_{ijkl}$  define the new plane with respect to a reference system. The elastic linear relation between stress and strain is given by the generalized Hooke's law (MAVKO; MUKERJI; DVORKIN, 1999):

$$\sigma_{ij} = \sum_{k,l} c_{ijkl} \epsilon_{kl}, \quad (5.3)$$

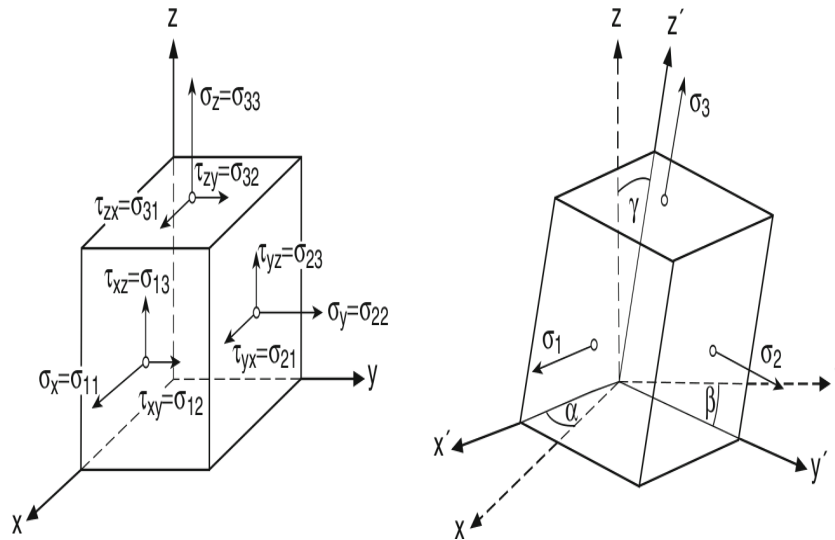
In this description, the first index ( $i$ ) in  $\sigma_{ij}$  and  $\epsilon_{ij}$  stands for the plane direction, and the second ( $j$ ) for the component direction. It follows that the stress-strain will depend on the plane orientation passing by a considered point  $Q$  (see figure 5.1), and calculated by their nine components. As we particularize the stress state, it is represented at a point  $Q$

by a matrix  $\mathbf{S}$ , with the elements are  $\sigma_{ij}$ :

$$\mathbf{S} = \begin{bmatrix} \sigma_{xx} & \sigma_{xy} & \sigma_{xz} \\ \sigma_{yx} & \sigma_{yy} & \sigma_{yz} \\ \sigma_{zx} & \sigma_{zx} & \sigma_{zz} \end{bmatrix}. \quad (5.4)$$

The differential equations that follow in the sequel are related to figure 5.1 (similar figures can be presented to described strain), that serve to represent a physical particle of the subsurface, and the solution of the equations correspond to the integration over these infinitesimal quantities.

Figure 5.1 – A physical particle, and the stress field representation,  $\sigma_{ij}$ , where  $\tau_{i,j}$  stands for the tangential components of  $\sigma_{ij}$ . The letters  $(\alpha, \beta, \gamma)$  are the rotation angles for the  $(z', y', z')$  with respect to the  $(x, y, z)$  system. The particle is referenced to the point  $Q$  located at the origin of the Cartesian system.



Source: From autor

### 5.2.2 Stress states

We now look at forms to represent the stress field. Therefore, turning to the stress matrix (5.4), it can be decomposed in three parts in the form:  $\mathbf{S} = \mathbf{S}_0 + \mathbf{S}_D + \mathbf{S}_N$ , such that it allows for a physical interpretation (PERSEN, 1975). For the state  $\mathbf{S}_0$  we have that:

$$\mathbf{S}_0 = \begin{bmatrix} P_H & 0 & 0 \\ 0 & P_H & 0 \\ 0 & 0 & P_H \end{bmatrix}, \quad (5.5)$$

where

$$P_H = \frac{1}{3}(\sigma_{xx} + \sigma_{yy} + \sigma_{zz}), \quad (5.6)$$

with the sum (5.6) of the normal stresses in equation (5.5) defining the called hydrostatic pressure. This state is present in any plane around the point  $Q$ .

For the state  $\mathbf{S}_D$  we have that:

$$\mathbf{S}_D = \begin{bmatrix} \sigma_{xx} - P_H & \frac{1}{2}(\sigma_{xy} + \sigma_{yx}) & \frac{1}{2}(\sigma_{xz} + \sigma_{zx}) \\ \frac{1}{2}(\sigma_{xy} + \sigma_{yx}) & \sigma_{yy} - P_H & \frac{1}{2}(\sigma_{yz} + \sigma_{zy}) \\ \frac{1}{2}(\sigma_{xz} + \sigma_{zx}) & \frac{1}{2}(\sigma_{zy} + \sigma_{yz}) & \sigma_{zz} - P_H \end{bmatrix}. \quad (5.7)$$

For the above equation (5.7), applying the symmetry property:  $\sigma_{xy} = \sigma_{yx}$ ,  $\sigma_{xz} = \sigma_{zx}$ ,  $\sigma_{yz} = \sigma_{zy}$ ,  $\mathbf{S}_D$  results in a null state; i. e.,  $\mathbf{S}_D = \mathbf{0}$ .

For the state  $\mathbf{S}_N$  we have that:

$$\mathbf{S}_N = \begin{bmatrix} 0 & \frac{1}{2}(\sigma_{xy} - \sigma_{yx}) & \frac{1}{2}(\sigma_{xz} - \sigma_{zx}) \\ \frac{1}{2}(\sigma_{xy} - \sigma_{yx}) & 0 & \frac{1}{2}(\sigma_{yz} - \sigma_{zy}) \\ \frac{1}{2}(\sigma_{xz} - \sigma_{zx}) & \frac{1}{2}(\sigma_{zy} - \sigma_{yz}) & 0 \end{bmatrix}. \quad (5.8)$$

Similarly, applying the symmetry property, the state  $\mathbf{S}_N$  simplifies to:

$$\mathbf{S}_N = \begin{bmatrix} \sigma_{xx} - P_H & \sigma_{xy} & \sigma_{xz} \\ \sigma_{yx} & \sigma_{yy} - P_H & \sigma_{xz} \\ \sigma_{zx} & \sigma_{zx} & \sigma_{zz} - P_H \end{bmatrix}. \quad (5.9)$$

called the deviatoric state for the diagonal elements (normal stresses), where the hydrostatic state is subtracted to remain the nonhydrostatic state.

From the above discussion, we posed physically the following stress field representation: the hydrostatic pressure state (5.6), and the deviatoric state (5.9). But, still other representations are possible as seen in the sequel, and all of them must be adapted here for analyzing the 2D case. The simple word ‘‘pressure’’ (positive or negative) is here always related to the normal stresses.

### 5.2.3 Isotropic media

For an isotropic media, perfect linear elastic, the relation between stress and strain is given by Hooke’s law in the form:

$$\sigma_{ij} = \lambda\theta\delta_{ij} + 2\mu\epsilon_{ij}, \quad (5.10)$$

where  $\lambda$  and  $\mu$  are the Lamé’s elastic parameters, and  $\delta_{ij}$  Kronecker’s delta ( $\delta_{ij} = 0$ , if  $i \neq j$  and  $\delta_{ij} = 1$ , if  $i = j$ ). The  $\theta$  parameter represents the dilatation given by the divergence of the displacement vector  $\vec{u}$  as:

$$\theta = \nabla \cdot \vec{u} = \frac{\partial u_x}{\partial x} + \frac{\partial u_y}{\partial y} + \frac{\partial u_z}{\partial z}. \quad (5.11)$$

The strain tensor components  $\epsilon_{ij}$  are defined in terms of the displacement components  $u_i$  as:

$$\epsilon_{ij} = \frac{1}{2} \left( \frac{\partial u_i}{\partial x_j} + \frac{\partial u_j}{\partial x_i} \right). \quad (5.12)$$

Also, the shear-extensional linear process produces a rotation tensor that is given by:

$$\varphi_{ij} = \frac{1}{2} \left( \frac{\partial u_i}{\partial x_j} - \frac{\partial u_j}{\partial x_i} \right). \quad (5.13)$$

Therefore, once we know the displacement vector components ( $u_i$ ), the functional quantities in equations (5.11), (5.12) and (5.13) can be calculated (LOWRIE, 2011).

From the above discussion, for an isotropic media only two constants are necessary to completely specify the stress-strain relation. Boundary conditions are usually described by stress and strain relations (mixed boundary problem) across an interface, as continuity, free condition, and discontinuity. And to be specific, discontinuity is the case of a boundary condition along the contour of a reservoir, with the form of an anticline, or of a stratigraphic trap.

We take in consideration only the constitutive parameters (density, Lamé's parameters); that means, the model does not separate the different contributions (porosity, fluids, etc) for changes in the velocities and density.

Since the model is related to the wave propagation in a perfect elastic medium, the elasto-dynamic equations of motion are given by:

$$\begin{cases} \frac{\partial \sigma_{xx}}{\partial x} + \frac{\partial \sigma_{xy}}{\partial y} + \frac{\partial \sigma_{xz}}{\partial z} = \rho \frac{\partial^2 u_x}{\partial t^2} \\ \frac{\partial \sigma_{yx}}{\partial x} + \frac{\partial \sigma_{yy}}{\partial y} + \frac{\partial \sigma_{yz}}{\partial z} = \rho \frac{\partial^2 u_y}{\partial t^2} \\ \frac{\partial \sigma_{zx}}{\partial x} + \frac{\partial \sigma_{zy}}{\partial y} + \frac{\partial \sigma_{zz}}{\partial z} = \rho \frac{\partial^2 u_z}{\partial t^2}. \end{cases} \quad (5.14)$$

resumed to the form,

$$\frac{\partial \sigma_{ij}}{\partial x_j} = \rho \frac{\partial^2 u_i}{\partial t^2}, \quad (i, j = 1, 2, 3); \quad \text{or} \quad (i, j = x, y, z). \quad (5.15)$$

That means that the spatial stress variation is related to the inertial force per unit volume, without internal forces (the gravity effect).

The velocities of the basic seismic body waves (P and S) in homogeneous, isotropic, elastic media are given by:

$$\begin{aligned} v_P &= \sqrt{\frac{K + \frac{4}{3}\mu}{\rho}} = \sqrt{\frac{\lambda + 2\mu}{\rho}}, \\ v_S &= \sqrt{\frac{\mu}{\rho}}, \end{aligned} \quad (5.16)$$

where  $K$  is the bulk modulus (the modulus of incompressibility),  $\mu$  is the shear modulus (modulus of rigidity),  $\rho$  is the density of the material through which the wave propagates, and  $\lambda$  is related to  $K$  and  $\mu$ .

From the above relations (5.16), the shear module is calculated by  $\mu = v_S^2\rho$ , the Lambda module by  $\lambda = v_P^2\rho - 2\mu$ , and the Gamma ratio by  $\gamma = \frac{v_S}{v_P}$ .

The density is usually a parameter admitted to change slowly with depth, from the surface to the top of the target interface; but, in some geological situations the density discontinuity can be rather severe. In the present solution the density varies with  $\rho = \rho(x, z)$ , and is integrated over the calculating grid.

Now we turn to our differential equation system to be integrated, and this system represents the problem's description for the static system, where the time variation is null. In this case, the equations are given by:

$$\begin{cases} \frac{\partial\sigma_{xx}}{\partial x} + \frac{\partial\sigma_{xy}}{\partial y} + \frac{\partial\sigma_{xz}}{\partial z} = 0 \\ \frac{\partial\sigma_{yx}}{\partial x} + \frac{\partial\sigma_{yy}}{\partial y} + \frac{\partial\sigma_{yz}}{\partial z} = 0 \\ \frac{\partial\sigma_{zx}}{\partial x} + \frac{\partial\sigma_{zy}}{\partial y} + \frac{\partial\sigma_{zz}}{\partial z} = \rho g \end{cases} \quad (5.17)$$

and resumed to the form,

$$\frac{\partial\sigma_{ij}}{\partial x_j} = \rho g \delta_{3j}, \quad (i, j = 1, 2, 3); \quad \text{or} \quad (i, j = x, y, z). \quad (5.18)$$

It means that the horizontal stress variations are considered null, and the vertical component is given by the gravity load in terms of force per unit area ( $\rho g$ ). Therefore, lateral tectonic stress is not here taken into consideration. The quantities  $\rho$  and  $g$  can be considered as spatial functions; i.e.,  $\rho = \rho(x, y, z)$  and  $g = g(x, y, z)$ .

We consider at first a simple model formed by a horizontally layered medium. The equation of equilibrium for the linear elastic medium for every single layer is given by:

$$\frac{\partial\sigma_{ik}}{\partial x_k} = \rho g_i, \quad (5.19)$$

where  $\sigma_{ik}$  are the components of stress tensor,  $\rho$  is the rock density, and  $g_i$  is the acceleration. For the case of vertical gravity,  $g_{i=z}(z) = g$ , it is taken as constant for a rather short depth, and a simpler equation (5.19) is written in the following form:

$$\frac{\partial\sigma_{zz}}{\partial x_z} = \rho g. \quad (5.20)$$

The above equation has an elementary solution given by:

$$\sigma_{zz}|_{z=z_0} = \int_{z=0}^{z=z_0} \rho g dz = \rho g z_0 = P_0(z_0), \quad (5.21)$$

where  $P_0 = \rho g z_0$  is the weight of rocks per unit area; that is, the vertical pressure due to the overload at any depth  $z_0$ .

In the physical aspects of this theory, we do not take in consideration geological faulting and lithological variations for the rock volume forming the reservoir (NELSON, 2001). Also, in another paper we deal with the case of bending of the geological formation resulting in an anticline structure (SIBIRYAKOV et al., 2013).

#### 5.2.4 Scalar pressure field

The pressure field in rocks is a main characteristic of the stress condition of the geological structures. Stress is nonhydrostatic even in horizontal layered media subject to only vertical gravity compaction without horizontal displacement. Lateral tectonic stress is, therefore, a condition to be explicitly considered in organizing the model.

For the present simplified model, the vertical stress,  $\sigma_{zz}(z)$ , is defined as equal to the weight of the overburden; i. e.:

$$\sigma_{zz} = P_z = P_0(z). \quad (5.22)$$

The horizontal stress,  $\sigma_{xx}(z)$ , considering that  $\sigma_{yy} = \sigma_{xx}$  in this case, is sufficiently lower than the vertical stress,  $\sigma_{zz}$ , and from equations (5.17) and (5.21), it is shown to be given by:

$$\sigma_{xx} = P_x = P_0(1 - 2\gamma^2), \quad (5.23)$$

where  $P_0 = P_0(z)$ ,  $\gamma = \gamma(z) = \frac{v_S(z)}{v_P(z)}$ .

The scalar invariant hydrostatic pressure field,  $P(z) = P_H$ , was defined above as the average  $P = P_H = \frac{1}{3}(\sigma_{xx} + \sigma_{yy} + \sigma_{zz})$ . Using the generalized Hooke's law in the form (5.10), this field can be calculated by:

$$P = P_H = (\lambda + \frac{2}{3}\mu)\theta, \quad (5.24)$$

where  $\theta(z)$  is the dilatation given by equation (5.11), and  $\lambda(z)$  and  $\mu(z)$  are the already described Lamé's parameters.

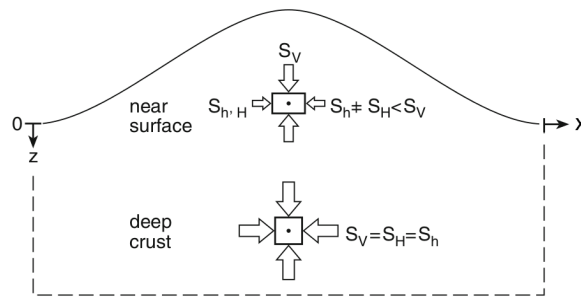
Another important physical characteristic is the overburden pressure discontinuity at layer boundaries ( $\Delta P = P^+ - P^-$ , at  $z$ , and  $z$  positive downwards), that will exist if the velocity  $\gamma$  ratio has a discontinuity. Considering the simplest case of layered media, and Hooke's law (5.10), the discontinuity  $\Delta P$  is given by:

$$\Delta P(z) = \frac{4}{3}(\gamma_1^2 - \gamma_2^2)P_0(z), \quad (5.25)$$

where  $\gamma_1$  is the upper and  $\gamma_2$  the lower layer parameters across the interface positioned at depth  $z$ . Therefore, overburden pressure varies stepwise as positive or negative with depth,

if the underlying  $\gamma$  ratio is different from the overlying  $\gamma$  ratio. This idea may appear rather strange in simple geology, but it is an important fact related to the nonelementary behavior of stress in solids, and at this point we can recall Heim's rule for lithostatic stress variation in the subsurface (ZANG; STEPHANSSON, 2010), as depicted in figure 5.2.

Figure 5.2 – Old geological concept known as Heim's rule for the stress variation in the crust.  $S_V$  stands for the vertical stress,  $S_H$  for the maximum horizontal stress,  $S_h$  for the minimum horizontal stress, and where these quantities equalize as depth increases. This figure was redrawn based on Zang and Stephansson (2010).



Source: From autor

Continuing now with the intensity of tangential stress, it is a form to measure the mechanical instability responsible for the failure of the solid rock skeleton and fracturing. For the simple layered media, the scalar invariant tangential stress,  $P_T(z)$ , is defined by the average of the difference between horizontal and vertical stress, and with the use of Hooke's law (5.10), we arrive at the result:

$$P_T = \frac{1}{2}(\sigma_{zz} - \sigma_{xx}) = \gamma^2 P_z. \quad (5.26)$$

Again, it also depends on velocity  $\gamma$  ratio.

For the computational experiments, where the data is of any origin, the vertical and horizontal numerical partial derivatives with respect to  $x$ ,  $y$  and  $z$  are calculated using symmetrical forms (ABRAMOWITZ; STEGUN, 1970). For the first order derivatives along  $x$  or  $z$  as:

$$\frac{\partial}{\partial x} f_{0,0} = \frac{1}{4h} (f_{1,1} - f_{-1,1} + f_{1,-1} - f_{-1,-1}) + O(h^2). \quad (5.27)$$

And for the second order derivatives along  $x$  and  $z$  as:

$$\frac{\partial^2}{\partial x \partial z} f_{0,0} = \frac{1}{4h^2} (f_{1,1} - f_{-1,1} + f_{1,-1} - f_{-1,-1}) + O(h^2). \quad (5.28)$$

The main full application is to predict 3D stress and strain around a geological reservoir volume, and to present the results in form of a data cube, from where vertical and horizontal sections can be extracted and interpreted. To be specific, here we have

only produced vertical sections, and this means that the blocks have unitary thickness across the  $y$  axis for the results to be in force per unit area.

In the next section we present one form of sensitivity analysis to measure qualitatively the decay of the resolution in the stress prediction, that depends on the smoothing of the input data. Another form of sensitivity analysis would take us to the domain of the differential components of stress-strain field in a feature work (FRANK, 1978). And in the present example we stay close to the seismic migration methodologies.

### 5.3 Results

The experiments were divided in two main parts based on the input data: Original and Smoothed input data ( $v_P$ ,  $v_S$  and  $\rho$ ). The selected results for presentation had symmetrical smoothing operators with the following lengths: 41, 81, and 101 points.

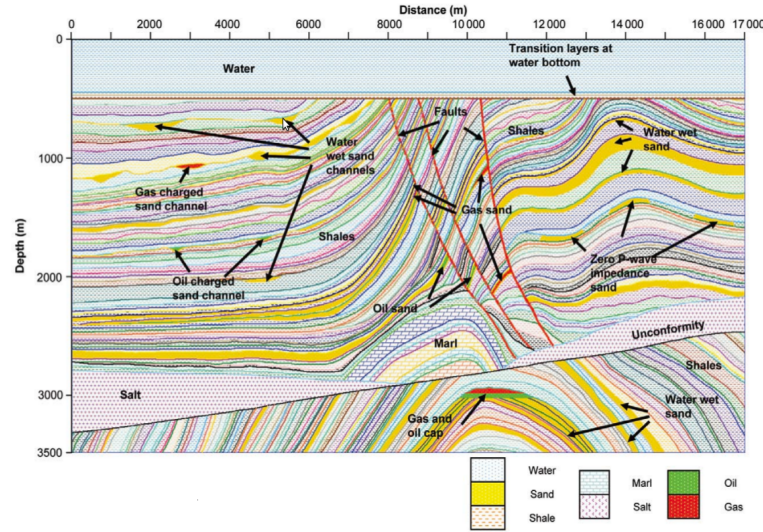
The same smoothing process was equally applied to the input model components ( $v_P$ ,  $v_S$  and  $\rho$ ) to analyze the resolution decay of the prediction results. We focused on some reservoir targets, as the input parameters systematically deviate from the original (real) values. This means that we used the same criteria as in the numerical tests for stack, inversion and migration experiments.

The tests start from the original input parameters, and continue with smoothed versions of the input parameters to analyze the result of the resolution decay. For the smoothing process, we used the routine *Smooth2a* that is present in the SU (COHEN; STOCKWELL, 2005) and Matlab (SCHILLING; HARRIS, 2005) codes, and it represents an averaging symmetric rectangular operator. And at the borders, the operator supplies with less points, as the central point of the rectangular operator reaches the end of the smoothing area (REEVES, 2009).

The data selected and used for the present test was from the Marmousi seismic project (VERSTEEGE; GRAU, 1991), and described by Martin, Wiley and Marfurt (2006) as we show in figure 5.3, where we call attention to the gas and oil reservoir targets.

The Marmousi model has the compressional and shear wave velocities and density models that are shown in the figure sequence organized in table 5.1, together with impedance calculation.

Figure 5.3 – Geological description of the Marmousi according to Martin, Wiley and Marfurt (2006) with the oil and gas reservoir targets pointed to. We underlined the target in the bottom sequence related to the classical anticline structure.



Source: From autor

Table 5.1 – Input data and impedance

Figure	Description
5.4	$v_P(x, z)$ velocity
5.5	$v_S(x, z)$ velocity
5.6	$\rho(x, z)$ density
5.7	$I_P(x, z) = v_P \rho$ , P wave impedance
5.8	$I_S(x, z) = v_S \rho$ , S wave impedance
5.9	$\Delta I_{PS}(x, z) = I_P - I_S$ , P-S waves impedance contrast
5.10	$R_{PS} = \frac{I_P - I_S}{I_P + I_S}$ , vertical normalized impedance contrast coefficient

Table 5.2 gives the sequence of figures of the calculated constitutive parameters based on the input data.

Table 5.2 – Constitutive parameters

Figure	Description
5.11	$\gamma(x, z)$ , gamma ratio
5.12	$\mu(x, z)$ , shear module
5.13	$\lambda(x, z)$ , lambda module
5.14	$\sigma(x, z)$ , Poisson module

There are different categories of figures for presenting the crust stress field, and table 5.3 lists the results for field magnitudes and ratios.

Table 5.3 – Pressure fields

Figure	Description
5.15	$\sigma_{zz} = P_z$ , vertical pressure
5.16	$\sigma_{xx} = P_x$ , horizontal pressure
5.17	$P_H$ , hydrostatic pressure field
5.18	$P_{XH} = \sigma_{xx} - P_H$ , horizontal deviatoric hydrostatic pressure field
5.19	$P_{ZH} = \sigma_{zz} - P_H$ , vertical deviatoric hydrostatic pressure field
5.20	$P_T = \frac{1}{2}(\sigma_{zz} - \sigma_{xx})$ , tangential stress, as a deviatoric pressure field
5.21	$k_{xz}(x, z)$ , dimensionless stress ratio, as a full section
5.22	$k_{xz} = \frac{\sigma_{xx}}{\sigma_{zz}}$ , dimensionless stress ratio, as depth profiles for details

The simple table 5.4 lists the figure that we put in evidence for the result of the vertical field discontinuity.

Table 5.4 – Pressure field discontinuity

Figure	Description
5.23	$\Delta P_z$ , vertical pressure discontinuity across interfaces

The double line of table 5.5 shows the results for the field variations calculated by spatial derivatives.

Table 5.5 – Spatial derivatives

Figure	Description
5.24	$\frac{\partial P_z}{\partial z}$ , vertical variation of the vertical pressure field
5.25	$\frac{\partial P_x}{\partial x}$ , horizontal variation of the horizontal pressure field

Based on theoretical aspects, different figures can be constructed as criteria for the analysis of the subsurface stress and pressure conditions. Here, we present some selected figures to focus at details and correlation with the low pressure areas below specific interfaces pointed as potential fluid accumulation zones.

It should be clear that the analysis is basically lithostratigraphical, and that we are not concerned with chronological concepts; even though, the smoothing process, that eliminates the high frequency content in the input data, can suggest a chronological and stratigraphical analysis, that is more complex and needs more constraints.

Figures 5.4, 5.5 and 5.6 show the input  $v_P$ ,  $v_S$  and  $\rho$  data, where the main aspects (low frequency) are still recognized, but the details (high frequency) have been very much attenuated with the smoothing process.

Figures 5.7 and 5.8 show the impedances for the P and S waves.

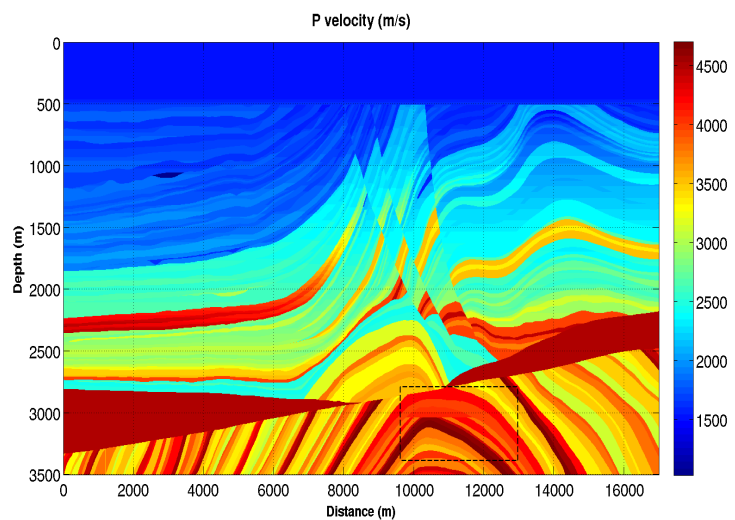
As we look for contrast informations to be able to point out the presence of a reservoir, figure 5.9 show the P-S impedance contrast. Figure 5.10 the normalized vertical impedance contrast coefficient between P and S waves defined as  $R_{PS} = \frac{I_P - I_S}{I_P + I_S}$ . Figure 5.9 keeps a good correlation with 5.23, and figure 5.10 with figure 5.21, characterized a linear oscillatory increasing behavior.

Figures 5.11, 5.12, 5.13 and 5.14 show the  $\gamma$ ,  $\mu$  and  $\lambda$  parameters calculated directly from the correspondent  $v_P$ ,  $v_S$  and  $\rho$  data. These figures also show similar characteristics, where the main aspects (low frequency content) are still recognized, but the details (high frequency content) have been attenuated. The Poisson ratio,  $\sigma = \frac{1-2\gamma^2}{2-2\gamma^2}$ , in figure 5.14, presents only positive values between 0.3 and 0.5.

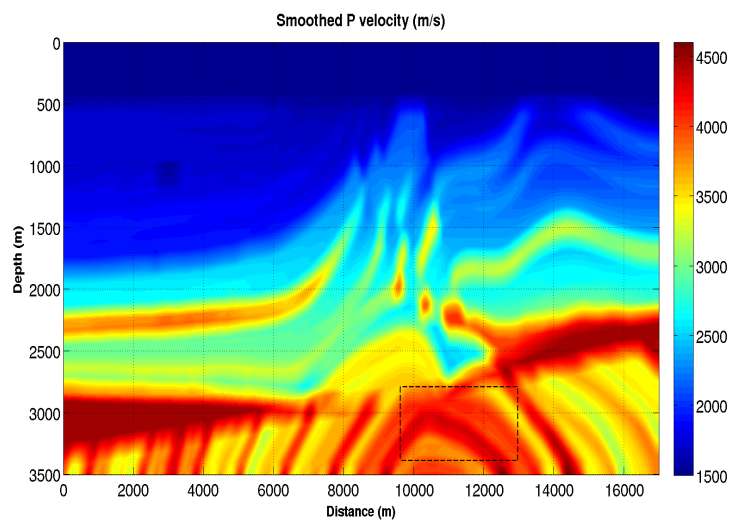
One goal, based on description for this model by Versteeg and Grau (1991), is marked with a rectangular window defined along the  $x$ -axis with the coordinates of 10.000 – 11.000 meters, and in the  $z$ -axis by the coordinates of 2.800 – 3.200 meters. That is, the top of the anticline defined as an oil and gas reservoir. Therefore, this spatial window marks a confined low pressure zone representing the reservoir.

Figure 5.4 – Velocity,  $v_P(x, z)$ .

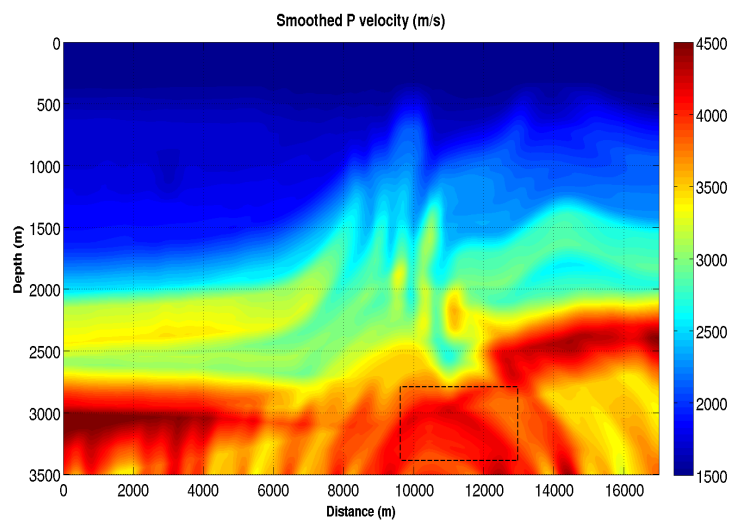
(a) Original model.



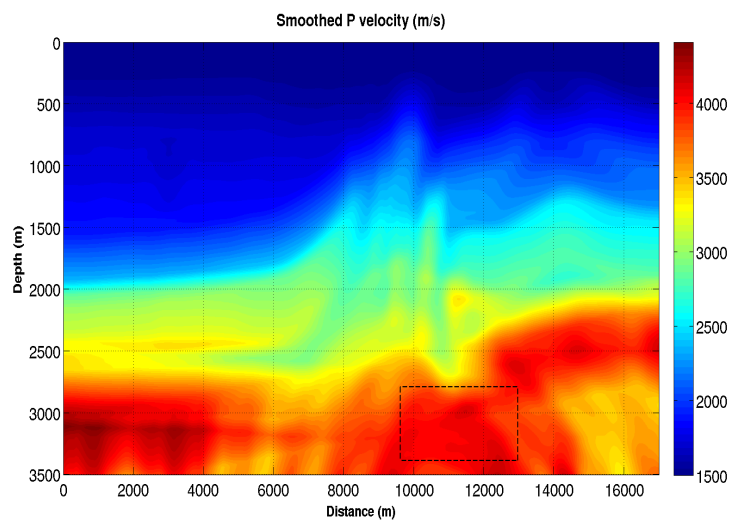
(b) Smoothing with 41 points.



(c) Smoothing with 81 points.



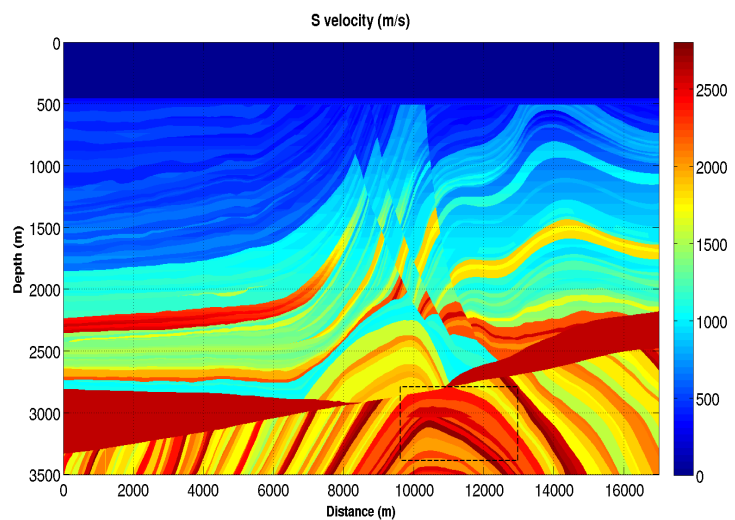
(d) Smoothing with 121 points.



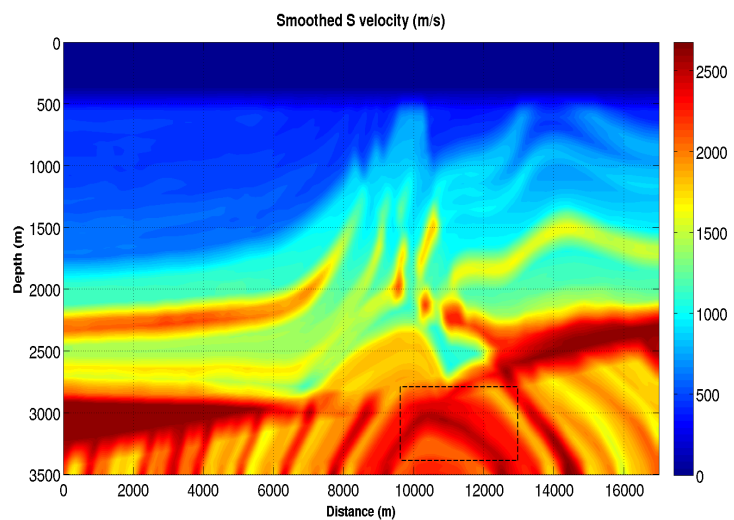
Source: From autor

Figure 5.5 – Velocity,  $v_S(x, z)$ .

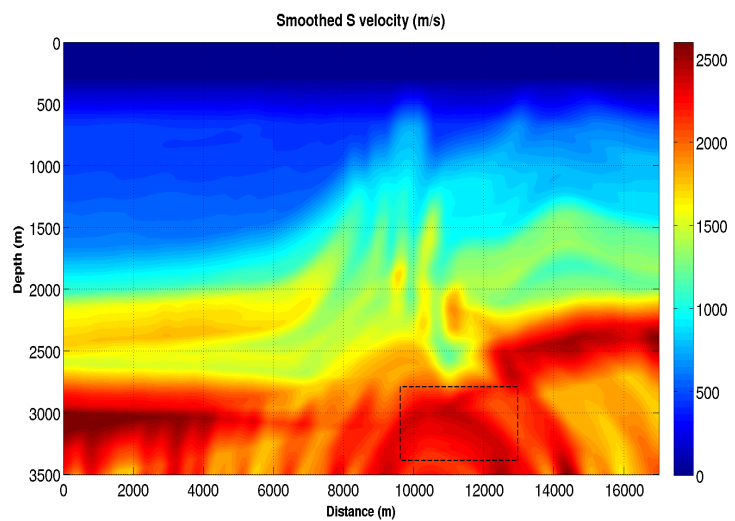
(a) Original model.



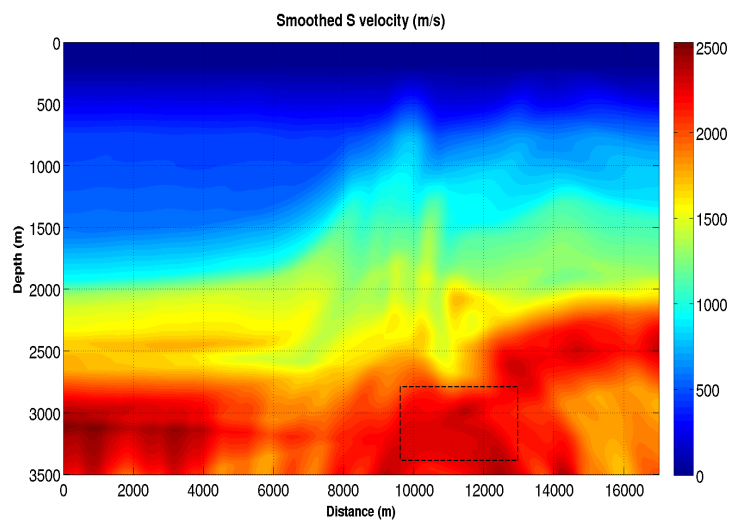
(b) Smoothing with 41 points.



(c) Smoothing with 81 points.



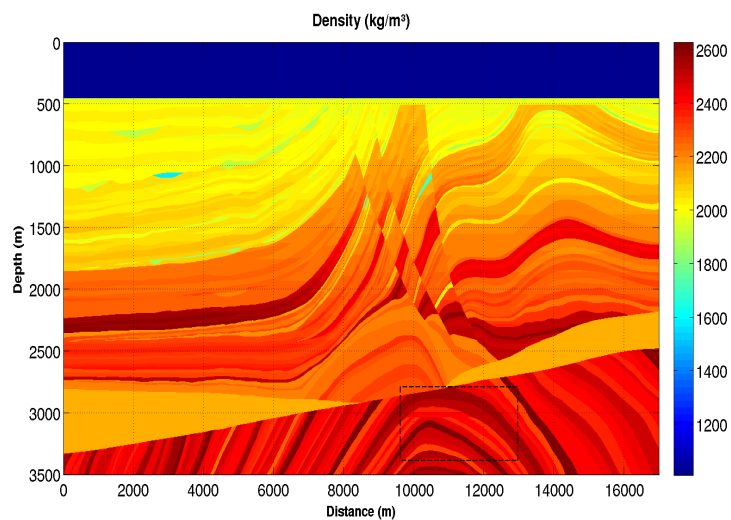
(d) Smoothing with 121 points.



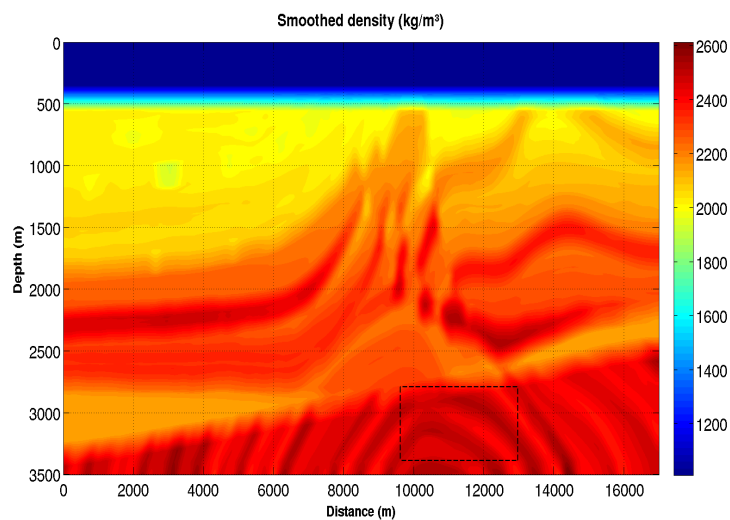
Source: From autor

Figure 5.6 – Density,  $\rho(x, z)$ .

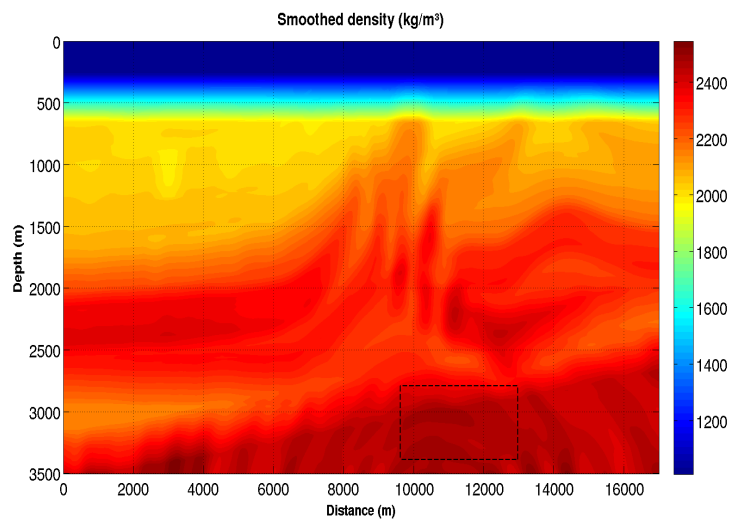
(a) Original model.



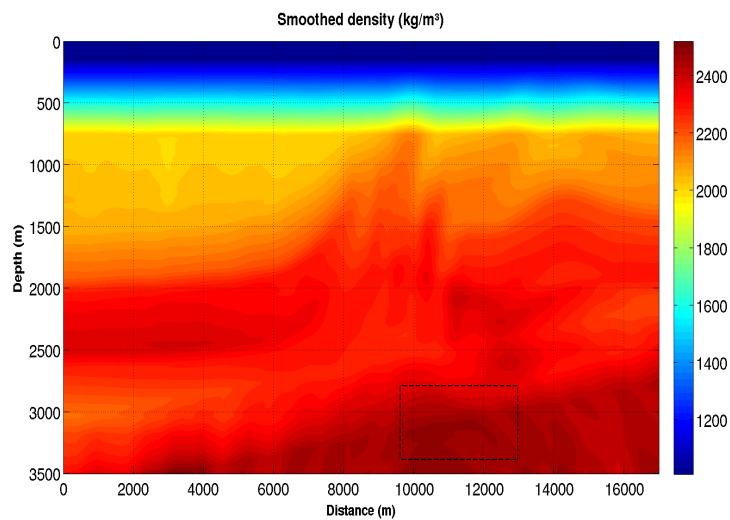
(b) Smoothing with 41 points.



(c) Smoothing with 81 points.



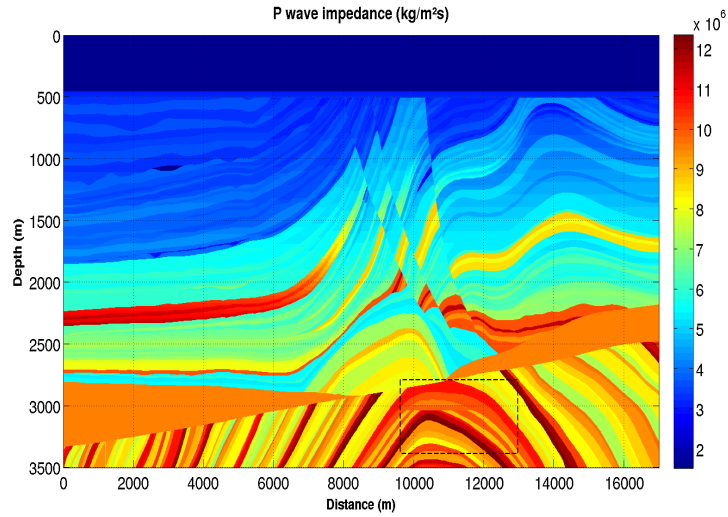
(d) Smoothing with 121 points.



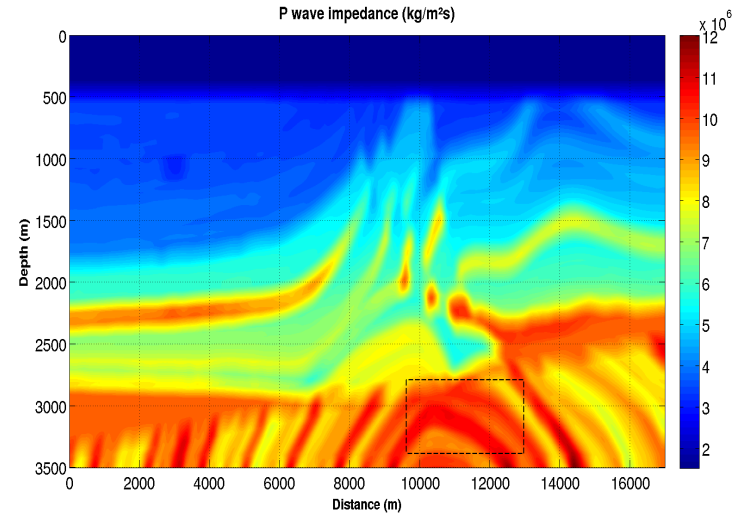
Source: From autor

Figure 5.7 – P wave impedance,  $I_P(x, z)$ .

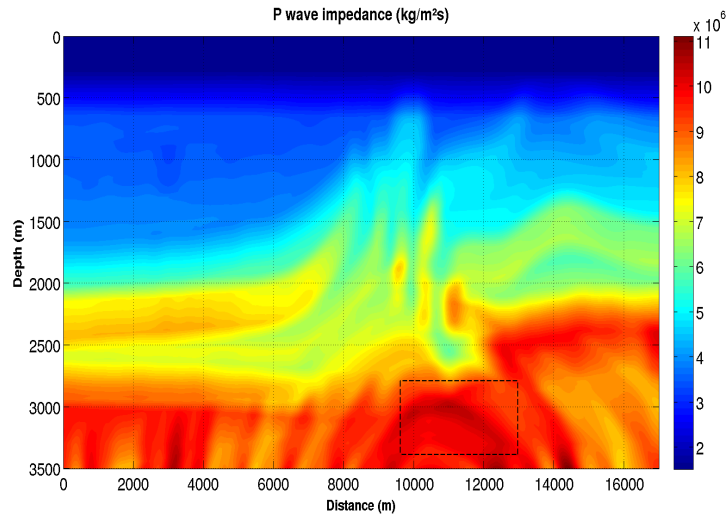
(a) Original model.



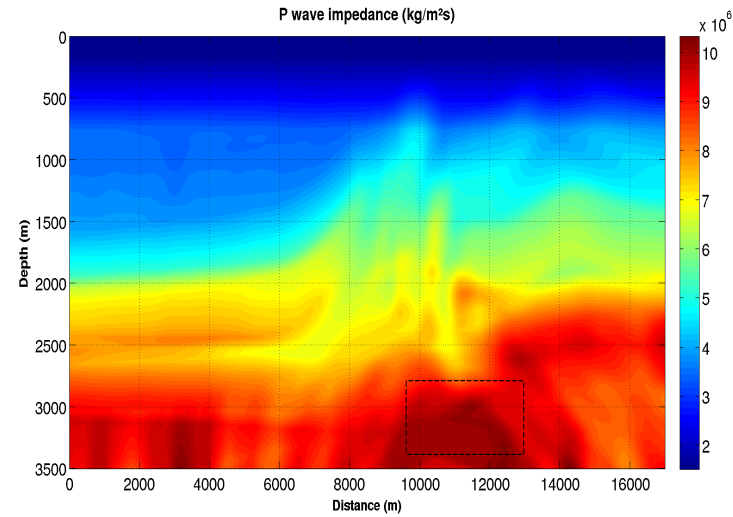
(b) Smoothing with 41 points.



(c) Smoothing with 81 points.



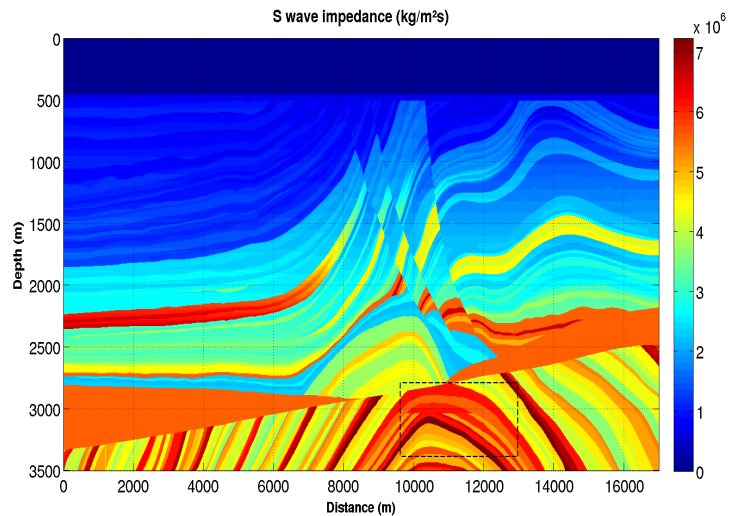
(d) Smoothing with 121 points.



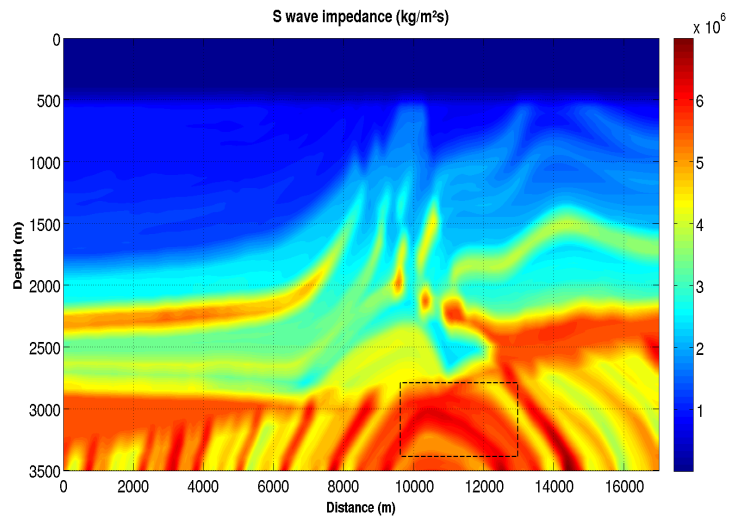
Source: From autor

Figure 5.8 – S wave impedance,  $I_S(x, z)$ .

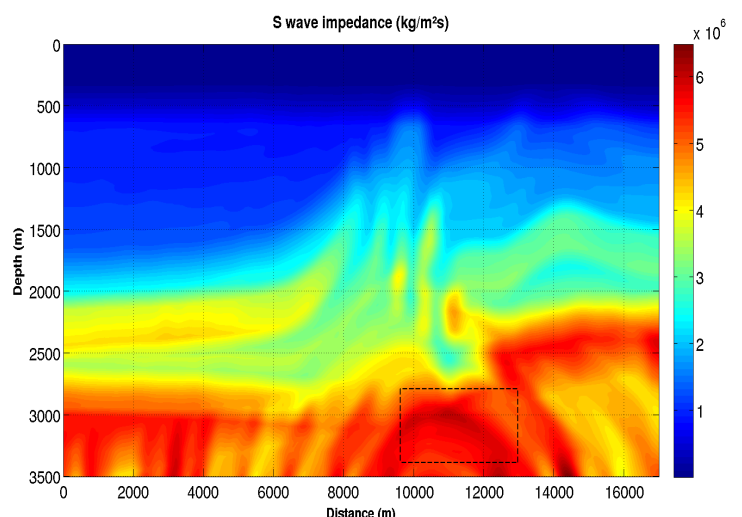
(a) Original model.



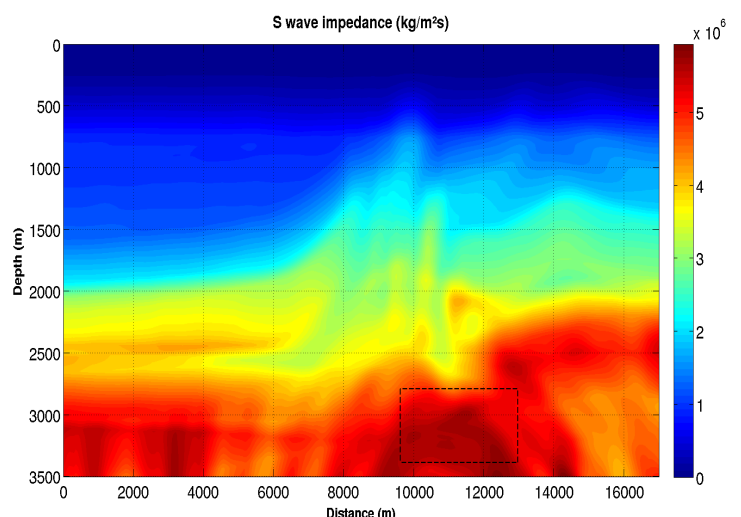
(b) Smoothing with 41 points.



(c) Smoothing with 81 points.



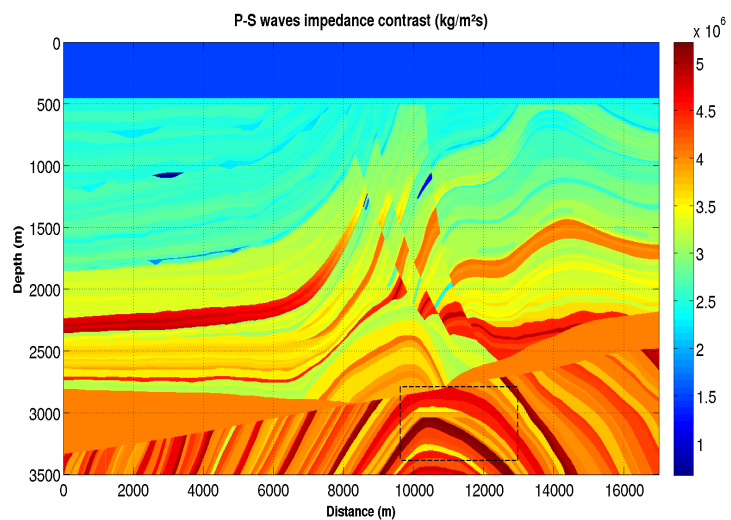
(d) Smoothing with 121 points.



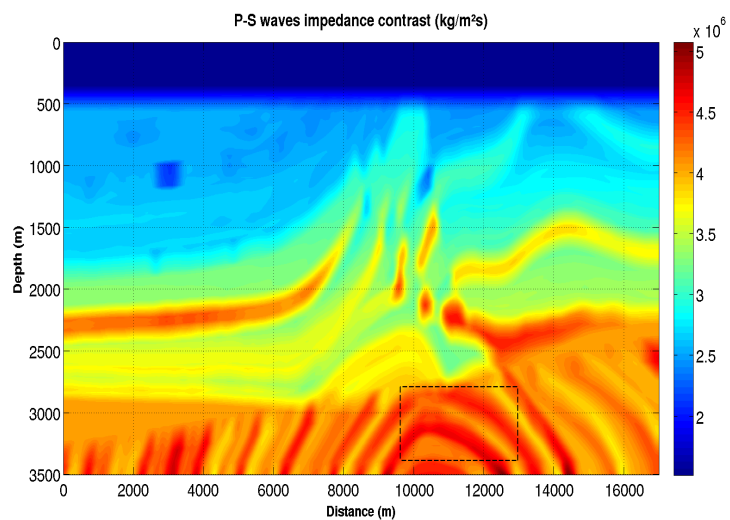
Source: From autor

Figure 5.9 – P-S wave impedance contrast,  $\Delta I_{PS}(x, z)$ .

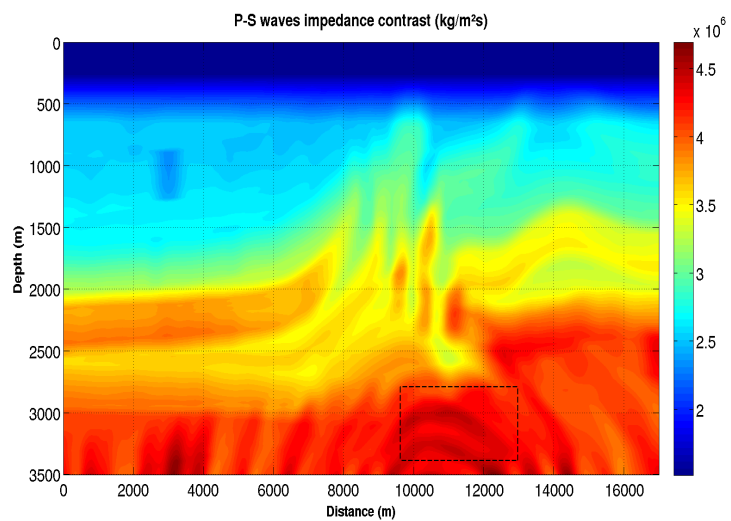
(a) Original model.



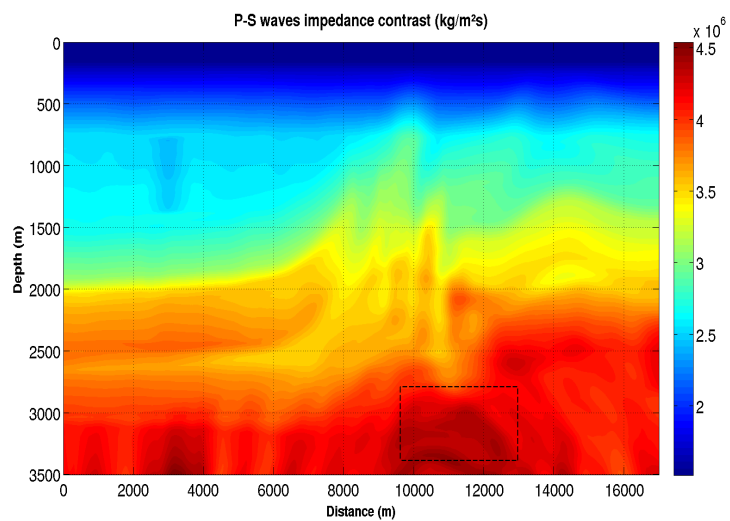
(b) Smoothing with 41 points.



(c) Smoothing with 81 points.



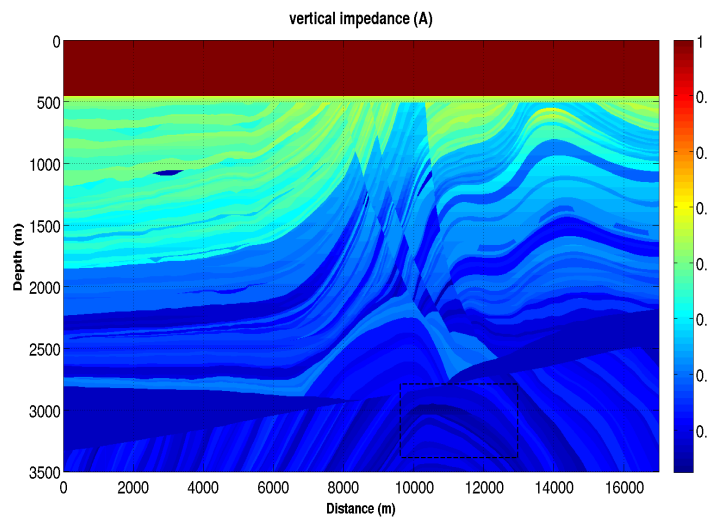
(d) Smoothing with 121 points.



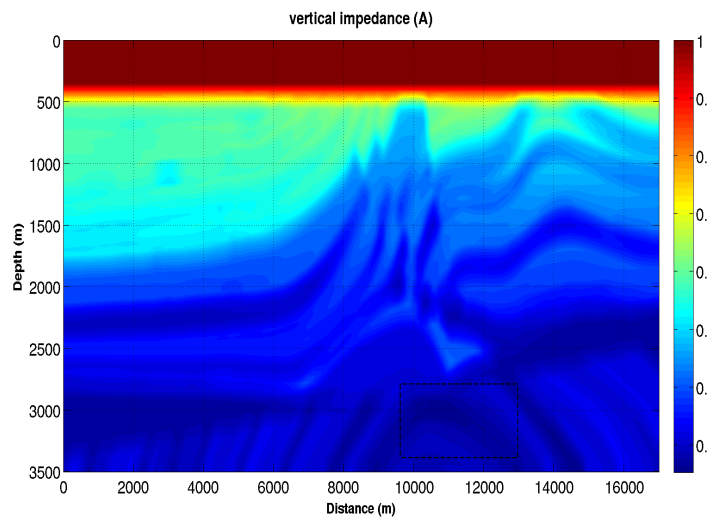
Source: From autor

Figure 5.10 – Normalized adimensional,  $(A)$ , vertical impedance coefficient contrast,  $R_{PS}(x, z) = \frac{I_P - I_S}{I_P + I_S}$ .

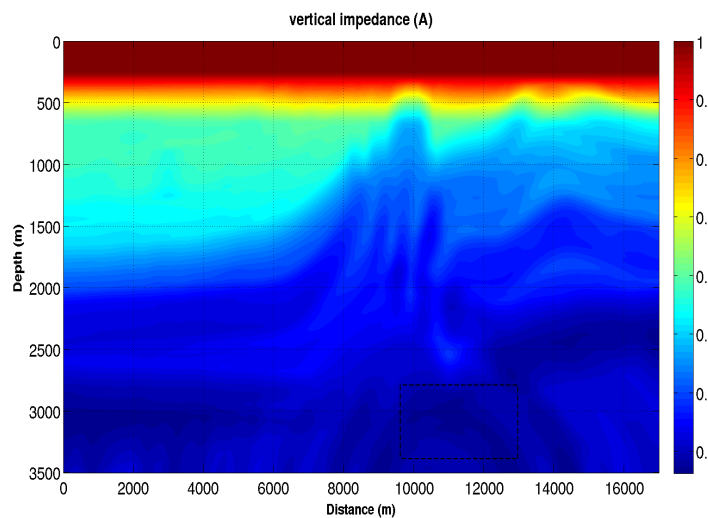
(a) Original model.



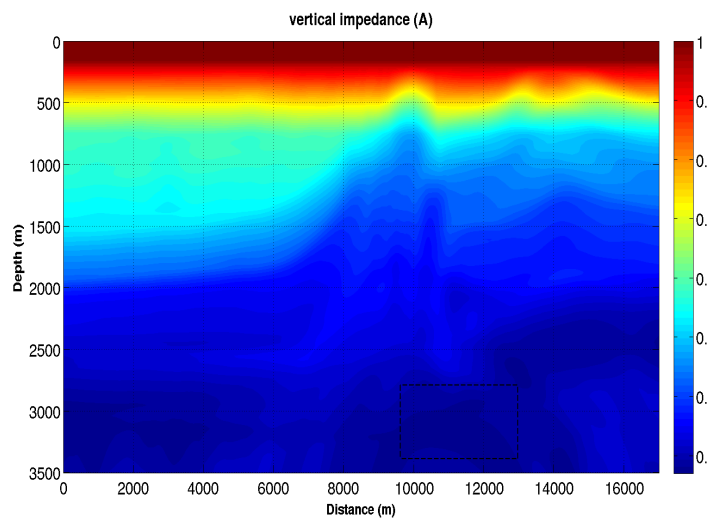
(b) Smoothing with 41 points.



(c) Smoothing with 81 points.



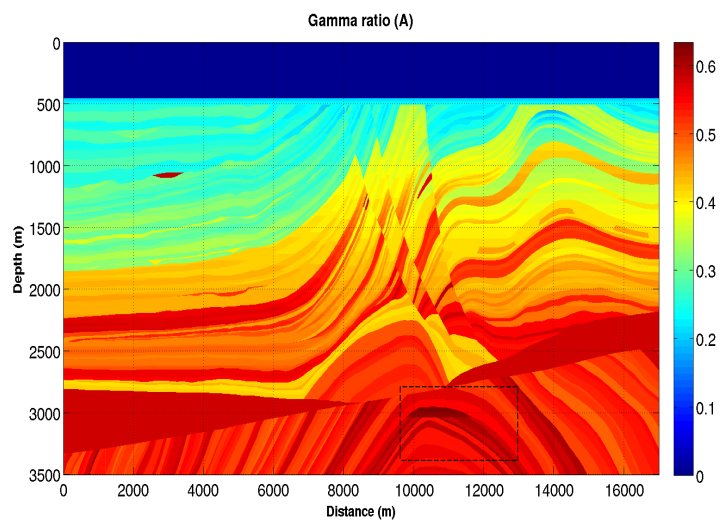
(d) Smoothing with 121 points.



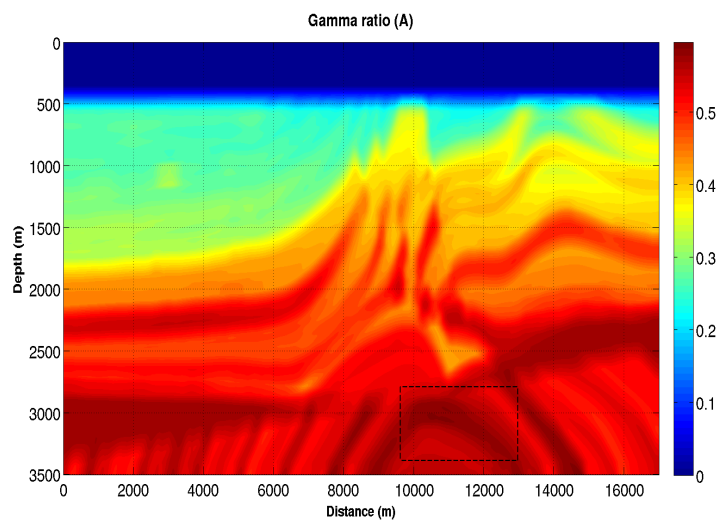
Source: From autor

Figure 5.11 – Gamma,  $\gamma(x, z)$ .

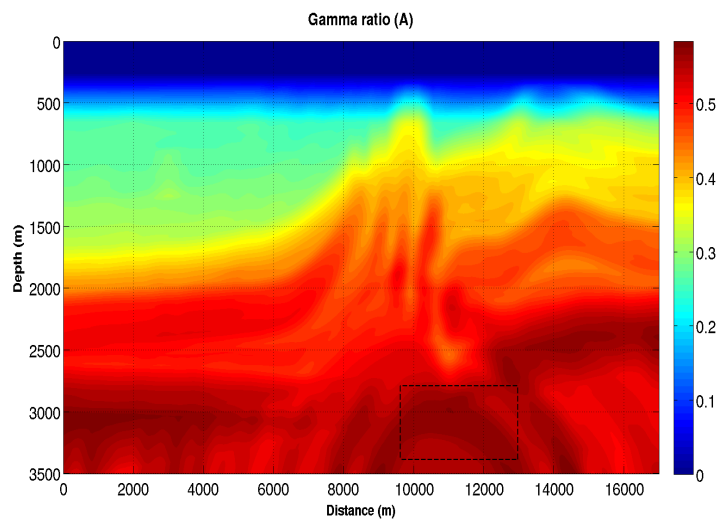
(a) Original model.



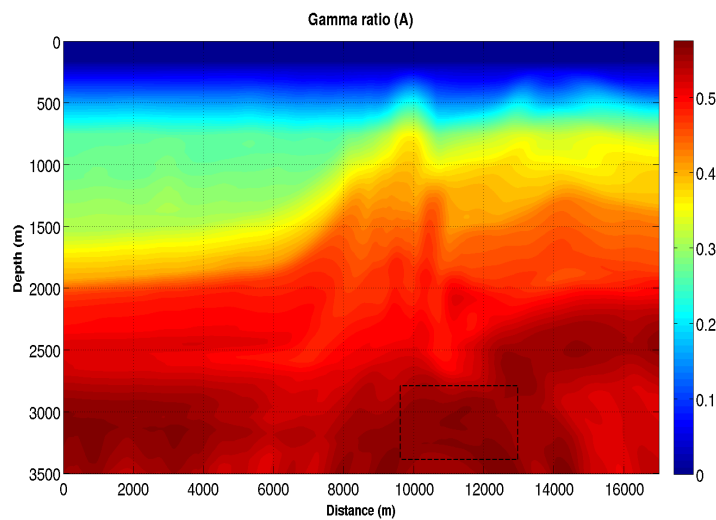
(b) Smoothing with 41 points.



(c) Smoothing with 81 points.



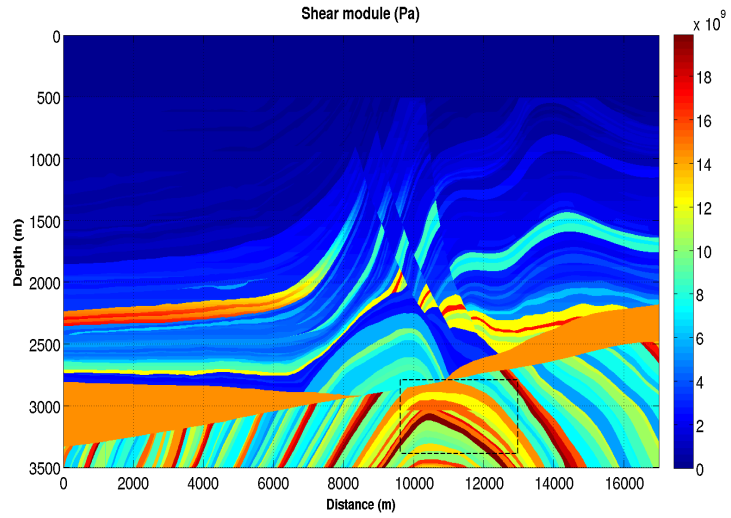
(d) Smoothing with 121 points.



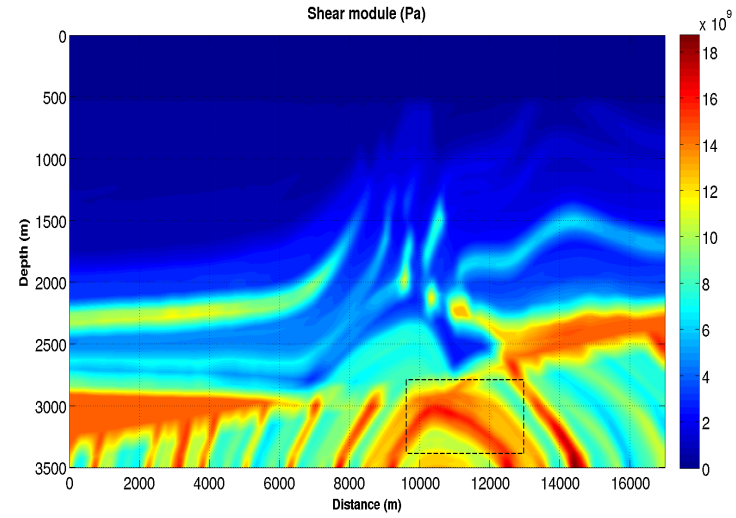
Source: From autor

Figure 5.12 – Mu,  $\mu(x, z)$ .

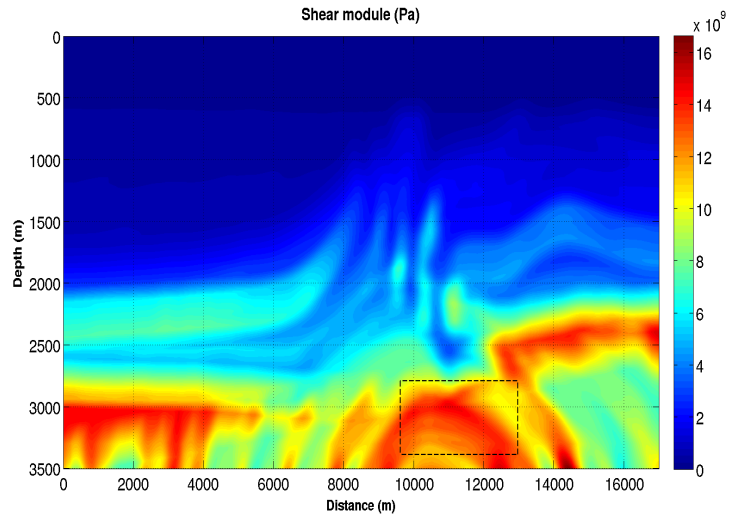
(a) Original model.



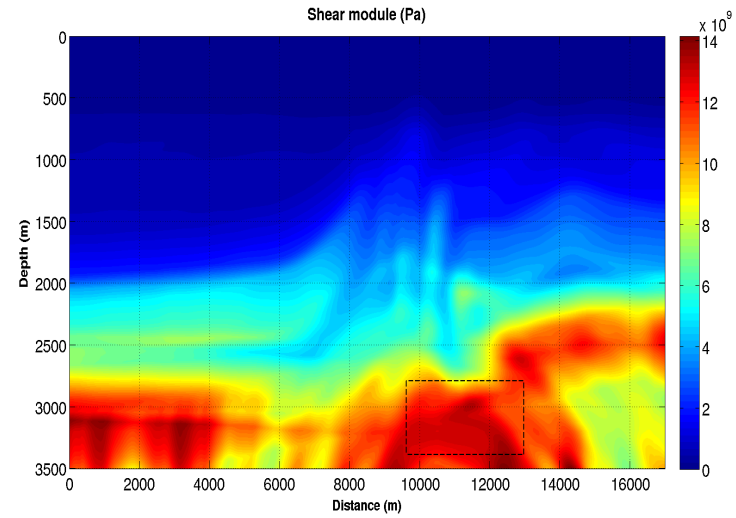
(b) Smoothing with 41 points.



(c) Smoothing with 81 points.



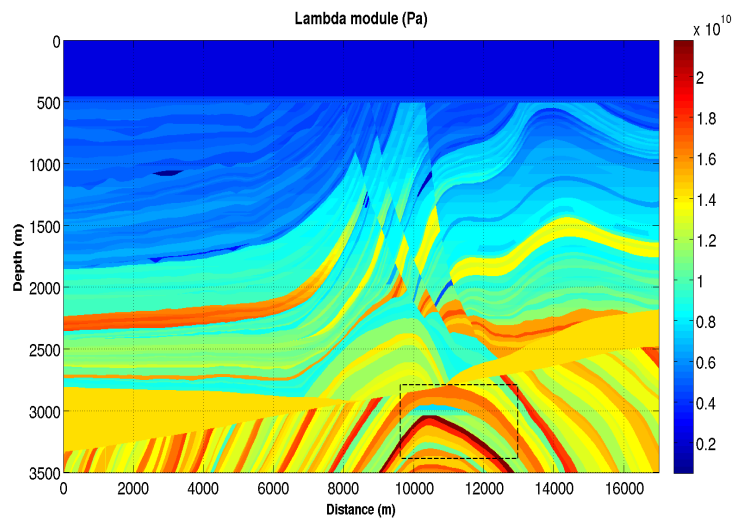
(d) Smoothing with 121 points.



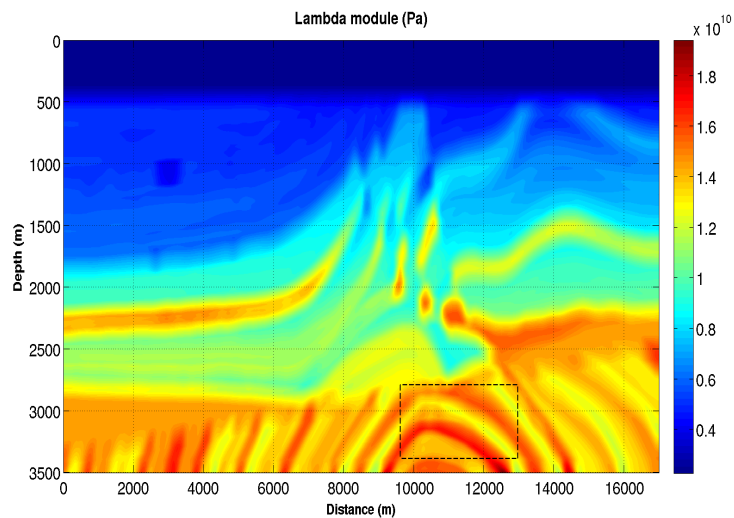
Source: From autor

Figure 5.13 – Lambda,  $\lambda(x, z)$ .

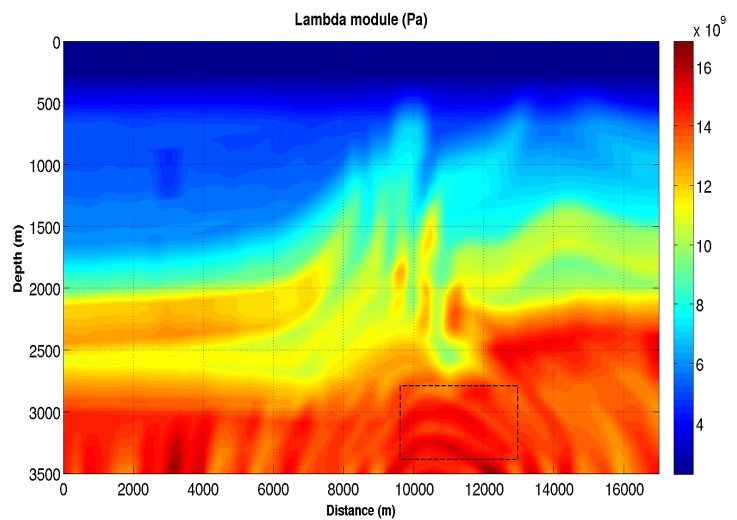
(a) Original model.



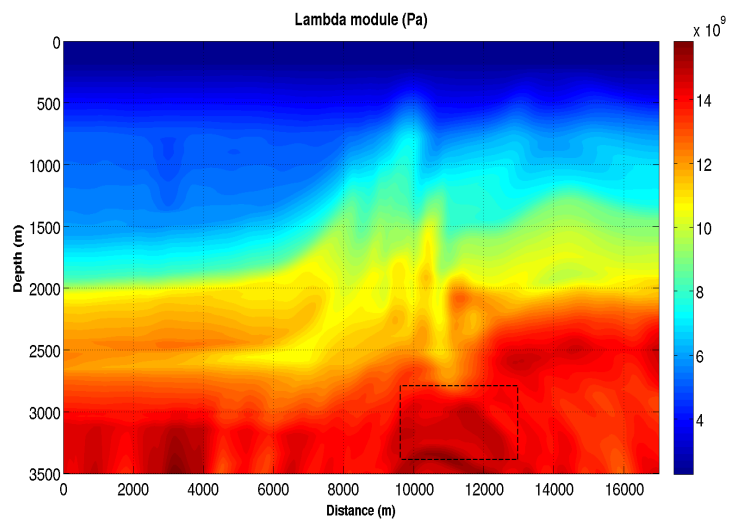
(b) Smoothing with 41 points.



(c) Smoothing with 81 points.



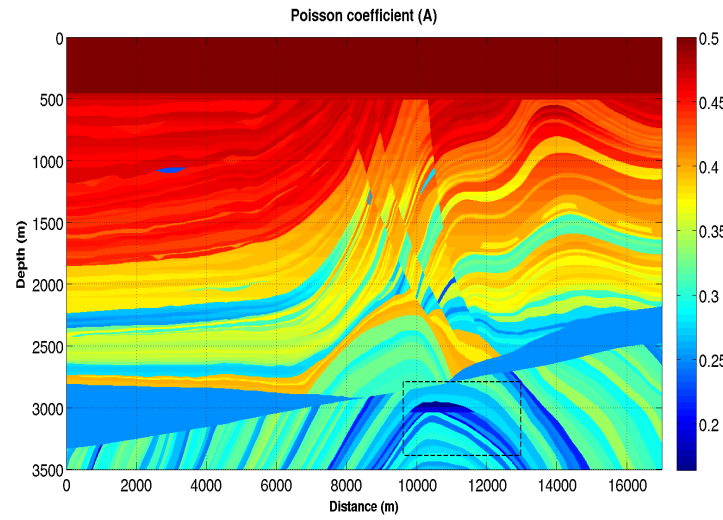
(d) Smoothing with 121 points.



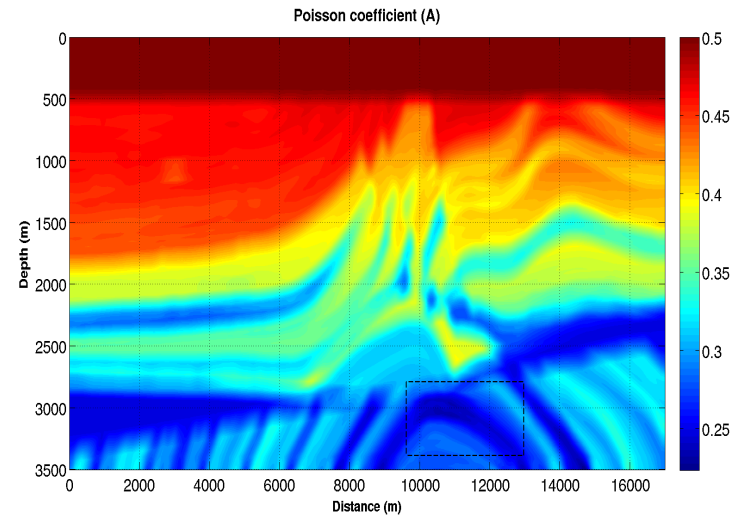
Source: From autor

Figure 5.14 – Poisson,  $\sigma(x, z)$ .

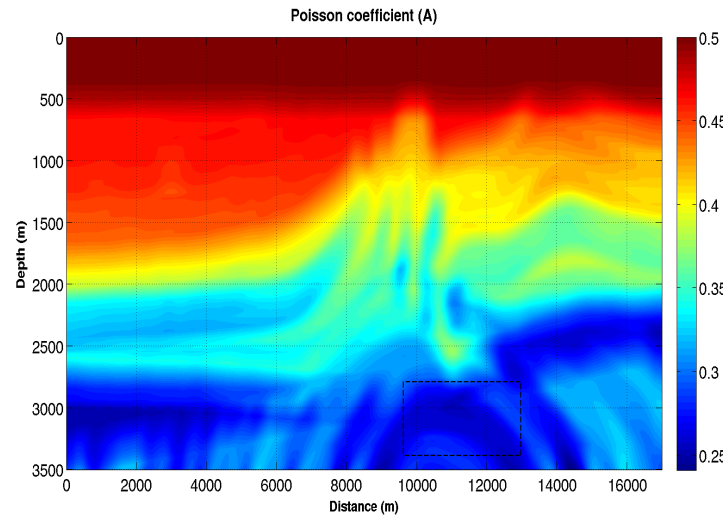
(a) Original model.



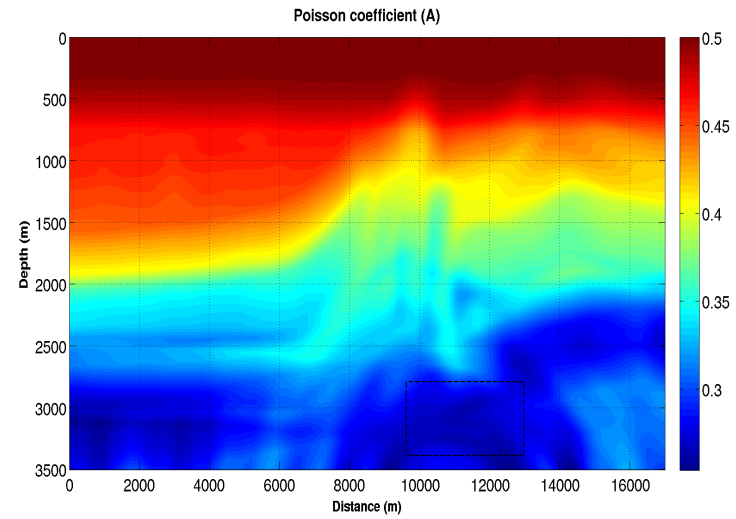
(b) Smoothing with 41 points.



(c) Smoothing with 81 points.



(d) Smoothing with 121 points.



Source: From autor

Figure 5.15 shows the vertical pressure field calculated by equation (5.22), and it displays a direct visual difficulty to identify reservoir structures as the smoothing increases.

Figure 5.16 shows the horizontal pressure field calculated by equation (5.23). This figure clearly still shows details of the target reservoir and of the geological structure as the smoothing increases, and it becomes one main conclusion of this study.

Figure 5.17 shows the hydrostatic pressure field calculated by equation (5.6) adapted to the 2D case as  $P = P_H = \frac{1}{2}(\sigma_{xx} + \sigma_{zz})$ , and it does not show details of the target reservoir in the geological structure as the smoothing increases, but a very smooth field expression.

Figure 5.18 shows the horizontal deviatoric hydrostatic pressure field,  $P_{XH} = \sigma_{xx} - P_H$ . Figure 5.19 shows the vertical deviatoric hydrostatic pressure field,  $P_{ZH} = \sigma_{zz} - P_H$ . Figure 5.20 shows the deviatoric tangential pressure field (average of the difference between the horizontal and vertical stress fields calculated by equation (5.26)). This result is built from the results in figures 5.15 and 5.16, and it also does not show details of the target in the geological structure as the smoothing process increases.

Figure 5.21 shows the stress dimensionless ratio section (ratio between the horizontal and vertical stress fields calculated by equations (5.23) and (5.22)). Figure 5.21 does not show details of the target in the geological structure, but rather a consistent linear behavior of  $k_{xz}$  with  $z$  as the smoothing process increases.

To make the section in figure 5.21 more visible, figure 5.22 shows the stress dimensionless ratio depth profiles,  $k_{xz}(z)$ , for a randomly chosen CDP at the coordinate of 12.500 m. The top left figure shows a vertical variation with superimposed strong oscillations, that clearly disappear with the smoothing process, and shows the linear to an exponential trend behavior. The scale shows the interval variation for  $0.2 < k_{xz}(z) < 1$ , where Heim's rule is still being supported as  $\sigma_{xx} \neq \sigma_{zz}$ .

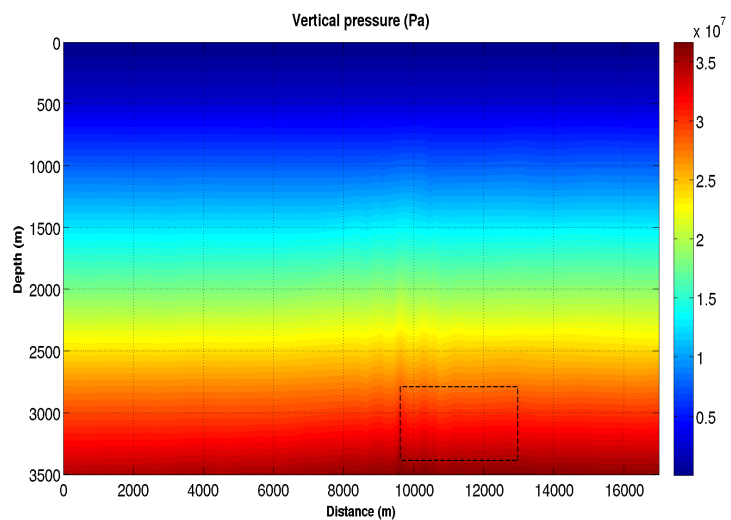
Figure 5.23 shows the vertical pressure discontinuities calculated by equation (5.25). In this special figure, we can identify the geological sequences of the model, and it also shows clearly details of the target reservoir as the smoothing increases. This is also another important conclusion of these numerical experiments.

Figure 5.24 shows the rate of vertical variation of the vertical pressure field calculated by a numerical derivative. Following the analysis for the correspondent vertical pressure field in figure 5.15, this figure also exhibit a difficulty to identify the target reservoir in the structure as the smoothing process increases.

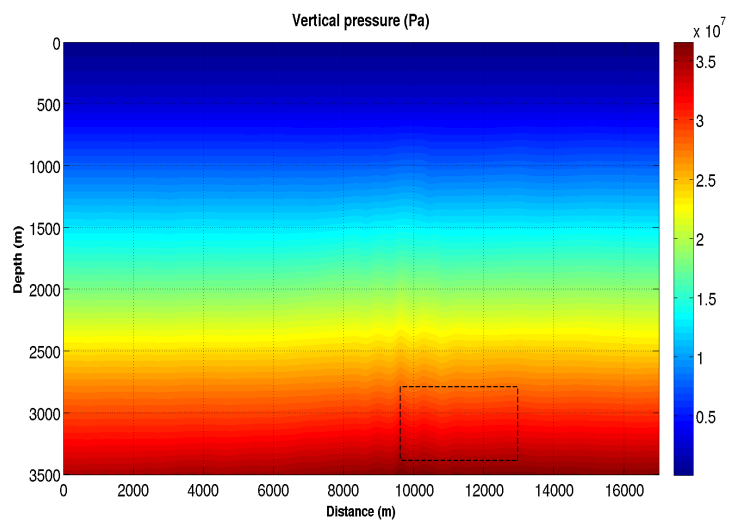
Figure 5.25 shows the rate of horizontal variation of horizontal pressure calculated by a numerical derivative. This figure exhibits an interesting behavior, and opposite to the other ones, since and it recovers aspects of the structure and discontinuities as the smoothing increases. Therefore, it serves also as a main conclusion in this work.

Figure 5.15 – Vertical pressure field,  $P_z(x, z)$ .

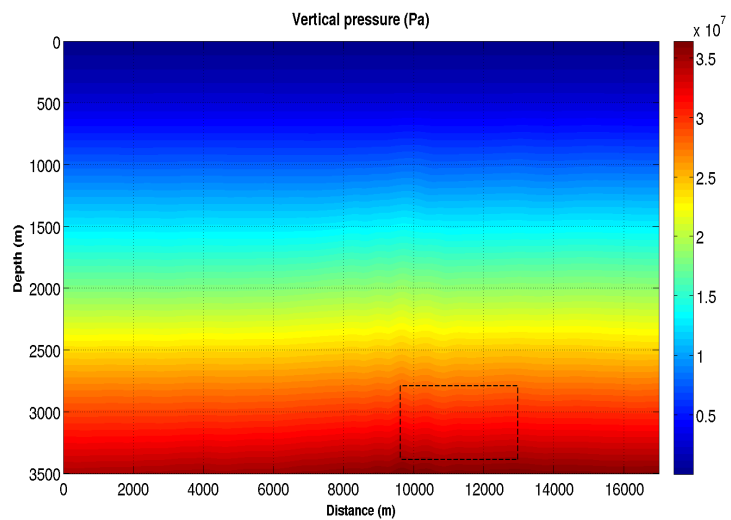
(a) Original model.



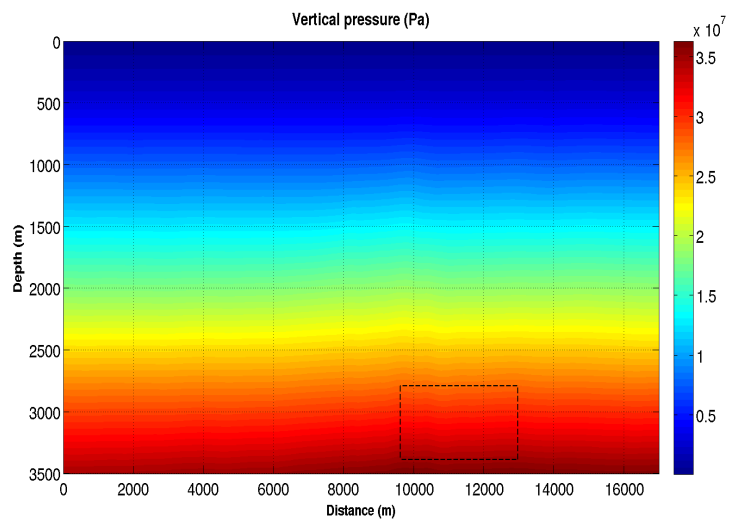
(b) Smoothing with 41 points.



(c) Smoothing with 81 points.



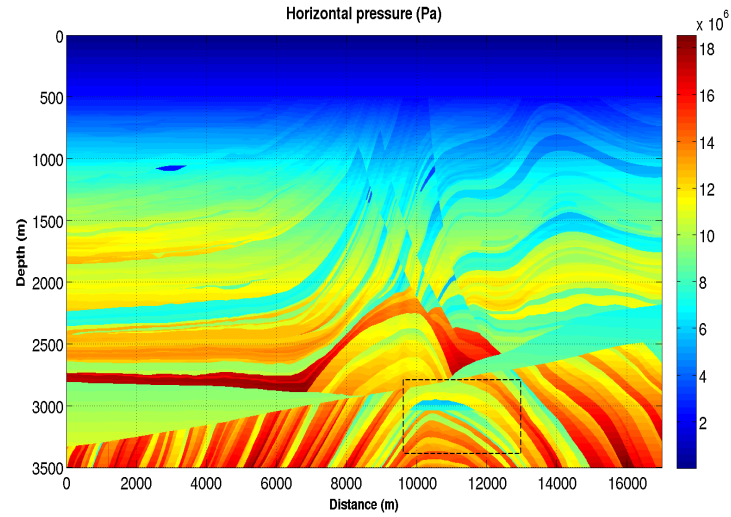
(d) Smoothing with 121 points.



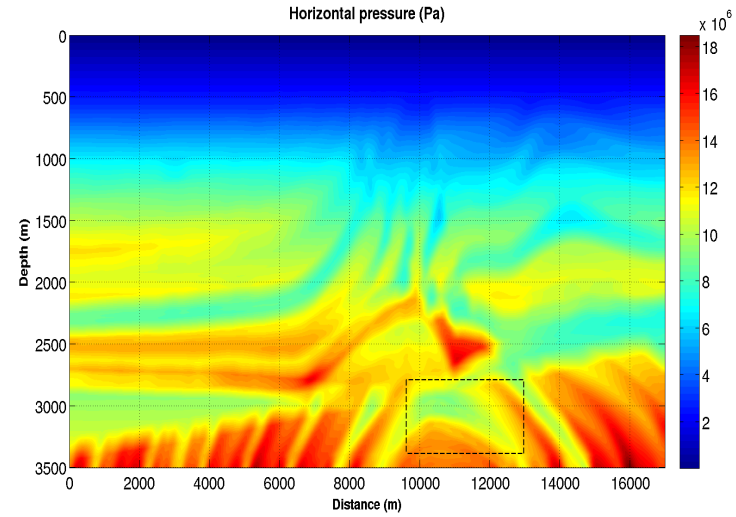
Source: From autor

Figure 5.16 – Horizontal pressure field,  $P_x(x, z)$ .

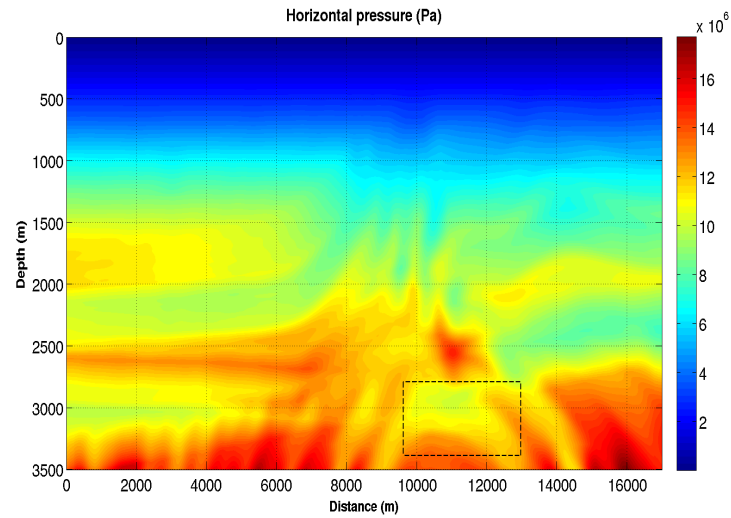
(a) Original model.



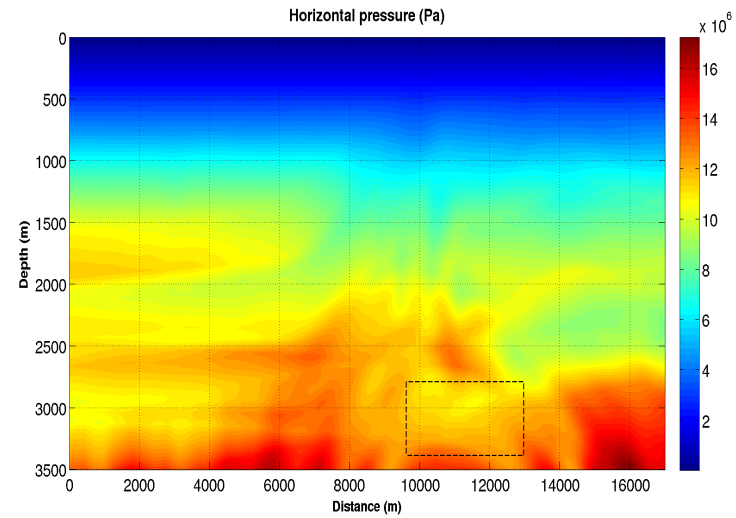
(b) Smoothing with 41 points.



(c) Smoothing with 81 points.



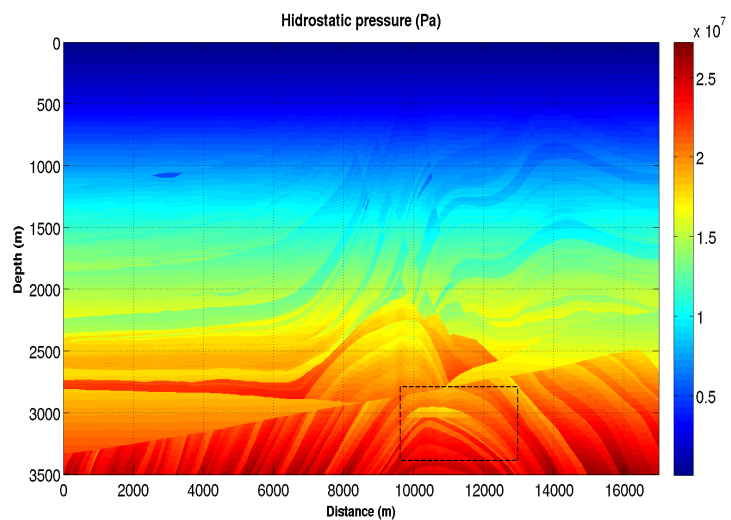
(d) Smoothing with 121 points.



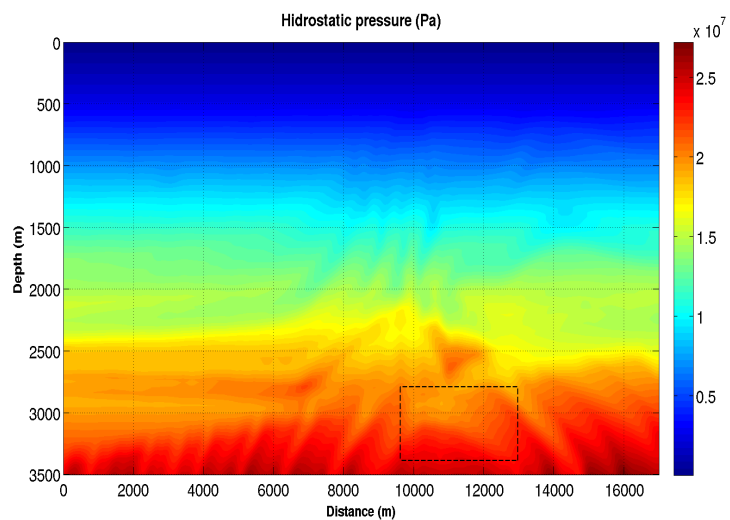
Source: From autor

Figure 5.17 – Hydrostatic pressure field,  $P_H(x, z)$ .

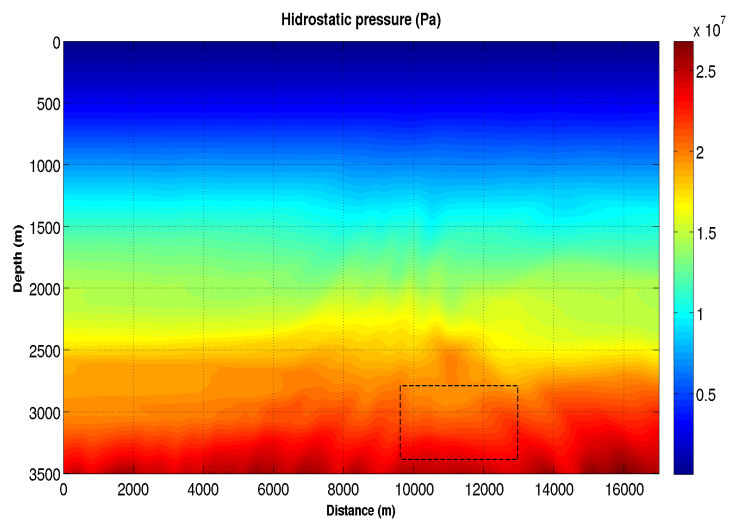
(a) Original model.



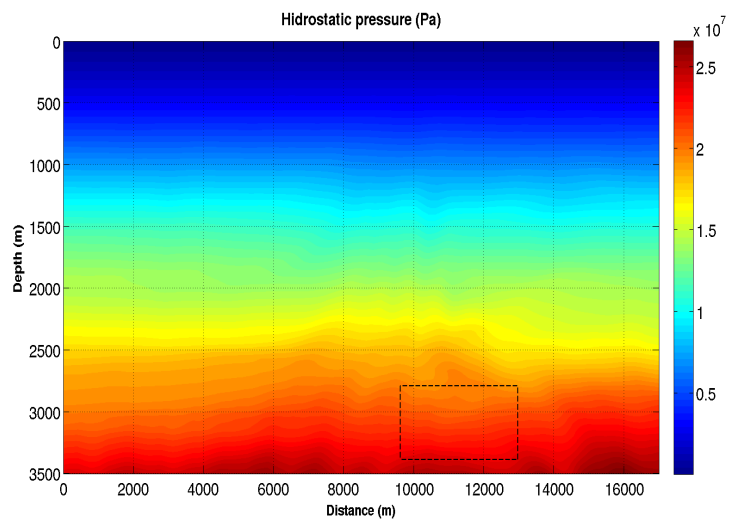
(b) Smoothing with 41 points.



(c) Smoothing with 81 points.



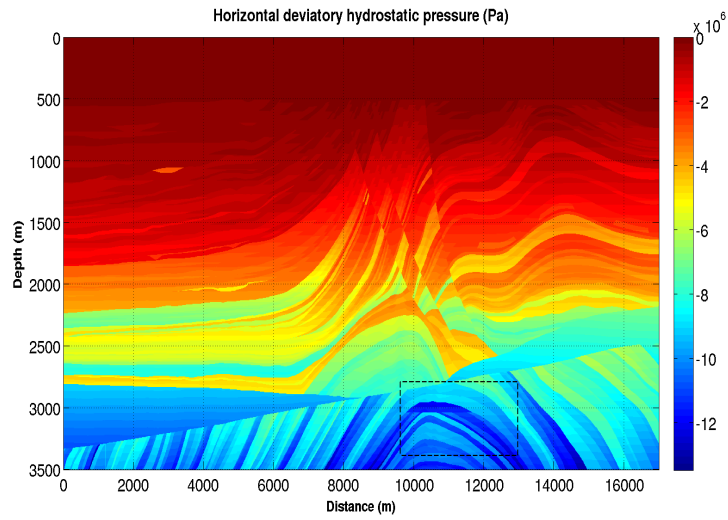
(d) Smoothing with 121 points.



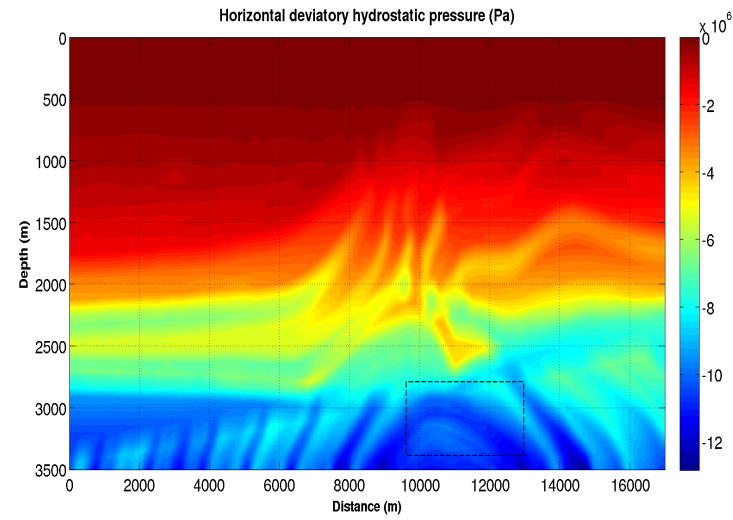
Source: From autor

Figure 5.18 – Horizontal deviatoric hydrostatic pressure field,  $P_{XH} = \sigma_{xx} - P_H$ .

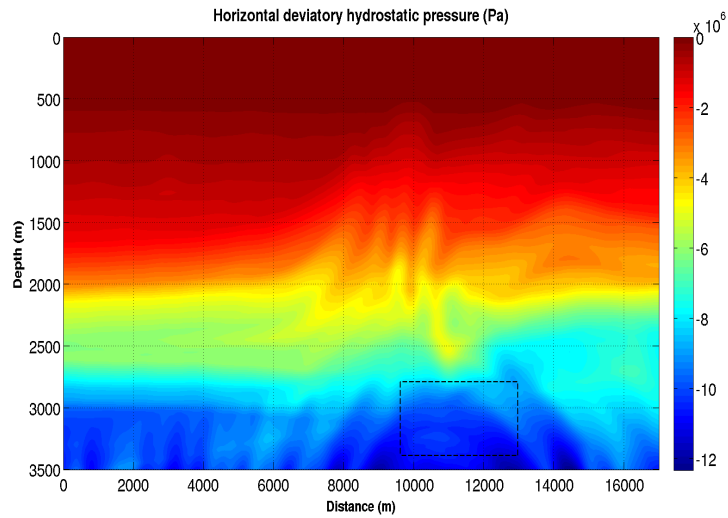
(a) Original model.



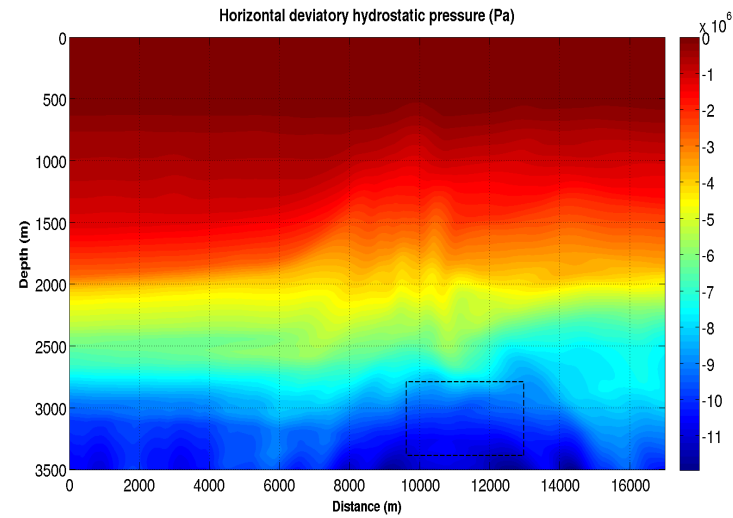
(b) Smoothing with 41 points.



(c) Smoothing with 81 points.



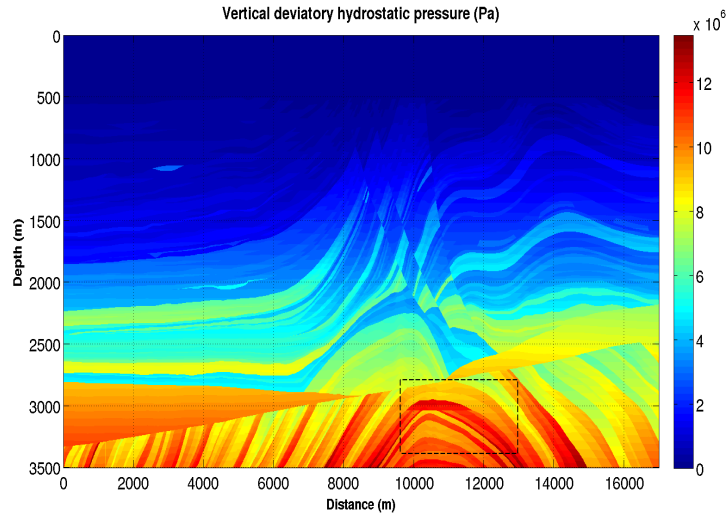
(d) Smoothing with 121 points.



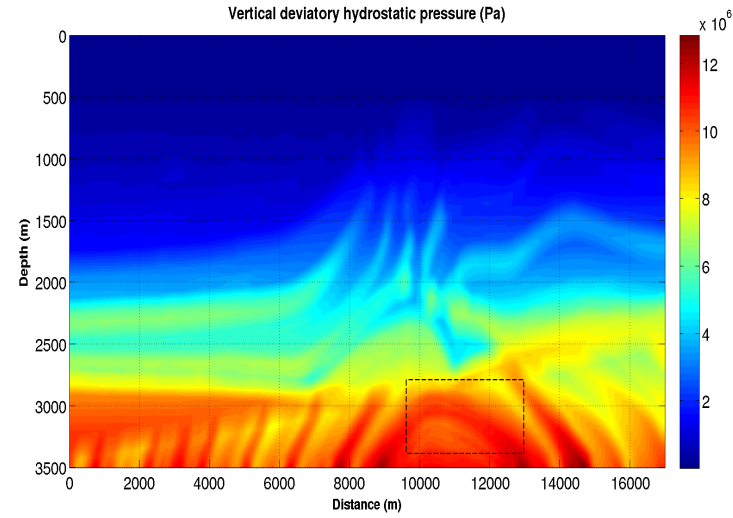
Source: From autor

Figure 5.19 – Vertical deviatoric hydrostatic pressure field,  $P_{ZH} = \sigma_{zz} - P_H$ .

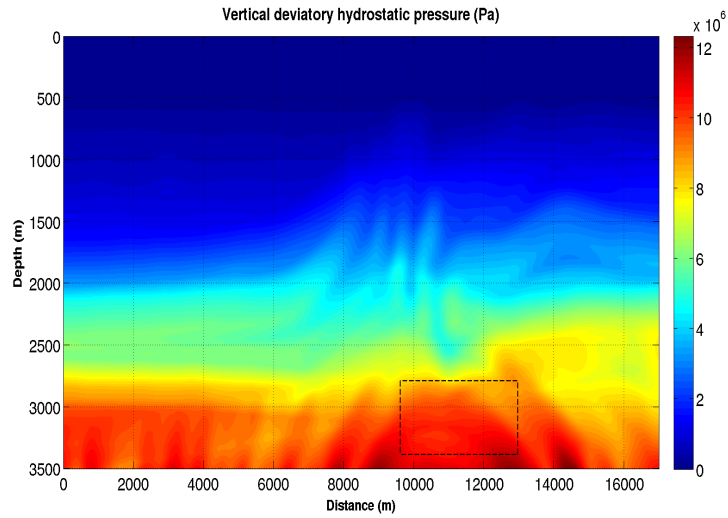
(a) Original model.



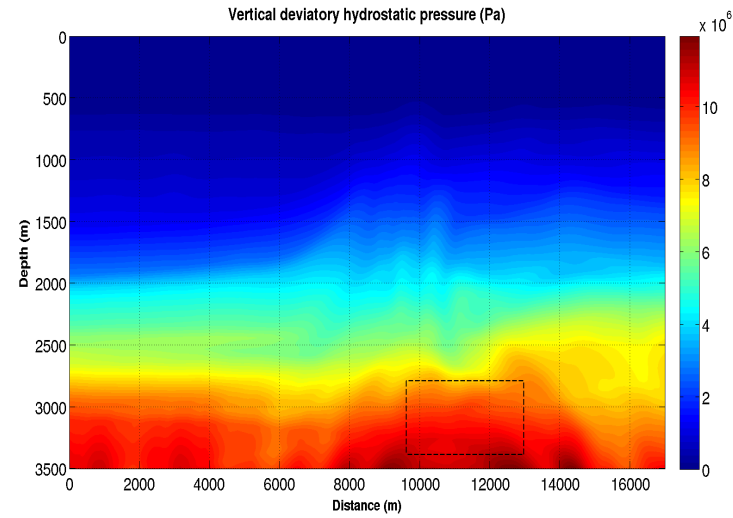
(b) Smoothing with 41 points.



(c) Smoothing with 81 points.



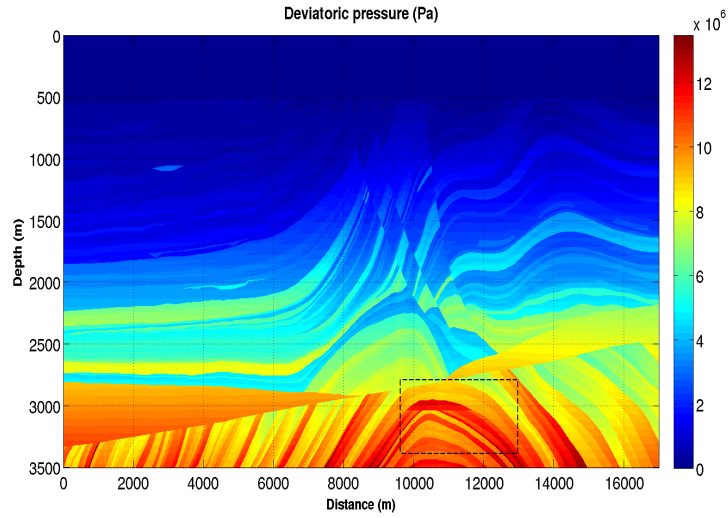
(d) Smoothing with 121 points.



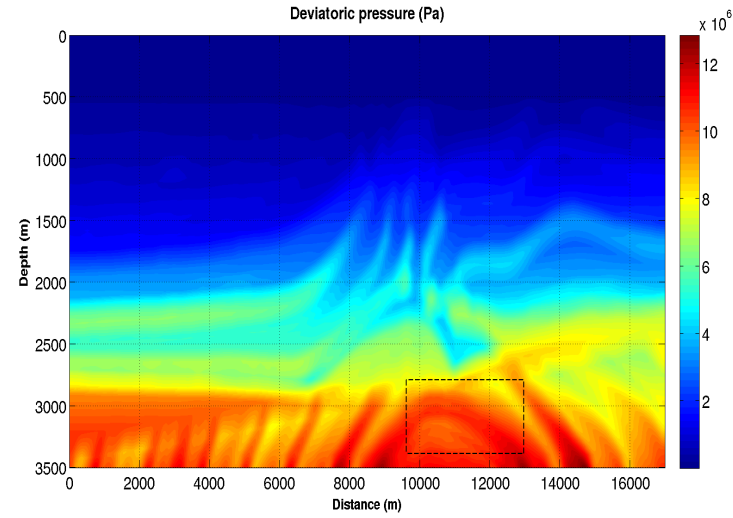
Source: From autor

Figure 5.20 – Tangential deviatoric pressure field,  $P_T(x, z)$ .

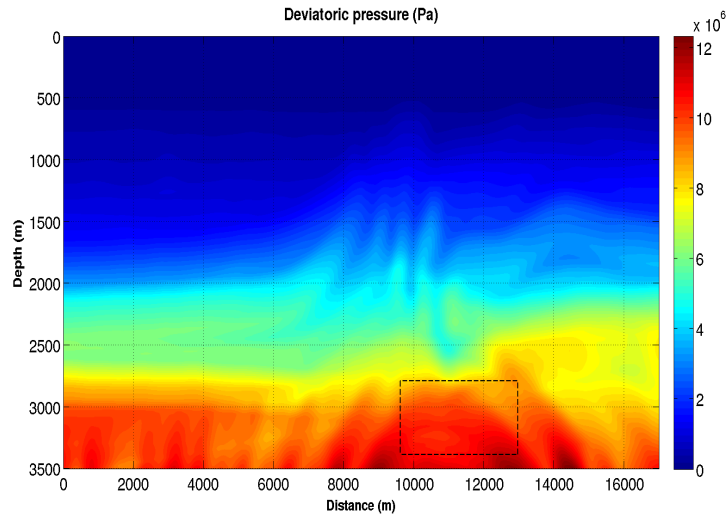
(a) Original model.



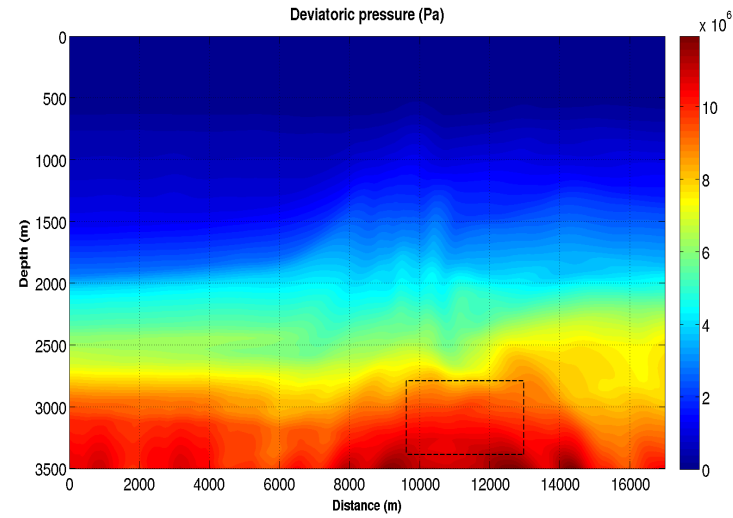
(b) Smoothing with 41 points.



(c) Smoothing with 81 points.



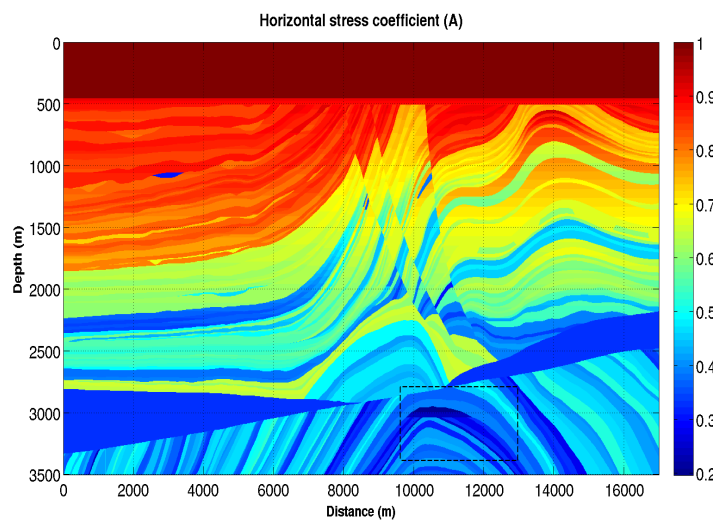
(d) Smoothing with 121 points.



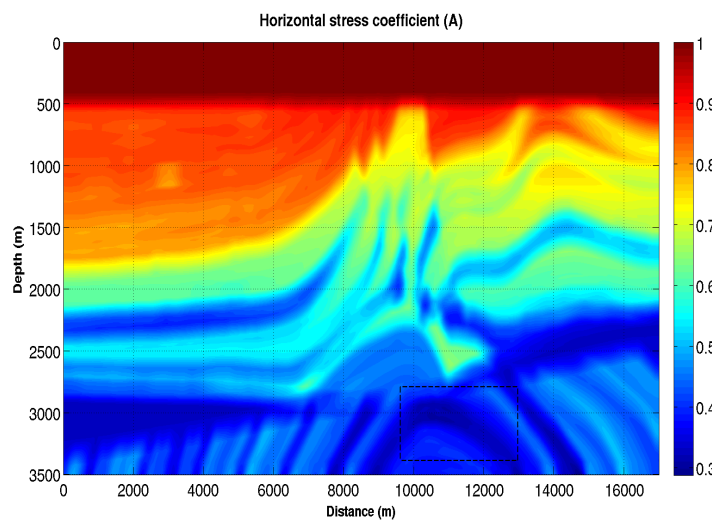
Source: From autor

Figure 5.21 – Horizontal/vertical stress ratio,  $k_{xz}(x, z)$ .

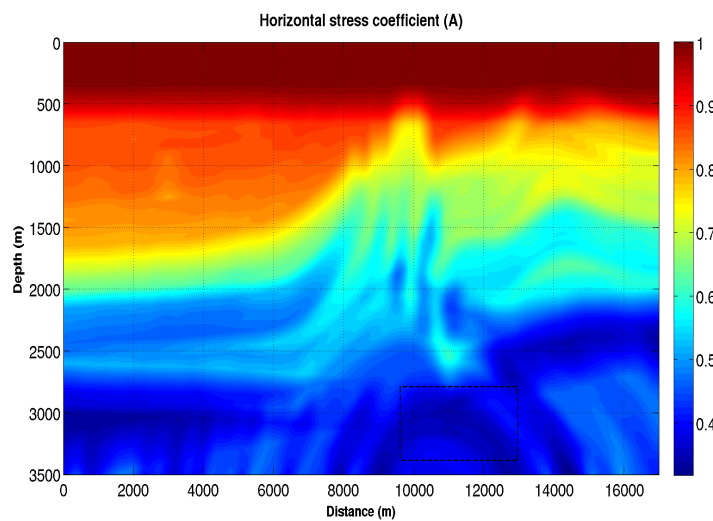
(a) Original model.



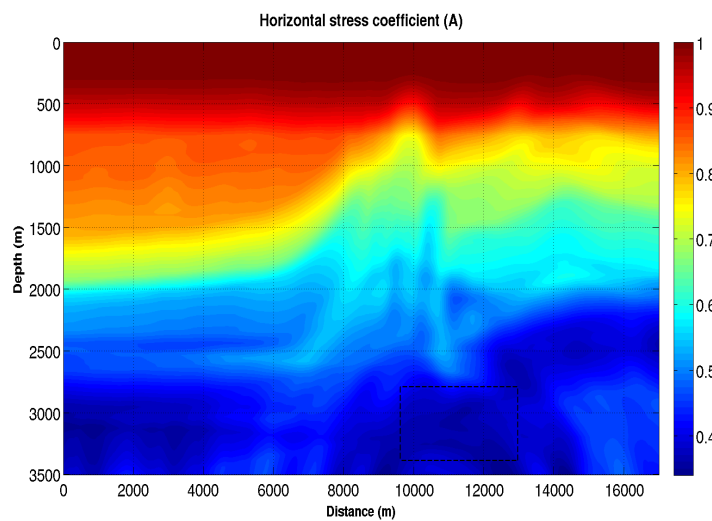
(b) Smoothing with 41 points.



(c) Smoothing with 81 points.



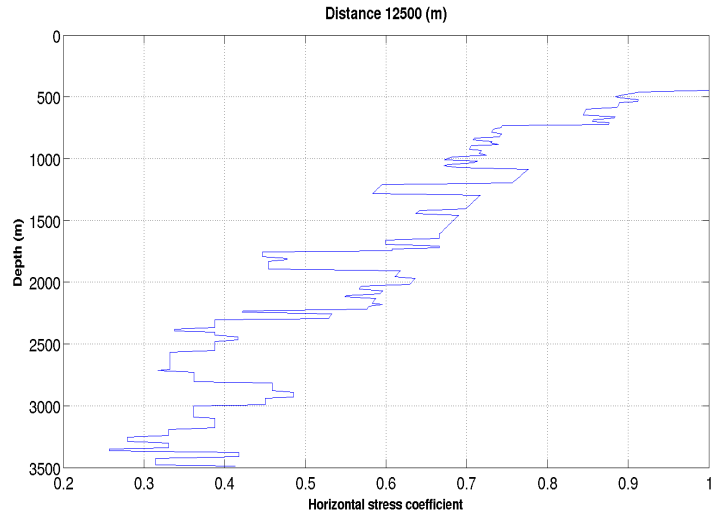
(d) Smoothing with 121 points.



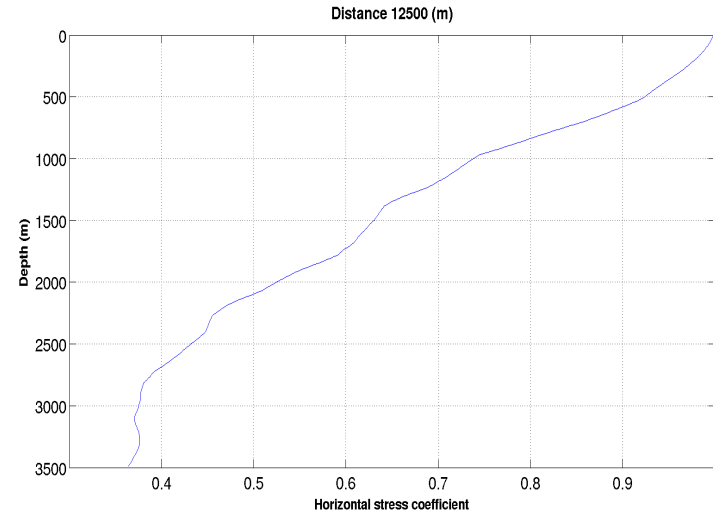
Source: From autor

Figure 5.22 – Horizontal/vertical stress ratio selected profile,  $k_{xz}(z)$ .

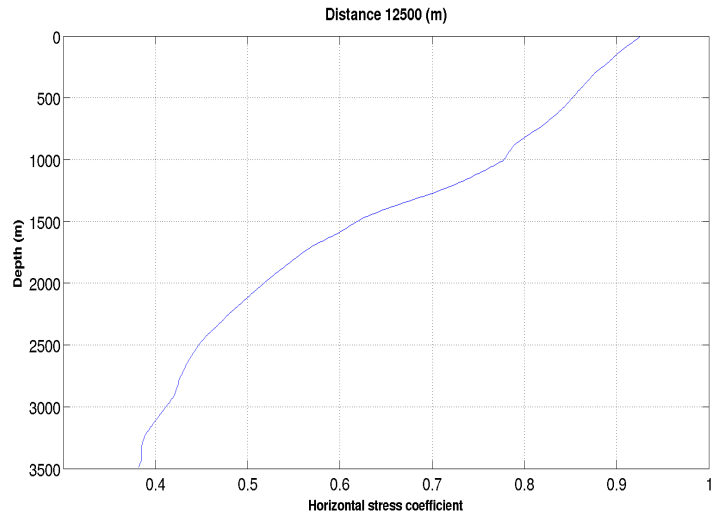
(a) Original model.



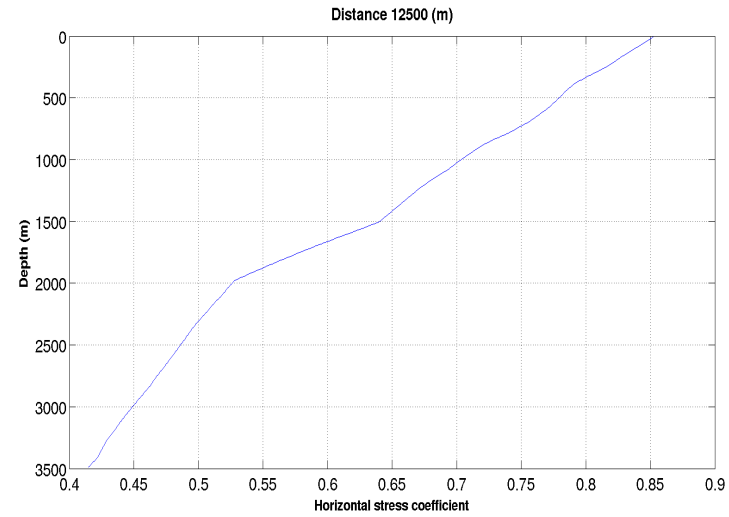
(b) Smoothing with 41 points.



(c) Smoothing with 81 points.



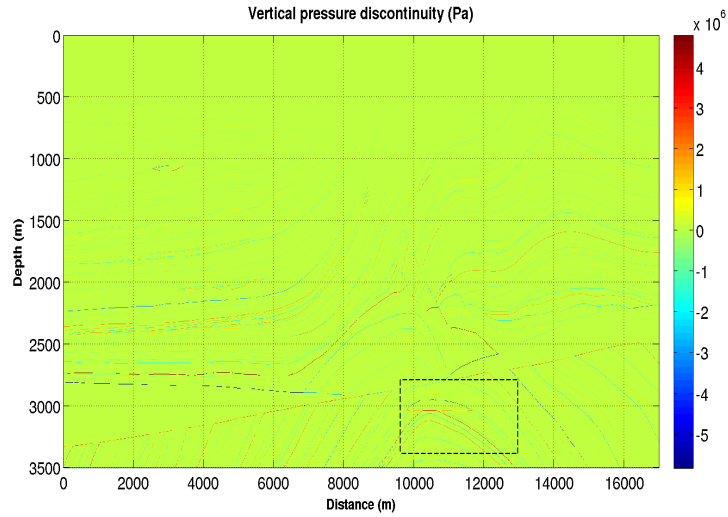
(d) Smoothing with 121 points.



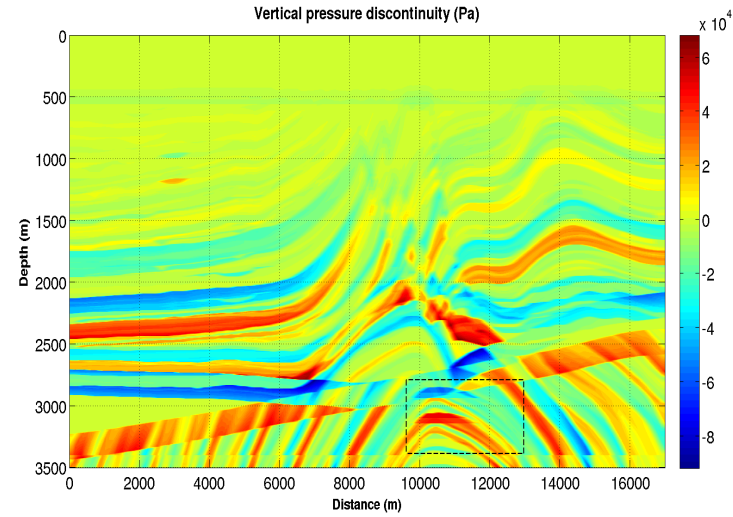
Source: From autor

Figure 5.23 – Vertical pressure discontinuities,  $\Delta P(x, z)$ , across the interfaces.

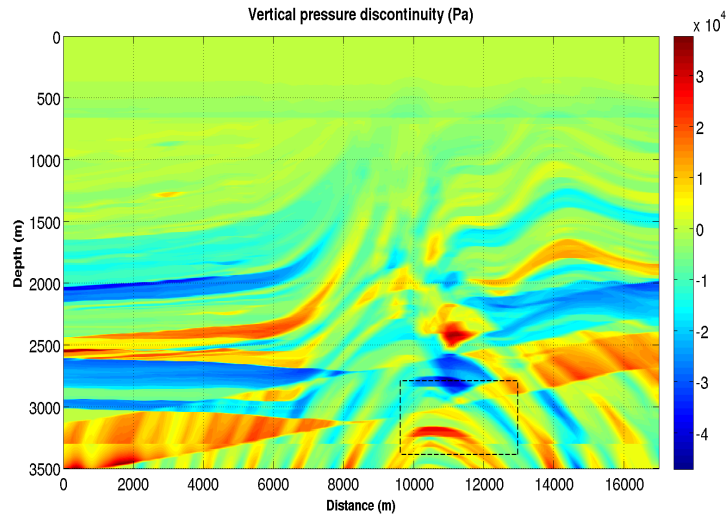
(a) Original model.



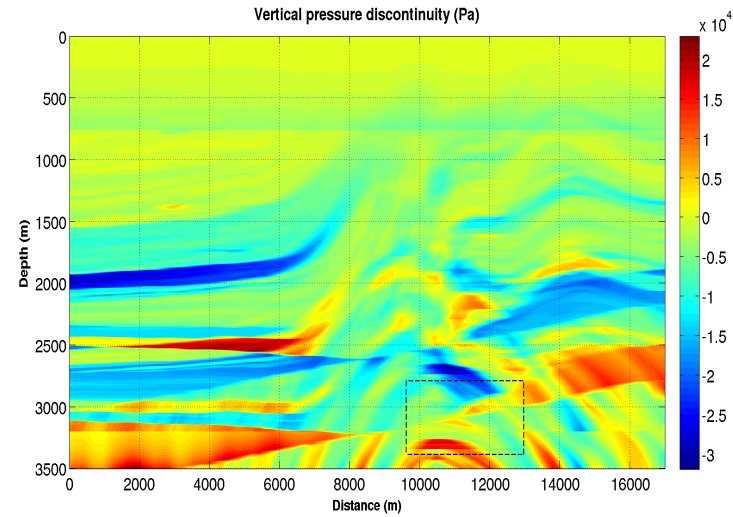
(b) Smoothing with 41 points.



(c) Smoothing with 81 points.



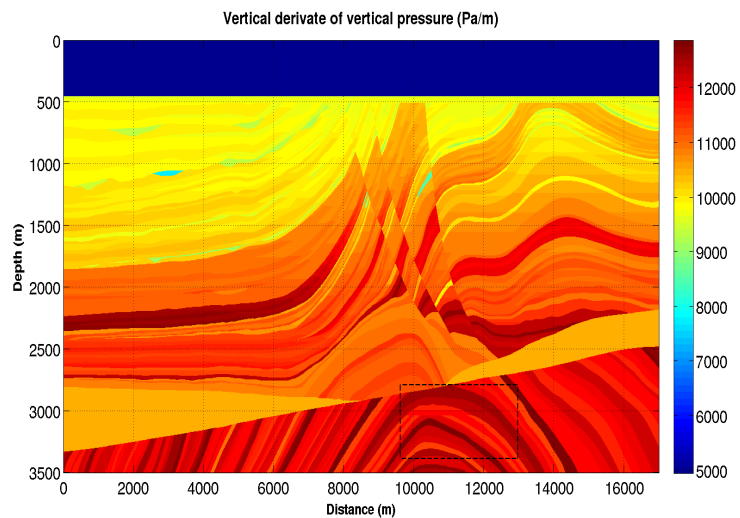
(d) Smoothing with 121 points.



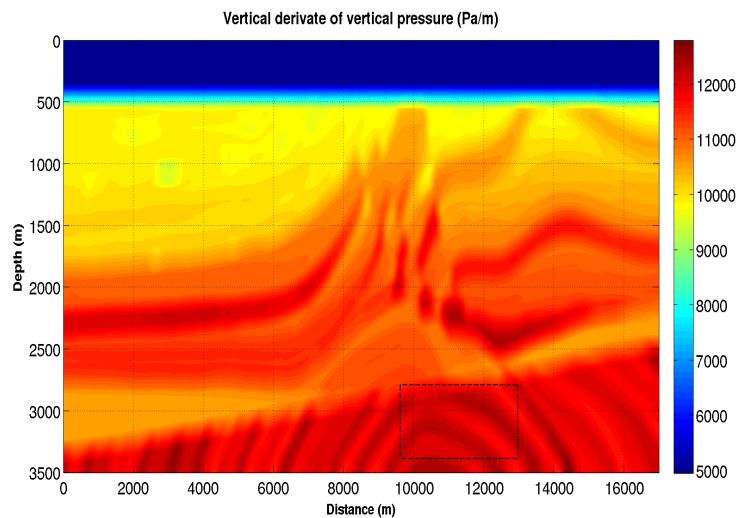
Source: From autor

Figure 5.24 – Vertical variation of the vertical pressure field,  $\frac{\partial P_z(x,z)}{\partial z}$ , given in figure 5.15.

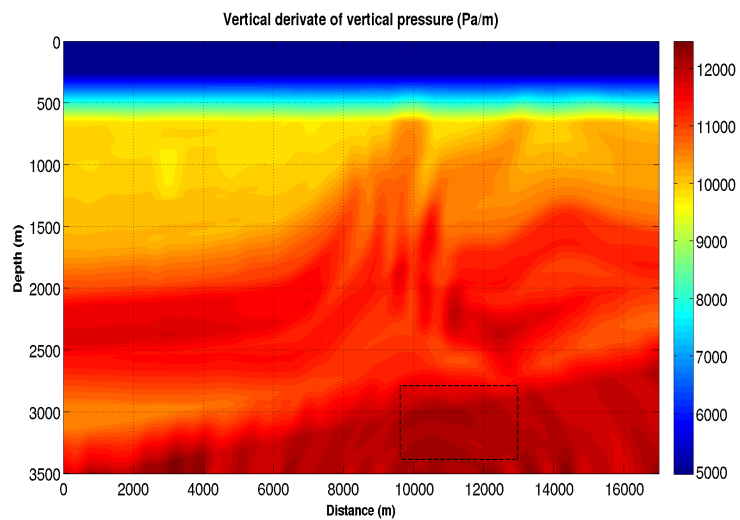
(a) Original model.



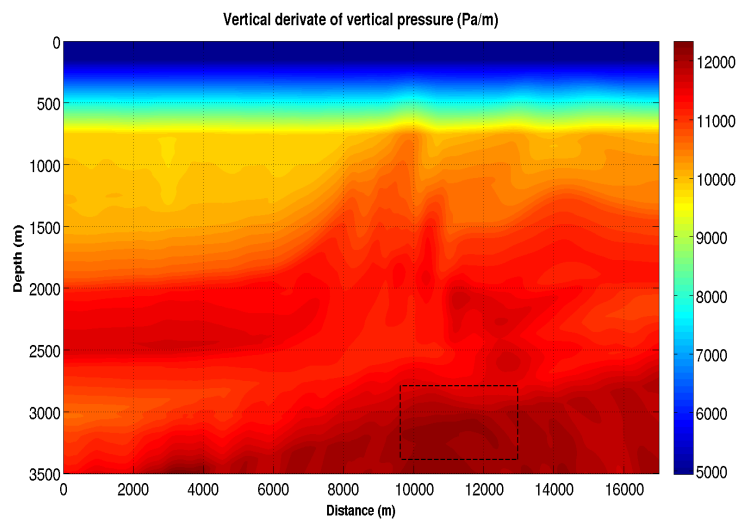
(b) Smoothing with 41 points.



(c) Smoothing with 81 points.



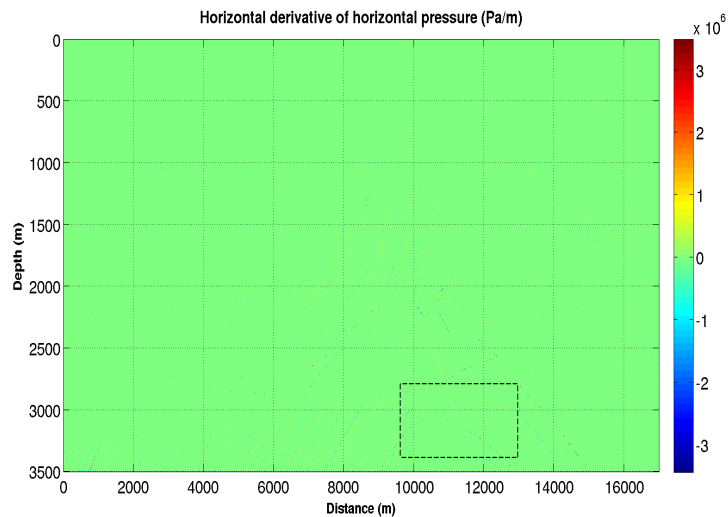
(d) Smoothing with 121 points.



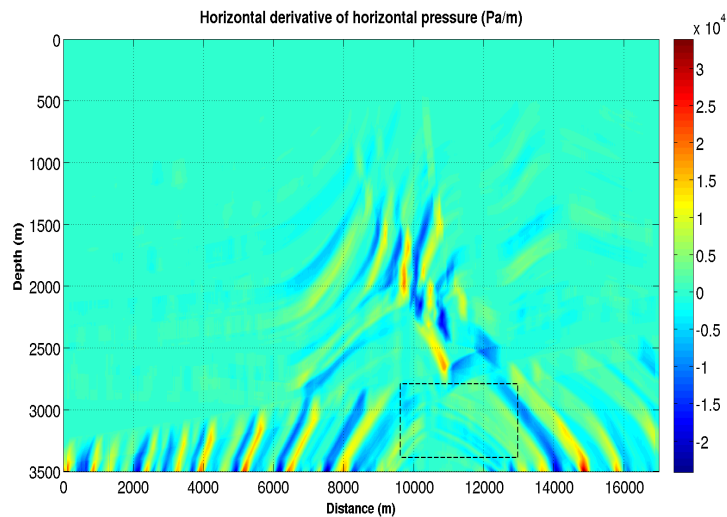
Source: From autor

Figure 5.25 – Vertical variation of the horizontal pressure field,  $\frac{\partial P_x(x,z)}{\partial z}$ , given in figure 5.16.

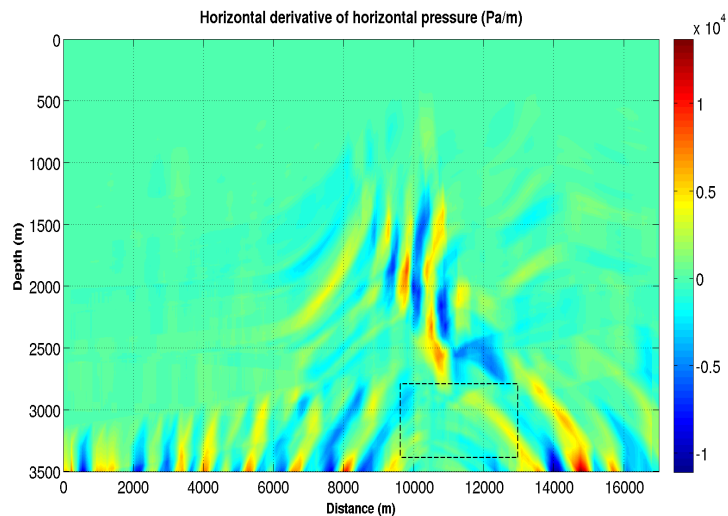
(a) Original model.



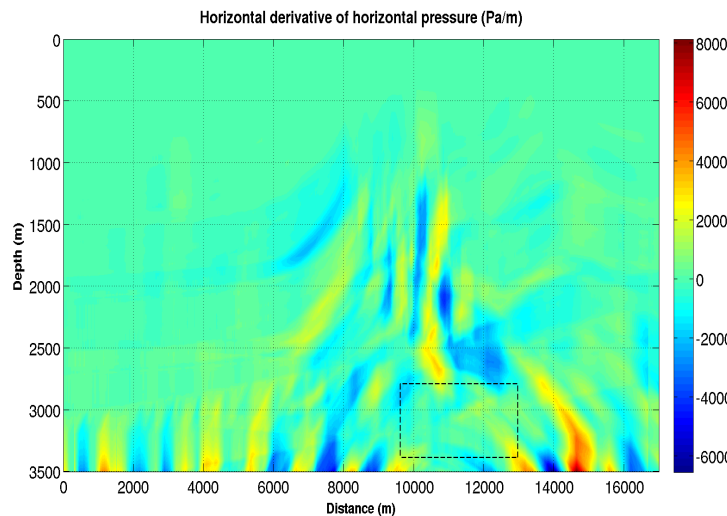
(b) Smoothing with 41 points.



(c) Smoothing with 81 points.



(d) Smoothing with 121 points.



Source: From autor

## 5.4 Conclusions

The conclusions are related to the main goal established by the initial question on how sensitive is the pressure prediction to the variation of velocity and density, principally around a geological reservoir zone, with the results should be presented in the form of depth sections in the geological domain.

In situ measurement of stress is described to be very important in several fields of engineering, geology and geophysics aiming at several applications, and here we are concerned with oil and gas exploration (AMADEI; STEPHANSSON, 1997).

We showed details of the calculus, and used an important example to show how pressure varies in the subsurface of the synthetic classical Marmousi model. In order words, we showed that pressure does not necessarily increases linearly, but in a complex form. The marked target by a spatial window defines a confined low pressure zone representing the reservoir, but other low pressure areas are also mapped.

As a detail, the theory limits the stress agent to be the vertical load of the geological rock formations, and does not take into account the reflector's curvatures, faulting and diagenesis.

Stress and pressure prediction is an important issue for the analysis of a sedimentary basins, aiming at oil and gas potentially productive areas. But the prediction needs a 3D model for its complete meaningful application (BROWN, 2011).

The sensitivity analysis to measure the decay in the resolution of the stress state prediction in this example followed the migration methodology, and the main conclusions are listed below.

- The horizontal pressure field in figure 5.16 exhibits details of the target reservoir in the geological structure as the smoothing process increases, and it is one of the main results obtained here.
- The vertical pressure discontinuities in figure 5.23 allows the identification of the geological sequences, and clearly shows details of the target confined reservoir as the smoothing process increases. This is also a special result in this work.
- The horizontal variation of the horizontal pressure field in figure 5.25 exhibits an interesting behavior opposite to the other figures commented above, and where the structures and discontinuities become clearer as the smoothing process increases. Due to this finding, it serves as a main conclusion from these numerical experiments.
- In this numerical experiment simulating a real case showed that all figures and concepts were useful as control tools in the modeling of sedimentary basins for

oil and gas exploration. Also, following the specialized literature, other figure constructions can be added, but would make the paper too long.

To end, this paper dealt with a potential application of a methodology to help the analyses of productive reservoirs, but the method needs a greater amount of information; namely, the  $v_P(\mathbf{x})$ ,  $v_S(\mathbf{x})$  and  $\rho(\mathbf{x})$ , that is based on 3D survey and 3D component seismic data, or on alternative techniques like VSP, AVO and petrophysics.

## 6 A NEW METHOD FOR THE SOLUTION OF THE ELASTO-DYNAMIC PROBLEM

We present here a new computer technology for solving three-dimensional problems of elastic stationary oscillations. The method can be used not only for applications in oil and gas exploration, but also for modeling buried structures and structural components such as foundations, tunnels, trenches, cavities, etc.

The basis of this method is the construction of the integral equations kernels as a response to an analog Delta loading, or to its derivatives.

The finiteness of the kernels gives the possibility to increase accuracy in many orders, and to solve the elastic problem in the case of discontinuity of the normal surface vector.

As an example, we show that the variation of characteristics of the static stress state under the influence of pore pressure depends essentially on the contact geometry, and a little on the type of boundary condition at the contact.

### 6.1 Introduction

This study is being conducted in two simultaneous parts. The first part is the present paper that describes the theory aiming at applications for oil and gas exploration, where we look, among other applications, for mapping low and high pressure zones that serve as natural suction pumps, where a reservoir is necessarily related to a low pressure zone in the subsurface. A second part deals with a specific application of this theory for a typical reservoir model as a numerical experiment.

To solve the elastic problem it is necessary to know the boundaries and the elastic parameters. The present model considers only isotropic layers, and it is necessary the knowledge of the  $v_P(\mathbf{x})$  and  $v_S(\mathbf{x})$  velocities and  $\rho(\mathbf{x})$  density distribution for the sedimentary basin. The model is discretized in an uniform 3D grid, where the layer cells forming the 3D geological structure have constant elastic parameters. Anisotropy, nonlinear elasticity, rupture, and chemical phase changes are not taken in consideration.

The data can be obtained from special 2D surveys with 3D sensor components, where a large amount of P wave information is conventional. For the S wave velocities, it can also be obtained from VSP technology, and by petrophysical measurements (BIONDI, 2010; GALPERIN, 1985; HARDAGE et al., 2011).

The theory is based on the system of isotropic elastic equations; either static or

stationary oscillations. And in this paper we take as a numerical example the case of effective pressure ( $p_{eff}$ ) around a granular structure.

Using the same approach, we aim further at a reservoir model described by a volume  $V$ , and surrounded by a surface  $S$ . Therefore, in Sibiryakov et al. (2013) we have already described this case, but characterized by its curvatures, and it is not to be understood as a plate model, what becomes a more complex problem. Continuing, the anticline structure can be a very useful trap, especially if it has a negative discontinuity (lower minus upper parameter) in the  $\gamma = \frac{v_S}{v_P}$  ratio. In this case, exists also an additional horizontal stretching due to the negative curvature of the anticline structure. It is interesting, that the effects of the structure slope and curvature are in opposite directions; the slopes produce an additional compression, while the average surface curvature (SMIRNOV, 1964) produces a horizontal stretching. If there is an anticline structure with a positive discontinuity in the  $\gamma$  ratio, it can be a compensational effect. The additional pressure due to the  $\gamma$  discontinuity, and the additional stretching due to the average curvature may eliminate each other. In this case, the anticline structure is not a fluid attractor.

It is shown that it is possible to calculate low pressure zones (which are important to locate a successful drilling) using maps of  $v_P$ ,  $v_S$  and  $\rho$ .

## 6.2 Method

It seems interesting to find solutions for stationary oscillations (including static) of 3D elastic problem without any kind of regularization (stabilization) procedures, because it gives the possibility to increase the reliability of the solution.

The proposed aims is not only related to the physical problem itself, but with a set of other practical problems as: stress-strain conditions of geological layers; development of standing waves; wave refraction in rough surfaces; and also may some other subjects can be called upon. A specific application in this paper is the problem of the effective pressure ( $p_{eff}$ ) and anomalous high porous pressure ( $p_{por}$ ).

The used term "effective pressure" is not the best because it is normally used in another field of physics (thin films, and so on); but, so far we did not find a better term to use, and the meaning of the phenomena is as follows. The porous pressure ( $p_{por}$ ) changes the properties of the media in opposite direction with respect to the confining pressure ( $p_{con}$ ), and it is known that in granular medium the changes of elastic parameters depend not only on the confining pressure, but on the so called effective pressure that is equal to the confining pressure minus the porous pressure multiplied by some coefficient ( $k$ ):

$$p_{eff} = p_{con} - kp_{por}.$$

So, the term disjoining pressure is used in the sense of the average normal loading

on the contact areas, proportional to the pore pressure, and causes the decrease of the loading on the contact due to the confining pressure.

The main difficulty is the possible presence of nonelastic effects in the process of a real reservoir. Even though, the present problem statement is equivalent to granular medium consisting of lattices, and limited by enough rigid boundaries. It is possible to find appropriate boundary condition for the granular medium, but the main subject in the modelling is linear elasticity.

### 6.2.1 Basic equatinos

The initial equation for the elastodynamic wave propagation is given by:

$$\mu\Delta u_i + (\lambda + \mu)\text{Grad}_i(\text{Div}\vec{\mathbf{u}}) = \rho\frac{\partial^2 u_i}{\partial t^2}, \quad [FL^{-3}], \quad (i = 1, 2, 3; x, y, z). \quad (6.1)$$

For  $u_i = U_i e^{i\omega t}$ , the representative differential equation becomes as:

$$\Delta U_i + k^2 U_i + \frac{\lambda + \mu}{\mu}\text{Grad}_i(\text{Div}\vec{\mathbf{U}}) = 0, \quad \left(k^2 = \frac{\rho\omega^2}{\mu}\right), \quad [A], \quad (6.2)$$

where  $\Delta U_i$  is the Laplace operator on the displacement  $U_i$  that results as an adimensional quantity,  $[L^{-1}][L] = [A]$ ;  $\lambda$  and  $\mu$  are the Lamé elastic moduli with dimension  $[FL^{-2}]$ ;  $\rho$ ,  $[ML^{-3}]$ , is the body density; and  $\omega$ ,  $[\text{rad/s}] = [T^{-1}]$ , is the angular frequency of the stationary oscillations.

The method of boundary integral equations (BIE) is used to find the displacement vector  $\vec{\mathbf{U}}$ , not only satisfying the equation of stationary oscillations obtained from (6.2), but also the boundary conditions.

The loading vector (traction or compression),  $p_i = \sigma_{in_0}$ , expresses the pressure component with a formula given by:

$$p_i = \sum_{k=1}^{k=3} \sigma_{ik} n_k = \sigma_{in_0}, \quad [FL^{-2}], \quad (6.3)$$

where  $\sigma_{ik}$  is the stress tensor,  $n_k$  is the projection cosine along the unit normal vector  $\vec{\mathbf{n}}$  to the  $S$  surface, and  $\sigma_{in_0}$  can be calculated by Hooke's law, and also by the rule of tensor projections; therefore, the loading is not defined by a simple normal stress. A complementary expression for  $\sigma_{ik}$  is given by:

$$\sigma_{ik} = \lambda\text{Div}\vec{\mathbf{U}}\delta_{ik} + \mu\left(\frac{\partial U_i}{\partial x_k} + \frac{\partial U_k}{\partial x_i}\right), \quad \text{Div}\vec{\mathbf{U}} = \theta = \frac{\partial U_i}{\partial x_i} + \frac{\partial U_j}{\partial x_j} + \frac{\partial U_k}{\partial x_k}. \quad (6.4)$$

In practical terms, if we have a reservoir at depth  $z_0$  (say, 2000m) we can calculate the loading  $p_i = \sigma_{ik} n_k$  if we have the displacement vector to calculate the strain tensor, and

by Hooke's law calculate the loading  $p_i$ . We can also use the gravity weight to calculate the loading, because we solve for the nonhomogeneous equation of equilibrium:

$$\mu\Delta U_i + (\lambda + \mu)\text{Grad}_i \vec{U} = -\rho g \delta_{iz}, \quad (6.5)$$

under the condition that  $p_i = 0$  at the surface ( $z = 0$ ), but the atmospheric pressure can be assigned for the normal component and zeros for the tangential components.

### 6.2.2 Fundamental solution of the first kind

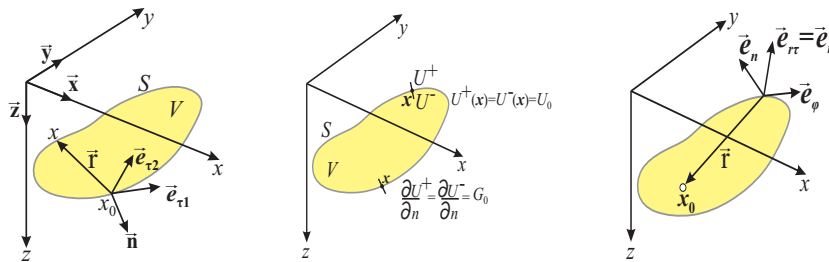
The solution for equation (6.2) is found in the form of a convolution with a kernel that satisfies the equation at any fixed point  $\mathbf{x}_0$  of a closed volume  $V$ , that can be arbitrarily close to the enclosing surface  $S$ . The integration is carried out over the position variable  $\mathbf{x}$ , and calculated with a surface element  $dS_{\mathbf{x}}$ ; i.e.:

$$U_i(\mathbf{x}_0) = \int_S M_{ik}(\mathbf{x}_0, \mathbf{x}) F_k(\mathbf{x}) dS_{\mathbf{x}}, \quad (k = 1, 2, 3), \quad [L] = [F^{-1}L][FL^{-2}][L^2], \quad (6.6)$$

where  $\vec{F}$  is called the vector potential, and  $\vec{U}$  is calculated such that the displacement vector does not only satisfies equation (6.2), but also the boundary conditions.

In terms of analogy to potential theory and the solutions of Laplace and Poisson equations, the solution (6.6) corresponds to the called single layer case. By knowing the displacement field, the loading  $\vec{p}$  can be calculated according to equation (6.3). Figure 6.1 shows the cartesian system related to equation (6.6).

Figure 6.1 – The Cartesian system  $(x, y, z)$ , the volume  $V$  enclosed by the surface  $S$ . (left) The fixed point  $\mathbf{x}_0$  inside the volume  $V$ , the integration point  $\mathbf{x}$ , and the unit vectors  $\vec{x}, \vec{y}$  and  $\vec{z}$ . (center) The boundary conditions for the Laplace equation and the Dirichlet and Neumann problems. (right) The tangent unit vectors  $\vec{e}_n, \vec{e}_\varphi$  and  $\vec{e}_{n\tau}$ .



Source: From autor

### Classical Tensor for the First Kind

The classical description is given by Kupradze (1963) for a three-dimensional full-space, and it is calculated with  $M_{ik}(\mathbf{x}_0, \mathbf{x})$  (also written as  $\Gamma_{ik}(\mathbf{x}_0, \mathbf{x})$  and as  $G_{ik}(\mathbf{x}_0, \mathbf{x})$  for specific cases), that is the tensor of the fundamental solutions as given by:

$$M_{ik}(\mathbf{x}_0, \mathbf{x}) = \Gamma_{ik}(\mathbf{x}_0, \mathbf{x}) = \frac{1}{\mu} \left( \frac{\cos(kr)}{r} \delta_{ik} + \frac{1}{k^2} \frac{\partial^2}{\partial x_i \partial x_j} \left[ \frac{\cos(kr)}{r} - \frac{\cos(\gamma kr)}{r} \right] \right), \quad [F^{-1}L], \quad (6.7)$$

where  $\delta_{ik}$  is the Kronecker delta;  $r = \sqrt{(x_0 - x)^2 + (y_0 - y)^2 + (z_0 - z)^2}$  is the distance between the fixed,  $\mathbf{x}_0$ , and integration,  $\mathbf{x}$ , points;  $\gamma = \frac{vs}{v_P} = \sqrt{\frac{\mu}{\lambda+2\mu}}$  velocity ratio; and  $x_i$  are the projections of the vector  $\mathbf{r}$  directed from the fixed point  $\mathbf{x}_0$  to the integration point  $\mathbf{x}$  for the Cartesian coordinate system  $(x, y, z)$ .

### Static Case

For the static case (i. e., for  $kr \ll 1$ ), the tensor (6.7) is simplified to the form:

$$\Gamma_{ik}(\mathbf{x}_0, \mathbf{x}) = \frac{1}{2\mu(\lambda+2\mu)} \left[ (\lambda+\mu) \frac{\partial r}{\partial x_i} \frac{\partial r}{\partial x_k} + (\lambda+3\mu)\delta_{ik} \right] \frac{1}{r(\mathbf{x}, \mathbf{y})}, \quad [F^{-1}L]. \quad (6.8)$$

The approximation (6.8) has several disadvantages, except for the Kronecker  $\delta_{ik}$  function, due to non-integrable singularities.

The loading  $P_{ik}(\mathbf{x}_0, \mathbf{x})$  is obtained with respect to the stress tensor  $\Gamma_{ik} = M_{ik}$  in (6.8) (for a fixed point  $\mathbf{x}_0$  and integration position  $\mathbf{x}$ ), and it has the form:

$$P_{ik}(\mathbf{x}_0, \mathbf{x}) = \frac{1}{\lambda+2\mu} \left\{ \left[ \mu\delta_{ik} + 3(\lambda+\mu) \frac{\partial r}{\partial x_i} \frac{\partial r}{\partial x_k} \right] \frac{\partial}{\partial \mathbf{n}_0} \frac{1}{r} + \mu \left[ \cos(\mathbf{n}_0, x_k) \frac{\partial}{\partial x_i} \frac{1}{r} - \cos(\mathbf{n}_0, x_i) \frac{\partial}{\partial x_k} \frac{1}{r} \right] \right\}, \quad [L^{-2}], \quad (6.9)$$

where  $\mathbf{n}_0$  is the unit normal vector at a fixed point  $\mathbf{x}_0$  on the  $S$  surface, and  $\delta_{ik}$  is the Kronecker delta.

If the tensor  $M_{ik}$  is taken as a set of 3 displacement vector components,  $U_i$ , for the real loading on the real  $S$  surface, then  $P_{ik}$  is taken as a set of the 3 loading vector components  $p_i$  calculated as  $p_i = \sigma_{ik}n_k$  by using Hooke's law.

If the tensor  $M_{ik}$  is taken as a set of 3 vector  $p_i$  as the real loading vector on the real  $S$  surface, then  $P_{ik}$  is a loading calculated analytically and formed by three vectors.

### Modified Classical Tensor for the First Kind

The tensor (6.9) gives the possibility to find a solution of the second kind for the elastic boundary problem, where the loading vector  $p_i$  is known on the boundary, that is necessary to find displacement vector in the volume. In this case the problem is reduced to finding a solution of the system of the 2D integral equations, not regular but singular integral equations; i.e., the kernels are not integrable and the integrals should be calculated in principle value (P.V.) sense. The last term in (6.9) causes this mentioned singularity. In practice, the use of such type of kernels are the cause for loosing accuracy.

In statics, this problem has been solved by using a slightly different form for the  $M_{ik}(\mathbf{x}_0, \mathbf{x})$  tensor for a half-space, as given in (SIBIRYAKOV, 2009), that is:

$$M_{ik}(\mathbf{x}_0, \mathbf{x}) = \frac{1}{2\mu} \begin{bmatrix} \frac{1}{r} + \frac{x_1^2}{r^3} + \frac{\mu}{\lambda+\mu} \frac{1}{r} & \frac{x_1x_2}{r^3} + \frac{\mu}{\lambda+\mu} \frac{\partial^2 g}{\partial x_1 \partial x_2} & \frac{x_1x_3}{r^3} + \frac{\mu}{\lambda+\mu} \frac{\partial^2 g}{\partial x_1 \partial x_3} \\ \frac{x_1x_2}{r^3} - \frac{\mu}{\lambda+\mu} \frac{\partial^2 g}{\partial x_1 \partial x_2} & \frac{1}{r} + \frac{x_2^2}{r^3} - \frac{\mu}{\lambda+\mu} \frac{\partial^2 g}{\partial x_2^2} & \frac{x_2x_3}{r^3} - \frac{\mu}{\lambda+\mu} \frac{\partial^2 g}{\partial x_2 \partial x_3} \\ \frac{x_1x_3}{r^3} - \frac{\mu}{\lambda+\mu} \frac{\partial^2 g}{\partial x_1 \partial x_3} & \frac{x_2x_3}{r^3} - \frac{\mu}{\lambda+\mu} \frac{\partial^2 g}{\partial x_2 \partial x_3} & \frac{1}{r} + \frac{x_3^2}{r^3} - \frac{\mu}{\lambda+\mu} \frac{\partial^2 g}{\partial x_3^2} \end{bmatrix} \quad (6.10)$$

where  $x_1$ ,  $x_2$  and  $x_3$  are the projections of the vector  $\mathbf{r}$  directed from the internal fixed point  $\mathbf{x}_0$  on the  $S$  surface to the integration point  $\mathbf{x}$  in the following form: on the unit

outward normal  $\mathbf{n}$  ( $x_1 = (\mathbf{r}, \mathbf{n})$ ), and on two mutually orthogonal directions tangential to the  $S$  surface as  $\mathbf{e}_{\tau 1}$  ( $x_2 = (\mathbf{r}, \mathbf{e}_{\tau 2})$ ), and  $\mathbf{e}_{\tau 2}$ , ( $x_3 = (\mathbf{r}, \mathbf{e}_{\tau 3})$ ). The index  $i$  denote the displacement direction on the surface, due to a  $\delta$ -loading applied in the  $k$  direction. The function  $g(x, y, z)$  that is under the derivatives has the form:

$$g(x, y, z) = |x_1| \ln(r + x_1) - r, \quad \text{where} \quad r = \sqrt{(x_{1,0} - x_1)^2 + (x_{2,0} - x_2)^2 + (x_{3,0} - x_3)^2}.$$

Denoting the derivative of the function  $g(x, y, z)$  in equation (6.10) with the corresponding coordinate subscript; for example,  $g_1 = \frac{\partial g}{\partial x_1}$ ,  $g_{12} = \frac{\partial g}{\partial x_{12}}$ , and  $g_{123} = \frac{\partial g}{\partial x_{123}}$ , then equation (6.10) is rewritten as:

$$\mathbf{P}^{\mathbf{x}}(M_{ik}) = \frac{-3(\mathbf{r}, \mathbf{n}_0)}{r^5} \begin{bmatrix} x_1^2 & x_1 x_2 & x_1 x_3 \\ x_1 x_2 & x_2^2 & x_2 x_3 \\ x_1 x_3 & x_2 x_3 & x_3^2 \end{bmatrix} + \frac{\mu}{\lambda + \mu} \begin{bmatrix} 0 & 0 & 0 \\ (\mathbf{n}_0, \mathbf{e}_{\tau 1})g_{133} - (\mathbf{n}_0, \mathbf{e}_{\tau 2})g_{123} & (\mathbf{n}_0, \mathbf{e}_{\tau 1})g_{223} - (\mathbf{n}_0, \mathbf{e}_{\tau 2})g_{223} & (\mathbf{n}_0, \mathbf{e}_{\tau 1})g_{333} - (\mathbf{n}_0, \mathbf{e}_{\tau 2})g_{223} \\ (\mathbf{n}_0, \mathbf{e}_{\tau 2})g_{122} - (\mathbf{n}_0, \mathbf{e}_{\tau 1})g_{123} & (\mathbf{n}_0, \mathbf{e}_{\tau 2})g_{222} - (\mathbf{n}_0, \mathbf{e}_{\tau 1})g_{223} & (\mathbf{n}_0, \mathbf{e}_{\tau 2})g_{223} - (\mathbf{n}_0, \mathbf{e}_{\tau 1})g_{233} \end{bmatrix} \quad (6.11)$$

The above tensor (6.11) is referred to as  $P_{ik}^{\mathbf{x}}$ . So, the operator  $\mathbf{P}^{\mathbf{x}}(M_{ik})$  is a set of three loading vectors calculated under the condition that (6.10) is a set of three displacement vectors.

The difference between formulas (6.10 and 6.11) and (6.9) is that (6.10 and 6.11) are calculated from the fundamental solution for the half-space, and (6.9) is calculated from the fundamental solution (6.8) for the 3D full-space.

### 6.2.3 Fundamental solution of the second kind

If the loading vector  $p_i$  is known on the  $S$  surface, it is possible to calculate the vector potential components ( $F_k, k = 1, 2, 3$ ) by solving of the system of the integral equations of the Fredholm type of the second kind as given by:

$$p_i(\mathbf{x}_0) = F_i(\mathbf{x}_0) - \frac{1}{2\pi} \int P_{ik}(\mathbf{x}_0, \mathbf{x}) F_k(\mathbf{x}) dS_{\mathbf{x}}, \quad (6.12)$$

as a result, it becomes easy to calculate the displacement vector  $\vec{\mathbf{U}}$  by using the integral (6.6). The quantity  $p_i$  is given by equation (6.3), and  $P_{ik}$  by equation (6.9).

So, the BIE is reduced to the solution of the integral equations of the second type, if it is desired to solve for the elastic boundary problem of the second type. The solution of the elastic problem of the first type (when the displacement vector is known on the boundary) is also reduced to the integral equations of the second kind by using another kernel, the double layer potential (MACMILLAN, 1930).

The general steps for solving both types of problems are summarized as follows:

- If it is given a vector loading  $\vec{\mathbf{p}}$  on a smooth  $S$  surface, then it is possible to calculate the displacement  $\vec{\mathbf{U}}$  by calculating first the vector potential  $\vec{\mathbf{F}}$  for the tensor  $\vec{\mathbf{P}}$ .
- If it is given the displacement vector  $\vec{\mathbf{U}}$  on the  $S$  surface, then the kernel of the integral equation takes the feedback from the derivative of the double layer  $\delta$ -function response (as similar to the dipole potential), and then calculate the displacement  $\vec{\mathbf{U}}$  everywhere in the volume  $V$ .

The disadvantages of this method is as follows.

- First at all, the  $S$  surface should be smooth. If the normal vector changes abruptly, then the integral  $\int P_{ik}(\mathbf{x}_0, \mathbf{x}) dS_{\mathbf{x}}$  diverges, what leads to the same problem as using equation (6.7) as the kernel tensor.
- It is very difficult to find a solution of the mixed type elastic problem, when on some part of the  $S$  surface the displacement vector is known, and on the rest part of the surface the loading vector is known.

If we use the dipole potential, the integral of the loading tensor,  $P_{ik}$ , diverges.

If we use equation (6.10), the system for finding the vector potential  $\vec{\mathbf{F}}$  will be of the type Fredholm of the second kind, and also of the first kind, which can leads to problems associated with poor system conditioning.

- It is not clear what to use as kernels in the case of stationary oscillations.
- It is necessary to build a new kernel in order to get rid of these drawbacks.

### Normal and Radial Components from Modified Tensor

The Green function for 3D full-space (6.8) uses Cartesian coordinates because it has appropriate symmetry caused by 3D delta function. If we have a half-space (this means that it must satisfy the boundary conditions automatically in a small vicinity to free surface, but in the remote points the amplitude of the kernel is significantly smaller), we have a very special direction that is the  $z$ -direction for the cylindrical coordinates, and two tangential coordinates with the directions defined by special symmetry. By this reason, all problems related to the half-space are usually solved by using cylindrical coordinates. Besides, it gives a possibility to use only five independent components in the library of fundamental displacements. Briefly, the cylindrical coordinates gives the possibility to have a more compact solution than the Cartesian coordinates. But, the cylindrical coordinates are used for the library only, and for a real surface we use at every fixed point the normal and the tangential directions that are in fact Cartesian.

The tensor in (6.10) is a static fundamental solution for the upper ( $x_1 > 0$ ) and the lower ( $x_1 < 0$ ) half-spaces. It would be logical to try to build a new kernel using the fundamental solutions for the half-space. However this approach has hidden problems.

Let's consider the result of the Lamb's problem for a monochromatic oscillation (displacements which are responses on the vertical  $\delta$ -loading) for a half-space  $x_1 > 0$  (if  $x_1 < 0$ , then the radial component changes sign) (NOVACKY, 1970). The use of the module is related to the change of sign for  $x_1 < 0$ . For the static solution (6.10) (for  $k \rightarrow 0$ ), the choice is:

$$\begin{aligned} U_n(x_1, k) &= \int_0^\infty J_0(k_r r_\tau) \frac{k_r^2}{2\pi\mu R(k_r, k)} (2k_r \exp(-|x_1|v_S) - (2k_r^2 - k^2) \exp(-|x_1|v_P)) dk_r, \\ U_r(x_1, k) &= \int_0^\infty J'_0(k_r r_\tau) \frac{k_r^2}{2\pi\mu R(k_r, k)} (-2v_S v_P \exp(-|x_1|v_S) + (2k_r^2 - k^2) \exp(-|x_1|v_P)) dk_r, \end{aligned} \quad (6.13)$$

where  $v_S = \sqrt{k_r^2 - k^2}$ ;  $v_P = \sqrt{k_r^2 - \gamma^2 k^2}$ ;  $x_1$  is the vertical coordinate (depth for the half-space);  $r_\tau$  is the horizontal tangential distance to the source represented by the  $\delta$ -loading; and  $J_0$  is the Bessel function of the first kind and zero order. The quantity

$$R(k_r, k) = 4k_r^2 \sqrt{k_r^2 - k^2} \sqrt{k_r^2 - \gamma^2 k^2} - (2k_r^2 - k^2)^2$$

is called the Rayleigh denominator, which is responsible for rather serious problems, which will be discussed below. The symbols  $n$  and  $\tau$  attached as subscripts denote the normal and radial tangential components, respectively.

### 6.3 Delta loading source

Formula (6.13) gives the amplitude response for the half-space, under the condition that the surface normal  $\delta$ -loading,  $p_n = \delta(S)$ , given by:

$$\delta(S) = -\frac{1}{2\pi} \int_0^\infty k_r J_0(k_r r_\tau) dk_r, \quad [FL^{-2}], \quad (6.14)$$

where  $k_r$  is the mnemonic integration variable, and  $k$  is the effective spatial frequency corresponding to the  $S$  waves. Also, all the dimensions of the involved quantities ( $\delta(S)$ ,  $p_i$ ,  $M_{ik}$ ,  $P_{ik}$ ,  $\Gamma_{ik}$ ) are compensated by the dimension of the vector potential ( $\vec{\mathbf{F}}$ ).

The solution (6.13) has been used primarily for analytical calculation of the properties of Rayleigh waves, and of the asymptotic properties of the longitudinal and transversal waves. The use of formula (6.13) as kernels has hidden difficulties as the same as formula (6.8), and it is difficult to use it for BIE.

The Rayleigh denominator for some value of  $k_r$  around the  $k$ , becomes zero. Despite of the fact that there are mathematical theorems for correcting such conditions, it means that by using these solutions as kernels, one will be facing with the same problems as the ones by using the Green's tensor for the 3D space given by equations (6.7-6.8). Secondly, the integrals (6.13) are improper, which again will lead to a loss of accuracy in the numerical solutions. That is, before using the solution (6.13) as the kernels for integral equations, it is reasonable to correct the indetermination present.

To get rid of the zeros in the Rayleigh denominator  $R(k_r, k)$ , it is not a difficult task. We can choose a slightly different representation for the  $\delta$ -function, since it does

not have a unique representation. For example,  $\delta = -\frac{\partial}{\partial x_1} \frac{1}{r}$ , or  $\delta = -\frac{\partial}{\partial x_1} \frac{\cos(kr)}{r}$ : the first representation is more appropriate for static case, and the second for stationary oscillations.

The question is: How to correct equation (6.12) for the possibility to have a more accurate integration? The answer is by changing the Delta function representation by involving the parameter  $k$  present in it.

In answering this question, we use the following plausible analogy. Different from  $\frac{1}{r}$ , in  $\frac{\cos(kr)}{r}$ , that satisfies the Laplace and the Helmholtz equations, the parameter  $k$  acts on all three dimensions in the Helmholtz equation. As in equation (6.13), the surface  $\delta$ -function contains two coordinates rather than one ( $r$  is radial,  $\tau$  is tangent). To avoid the above shortcomings mentioned, it is reasonable to present the  $\delta$ -function in another form like:

$$\delta_1(S) = -\frac{1}{2\pi} \int_0^\infty k_r J_0 \left( r_\tau \sqrt{k_r^2 + 2k^2} \right) dk_r \quad (6.15)$$

About the second shortcoming, it is reasonable to mention that the  $\delta$ -function does not exist in nature. The mathematician can say that this is not a function at all (they will apologize for not correct enough phrases from the mathematical point of view, and that it is a functional), but we can use some functions as it's approximation.

The sense of using the Delta function is to achieve the kernel completeness (it gives an existence of the solution at whatever boundary conditions). But, in numerical experiments we have restrictions related with the grid interval (for example, oscillations on the boundary is restricted to the Nyquist frequency). This gives a bases for using numerical methods that are frequency limited analogs of the Delta function (or its derivatives). This also means that finite analog of the Delta function (the Delta function spreads on some small area) gives enough (for numerical methods) completeness also, but gives also the possibility to use finite kernels. The results show a fantastic accuracy.

The simplest way for creating such function is by changing the infinite interval of integration to finite one, and given as equal to the inverse of the discretization interval.

It is accepted that the effort to obtain solutions as a response to a point source was nothing like, in the first place, the effort to obtain the conditionality (i. e., for obtaining the equations of the Fredholm type of the second kind). And secondly, the struggle for completeness (since the spectrum of  $\delta$ -function is unlimited, the existence of solutions using equation (6.6) is quite obvious for any continuous function in the right-hand side).

It is generally accepted that equation like (6.12) is the correct problem construction, but something like (6.6) is incorrect because of bad conditioning. Roughly speaking the difference between them is in Delta function presence in the kernels of (6.12) (this gives equations of the second kind), and the absence of the Delta function in equation (6.6).

So, the finite analog of Delta function can be written as:

$$\delta_1(S) = -\frac{1}{2\pi} \int_{k_r=0}^{k_r=N} k_r J_0 \left( r_\tau \sqrt{k_r^2 + 2k^2} \right) dk_r. \quad (6.16)$$

The limits of integration is from 0 to the inverse of the sampling interval; i. e.,  $N \sim \frac{1}{h}$ .

Formally the finiteness of the kernel causes the necessity to solve the Fredholm equation of the first kind (loosing conditioning) for finding of the vector potential, and also loosing completeness. But, in reality there may be enough conditioning and completeness for the numerical solutions (if the free term does not contain too high spatial frequencies; it means that good properties of the Fredholm equations of the second kind are hidden in the initial one).

## 6.4 Normal and radial components from finite analogs

So, the displacement response to the normal loading (6.16), instead of (6.14), is a finite analog of fundamental solution (6.15). Replacing  $k_r$  as  $k_r \rightarrow \sqrt{k_r^2 + 2k^2}$  gives the possibility to an easy enough calculation, that is:

$$\begin{aligned} U_n(x_1, k) &= \int_0^N J_0(v_3 r_\tau) \frac{k_r v_2}{2\pi\mu R_1(k_r, k)} (2v_3^2 \exp(-|x_1|v_1) - (2k_r^2 + 3k^2) \exp(-|x_1|v_2)) dk_r, \\ U_r(x_1, k) &= \int_0^N J_0'(v_3 r_\tau) \frac{k_r v_3}{2\pi\mu R_1(k_r, k)} (-2v_1 v_2 \exp(-|x_1|v_1) + (2k_r^2 + 3k^2) \exp(-|x_1|v_2)) dk_r, \end{aligned} \quad (6.17)$$

where,

$$v_1 = \sqrt{k_r^2 + k^2}, \quad v_2 = \sqrt{k_r^2 + k^2(2 - \gamma^2)}, \quad v_3 = \sqrt{k_r^2 + 2k^2}, \quad (6.18)$$

and

$$R_1(k_r, k) = 4(k_r^2 + 2k^2) \sqrt{k_r^2 + k^2} \sqrt{k_r^2 + k^2(2 - \gamma^2)} - (2k_r^2 + 3k^2)^2. \quad (6.19)$$

It is reasonable to note that the denominator  $R_1(k_r, k)$  is not equal to zero, except for the static case,  $k = 0$ , when the kernel does not consist in singularity, but only in uncertainty. The solution (6.17) is limited if  $x_1 = r_\tau = 0$ , and decreases with increasing distance between fixed and integration points.

Because of the decomposition of the Bessel function given by:

$$J_0(\sqrt{x^2 + y^2}) = J_0(x)J_0(y) + 2(-1)^k \sum_{k=1}^{k=\infty} J_{2k}(x)J_{2k}(y)$$

if the number  $N$  tends to infinity, then (6.17) is the fundamental solution for the half-space, but in another form than (6.13). The solution (6.17) is a more convenient form for the fundamental solution of the elastic half-space than the solution (6.13).

### Amplitude Response to Tangential Loading

It is convenient to use the solution of Ziatdinov and Chestnut (2005) for the displacement caused by a monochromatic tangential concentrated loading with a more convenient notation, but obtaining the same results.

Therefore, the coordinates  $x_1$ ,  $x_2$  and  $x_3$  are not Cartesian coordinates, but the projections of the vector directed from fixed point,  $\mathbf{x}$ , of the surface to the integration point (also on the same surface),  $\mathbf{x}_0$ . So,  $x_1$  is given by the internal product  $(\mathbf{r}, \mathbf{n})$ , and  $x_2$  is one of the two orthogonal tangential directions.

The direction of the  $x_2$  axis coincides with one of the tangential directions  $\mathbf{e}_{\tau 1}$  that is the direction of the applied loading. If  $x_1 < 0$ , the normal component of displacement changes sign (case for the lower half-space).

For a tangential force applied in the direction  $\mathbf{e}_{\tau 1}$  (it also coincides with the direction of the axis  $x_2$ ), then the displacement vector response of the half-space is given by:

$$\begin{aligned} \vec{\mathbf{U}}_{x_2}(x_1, x_2, x_3) = & \int_0^N \left\{ \frac{k_r \exp(-|x_1|v_1)}{2\pi\mu v_1} \begin{bmatrix} 0 \\ [J_0(v_3 r_\tau) + J_0''(v_3 r_\tau)] \vec{\mathbf{e}}_\tau \cos \varphi \\ J_0''(v_3 r_\tau) \vec{\mathbf{e}}_\varphi \sin \varphi \end{bmatrix} \right. \\ & + \frac{k_r(v_1^2 + v_3^2) \exp(-|x_1|v_1)}{2\pi\mu R_1(k_r, r)} \begin{bmatrix} -v_3 J_0'(v_3 r_\tau) \vec{\mathbf{e}}_\mathbf{n} \cos \varphi \\ v_1 J_0''(v_3 r_\tau) \vec{\mathbf{e}}_\mathbf{r} \cos \varphi \\ v_1 [J_0(v_3 r_\tau) + J_0''(v_3 r_\tau)] \vec{\mathbf{e}}_\varphi \sin \varphi \end{bmatrix} \\ & \left. - \frac{2k_r v_1 v_3 \exp(-|x_1|v_2)}{2\pi\mu R_1(k_r, r)} \begin{bmatrix} -v_2 J_0'(v_3 r_\tau) \vec{\mathbf{e}}_\mathbf{n} \cos \varphi \\ v_3 J_0''(v_3 r_\tau) \vec{\mathbf{e}}_\mathbf{r} \cos \varphi \\ v_3 [J_0(v_3 r_\tau) + J_0''(v_3 r_\tau)] \vec{\mathbf{e}}_\varphi \sin \varphi \end{bmatrix} \right\} dk_r \end{aligned} \quad (6.20)$$

In the above,  $\vec{\mathbf{e}}_\mathbf{r}$  and  $\vec{\mathbf{e}}_\varphi$  correspond, respectively, to the radial and azimuthal direction on a cylindrical coordinate system, and the connection with the coordinates used previously in the static formula (6.10) is defined by the following relations, and shown in figure 6.1:

$$\vec{\mathbf{e}}_{x_2} = \vec{\mathbf{e}}_{\mathbf{r}\tau} \cos \varphi - \vec{\mathbf{e}}_\varphi \sin \varphi, \quad \vec{\mathbf{e}}_{x_3} = \vec{\mathbf{e}}_{\mathbf{r}\tau} \sin \varphi + \vec{\mathbf{e}}_\varphi \cos \varphi, \quad \cos \varphi = \frac{x_2}{r_\tau}, \quad \sin \varphi = \frac{x_3}{r_\tau}, \quad r_\tau = \sqrt{x_2^2 + x_3^2}. \quad (6.21)$$

### Tensor for the Half-space in Simplified Cylindrical Coordinates

The next step is to calculate the tensor components  $M_{ik}$ . This tensor depends on two directions: (1st) on the loading vector; and (2nd) on the displacement (which is the response to the loading).

After rotation to the directions  $\vec{\mathbf{n}}$ ,  $\vec{\mathbf{e}}_{\tau 1}$  and  $\vec{\mathbf{e}}_{\tau 2}$ , or  $\vec{\mathbf{n}}$ ,  $\vec{\mathbf{e}}_\mathbf{r}$  and  $\vec{\mathbf{e}}_\phi$  (according to the rule of the second rank tensor components, calculated after rotation of the coordinate system), it is possible to write the full tensor for the static elastic half-space in the new directions from (6.10), and  $M_{ik}(x_1, x_2, x_3)$  goes to:

$$M_{ik} = \frac{1}{2\mu} \begin{bmatrix} \frac{1}{r} + \frac{x_1^2}{r^3} + \frac{\mu}{\lambda + \mu} g_{11} & \frac{x_1 x_2}{r^3} + \frac{\mu}{\lambda + \mu} g_{1r_t} & 0 \\ \frac{x_1 x_2}{r^3} - \frac{\mu}{\lambda + \mu} g_{1r_t} & \frac{2}{r} - \frac{x_1^2}{r^3} - \frac{\mu}{\lambda + \mu} g_{r_t r_t} & 0 \\ 0 & 0 & \frac{1}{r} - \frac{\mu}{\lambda + \mu} \frac{g_{r_t}}{r_t} \end{bmatrix} \quad (6.22)$$

Then, it happens that this tensor consists only of five independent components.

If we write the components for  $\mathbf{e}_n$ ,  $\mathbf{e}_{r\tau}$  and  $\mathbf{e}_\varphi$ , the tensor for the static fundamental solutions for the half space,  $M_{ik}(x_1, x_2, x_3)$ , has only five independent components. The transformation rules of tensors for coordinate rotation gives for the static case ( $k = 0$ ) that:

$$M_{ik} = \frac{1}{2\mu} \begin{bmatrix} \frac{1}{r} + \frac{x_1^2}{r^3} + \frac{\mu}{\lambda + \mu} g_{11} & \frac{x_1 r_\tau}{r^3} + \frac{\mu}{\lambda + \mu} g_{1r_\tau} & 0 \\ \frac{x_1 r_\tau}{r^3} - \frac{\mu}{\lambda + \mu} g_{1r_\tau} & \frac{2}{r} - \frac{x_1^2}{r^3} - \frac{\mu}{\lambda + \mu} g_{r_\tau r_\tau} & 0 \\ 0 & 0 & \frac{1}{r} - \frac{\mu}{\lambda + \mu} \frac{g_{r_\tau}}{r_\tau} \end{bmatrix} \quad (6.23)$$

## 6.5 The new tensor

So, the components of the results for the new tensor,  $M_{ik}(x_1, x_2, x_3)$ , for half-space and  $k \neq 0$ , are written as:

$$M_{nn} = \int_0^N J_0(v_3 r_\tau) \frac{k_r v_2}{2\pi\mu R_1(k_r, r)} (2v_3^2 \exp(-|x_1|v_1) - (v_1^2 + v_3^2) \exp(-|x_1|v_2)) dk_r, \quad (6.24)$$

$$M_{nr} = \int_0^N J'_0(v_3 r_\tau) \frac{k_r v_3}{2\pi\mu R_1(k_r, r)} (-2v_1 v_2 \exp(-|x_1|v_1) + (v_1^2 + v_3^2) \exp(-|x_1|v_2)) dk_r, \quad (6.25)$$

$$M_{rn} = \int_0^N J'_0(v_3 r_\tau) \frac{k_r v_3}{2\pi\mu R_1(k_r, r)} (2v_1 v_2 \exp(-|x_1|v_2) - (v_1^2 + v_3^2) \exp(-|x_1|v_1)) dk_r, \quad (6.26)$$

$$M_{rr} = \int_0^N J''_0(v_3 r_\tau) \frac{k_r v_1}{2\pi\mu R_1(k_r, r)} ((v_1^2 + v_3^2) \exp(-|x_1|v_1) - 2v_3^2 \exp(-|x_1|v_2)) dk_r \\ + \int_0^N (J_0(v_3 r_\tau) + J''_0(v_3 r_\tau)) \frac{k_r \exp(-|x_1|v_1)}{2\pi\mu v_1} dk_r, \quad (6.27)$$

$$M_{\varphi\varphi} = \int_0^N -(J_0(v_3 r_\tau) + J''_0(v_3 r_\tau)) \frac{k_r v_1}{2\pi\mu R_1(k_r, r)} ((v_1^2 + v_3^2) \exp(-|x_1|v_1) - 2v_3^2 \exp(-|x_1|v_2)) dk_r \\ - \int_0^N J''_0(v_3 r_\tau) \frac{k_r \exp(-|x_1|v_1)}{2\pi\mu v_1} dk_r. \quad (6.28)$$

The other components in the mentioned coordinate system are equal to zero.

The components of the full tensor (6.17) and (6.24) to (6.28) can be used as kernels for the solution of the elastic problem of the second type (the loading vector is given on the boundary). But, for the problem of the first type, where the displacement vector is given on the boundary; or, for the mixed type elastic problem, it can be reasonable to multiply the integrands in (6.17) and (6.23 to 6.28) by  $k$ .

So, (6.17) and in (6.24) to (6.28) are finite analogs of the fundamental solution for the half-space, and with the integrand multiplied by  $k$  are finite analogs of the kernels for so called dipole potential (response to the loading that is the derivative of the Delta function, or a pair of forces as a dipole). It means that formally all equations will be

imperfect (first type), but all good properties (conditioning) of the second type Fredholm equations will be hidden inside the kernels.

This arrangement gives a possibility, not only to exchange “excessive” conditioning (and completeness) for significant increasing of the accuracy that comes from a form of finiteness of the kernels, but also to increase conditioning for the mixed type problems by the multiplication by  $k$  in the integrand (this should give enough attenuation with respect to distance, and still enough concentration of power within the source).

It is reasonable to note that generally the accepted BEM method (KUPRADZE, 1963) gives algorithms for the solution of the second type problem (by using the Green tensor for the full space), or for the first type problem (by using the loading vector form for the Green tensor for the full space, the so called kernel for the dipole potential), but gives almost no clues for the mixed type problem (this includes all elastic problems which contain interfaces).

### 6.5.1 Boundary conditions and the mixed type elastic problem

On the contact skeleton-fluid, the normal component of the loading vector is equal to the pressure in the fluid. Tangential components of the loading vector are equal to zero ( $p_n = p_0$ ,  $p_{\tau_1} = p_{\tau_2} = 0$ ).

On the interface between two solid bodies, there are two main types of the boundary conditions: rigid and slip.

The rigid contact means that there are no forces on the interface and, despite of the interface existence, the displacement vector is continuous, and the vector summation of the loading vector is a zero vector. Taking into account that the external normal vector changes sign, and the tangential vectors coincide on the upper and lower layers, it means that:

- $U_n^+ = -U_n^-$ ,  $U_{\tau_1}^+ = U_{\tau_1}^-$ ,  $U_{\tau_2}^+ = U_{\tau_2}^-$ ,
- $p_n^+ = p_n^-$ ,  $p_{\tau_1}^+ = -p_{\tau_1}^-$ ,  $p_{\tau_2}^+ = -p_{\tau_2}^-$ .

The symbols “+” and “-” stand for the upper and lower layers.

The slip contact (it can have a modification to include a friction coefficient) means that the tangential forces are zero, and only the normal component of the displacement vector is continuous:

- $U_n^+ = -U_n^-$ ,
- $p_n^+ = p_n^-$ ,  $p_{\tau_1}^+ = -p_{\tau_1}^- = 0$ ,  $p_{\tau_2}^+ = -p_{\tau_2}^- = 0$ .

It is clear enough that the mixed type problems (with rigid and slip conditions) are the most important for geophysics.

So our main idea for mixed type elastic problem consists of:

1. The analytical solutions for the elasticity equations (displacement vector) as a response to normal and tangential (on each of two tangential components) loading suitable for the case, and that is a finite analog of the Delta derivative (finite analog for the dipole loading for the half-space),

$$\delta_1(S) = -\frac{1}{2\pi} \int_{k_r=0}^{k_r=N} k_r J_0 \left( r_\tau \sqrt{k_r^2 + 2k^2} \right) dk_r.$$

2. Derivatives used for calculating the loading vector from the displacement vector mentioned in (1) above.
3. The five components of the tensor and its derivative (first, second and third order), comprising 50 files to create a numerical library. In cylindrical coordinate system tensor, the components depend on only two parameters.
4. Use of the numerical library (and interpolation formula) to calculate projections of the tensor and loading tensor (which is calculated by using Hook's law and the derivatives of the above mentioned tensor) on the real surface along the normal and tangential directions (to take proper orientation of tensors).

There was previously an attempt to find a solution of the mixed type static elastic problem on the sphere with two plane platforms of contact, axial symmetric, by using the tensor given in equation (6.10) as kernel. And the problem of pure conditioning was solved by using Fourier decomposition of the vector potential. As a result, the number of equations was reduced to  $\approx 40$ , and the solution was stable.

The results of the present proposed method for mixed type of elastic problems, for real 3D problems, with a total number of equations ( $\approx 10.000$ ) will be presented below. We hope that the described method will be used further, and not only for static problems.

An advantage (first is accuracy) of finite kernels is the possibility to solve problems on a surface with lineaments, where the normal vector changes abruptly; for example, corners and angles (of course, angle is in reality smoothed with a radius approximately equal to step of subinterval).

We propose that the use of finite analogs, so called dipole potential, is an appropriate balance between conditioning and convergence.

### 6.5.2 Appropriate rotation of axes and libraries

The tensor solutions (6.24)-(6.28) are for the half-space and  $k \neq 0$ . Is it possible to use this solution as kernels for the problems of a body surrounded by an arbitrary surface,

or even for a group of bodies with interfaces? The answer is yes, but it is necessary to set the orientation properly for the geometry of the structure.

Each second rank tensor depend not only on the coordinates, but also on two other directions given by the indexes ( $i$  and  $k$ ). On the each fixed point of the surface,  $\mathbf{x}_0$ , there are three independent directions; the normal and two tangential ( $\vec{\mathbf{n}}_0, \vec{\mathbf{e}}_{\tau 10}, \vec{\mathbf{e}}_{\tau 20}$ ), and the directions related with first symbol, index  $i$ . Also there are the same directions for every integration point,  $\mathbf{x}$ ; the normal and two tangential ( $\vec{\mathbf{n}}, \vec{\mathbf{e}}_{\tau 1}, \vec{\mathbf{e}}_{\tau 2}$ ), and the directions related with the second symbol, index  $j$ . So, we have the relations:  $x_1 = (\vec{\mathbf{r}}, \vec{\mathbf{n}})$ ,  $x_2 = (\vec{\mathbf{r}}, \vec{\mathbf{e}}_{\tau 1})$ ,  $x_3 = (\vec{\mathbf{r}}, \vec{\mathbf{n}}_{\tau 2})$ ,  $r_\tau = \sqrt{x_2^2 + x_3^2}$ , of internal products and radial distance.

To construct the equations (6.24)-(6.28) we need to calculate 18 quantities.

- 9 tensors related with the displacement  $\vec{\mathbf{U}}$ :  $M_{n_0n}, M_{n_0e_{\tau 1}}, M_{n_0e_{\tau 2}}, M_{e_{\tau 1}0n}, M_{e_{\tau 10}e_{\tau 1}}, M_{e_{\tau 10}e_{\tau 2}}, M_{e_{\tau 20}n}, M_{e_{\tau 20}e_{\tau 1}}, M_{e_{\tau 20}e_{\tau 2}}$ .
- And 9 tensors related with the loading  $p_i$ :  $P_{n_0n}, P_{n_0e_{\tau 1}}, P_{n_0e_{\tau 2}}, P_{e_{\tau 10}n}, P_{e_{\tau 10}e_{\tau 1}}, P_{e_{\tau 10}e_{\tau 2}}, P_{e_{\tau 20}n}, P_{e_{\tau 20}e_{\tau 1}}, P_{e_{\tau 20}e_{\tau 2}}$ .

The above  $M_{nm}$  tensors are properly orientated solutions (6.24-6.28); i.e., they can be calculated by using scalar products in the form:

$$\begin{aligned} M_{n_0n} &= M_{nn}(\vec{\mathbf{n}}_0, \vec{\mathbf{n}}) + M_{rn}(\mathbf{n}_0, \vec{\mathbf{r}}), \\ e_r &= e_{\tau 1} \cos(\varphi) + e_{\tau 2} \text{sen}(\varphi), \\ \cos(\varphi) &= \frac{x_2}{r_\tau}, \quad \text{sen}(\varphi) = \frac{x_3}{r_\tau}. \end{aligned} \quad (6.29)$$

The tensors  $P_{ik}$  can be calculated by using derivatives of (6.24-6.28) (these are components of the displacement vectors), by Hook's law, and by the transformation law of the second rank tensor during rotation. For example:

$$\begin{aligned} P_{n_0n} &= \lambda \left[ \frac{\partial}{\partial x_1} M_{nn} + \frac{\partial}{\partial r_\tau} M_{rn} + \frac{1}{r_\tau} M_{rn} \right] \\ &+ 2\mu \left[ (\vec{\mathbf{n}}_0, \vec{\mathbf{n}})^2 \frac{\partial}{\partial x_1} M_{nn} + (\vec{\mathbf{n}}_0, \vec{\mathbf{e}}_\tau)^2 \frac{\partial}{\partial r_\tau} M_{rn} + (\vec{\mathbf{n}}_0, \vec{\mathbf{e}}_\varphi)^2 \frac{1}{r_\tau} M_{rn} \right. \\ &\left. + \left( \frac{\partial}{\partial x_1} M_{rn} + \frac{\partial}{\partial r_\tau} M_{nn} \right) (\vec{\mathbf{n}}_0, \vec{\mathbf{n}}) (\vec{\mathbf{n}}_0, \vec{\mathbf{e}}_\tau) \right]. \end{aligned} \quad (6.30)$$

It is reasonable to observe that the  $M_{nm}$  values decrease (asymptotically) as  $r^{\frac{1}{2}}$ , as a response due to a pair of delta-loadings with opposite directions (dipole-loading).

As an example of an equation for the displacement due to a normal loading is:

$$U_{n0}(\mathbf{x}_0) = \int (M_{n0n}(\mathbf{x}_0, \mathbf{x}) F_n(\mathbf{x}) + M_{n0\tau 1}(\mathbf{x}_0, \mathbf{x}) F_{\tau 1}(\mathbf{x}) + M_{n0\tau 2}(\mathbf{x}_0, \mathbf{x}) F_{\tau 2}(\mathbf{x})) dS_{\mathbf{x}}. \quad (6.31)$$

As another example is the equation for the first tangential loading component:

$$p_{\tau 10}(\mathbf{x}_0) = \int [P_{\tau 10n}(\mathbf{x}_0, \mathbf{x}) F_n(\mathbf{x}) + P_{\tau 10\tau 1}(\mathbf{x}_0, \mathbf{x}) F_{\tau 1}(\mathbf{x}) + P_{\tau 10\tau 2}(\mathbf{x}_0, \mathbf{x}) F_{\tau 2}(\mathbf{x})] dS_{\mathbf{x}}. \quad (6.32)$$

The quantity  $F_k$  are the components of the vector potential.

The obtained kernels do not depend on the real boundary conditions and geometry, but the vector potential components  $F_k$  should take the boundary conditions into account. The kernels depend only two variables,  $|x_1|$  and  $r_\tau$  (both are non-negative); i.e., they depend on the maximum linear size of the body. This property gives a clue to create a library of five tensors (6.24-6.28); each of them being two-dimensional ( $|x_1|$  and  $r_\tau$ ), and each parameter varying from 0 to the maximum linear size of the body.

The accuracy of the numerical problem depends on the grid's spatial sampling intervals.

A library of 5 tensors and their derivatives (first, second and third with respect to the two variables,  $|x_1|$  and  $r_\tau$ , that makes 45 in total) gives a possibility to use 50 files and an interpolation formula (for instance, Taylor's decomposition) to calculate the 18 necessary tensor components in each node of the surface (the interfaces), and to be fast enough to bring back an idea of using BEM as an alternative of FEM.

For the example given below, if the maximum distance between points on the surface is equal to 2, then the optimal value of  $N$  in formulas (6.24-6.28) is 100. The formulas (6.33-6.37) are the formulas (6.24-6.28) under condition  $k \rightarrow 0$  (static condition), that are the finite analog of the dipole tensor (tensor for the dipole potential) for the static case. So, the sampling interval  $h = 10^{-3}$ , and each library file is an array of size  $2001 \times 2001$ .

### 6.5.3 The static mixed bvp

The new results for the static case ( $k \rightarrow 0$ ), for the half-space, are obtained from formulas (6.24) to (6.28),  $M_{ik}(x_1, x_2, x_3)$  :

$$M_{nn} = \int_0^N J_0(k_r r_\tau) \frac{\exp(-|x_1|k_r)}{4\pi\mu(1-\gamma^2)} (1 + k_r|x_1|(1-\gamma^2)) dk_r \quad (6.33)$$

$$M_{nr} = \int_0^N -J'_0(k_r r_\tau) \frac{\exp(-|x_1|k_r)}{4\pi\mu(1-\gamma^2)} (-\gamma^2 + k_r|x_1|(1-\gamma^2)) dk_r \quad (6.34)$$

$$M_{rn} = \int_0^N -J'_0(k_r r_\tau) \frac{\exp(-|x_1|k_r)}{4\pi\mu(1-\gamma^2)} (\gamma^2 + k_r|x_1|(1-\gamma^2)) dk_r \quad (6.35)$$

$$M_{rr} = \int_0^N \left\{ \begin{array}{l} 2J_0(k_r r_\tau)(1-\gamma^2) + J''_0(k_r r_\tau)(1-2\gamma^2) + \\ + k_r|x_1|(1-\gamma^2)J''_0(k_r r_\tau) \end{array} \right\} \frac{\exp(-|x_1|k_r)}{4\pi\mu(1-\gamma^2)} dk_r \quad (6.36)$$

$$M_{\varphi\varphi} = \int_0^N \left\{ \begin{array}{l} J_0(k_r r_\tau) - J''_0(k_r r_\tau)(1-2\gamma^2) - \\ - k_r|x_1|(1-\gamma^2)(J_0(k_r r_\tau) + J''_0(k_r r_\tau)) \end{array} \right\} \frac{\exp(-|x_1|k_r)}{4\pi\mu(1-\gamma^2)} dk_r \quad (6.37)$$

A library gives the possibility to provide a labor division; i.e., to accelerate the calculation process by many orders. The calculation in every node integration point (with unit vectors  $\vec{\mathbf{n}}, \vec{\mathbf{e}}_{\tau 1}, \vec{\mathbf{e}}_{\tau 2}$ ) with respect to a fixed point (with unit vectors  $\vec{\mathbf{n}}_0, \vec{\mathbf{e}}_{\tau 10}, \vec{\mathbf{e}}_{\tau 20}$ ). This integration involves the scalar products of the mentioned unit vectors (for surface parameters), the free term column (that depends on the boundary condition), and is a much faster process with respect to the calculation of the integrals (6.33-6.37). So the process of coefficient calculation for the linear system, where its solution is the vector potential, becomes compatible with respect to FEM.

As a summary, the main steps of the present methodology are:

1. to construct the numerical library at the fixed frequency (50 files);
2. to calculate the 18 tensors (where each tensor is a matrix) at each fixed point of the surface (they depend on the integration point). The matrix of the main system for the potential calculation are combination of the mentioned matrices:  $M_{n_0 n}, M_{n_0 e_{\tau 1}}, M_{n_0 e_{\tau 2}}, M_{e_{\tau 1} 0 n}, M_{e_{\tau 1} 0 e_{\tau 1}}, M_{e_{\tau 1} 0 e_{\tau 2}}, M_{e_{\tau 2} 0 n}, M_{e_{\tau 2} 0 e_{\tau 1}}, M_{e_{\tau 2} 0 e_{\tau 2}}$ . And the 9 tensors:  $P_{n_0 n}, P_{n_0 e_{\tau 1}}, P_{n_0 e_{\tau 2}}, P_{e_{\tau 1} 0 n}, P_{e_{\tau 1} 0 e_{\tau 1}}, P_{e_{\tau 1} 0 e_{\tau 2}}, P_{e_{\tau 2} 0 n}, P_{e_{\tau 2} 0 e_{\tau 1}}, P_{e_{\tau 2} 0 e_{\tau 2}}$ .
3. and once the vector potential components,  $F_k$ , are calculated, then everything is possible to be calculated in the frame of elasticity theory. That means, the problem is considered solved.

#### 6.5.4 An integral criterion for accuracy

The knowledge of both displacement and loading vectors on any surface (which is surrounds elastic and homogeneous body) gives a possibility to estimate an accuracy for the numerical solution by using some well-known theorems (but, only for the static case). The average values (for the volume) of the components of the stress tensor can be calculated for the loading vector on the surface as:

$$\bar{\sigma}_{ik} = \frac{1}{V} \oint p_i x_k dS. \quad (6.38)$$

It is also possible to calculate the average value (for the volume) of the derivatives of the displacement vector, and of the unit normal vector by the gradient theorem as:

$$\int \text{Grad} \Phi dV = \int \Phi \mathbf{n} dS. \quad (6.39)$$

As an example we have that,

$$\int \frac{\partial \Phi}{\partial x} dV = \int \Phi n_x dS. \quad (6.40)$$

If the derivatives of the displacement vector are known, then all average components of the strain tensor are also known. If the average value of the components of stress and

strain tensors are known, then it is possible to calculate the average value of the elastic parameters,  $\bar{\lambda}$  and  $\bar{\mu}$ .

As a detail of the numerical experiment, real values of the elastic parameters  $\lambda$  and  $\mu$  were used during the solution of the elastic problem. So, it is reasonable to use as criteria for the numerical solution's accuracy the relative difference between calculated (average) and used elastic parameters in the form:  $\delta_1 = \frac{\lambda - \bar{\lambda}}{\lambda}$  and  $\delta_2 = \frac{\mu - \bar{\mu}}{\mu}$ .

Also, it is necessary to take into account that integration means a summation over all deterministic errors; it also means that the mentioned criteria are rigorous. We propose to use this relative measure to analyze quantitatively the accuracy of numerical solutions.

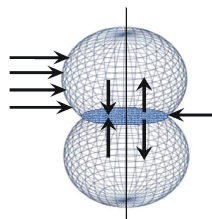
## 6.6 Effective pressure, rigid and slip contacts

Often enough, effective properties,  $p_{eff}$ , of porous granular media does not depend on the confining (external) pressure,  $p_{conf}$ , but on the difference between confining and porous,  $p_0 = p_{por}$ , (fluid) pressures:  $p_{eff} = p_{conf} - p_0$ .

The opinion that porous pressure *impedes* the approximation of contacts is not correct, because pressure is a scalar quantity, and only the surface forces can approximate or separate contacts. Sometimes it is necessary to use a dimensionless factor of unknown nature for  $p_{eff}$ .

Now, let's consider the physics on a minimum representative volume which consists of grains with flat contacts (called here platforms) as shown in figure 6.2.

Figure 6.2 – Geometry of grains with a contact surface (called platform by being flat), and force distribution around the surface.



Source: From autor

The problem is that porous pressure ( $p_0$ ) in granular media causes two opposite processes (see figure 6.2). First, that the distances between grain centers (right side of figure 6.2) to increase, and this effect is significant around the edges. Second, the compression should decrease the distance between grain centers (left side of figure 6.2).

The question that we raise is which effect is stronger and will prevail?

In the literal sense, granular media is not continuous. Of course, this means that we can have some average effective properties, but it is impossible to understand the dependence of the effective properties on external parameters in the frame of continuous medium by using “average” forces in every point.

In order to analyze the dependence of the effective pressure ( $p_{eff}$ ) on porous pressure ( $p_0$ ), and on the structure of the porous state, it is necessary to solve static elastic problem of the mixed type. The boundary condition is described for the part of the grain (spherical) that is in contact with fluid is obvious: the normal component of the loading vector is equal to the porous pressure, and the tangential components are zero.

As for the boundary conditions for contact platforms, between grains, there are two variants: (1st) the rigid contact (platforms are welded), where the displacement vector is null; (2nd) slip contact, where the normal component of the displacement vector and tangential components of the loading vector are null. So, the effective pressure ( $p_{eff}$ ) is formed by the confining pressure, and by the average normal loading vector on the contact platforms.

Sibiriyakov and Sibiriyakov (2010) solved the same problem by using the tensor (6.23) for an axial symmetry for two contact platforms. In this paper, it was shown that the average normal component of the loading vector cannot be only negative, it can also be positive.

### 6.6.1 Numerical example

Now, it is interesting to solve this problem for a grain with 6 contact surfaces, as follows below. This experiment gives an opportunity to test not only the new tensor formulas (6.33-6.37), but also to understand the dependence of the effective properties of granular media on the area of the contact platforms, and on the type of the boundary conditions.

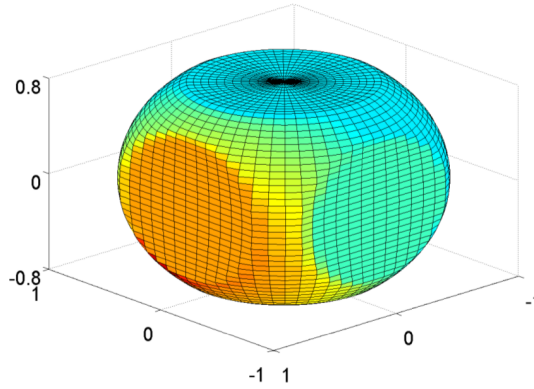
### 6.6.2 Assigning the surface

The surface,  $S$ , is of a sphere of unit radius, and with six contact platforms, as shown in figure 6.3. The size of the platform is determined by the parameter  $h_0$ , that is the distance from the center of the sphere to the center of the contact platform. The equation for the surface is parametric; for example, the equations for the x-coordinate are given by:

$$\begin{cases} \text{if } \sin\theta \cos\varphi > h_0, & \text{then } x = h_0; \\ \text{else if } \sin\theta \cos\varphi < -h_0, & \text{then } x = -h_0; \\ \text{else } x = \sin\theta \cos\varphi. \end{cases} \quad (6.41)$$

Similar relations hold for the  $y$  and  $z$  coordinates.

Figure 6.3 – The clipped ball model with six flat contact areas (platforms) represented in Cartesian coordinates  $(x, y, z)$ , and to be submitted to stress loading and boundary conditions.



Source: From autor

Such surface assigning is more convenient than assigning 7 surfaces (6 platforms, and the rest of the sphere which is in contact with the fluid), but the contours of the platforms are not circumferences, instead they are close to a polygon (see figure 6.4).

To construct the surface is necessary to run over the parameter (as on spherical coordinates)  $\theta$  from 0 to  $\pi$ , and over the parameter  $\varphi$  from 0 to  $2\pi$ . Figure 6.4 is the Indicator surface presented to clarify the next figures, and the role of the parameters  $\theta$  and  $\varphi$  ( $h_0 = 0.8$ ). The parameter  $I = 1$  on the platform (solid-solid contact), and  $I = 0$  on the rest of the sphere (solid-fluid contact).

The problem is reduced to the elastic mixed type, and to calculate the average normal component of the loading vector on the platforms (solid-solid contact) for different values of  $h_0$  (i.e., different areas of the contact), and for different boundary condition (solid-solid, either rigid or slip conditions). The average normal component is the second summation in the formula for the effective pressure ( $p_{eff}$ ).

The Lamé's parameter and the porous pressure were set equal to 1; therefore, the result is proportional to  $p_0$ . There was 59 mesh nodes on the parameter  $\theta$ , and 60 on the parameter  $\varphi$  (i.e., the intervals were  $h_\theta = \frac{\pi}{60}$  and  $h_\varphi = \frac{\pi}{30}$ ). The  $h_0$  parameter had values set to: 0.8, 0.85, 0.9 and 0.95. Also, there were the two mentioned types of the boundary conditions; rigid and slip. The size of the final matrix (for the calculation of the vector potential by matrix inversion) was  $10620 \times 10620$ . This matrix includes either,  $p_i(\mathbf{x}_0) = - \int P_{ik}(\mathbf{x}_0, \mathbf{x}) F_k(\mathbf{x}) dS_{\mathbf{x}}$ , or  $U_i(\mathbf{x}_0) = \frac{1}{2\pi} \int M_{ik}(\mathbf{x}_0, \mathbf{x}) F_k(\mathbf{x}) dS_{\mathbf{x}}$ , where the one to be selected depends on boundary conditions.

If the vector potential,  $\vec{\mathbf{F}}$ , is known, then the loading vector,  $p_i(\mathbf{x}_0) = - \int P_{ik}(\mathbf{x}_0, \mathbf{x}) F_k(\mathbf{x}) dS_{\mathbf{x}}$ ,

is also known.

The average of the normal component of the loading vector was calculated by integration over the contact platforms:

$$\bar{p}_n(\mathbf{x}_0) = \frac{1}{S} \int p_n(\theta, \varphi) I(\theta, \varphi) dS, \quad (6.42)$$

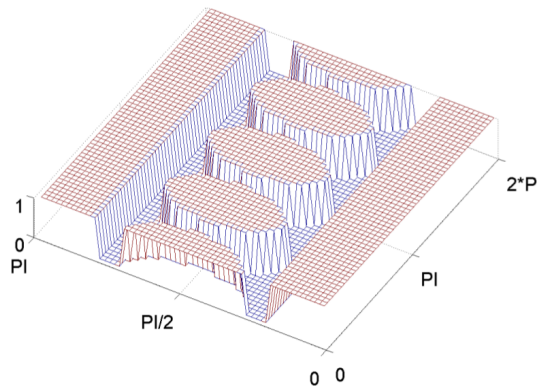
where  $S$  is the total area.

Figure 6.4 is another representation of the clipped ball model, and associated with the  $S$  surface for analysis of discontinuities. In this case, it is represented in the  $\theta$  and  $\varphi$  coordinates by the  $I$ -Indicator, that means:  $I = 1$  for the flat contact area, and  $I = 0$  for the spherical area. The surface parameter height is  $h_0 = 0.8$ .

The boundary conditions in both  $I$ -cases are as follows:

1. if the point is on the spherical side of figure 6.3, and on the area for  $I = 0$  of figure 6.4, then the normal component of the loading vector, ( $p_n$ , equation (6.6)), is equal to the pore pressure ( $p_n = p_0$ ), and the tangential components are zero ( $p_\tau = 0$ ).
2. if the point is on the flat side of figure 6.3, and on the area for  $I = 1$  of figure 6.4, then the normal component of the loading vector, ( $p_n$ , equation (6.6)), is equal zero ( $p_n = 0$ ), and either the tangential components of the displacement vector are zero (rigid contact condition,  $U_\tau = 0$ ), or the tangential components of the loading vector ( $p_\tau$ , equation (6.6)) are zero (for slip contact condition,  $p_\tau = 0$ ).

Figure 6.4 – Discontinuity surface images of the clipped ball model with six flat areas of figure 6.3 in the  $\theta$  and  $\varphi$  cylindrical coordinates using the  $I$ -Indicator function, with the conditions:  $h_0 = 0.8$ ;  $I = 1$  in the flat contact area; and  $I = 0$  on the boundary part with the presence of fluid. The amplitude scale shows 1 and 0, and the six polygonal shapes of the flat contact area. On the two lateral parts  $I = 1$ , and have an extended flat form.



Source: From autor

The problem is when there are different values for  $h_0$  (i. e., different flat contact area sizes), and two different types of boundary conditions to determine the normal and the average stress loading on the contacts sides. This, in order to understand the dependence of the effective pressure ( $p_{eff}$ ) on the size of the contact area.

For figure 6.4 we had the following considerations and established values.

1. In formulating the problem we focused on the analyzes of the effective pressure ( $p_{eff}$ ).
2. The pore pressure  $p_0$  was set equal to 1.
3. Also, both the elastic Lamé's parameters ( $\lambda$  and  $\mu$ ) were set equal to 1.
4. The surface was divided in  $59 \times 60$  points along the  $\theta \times \varphi$  coordinates.
5. The parameters  $h_0$  took the values: 0.80, 0.85, 0.90 and 0.95.
6. The boundary conditions at the contacts were of two types: rigid and slip conditions.
7. First was calculated the coefficient matrix of the linear algebraic equations (6.33 to 6.37).
8. The use of the above matrix is first to calculate the vector potential  $\vec{\mathbf{F}}$ .
9. The loading vector had the matrix dimension of  $10620 \times 10620$ , and was calculated for the entire surface (but, it was set for a part of the surface).
10. The average value of the contact area was calculated by integration.

### 6.6.3 Adjusting the numerical analog

The singularity of the kernels (despite of the singularity type) causes in any case the necessity for calculating improper integrals. This means that it is necessary to add to the numerical summation an additional term based on an analytical calculation (an integral on a small area that includes a point of function singularity). But, the accuracy of such additional term is low enough ( $h^2$ ). It makes no sense using high order integrating formulas; for example, Simpson quadrature.

The finite kernels give the possibility to answer interesting questions about the dependence of the accuracy of the solution of the elastic problem, and about the integration formula for accuracy estimation. Is it reasonable to use high order formulas for the integral's calculation? The found results showed to be very interesting and surprising.

Different integral formulas give different vector potentials, but the loading vectors (final result of the elastic problem solution) proved to be identical, where the maximum difference is in the order of  $10^{-9}$ .

The question now is: what is the reason for this type of result? The case is that the integral is approximated by a finite summation. The kernel satisfies the equation

of equilibrium exactly. The dependence between displacement and loading vectors are calculated analytically; i.e., it is also exact.

For example, if in the formula  $p_i(x_0) = -\frac{1}{2\pi} \int P_{ik}(x_0, x)F_k(x)dS_x$  we denote  $F_k(x)dS_x$  as a new  $F_k(x)$ , it means that the accuracy of the  $U_i(p_i)$  did not depend on the order of the integration formula (of course, if the displacement vector is calculated by the same integration formula). It means that there is no need to calculate integrals.

It is possible from the beginning to use summations, instead of the integrals, in the form  $U_i(x_0) = \sum M_{ik}(x_0, x)F_k(x)$ . The summation is over integration points of the surface. The loading vector is dependent on the displacement vector analytically; i.e.,  $p_i(x_0) = -\sum P_{ik}(x_0, x)F_k(x)$ , where  $P_{ik}(x_0, x)$  is the loading vector under condition that  $M_{ik}$  is a displacement vector.

So, by changing the classical Delta function by its finite analog for the numerical methods gives the possibility to solve the mixed type elastic problems (not only the static, dynamic also), and to use finite summation for the solution instead of the integrals.

## 6.7 Results

Figure 6.5 shows the results of the system of linear equations (6.33 to 6.37) for the vector potential for the clipped ball. The model parameter was  $h_0 = 0.85$ , and conditions of rigid contact. The result of the matrix inversion was stable and reliable.

Figure 6.6 shows the normal component of the vector potential (for the same conditions and  $h_0 = 0.85$  as in figure 6.5). The small absolute values of the potential is caused by using formulas like,

$$U_i(\mathbf{x}_0) = \sum M_{ik}(\mathbf{x}_0, \mathbf{x})F_k(\mathbf{x}), \quad (6.43)$$

instead of

$$U_i(\mathbf{x}_0) = \frac{1}{2\pi} \int M_{ik}(\mathbf{x}_0, \mathbf{x})F_k(\mathbf{x})dS_{\mathbf{x}}, \quad (6.44)$$

what would mean the rejection of the multiplication by the surface element  $dS_{\mathbf{x}}$ , that would be compensated by multiplying by the large values of  $M_{ik}$ .

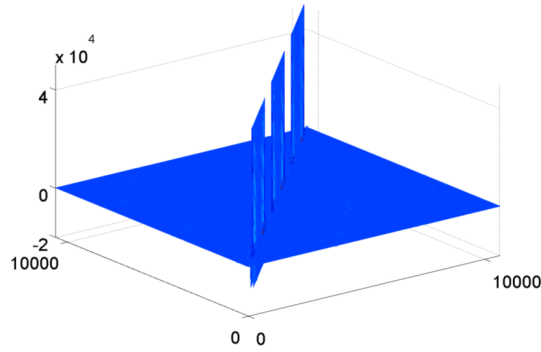
Figure 6.7 shows the normal component of the loading vector,  $p_n$ , under the same conditions as given in figure 6.6. It is the result of the convolution of the vector potential components,  $F_k(\mathbf{x})$ , with the modified stress tensor,  $P_{ik}(\mathbf{x}_0, \mathbf{x})$ , of the fundamental loading; i. e.,

$$p_i(\mathbf{x}_0) = -\sum P_{ik}(\mathbf{x}_0, \mathbf{x})F_k(\mathbf{x}). \quad (6.45)$$

Figure 6.8 shows details of the loading vector component  $p_n$  as in figure 6.7, but for  $0 \leq \theta \leq 0.5548$ , that corresponds to the upper contact platform. It is visible that the loading

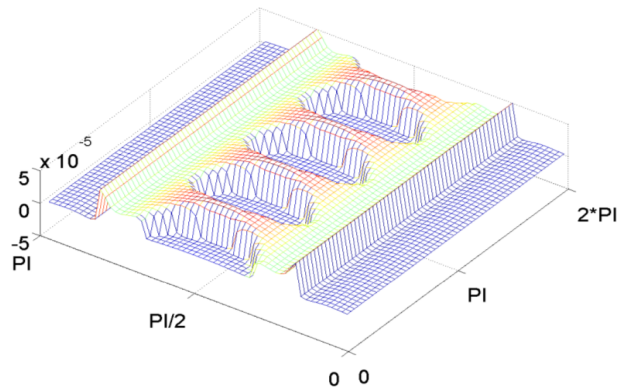
depends slightly on the parameter  $\varphi$ , and it means that the contacts are interacting with each other. With a further decrease in the size of contacts (i. e., by increasing the parameter  $h_0$ ), the loading (on the upper and lower platforms) ceases to depend on the coordinate  $\varphi$ .

Figure 6.5 – Amplitude of the coefficients of the linear system matrix  $M_{ik}$  (6.33) to (6.37) versus  $\theta$  and  $\varphi$  for calculating the vector potential components  $[F_n(\theta, \varphi)]$ , for  $h_0 = 0.85$  and rigid contact.



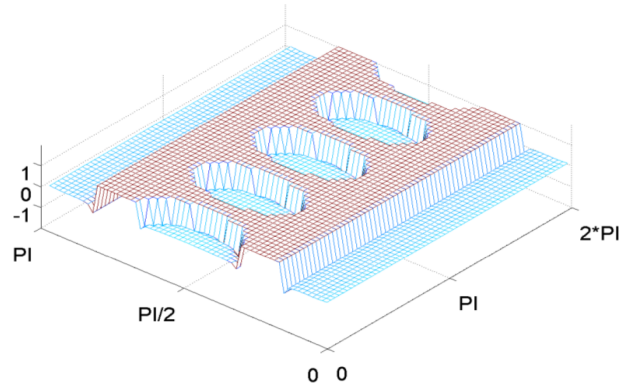
Source: From autor

Figure 6.6 – Dependence of the normal component of the vector potential components,  $F_n$ , on the reliability and stability. This result says that it is a pleasant fact that the part of the surface bordered by the fluid, where the normal loading was well defined, did not change after the numerical calculations for the vector potential,  $F_n$ . The values were:  $h_0 = 0.85$ ; and the parameters  $\theta$  and  $\varphi$ :  $0 \leq \theta \leq \pi$ ,  $0 \leq \varphi \leq 2\pi$ .



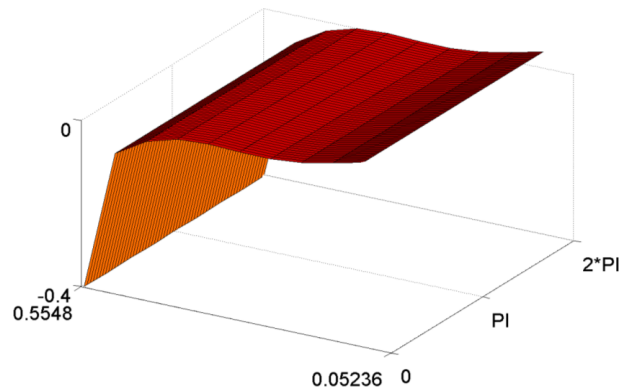
Source: From autor

Figure 6.7 – The normal component of the loading vector  $p_n$  for  $h_0 = 0.85$ , as a function of the  $0 \leq \theta \leq \pi$  and  $0 \leq \varphi \leq 2\pi$  parameters. The borders with fluid have loading  $p_i$  equal to 1. On the platform boundaries, the normal loading and maximum modulus change rapidly. This result comes from a convolution with a modified stress tensor potential given by equation (6.45).



Source: From autor

Figure 6.8 – Details of the normal component of the loading vector  $p_n$  of figure 6.7 showing the upper platform for a narrow band of the parameters  $\theta$  and  $\varphi$ .



Source: From autor

In all cases, the normal component of the displacement vector was defined on the contact solid-fluid (on a part of the whole surface). Also, the loading vector was computed by using a formula of the type  $p_i = -\sum P_{ik}(x_0, x)F_k(x)$  (for the whole surface, including the part where the loading vector,  $p_i$ , was defined). From one point of view, the calculated loading vector on the contact fluid-solid was coincident with the prescribed conditions, and almost absolutely. From another view, an integral criterion for accuracy gives a coincidence of the average elastic parameters with prescribed (real values) with an accuracy to the sixth decimal place.

The algorithm is stable, and gives the possibility to increase the accuracy of BEM in many orders.

Although the solution was stable and precise, the condition number of the linear system for calculating the potential was catastrophically large; i.e.,  $\sim 10^9$ . The clue for this paradox is that the kernel is the response to a finite analog of the Delta-dipole (derivative of the Delta function) loading. It means that the concentrated force is spread (to the half-space), but remains concentrated enough (with respect to energy) in a small area.

This also means that small enough (in module) eigenvalues correspond to very high oscillating eigenvectors, but the scalar product of the free term with the eigenvector (that corresponds to the very small eigenvalues) decreases faster than the eigenvalues.

So, the classical condition number of the matrix of the linear system is calculated as  $\text{Cond}(A) = \max \frac{|\lambda_i|}{|\lambda_j|}$ , where  $\lambda_i$  is the minimum and  $\lambda_j$  the maximum eigenvalues of the matrix, and it is a good criterion for measuring the quality of any system, and of any free term; but, if the free term did not oscillate with high frequency as mentioned, this criterion would be too much rigorous.

Perhaps, it would be more useful to use another condition number that depends not only on the matrix, and also in the free term as:  $\text{Cond1}(\mathbf{A}|\mathbf{B}) = \max \left[ \frac{|\lambda_i|}{|\lambda_j|} \times \frac{|(\mathbf{b}, \mathbf{v}_j)|}{|(\mathbf{b}, \mathbf{v}_i)|} \right]$ , where  $\mathbf{b}$  are column of free terms,  $\mathbf{v}_k$  is the eigenvector corresponding to the eigenvalue  $\lambda_k$ . This is a possible explanation why there was no need to use regularization, despite of the so high condition number.

Results of the dependence of the average normal component of the loading vector,  $\bar{p}_n$ , and on the porous pressure and on the parameter  $h_0$  (under the condition that the porous pressure is unit) is presented in Table 6.1.

Table 6.1 – Dependence of the average normal loading,  $\bar{p}_n$ , (as effective pressure,  $p_{eff}$ ) on the  $h_0$  parameters, and on the type of boundary contact, with the condition that the pore pressure is equal to 1. From the table, the effective pressure is proportional to the pore pressure, as can be seen from the increasing negative values on both right columns with respect to the left column.

$h_0$	rigid contact, $\bar{p}_n$	slip contact, $\bar{p}_n$
0.80	-0.018	-0.020
0.85	-0.031	-0.039
0.90	-0.075	-0.103
0.95	-0.342	-0.416

Source: From autor

The main difference between Sibiriyakov and Sibiriyakov (2010)'s and the presented method, from the mechanical point of view, was the interaction between the platforms of the grain's contacts. In the axial symmetric case, there was two platforms only ((SIBIRYAKOV; SIBIRYAKOV, 2010)), there was no dependence on the  $\varphi$  parameter, and the average normal loading was positive for the case of large enough platforms (it corresponds to reinforcement of the granular medium); but, for the present case of six platforms, it has been proved that the reinforcement to be impossible.

The common fact is that, when the area of the contact is large enough, then the dependence of effective pressure ( $p_{eff}$ ) on the porous pressure ( $p_{por}$ ) is not significant. The smaller the grain contact area, the stronger the dependence on the porous pressure, and on the type of the boundary conditions (rigid or slip). In the case of the slip contact the influence of the porous pressure on the effective pressure is larger.

The most probable areas for destruction by increasing the porous pressure are the small contact platforms. The process of destruction will be irreversible, because normal loading at the edge is maximum, and the beginning of rupture means decreasing of the contact area.

The decreasing of the contact area causes the increasing of the normal component of the loading vector on the edge of the contact platform.

## 6.8 Conclusions

1. It has been developed and numerical tested, a new method for the numerical solution of the elastic boundary value problems. This method can be used to solve static and stationary oscillation problems.
2. The use of finite analogue for the dipole potential is a reliable and valid method to solve mixed boundary value problems.
3. The advantage of this method is the finiteness and the smoothness of the kernel, that makes it possible to solve the elastic problem on surfaces, where the normal vector may have a point of discontinuity.
4. The accuracy of this method is not dependent on the accuracy of the numerical integral formula. Moreover, this method makes it possible to eliminate the use of integral equations by replacing the integrals by finite summations.
5. The effective pressure ( $p_{eff}$ ) should have the meaning of an average normal loading to all the contacts under the influence of pore pressure. The effective pressure ( $p_{eff}$ ) is proportional

to the pore pressure ( $p_{por}$ ), and it has opposite sign, but the proportionality coefficient depends substantially on the area of contact. If the contact area is sufficiently large, then, as in rigid and in the slip contact type, this proportionality factor is small enough. By reducing the contact area, the effective pressure increases.

## 7 GENERAL CONCLUSIONS

The general conclusions follow the general objectives delineated in the Introduction, (chapter 1), and below we follow the chapters for highlighting some specific conclusions. As can be observed we concentrate the conclusions on what can be done with velocity and density models as a post-migration technology for basin modeling and analysis.

- Chapter 2: Fluid percolation theory based on Darcy's law ignores stress-strain state in solids, this theory contains porosity, but does not contain the SSA parameter that creates forces to stop percolation.

There is a need to predict the stress-strain state in solids representing the sedimentary basin, and as a consequence calculate pressure discontinuity between solid and fluid phases. This discontinuity depends on the structure of pore space, and not only on porosity.

It is not necessary to use Darcy's law for determining permeability, because permeability is only a geometric property of porous medium. The permeability value is directly proportional to porosity, and is inversely proportional to the square of the SSA parameter for a specimen. Porosity and the SSA parameter enable using alternative methods to measure the permeability.

- Chapter 3: Another important conclusion was the estimation of complex stress behavior in a given structural-velocity model of a medium, and at the calculation of the storage capacity of buried traps. The first results of mathematical modeling and geological interpretation of the obtained fluid-stress maps are associated with the formation of a new step in applied geodynamics, namely fluid-stress modeling of oil and gas traps.

The relationship between overburden pressure, which is a scalar function, and rock stress is a fairly complex function in the general case. However, it is obvious that fluids accumulate in closed sites of porous reservoirs where the overburden pressure is minimum.

Maps of horizontal gradients of overburden pressure are especially informative for the detection and outlying these traps, and they reveal: convergent (inflow) and divergent (outflow) pressure gradients; isolated inflow regions in the detected trap separated by the geometry of outflow lines (fluid-stress barriers); and possible fluid-stress traps in structural and non-structural conditions. The results show that the main factor of oil production is the specific surface area of porous and cracks. The solution does not contain the permeability; instead, there is the inverse square of the SSA that plays the role of permeability.

- Chapter 4: Low pressure zones exist not only for anticline structures; but, they can also be present in horizontal layers if the  $\gamma$  ratio is smaller in the layer above than in the layer below with respect to the structure surface.

The local decrease of pressure near the dome of an anticline structure depends on the discontinuity of the physical parameters across the structural surface, and on the geometrical parameters (slope angle and curvature). The quantity physically affected is the stress field, and the constitutive parameters (density, Lamé's, and if needed the porosity, specific surface area, etc) are admitted constant for the volume rock under the static condition.

The negative discontinuity of pressure causes the decrease of pressure below the structure surface, which turns it an attractor for fluid accumulation. The positive discontinuity of pressure causes an increase of pressure below the structure surface, and as a result this structure is not an attractor feature for fluid accumulation.

The role of structural curvature is to increase its effect on the pressure value as a function of depth of the structure; that means, as the depth increases the role of the curvature also increases.

- Chapter 5: Another important conclusion is related to establish on how sensitive is the pressure prediction to the variation of velocity and density distributions, principally around a geological reservoir zone. The analysis for this investigation were presented in the form of sections in the geological domain. The sensitivity analysis to measure the decay in the resolution of the stress state prediction in this example followed the migration methodology, and the main conclusions are listed below.

Using a model, we showed that pressure does not necessarily increases linearly, but in a complex form. The target is a confined low pressure zone representing the reservoir, but other low pressure areas are also mapped.

- Chapter 6: It has been developed and numerical tested, a new method for the numerical solution of the elastic boundary value problems, where the use of finite analogue for the dipole potential is a reliable and valid method to solve mixed boundary value problems.

The accuracy of this method is not dependent on the accuracy of the numerical integral formula, and it is possible to eliminate the use of integral equations by replacing the integrals by finite summations.

The effective pressure is given the meaning of an average normal loading to all the contacts under the influence of pore pressure. The effective pressure is proportional to the pore pressure, and it has opposite sign, but the proportionality coefficient depends substantially

on the area of contact. If the contact area is sufficiently large, then, as in rigid and in the slip contact type, this proportionality factor is small enough. By reducing the contact area, the effective pressure increases.

## Bibliography

- ABRAMOWITZ, M.; STEGUN, I. A. *Handbook of mathematical functions*. New York: Dover Publications, Inc., 1970. 1046 p.
- ALLEN, P. A.; ALLEN, J. R. *Basin Analysis*. [S.l.]: Wiley-Blackwell, 2013. 619 p.
- AMADEI, B.; STEPHANSSON, O. *Rock Stress and Its Measurement*. London, England: Springer Science, 1997. 490 p.
- AMEEM, M. S. *Fracture and In-Situ Stress Characterization of Hydrocarbon Reservoirs*. London: The Geological Society of London, 2003. 216 p.
- BERNABINI, M. et al. *Deconvolution and Inversion*. [S.l.]: Blackwell Scientific Publications, 1987. 355 p.
- BIONDI, L. B. *3D seismic imaging*. Tulsa, OK, USA: Society of Exploration Geophysicists, 2010. 224 p.
- BIOT, M. A. Mechanics of deformation and acoustic propagation in porous media. *Journal of Applied Physics*, v. 23, p. 1492–1498, 1962.
- BRACHETTI, P. et al. A new version of Price's algorithm for global optimization. *Journal of Global Optimization*, p. 165–184, 1997.
- BROWN, A. R. *Interpretation of three-dimensional seismic data*. Tulsa, OK, USA: Society of Exploration Geophysicists, 2011. 646 p.
- CHOPRA, S.; MARFURT, K. J. *Seismic attributes for prospect identification and reservoir characterization*. Tulsa, USA: Society of Exploration Geophysicists, 2007. 464 p.
- COHEN, J. K.; STOCKWELL, J. J. W. *CWP/SU: Seismic Unix Release 39 – a free package for seismic research and processing*. [S.l.]: Center for Wave Phenomena, Colorado School of Mines, 2005.
- DAZIN, P. G.; JOHNSON, R. S. *Solitons: an Introduction*. [S.l.]: Cambridge University Press, 1989.
- DUVENECK, D. *Tomographic determination of seismic velocity models with kinematic wavefield attributes*. 181 p. Tese (Doutorado) — Universität Fridericiana Karlsruhe, 2004.
- EGOROV, G. V.; MASHINSKII, E. I. Biharmonic compressional and shear waves in the porous sample of artificial sandstone under axial pressure (in russian). *Technology of Seismic Exploration*, v. 1, n. 1, p. 72–77, 2002.
- FLETCHER, R. *Practical methods of Optimization*. [S.l.]: John Wiley and Sons, 2001. 436 p.
- FOMEL, S.; KAZINNIK, R. Non-hyperbolic common reflection surface. *79th Annual Internationall Meeting of the Society of Exploration Geophysics. (CD-Rom)*., v. 1, n. 1, p. 1–6, 2010.

- FRANK, P. M. *Introduction to System Sensitivity Theory*. [S.l.]: Academic Press, 1978. 400 p.
- GALPERIN, E. I. *Vertical seismic profiling and its exploration potential*. Boston: D. Reidel Publishing Company, 1985. 472 p.
- GREGORY, A. R. Fluid saturation effect on dynamic elastic properties of sedimentary rocks. *Geophysics*, v. 41, n. 5, p. 895–921, 1976.
- HANTSCHHEL, T.; KAUERAUF, A. I. *Fundamentals of Basin and Petroleum Systems Modeling*. Berlin: Springer-Verlag, 2009. 476 p.
- HARDAGE, B. A. et al. *Multicomponent seismic technology*. Tulsa, OK, USA: Society of Exploration Geophysicists, 2011. 318 p.
- KUPRADZE, V. D. *The potential method in elasticity*. Moscow: Physics and Mathematics Issue, 1963. 472 p.
- LANDAU, L.; LIFSCHITZ, M. *Course of theoretical physics: theory of elasticity*. Moscow: Nauka, 1961.
- LANDAU, L. D. *Hydrodynamics (in Russian)*. [S.l.]: Nauka. Moscow, Russia, 1988.
- LEITE, L. W. B.; MANN, J.; VIEIRA, W. W. S. Processing and imaging of marine seismic data from the jequitinhonha basin (bahia, brazil) (submitted). *Brazilian Journal of Geophysics*, 2014.
- LEITE, L. W. B.; SIBIRYAKOV, E. P.; VIEIRA, W. W. S. Mathematical modeling anticline reservoirs. In: . [S.l.]: Fourteenth International Congress of The Brazilian Geophysical Society (Submitted), 2015.
- LEITE, L. W. B.; VIEIRA, W. W. S. Sensitivity, resolution and ambiguity of the crs stack operator. *Brazilian Journal of Geophysics*, v. 31, n. 4, p. 663–659, 2013.
- LOWRIE, W. *A Student's guide to Geophysical Equations*. London: Cambridge University Press, 2011. 281 p.
- MACMILLAN, W. D. *Theoretical Mechanics. The Theory of the Potential*. New York, USA: Dover Publications, Inc., 1930. 469 p.
- MANN, J. *Extensions and applications of the common-reflection-surface stack method*. 165 p. Tese (Doutorado) — Universität Fridericiana Karlsruhe, 2002.
- MARTIN, G. S.; WILEY, R.; MARFURT, K. J. Marmousi2: An elastic upgrade for marmousi. *The Leading Edge. SEG.*, p. 156–166, 2006.
- MASHINSKII, E. I.; EGOROV, G. V. The amplitude effects in direct wave, which propagate in cemented sandstone with pressure (in russian). *Russian Geology and Geophysics*, v. 52, n. 5, p. 725–731, 2011.
- MASLOV, V. P. *Theory of Operators*. Moscow: Nauka, 1973.
- MAUCH, R. *Coherency analysis of seismic data*. 142 p. Dissertação (Mestrado) — Universität Fridericiana Karlsruhe, 1999.

- MAVKO, G.; MUKERJI, T.; DVORKIN, J. *The rock physics handbook*. London: Cambridge University Press, 1999.
- MENKE, W. *Geophysical Data Analysis: Discrete Inverse Theory*. [S.l.]: Academic Press, 2002. 285 p.
- MULLER, T. *The Common Reflection Surface Stack - Seismic Imaging Without Explicit Knowledge of the Velocity Model*. 193 p. Tese (Doutorado) — Universität Fridericiana Karlsruhe, 1999.
- NELSON, R. A. *Geologic Analysis of Naturally Fractured Reservoirs*. Boston, USA: Gulf Professional Publishing, 2001. 332 p.
- NOVACKY, W. *Elasticity Theory*. [S.l.]: Warsaw, 1970. 872 p.
- PARTON, V. Z.; PERLIN, P. I. *Mathematical Methods of the Theory of Elasticity*. [S.l.]: Imported Pubn, 1985. 673 p.
- PERSEN, L. N. *Rock Dynamics and Geophysical Exploration*. Amsterdam, Holland: Elsevier Scientific Publishing Company, 1975. 270 p.
- PRICE, W. Global optimization by controlled random search. *Journal of Optimization Theory and Applications*, v. 40, n. 3, p. 333–348, 1983.
- REEVES, G. Smooth2a. *Division of Biology, Caltech, USA*, v. 1, n. 1, p. 1, 2009.
- ROACH, G. F. *Green's Functions*. London: Cambridge University Press, 1986. 325 p.
- SALTELLI, A. et al. *Sensitivity Analysis in Practice. A Guide to Assessing Scientific Models*. [S.l.]: John Wiley and Sons, 2004. 219 p.
- SANTALO, L. *Introduction to integral geometry*. [S.l.]: Hermann and Cia. Editors, 1953. 123 p.
- SAVARENSKY, E. *Seismic Waves*. Moscow, Russia: Mir, 1975. 349 p.
- SCHILLING, R. J.; HARRIS, S. L. *Fundamentals of Digital Signal Processing Using MATLAB*. [S.l.]: Cengage, 2005. 766 p.
- SIBIRIAKOV, B. P. et al. The prediction of stresses and elements of hydrodynamics by multiwave seismic. *Russian Geology and Geophysics*, v. 1, n. 6, p. 752–759, 2004.
- SIBIRYAKOV, B. P. The one dimensional problem of attenuation of nonlinear waves in grounds (in russian). *Geology and Geophysics*, v. 13, n. 11, p. 108–115, 1974.
- SIBIRYAKOV, B. P. The stress-strain situation of rocks in vicinity of borehole. *Russian Geology and Geophysics*, v. 34, n. 6, p. 73–80, 1993.
- SIBIRYAKOV, B. P. Supersonic and intersonic cracking in rock-like material under remote stresses. *Theoretical and Applied Fracture Mechanics*, v. 38, n. 3, p. 255–265, 2002.
- SIBIRYAKOV, B. P. *Dynamics of microinhomogeneous geological media*. [S.l.]: Novosibirsk State University, 2004. 234 p.

- SIBIRYAKOV, B. P.; PRILOUS, B. I. The unusual small wave velocities in structural bodies and instability of pore or cracked media by small vibration. *WSEAS Transactions on Applied and Theoretical Mechanics Issue 7*, v. 2, p. 69–79, July 2007.
- SIBIRYAKOV, B. P.; PRILOUS, B. I.; KOPEYKIN, A. V. The nature of instabilities in blocked media and seismological law of Gutenberg-Richter. *WSEAS Transactions on Applied and Theoretical Mechanics Issue 2*, v. 6, p. 69–79, April 2011.
- SIBIRYAKOV, B. P.; ZAIKIN, A. D. Multiple seismics and applied geodynamics in petroleum-bearing regions. *Russian Geology and Geophysics*, v. 35, n. 5, p. 49–55, 1994.
- SIBIRYAKOV, E. P. On a boundary integral equation method used to determine parameters of microheterogeneous media (in Russian). *Physical Mesomechanics*, v. 9, p. 97–101, 2006.
- SIBIRYAKOV, E. P. The dependence of the elastic moduli microinhomogeneous medium on the structure of the pore space. *Physical Mesomechanics*, v. 12, n. 1, p. 115–120, 2009.
- SIBIRYAKOV, E. P. et al. Local low pressure areas in anticline structures (accepted). *Brazilian Journal of Geophysics*, 2013.
- SIBIRYAKOV, E. P. et al. Subsurface stress prediction using seismic data for oil and gas exploration (submitted). *Brazilian Journal of Geophysics*, 2014.
- SIBIRYAKOV, E. P. et al. A new method for the solution of the elasto-dynamic problem (to be submitted). *EAGE Latin American Journal*, 2015.
- SIBIRYAKOV, E. P. et al. Numerical applications of the new method for the solution of the elasto-dynamic problem for asymmetrical reservoirs. (to be submitted). *EAGE Latin American Journal*, 2015.
- SIBIRYAKOV, E. P.; LEITE, L. W. B.; VIEIRA, W. W. S. Model of structured continuum and relation between specific surface, porosity and permeability. In: . [S.l.]: Thirteenth International Congress of The Brazilian Geophysical Society, 2013.
- SIBIRYAKOV, E. P.; LEITE, L. W. B.; VIEIRA, W. W. S. Model of the structured continuum, and the relation between specific surface area, porosity and permeability. *Brazilian Journal of Geophysics*, v. 31, n. 4, p. 559–568, 2013.
- SIBIRYAKOV, E. P.; LEITE, L. W. B.; VIEIRA, W. W. S. Behavior of stresses in structures and the effect on hydrodynamics analyzed from multicomponent seismic data. *Brazilian Journal of Geophysics*, v. 33, n. 1, p. 1–14, 2015.
- SIBIRYAKOV, E. P.; SIBIRYAKOV, B. P. The structure of pore space and disjoining pressure in granular medium. *Physical Mesomechanics (Special Issue)*, v. 13, p. 40–43, 2010.
- SMIRNOV, V. I. *Course of higher Mathematics*. London: Pergamon Press, 1964. 630 p.
- TARANTOLA, A. *Inverse Problem Theory*. [S.l.]: SIAM, 1984. 342 p.
- TOLDI, J. L. *Velocity analysis without picking*. 181 p. Tese (Doutorado) — Stanford University, 1985.

- VERSTEEGE, R. J.; GRAU, G. The marmousi experience. *Proc. EAGE Workshop on Practical Aspects of Seismic Data Inversion. Copenhagen, 1991.*
- VIEIRA, W.; LEITE, L. Sensitivity and resolution of the CRS stack operator (in portuguese). *Workshop of the Exploration Geophysics Network. Salvador, Bahia, Brazil. (CD-Rom)*, v. 1, n. 1, p. 1–6, 2009.
- VIEIRA, W.; LEITE, L.; NUNES, F. S. M. Automatic picking in the semblance domain. *12th International Congress of the Brazilian Geophysical Society. Rio de Janeiro, Brazil. (CD-Rom)*., v. 1, n. 1, p. 1–6, 2011.
- VIEIRA, W. W. S.; LEITE, L. W. B.; SIBIRYAKOV, E. P. Stress prediction and hydrodynamics from multicomponent seismic data. In: . [S.l.]: VI Brazilian Symposium on geophysics, 2014.
- VIEIRA, W. W. S.; SIBIRYAKOV, E. P.; LEITE, L. W. B. Pressure variation prediction using seismic data for oil and gas exploration. In: . [S.l.]: Fourteenth International Congress of The Brazilian Geophysical Society (Submitted), 2015.
- WHITE, J. E. *Underground sound. Applications of seismic waves.* Amsterdam, Netherlands: Elsevier, 1983. 253 p.
- ZANG, A.; STEPHANSSON, O. *Stress Field of the Earth's Crust.* Berlin: Springer-Verlag, 2010. 322 p.
- ZELDOVICH, Y. B.; RAIZER, Y. P. Physics of the shock waves and high temperature hydrodynamics phenomena. *Nauka, Moscow*, p. 64–66, 1966.
- ZIATDINOV, S. R.; CHESTNUT, B. M. Extrinsic components of the rayleigh wave. *Geophysical Questions. Issue 38*, Saint Petersburg, Russia, p. 46–55, 2005.
- ZOBACK, M. *Reservoir Geomechanics.* [S.l.]: Cambridge University Press, 2007. 505 p.

## **APPENDIX**

## APPENDIX A – SENSITIVITY, RESOLUTION AND AMBIGUITY OF THE CRS STACK OPERATOR

This appendix describes an investigation about the sensitivity and ambiguity of the CRS stack operator parameters ( $v_0, R_{NIP}, R_N, \alpha_0$ ), and their resolution in terms of statistical properties of the solution of a nonlinear multi-parametric optimization problem for surface fitting between the forward model and a synthetic data, in the least-square sense. The sensitivity method is borrowed from dynamic system analysis and synthesis, and the definitions are based on the Miller-Murray model. The results are analyzed in terms of the CRS attributes search strategies during the stack process.

The investigation principle is to combine global and local optimization methods to reach a minimum of the object function of minimization, where the problem matrix has a better linear relation to the parameters. A first search for a minimum is performed with a controlled random search method, followed by a gradient method for the last steps for the optimization to calculate the data and parameter resolution and covariance matrices, and any further model statistical properties.

The sensitivity functions are represented by the columns of the optimization problem matrix, and they in general exhibit a linear behavior instead of a convex form; as a result, this linear behavior establish the necessity of a good starting point for the optimized multi-parametric attributes search.

### Introduction

The motivations of the present work come from two aspects of the CRS (Common Reflection Surface) stack: (1st) the presence of noise in the recovered attributes; and (2nd) the strategy for the parameter search. The analysis of the CRS outputs (stack, coherence, migration) show that as the observed input data improves on the signal/noise ratio, the attribute sections show a structure that resembles more the stack section that is used as reference. Sensitivity analysis can be used to determine how sensitive the model is to changes in the value of the parameters and to the geometry of the model, as part of a curve (CRS operator surface) fitting problem.

The present description is structured in three main parts related to curve fitting between the synthetic data and the forward model represented by the CRS stack operator, as an optimization problem in the least-square sense. The parts are: (1st) Controlled random global search

for the parameters; (2nd) second order gradient method, resolution and ambiguity; and (3rd) sensitivity analysis and its relation to the CRS attributes search.

Sensitivity and ambiguity calculus can be performed in the forward model as a first step in the analysis of the data fitting problem, and it is independent of the object function and of the mathematical optimization problem. This calculus is used for the purpose of analysis and synthesis of mathematical models. To be able to give a unique formulation of the mathematical problem, the mathematical model is usually considered to be known exactly, but this assumption is unrealistic since there is always a certain discrepancy between the actual system (data) and its mathematical model (operator). This discrepancy results from the following partial reasons, as we paraphrase Saltelli et al. (2004):

- A real system cannot be identified exactly because of the restricted accuracy of the measuring devices;
- Mathematical models are often simplified or idealized intentionally to simplify the mathematical problem, or to make it solvable at all.

For these reasons, the results of mathematical synthesis need not necessarily be practicable, or they may even be very poor, if there is considerable deviations between the real system and the mathematical model, and the solution be very sensitivity to the parameters. Therefore, it should be part of the practical problem to learn about parameter sensitivity prior to its implementation, or to reduce the sensitivity systematically if this turns out to be necessary.

This is important if one is involved in optimization procedures, since a natural property of optimization is to extremize the performance of a certain parameter set that controls the operation. Example of this are gradient methods, adaptative and self-learning systems.

Among the specific aims of the present study are: (1) to analyze the sensitivity of the CRS hyperbolic stack operator to its parameters; and (2) to compare the results of the parameter sensitivities with the strategy for the CRS attribute search as described by Muller (1999) and Mann (2002).

For the sensitivity analysis here discussed, we organized it as a nonlinear optimization problem, with the statistical properties obtained from the derivatives forming the problem matrix in the gradient method. The norm-2 was selected due to its simplicity and elegance, and we follow Tarantola (1984) for its description. Data and parameter resolution matrices, and the unit covariance matrix are calculated and analyzed at the object function minimum, where the problem is considered linearized based on Taylor series expansion to the first order.

The CRS parameter search strategies in the Semblance domain can be divided in two main parts: (1st) the first part is a search to determine initial parameter values to start the optimization iterations; (2nd) a second part is a simultaneous search for all parameters starting from the initial values. The searches are performed in the CMP (common-mid-point), therefore subject to properties of this family, as the reciprocity principle, and the aperture.

The forward model is represented by the CRS stack operator in terms of  $t(x_m, h; \mathbf{m})$ , where the independent variables are the mid-point  $x_m$  and the source-sensor offset  $h$ , and  $\mathbf{m}$  standing for the parameters represented by the attributes  $\mathbf{m} = (R_{\text{NIP}}, R_{\text{N}}, \alpha_0)$ , with  $v_0$  considered fixed.

The optimization problem is presented in the following form: Given an observed seismic section  $t^{(\text{obs})}(x_m, h)$  in the data space  $D$ , we wish to find a model  $\mathbf{m}$  in the parameter space  $M$  such that the forward model  $t^{(\text{pre})}(x_m, h; \mathbf{m})$  fits the observed data in the least-square sense.

The problem is classified as nonlinear, multiparametric, overdetermined. The synthetic data can be constructed with different noise levels, and to avoid local minimum, a solution is constructed by the combination of the Controlled Random Search Global Method (CRSGM), followed by the Gradient Method (GM) to allow for the statistical analysis of the solution (FLETCHER, 2001). The combination of these methods follows the principle that CRSGM defines a region around the global minimum, theoretically well defined, followed by last iterations around a local minimum with better linear properties to construct the correlation and resolution matrices.

Numerical experiments were realized for randomly chosen points  $P_0(x_0, t_0)$ , therefore, neither to extend along the time traces, ( $t_0 = 0, t_{\text{total}}$ ), nor along the mid-points ( $x_0 = 0, x_{\text{total}}$ ), what would take the problem to be non-practicable. As established, the solution by the CRSGM can be used as an automatic input to the GM method, but in the present work these experiments were performed in two separate steps without degrading the strategy.

The structure of the sensitivity analysis is based on the polynomial function of the CRS operator represented by  $t(x_m, h; \mathbf{m})$ , where now  $\mathbf{m} = (v_0, R_{\text{NIP}}, R_{\text{N}}, \alpha_0)$ , including  $v_0$ , and the quantitative properties of this system with respect to the  $\mathbf{m}$  parameters are shown as functions of the independent variables  $x_m$  and  $h$ .

The methodology for sensitivity analysis has been borrowed from the analysis and design of dynamic systems, as described, e.g., by Frank (1978) for engineering applications, and by many others for partial differential equations, e.g., Saltelli et al. (2004). Among the several methods for uncertainty and sensitivity analysis, the method adopted here is the local method which is derivative based.

The definitions to quantify the parameter sensitivity of a system is summarized later in

the text, and we start defining the forward model to adjust the classical nomenclature to our subject.

## Forward Model

The CRS stack operator describes the impulsive traveltimes for curved reflectors based on the paraxial ray theory, and takes into account only primary reflection trajectories (MANN, 2002). The paraxial ray theory is based on Taylor series that handles general smooth functions of many variables. The quadratic model obtained by the truncated Taylor series of  $t(x_m, h; \mathbf{m})$  about  $(x_m = x_0, h = h_0)$  is denominated the parabolic traveltimes for 3D, that can be written as:

$$t(x_m, h; \mathbf{m}) = t_0(\mathbf{m}) + \mathbf{p}^T \Delta \mathbf{x} + \frac{1}{2} \Delta \mathbf{x}^T \mathbf{M} \Delta \mathbf{x}. \quad (\text{A.1})$$

The transit time  $t(x_m, h; \mathbf{m})$  is calculated with respect to a central reference ray with traveltimes  $t_0(x_0, h_0; \mathbf{m})$ , usually taken as the Normal Incidence Ray. Making  $x_1 = x_m$  and  $x_2 = h$ ,  $\Delta x_1 = x_m - x_0$ ,  $\Delta x_2 = h - h_0$ , the Gradient  $\mathbf{p}$  and the Hessian  $\mathbf{M}$  are written as:

$$\mathbf{p}^T \Delta \mathbf{x} = \sum_{n=1}^2 \Delta x_n \frac{\partial}{\partial x_n} t(x_m, h; \mathbf{m}); \quad \frac{1}{2} \Delta \mathbf{x}^T \mathbf{M} \Delta \mathbf{x} = \frac{1}{2} \sum_{l=1}^2 \sum_{n=1}^2 \Delta x_l \Delta x_n \frac{\partial^2}{\partial x_l \partial x_n} t(x_m, h; \mathbf{m}).$$

These equations also have time derivatives with respect to the survey space coordinates, where  $\mathbf{p}$  and  $\mathbf{M}$  can be calculated by Dynamic Ray Tracing.

The CRS operator can be physically interpreted by the N and NIP waves as shown in Fig. A.1. (DUVENECK, 2004), among others, describe the transformation of Eq. (A.1) in terms of wave front parameters for 3D. But, limiting the discussion to the CRS-2D, flat observation surface, and using the relations:

$$p = \frac{\sin \alpha_0}{v_0}, \quad M_N = \frac{\cos^2 \alpha_0}{v_0} K_N \quad \text{and} \quad M_{\text{NIP}} = \frac{\cos^2 \alpha_0}{v_0} K_{\text{NIP}}, \quad (\text{A.2})$$

the CRS parabolic operator is given by

$$t(x_m, h; \mathbf{m}) = t_0 + \frac{2 \sin \alpha_0}{v_0} (x_m - x_0) + \frac{2 t_0 \cos^2 \alpha_0}{v_0} \left[ \frac{(x_m - x_0)^2}{R_N} + \frac{h^2}{R_{\text{NIP}}} \right], \quad (\text{A.3})$$

and the hyperbolic form by

$$t(x_m, h; \mathbf{m}) = \sqrt{\left[ t_0 + \frac{2 \sin \alpha_0 (x_m - x_0)}{v_0} \right]^2 + \frac{2 t_0 \cos^2 \alpha_0}{v_0} \left[ \frac{(x_m - x_0)^2}{R_N} + \frac{h^2}{R_{\text{NIP}}} \right]}. \quad (\text{A.4})$$

$R_{\text{NIP}} = \frac{1}{K_{\text{NIP}}}$ ,  $R_N = \frac{1}{K_N}$  and  $\alpha_0$  are the wave front attributes, and the quantity  $v_0$  stands for the velocity of the upper layer, that in practical work is established as a fixed value estimated around the stack reference point  $P_0(x_0, t_0)$ .

The justification for  $v_0$  be included as an ambiguity parameter is that the values attributed to  $v_0$  can vary, and can even be used as a filter for analyzing multiple attenuation. Besides, this velocity will depend on the source dominant band frequency, and velocity may considerably vary along the survey line, and even in its aperture; the exception would be marine surveys due to the smaller variation in water velocity.

Fig. A.2 simulates an observation surface (blue) calculated by ray theory, and the CRS stack surface (green) calculated by Eq. (A.4). The CRS stack has the intention to fit these two surfaces in terms of correlation Semblance analysis, and in the CRS case performed in an automatic way, and in Steps summarized below. Each Step searches for one of the attributes ( $R_{\text{NIP}}$ ,  $R_{\text{N}}$ ,  $\alpha_0$ ), and produces a stack related to each reference point  $P_0(x_0, t_0)$ , that are finally followed by 3-parameter optimization Step.

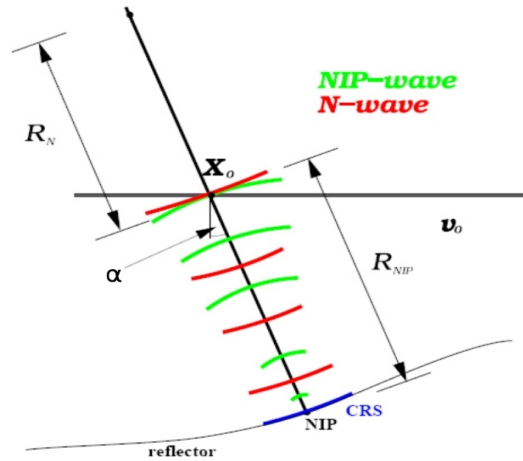
To satisfy the Paraxial Ray Theory, the central ray of reference is taken the zero offset ray, or the Normal Incidence Ray in subsurface. This central ray satisfies Snell's law through the interfaces, and the wave front curvatures of the NIP and N waves change according to the refraction and transmission laws.

Fomel and Kazinnik (2010) compares Multifocusing (MF) and CRS methods, where he proposes non-hyperbolic Common Reflection Surface approximations. Also, the CRS operator can be written in other forms for dealing with velocity analysis, like

$$t(x_m, h; \mathbf{m}) = t_0 + A(x_m - x_0) + B(x_m - x_0)^2 + Ch^2, \quad (\text{A.5})$$

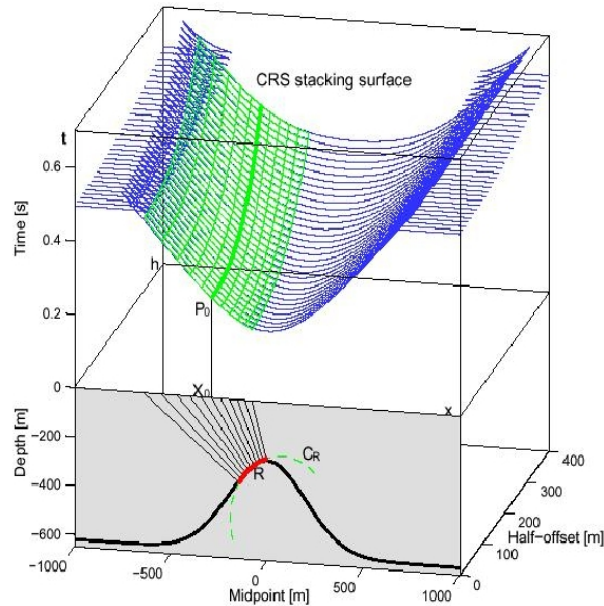
where the three coefficients,  $A$ ,  $B$  and  $C$ , are related to the four parameters  $v_0$ ,  $R_{\text{NIP}}$ ,  $R_{\text{N}}$  and  $\alpha_0$ , but the interest here are directly in the wave attributes (DUVENECK, 2004).

Figure A.1 – Physical illustration of the CRS model formed by one layer over a half-space separated by a curved interface. The velocity  $v_0$  characterizes the upper layer involving the observation aperture. The emergence angle  $\alpha_0$  is common to both N and NIP waves.  $R_{NIP}$  is the NIP-wave radius and curvature  $K_{NIP}$ , and  $R_N$  is the N-wave radius and curvature  $K_N$ . (MANN, 2002).



Source: From autor

Figure A.2 – 3D perspective of the surfaces to be indirectly fit in the stack process: the CRS operator in green [Eq. (A.4)], and the simulated observed data in blue. (MANN, 2002).



Source: From autor

Bernabini et al. (1987) describe functionals to be evaluated quantitatively on a given CMP gather for the goodness of fit between data and a model function, particularly for a stack-

ing velocity value of the hyperbolic reflection response. The most common functional measures the likeness of the corrected gather's trace amplitudes ( $\bar{u}$ ), based on correlation and choices of normalization. The extended normalized correlation Semblance measure,  $\phi(t_0; \mathbf{m})$ , to the  $(h, x_m, t)$  coordinates, is composed by averages and given, without mathematical simplification, by:

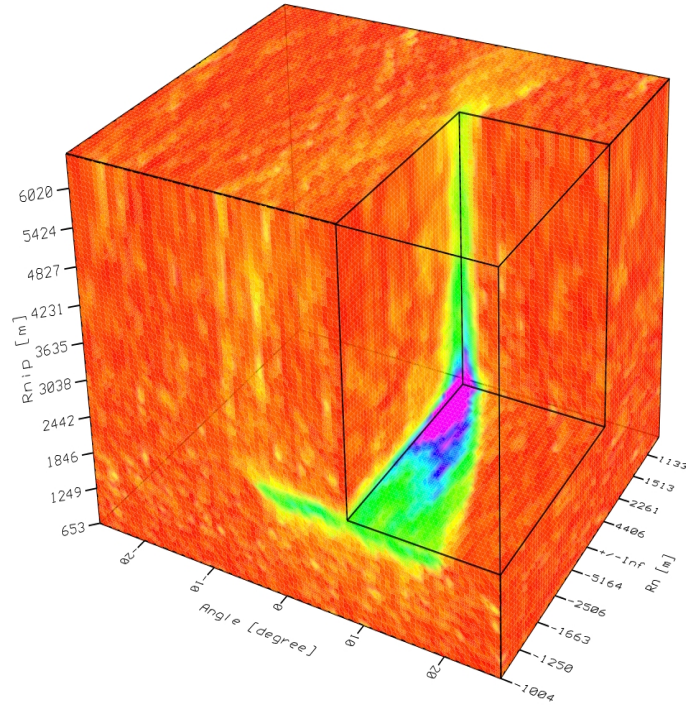
$$\phi(t_0; \mathbf{m}) = \frac{\frac{1}{N_t} \sum_{t=t_0-\delta t}^{t=t_0+\delta t} \frac{1}{N_{x_m}} \sum_{x_m=x_F}^{x_m=x_L} \left[ \frac{1}{N_h} \sum_{h=h_F}^{h=h_L} \bar{u}(x_m, h; t(t_0), \mathbf{m}) \right]^2}{\frac{1}{N_t} \sum_{t=t_0-\delta t}^{t=t_0+\delta t} \frac{1}{N_{x_m}} \sum_{x_m=x_F}^{x_m=x_L} \frac{1}{N_h} \sum_{h=h_F}^{h=h_L} \bar{u}^2(x_m, h; t(t_0), \mathbf{m})}, \quad (\text{A.6})$$

where the set of parameters  $\mathbf{m}$  are related to the trajectory,  $t = t(t_0)$ , of the summation defined by Eq. (A.4), and its different adapted forms. The  $h$ -window goes from a near first  $h = h_F$  to a last  $h = h_L$  offset with  $N_h$  points. The  $x_m$ -window goes from a near first  $x_m = x_F$  to a last  $x_m = x_L$  mid-point with  $N_x$  points. The  $t$ -window is specified by some  $\delta t$  around  $t_0$ .  $\phi(t_0; \mathbf{m})$  takes values in the interval  $[0,1]$  regardless of the signal amplitude, and it quantifies the uniformity of the signal polarity across the normal moveout corrected gather amplitude,  $\bar{u}(t)$ .

Eq. (A.6) is written in a form that does not explicitly carry information about the theoretical model,  $t^{(\text{pre})}(x_m, h)$ , as Eq. (A.14) does; therefore, it is not used here as a direct curve fitting measure, and we call the stack process an indirect optimization process. Toldi (1985), and extensions referenced to his work (for example, Vieira, Leite and Nunes (2011)), treats the indirect optimization aiming at velocity estimation ( $v_{\text{RMS}}$ , or  $v_{\text{INT}}$ ), with the trajectory  $t = t(t_0)$  written in an explicit form of the type  $t(h; t_{0,n}) = \sqrt{t_0^2 + \frac{(2h)^2}{v_{\text{RMS},n}^2}}$ , where  $v_{\text{RMS},n}^2 = \frac{\sum_{i=1}^n v_{\text{INT},i}^2 \Delta t_i}{\sum_{i=1}^n \Delta t_i}$ , with time  $\Delta t_i$  for vertical interval trajectories between two sequential reflections.

Fig. A.3 serves to represent the Semblance function, Eq. (A.6), where the aim of the optimization is to search for the global minimum represented in red. Local minimum can also be seen as yellow spots. Muller (1999) shows plots of Eq. (A.6) in form of cube perspectives and slices, as combination maps of  $R_{\text{NIP}}$  versus  $R_{\text{N}}$ ,  $R_{\text{NIP}}$  versus  $\alpha_0$ ,  $R_{\text{N}}$  versus  $\alpha_0$ , where the global minimum present a clearly elongated valley form.

Figure A.3 – Cube perspective of the coherence Semblance values calculated by Eq. (A.6) as function of the wavefield attributes  $\alpha_0$ ,  $R_N$  and  $R_{NIP}$ . (MAUCH, 1999).

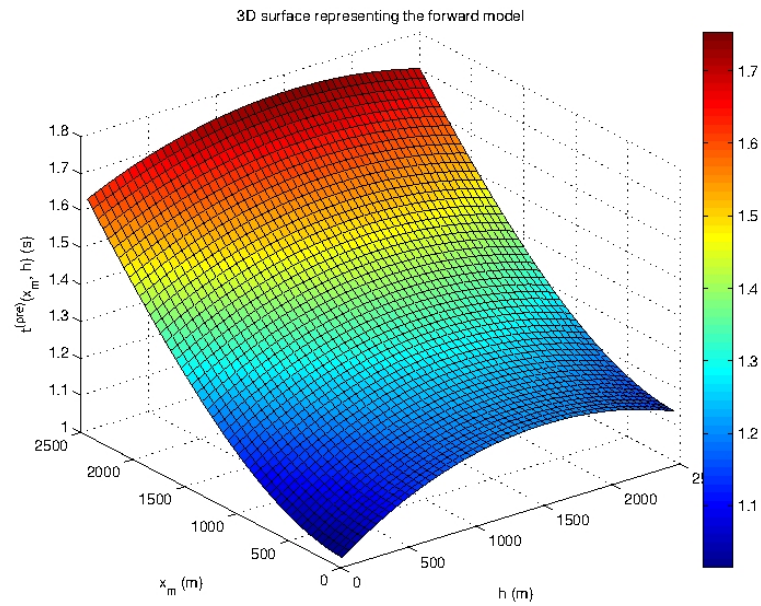


Source: From autor

The space sampling to construct the experiment were  $\Delta x_m = 50$  m and  $\Delta h = 50$  m, with the respective number of points  $N_{x_m} = 50$  and  $N_h = 50$ . The first geophones were placed at  $h_F = 50$  m and  $x_F = 50$  m. The nominal values for the CRS parameters were  $v_0 = 1500$  m/s,  $R_{NIP} = +5000$  m,  $R_N = -5000$  m,  $\alpha_0 = 0,2094$  rad, and  $t_0 = 1$  s.

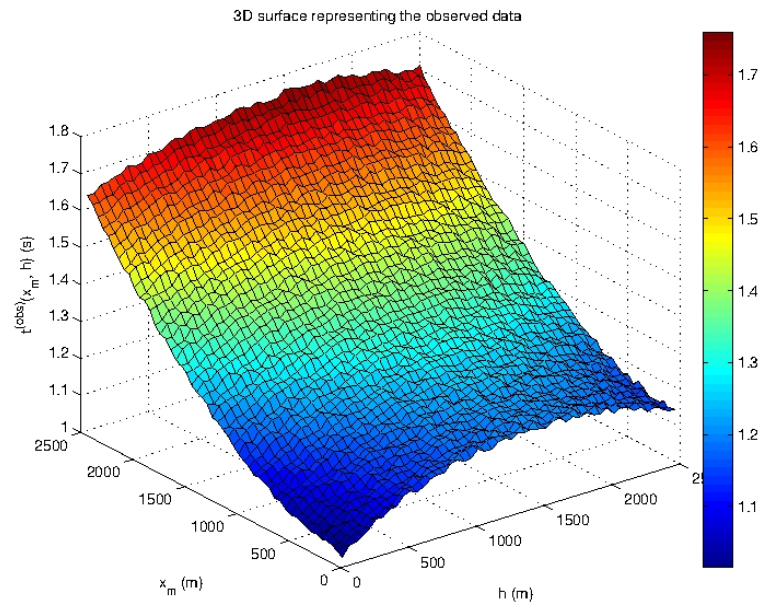
Fig. A.4 represents the forward model (no noise added), and Fig. A.5 represents the synthetic data, obtained from Fig. A.4 where noise has been added to. Both informations were calculated by Eq. (A.4), and the additive random noise calculated with a normal distribution, and visually controlled. Therefore, this work does not have manually or automatic picked events, or real data.

Figure A.4 – 3D perspective of the time surface to be fit representing the forward model calculated by Eq. (A.4) showing the hyperbolic aspect along  $h$  and  $x_m$ .



Source: From autor

Figure A.5 – 3D perspective of the time surface to be fit representing the synthetic data calculated by Eq. (A.4), where random noise was added to Fig. A.4, and still showing some hyperbolic aspect. The additive noise was calculated with 0.01% with respect to the maximum value of the traveltime.



Source: from Autor

## Attribute search

Depending on the application, the number of the CRS attributes will be different, what also will depend on the dimension of the problem (if 2D or 3D), and on the observation topography. For the flat observation surface and 2D problems, the model only considers the triplet  $(R_{\text{NIP}}, R_{\text{N}}, \alpha_0)$ . The parameter  $v_0$  is admitted fixed, but the value adopted is considered as an a priori information, and to be decided for. We follow the descriptions of Muller (1999) and Mann (2002) for the stack implementation, where the triplet search is described as a nonlinear optimization problem; again, there is no search for  $v_0$  in the practice of CRS stack.

For the triplet optimization Step, it needs a starting point  $(R_{\text{NIP}}, R_{\text{N}}, \alpha_0)^{(\text{Ini})}$  that is obtained in previous specific steps performed in the CMP domain. The parameter picking should be associated with maximum coherence values used to simulate the correspondent ZO point, and finally the complete section.

**First Step.** It is one-parameter search for the combined  $v_{\text{stack}}$  for obtaining a first ZO section by setting  $x_m = x_0$  in Eq. (A.4) that is reduced to:

$$t(h)|_{x_m=x_0} = \sqrt{t_0^2 + \frac{2t_0 \cos^2 \alpha_0}{v_0 R_{\text{NIP}}} h^2}; \quad (\text{A.7})$$

that, compared with  $t(h) = \sqrt{t_0^2 + \frac{4h^2}{v_{\text{NMO}}^2}}$ , the stacking velocity can be expressed in terms of  $\alpha_0$  and  $R_{\text{NIP}}$ , for  $v_{\text{NMO}} = v_{\text{stack}}$ , as

$$v_{\text{stack}}^2 = \frac{2v_0 R_{\text{NIP}}}{t_0 \cos^2 \alpha_0}. \quad (\text{A.8})$$

This step is called Automatic NMO stack (or, CMP stack), and it represents a non-interactive velocity analysis.

**Second Step.** It is also one-parameter search for non-combined  $\alpha_0$  attribute for obtaining a second ZO section by setting  $h = 0$  and  $R_{\text{N}} = \infty$  in Eq. (A.4) that reduces it to:

$$t(x_m)|_{(h=0, R_{\text{N}}=\infty)} = t_0 + \frac{2\text{sen}\alpha_0(x_m - x_0)}{v_0}, \quad (\text{A.9})$$

This first-order approximation can be regarded as a plane wave approximation, and this step is called Automatic Plane Wave stack, from where the emergence angle  $\alpha_0$  is obtained based on a small aperture. Inserting this angle value into Eq. (A.8), a value for  $R_{\text{NIP}}$  is calculated.

**Third Step.** It is one-parameter search for the non-combined  $R_{\text{N}}$  attribute for obtaining a third ZO section by setting  $h = 0$  in Eq. (A.4) that reduces it to:

$$t(x_m)|_{(h=0)} = \sqrt{\left[ t_0 + \frac{2\text{sen}\alpha_0(x_m - x_0)}{v_0} \right]^2 + \frac{2t_0 \cos^2 \alpha_0}{v_0} \frac{(x_m - x_0)^2}{R_{\text{N}}}}. \quad (\text{A.10})$$

In this step, the values of  $\alpha_0$  and  $R_{\text{NIP}}$  would already be known from the previous search, and this step is called Automatic Hyperbolic stack for  $R_{\text{N}}$ .

**Fourth Step.** From the previous 3 steps, the initial values  $(R_{\text{NIP}}, R_{\text{N}}, \alpha_0)^{(\text{Ini})}$  are known, and (with  $v_0$  fixed) an Initial stack is performed to obtain a fourth ZO section.

**Fifth Step.** With the set  $(R_{\text{NIP}}, R_{\text{N}}, \alpha_0)^{(\text{Ini})}$ , and  $v_0$  fixed, the simultaneous search provides the Optimized CRS stack producing another attribute set,  $(R_{\text{NIP}}, R_{\text{N}}, \alpha_0)^{(\text{Opt})}$ , and another ZO section.

Forward modeling can now be performed by calculating traveltime surfaces with Eq. (A.4) and the set of attributes  $(R_{\text{NIP}}, R_{\text{N}}, \alpha_0)^{(\text{Opt})}$ . We can now take one random subset for the sensitivity analysis.

## Sensitivity model

Sensitivity analysis can only be done on theoretical models, where closed derivatives can be taken, and by definition it is a model compromise. Therefore, sensitivity analysis on real data only makes partial sense here. Frank (1978) describes applications of model parameter sensitivity for physical prediction and applications. The system function is denoted by  $t_i = t_i(\mathbf{m})$ , dependent on the parameter vector  $\mathbf{m} = [m_1, m_2, \dots, m_M]^T$ , and in this case we have  $\mathbf{m}$  specifically given by  $\mathbf{m} = [v_0, R_{\text{NIP}}, R_{\text{N}}, \alpha_0]^T$ . The nominal parameters and system function are denoted with the lower script 0 in  $\mathbf{m}_0$  and  $t_0$ .

Considering continuity conditions, the following definitions for the sensitivity function, matrix  $\mathbf{S}$ , are applied, and some are presented for comparison, and Appendix A is devoted to some details on this technique.

The adopted measure here was the Relative Logarithmic sensitivity function,  $\bar{\mathbf{S}}$ , defined by:

$$\bar{S}_{ij} \triangleq \left. \frac{\partial \ln t_i(\mathbf{m})}{\partial \ln m_j} \right|_{\mathbf{m}_0} = \bar{S}_{ij}(\mathbf{m}_0) = S_{ij} \frac{m_{0j}}{t_{0i}}, \quad (\text{A.11})$$

where  $S_{ij}$  is the  $ij$ th element of absolute sensitivity function  $\mathbf{S}$  of Eq. (A.20). The  $i$ th element of the Relative Error of the system function is defined by:

$$E_{\text{R}}(x_m, h) = \frac{\Delta t_i}{t_{0i}} \triangleq \sum_{j=1}^{j=M} S_{ij} \frac{\Delta m_j}{m_{0j}}, \quad (\text{A.12})$$

and the Maximum Relative Error of the system function by

$$E_{\text{A}}(x_m, h) = \left| \frac{\Delta t_i}{t_{0i}} \right| \triangleq \sum_{j=1}^{j=M} |S_{ij}| \left| \frac{\Delta m_j}{m_{0j}} \right|. \quad (\text{A.13})$$

Examples of the  $\bar{\mathbf{S}}$  function are presented in Figs. A.10, A.11, A.12 and A.13.

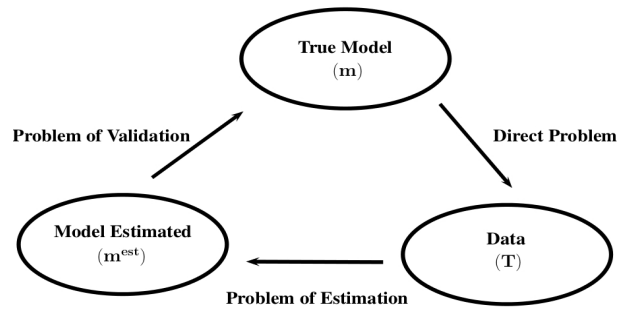
## Optimization methods

This short description is to present a relation between the optimization technique and the sensitivity analysis for completeness. Vieira and Leite (2009) presented strategies with two optimization methods combined to investigate the convergence and resolution of the CRS operator aiming at practical applications. The concepts involved are the Random Controlled Search, and the Gradient methods. The misfit measure used,  $\chi(\mathbf{m})$ , is given by:

$$\chi(\mathbf{m}) = \sqrt{\frac{\sum_{i=1}^N [t_i^{(\text{obs})} - t_i^{(\text{pre})}(\mathbf{m})]^2}{N}}. \quad (\text{A.14})$$

This measure is not to be confused with the Semblance function, and Fig. A.6 shows the layout of the inversion process. The function  $\chi(\mathbf{m})$  has the properties to be positive, convex, multimodal, and not necessarily smooth, what will depend on the  $\Delta\mathbf{t}(\mathbf{m}) = \mathbf{t}^{\text{obs}} - \mathbf{t}^{\text{pre}}(\mathbf{m})$  relation. The parameter,  $\mathbf{m}$ , search is to minimize the function  $\chi(\mathbf{m})$ .

Figure A.6 – Canonic representation of the optimization principle.



Source: From autor

The CRSGM formalism applied was originally described by Price (1983) to solve the global optimization problem, and Appendix B is devoted to some details on this method to show the necessity of control, what makes the curve fitting process a little more nonlinear. A common characteristic of the global methods, as described by Brachetti et al. (1997), is that they attack two distinct problems at the same time:

1. The global search problem that is the examination of all region of interest aiming at to localize “more promising” sub-regions that contains the global minimum ( $\mathbf{m}^{**}$ );
2. The local search problem that is the determination of the global minimum ( $\mathbf{m}^{**}$ ) using a local strategy, once a rather small neighborhood has been detected around the minimum.

The Gradient Method (GM) is a Local search formalism described to some details in Appendix C. The main point is that the GM is based on the multivariate Taylor series expansion of a function used to represent the observed data in a nonlinear problem, that is summarized as  $\mathbf{G}(\mathbf{m})\Delta\mathbf{m} = \Delta\mathbf{t}$ , where  $\mathbf{G}(\mathbf{m})$  is the problem matrix function of the parameters  $\mathbf{m}$  to be resolved for iteratively. The series linearizes the problem to allow for an iterative solution, which is based on the linear counterpart form,  $\mathbf{G}\mathbf{m} = \mathbf{t}$ , where  $\mathbf{G}$  is not a function of the  $\mathbf{m}$  parameters.

In the least-square sense, the optimization here is defined as an over-determined (pure) problem, the number of data being greater than the number of parameters to be resolved for, ( $N > M$ ), and all parameters considered to have the same illumination. The minimization method uses the principle that  $\partial\chi(\mathbf{m})/\partial m_j = 0$ , what establishes a local minimum, with the solution represented by the normal equation  $\mathbf{G}(\mathbf{m})\Delta\mathbf{m} = \Delta\mathbf{t}$ . The iterative solution of the nonlinear problem is represented by the equation:

$$\Delta\mathbf{m}|_k = [\mathbf{G}^T\mathbf{G}]^{-1}\mathbf{G}^T\Delta\mathbf{t}|_k, \quad (\text{A.15})$$

under the parameter update given by

$$\mathbf{m}^{(k+1)} = \mathbf{m}^{(k)} + \gamma^{(k)}\Delta\mathbf{m}^{(k)}, \quad (\text{A.16})$$

where  $\gamma$  is an attenuation/amplification factor for the solution  $\Delta\mathbf{m}$ , and  $k$  is the iteration number in the optimization process cycle.

A statistical analysis for the method is done by the Data and Parameter Resolution Matrices, and by the Unitary Covariance Matrix (MENKE, 2002). These matrices are attributes of the method involving the matrix  $\mathbf{G}$ , and its generalized inverse  $\mathbf{G}^{-g}$ , that in the present case has the form  $\mathbf{G}^{-g} = [\mathbf{G}^T\mathbf{G}]^{-1}\mathbf{G}^T$ . The Parameter Resolution matrix,  $\mathbf{R}_p$ , is given by:

$$\mathbf{R}_p = \mathbf{G}^{-g}\mathbf{G}, \quad (\text{A.17})$$

the Data Resolution matrix,  $\mathbf{R}_d$ , by

$$\mathbf{R}_d = \mathbf{G}\mathbf{G}^{-g}, \quad (\text{A.18})$$

and the Unitary Covariance matrix,  $\mathbf{cov}_u$ , by

$$\mathbf{cov}_u(\mathbf{m}) = \sigma^{-2}\mathbf{G}^{-g}[\mathbf{cov}(\mathbf{t})]\mathbf{G}^{-gT} = \mathbf{G}^{-g}\mathbf{G}^{-gT}. \quad (\text{A.19})$$

The CRSGM is classified as a Direct Search Method, and therefore does not have statistical operators as for the GM described above.

Examples of the two optimization processes are presented below in the Results section, where control values for the inversion processes are also given immediately after the calculation flow description.

## The sensitivity functions

This description follows mostly (FRANK, 1978) and (SALTELLI et al., 2004), where applications for different scientific fields are presented.

The Absolute sensitivity function is defined ( $\triangleq$ ) by:

$$S_{ij} \triangleq \left. \frac{\partial t_i(\mathbf{m})}{\partial m_j} \right|_{\mathbf{m}_0} = S_{ij}(\mathbf{m}_0), \quad (i = 1, 2, \dots, N), \quad (j = 1, 2, \dots, M), \quad (\text{A.20})$$

the parameter-induced error by

$$\Delta t_i \triangleq \sum_{j=1}^M S_{ij} \Delta m_j, \quad (\text{A.21})$$

and the maximum error by

$$|\Delta t_i| \triangleq \sum_{j=1}^M |S_{ij}| |\Delta m_j|, \quad (\text{A.22})$$

where the vertical bars stand for the absolute values of the elements of the corresponding vector  $\mathbf{m}$  or  $S_{ij}$ .

The Relative Logarithmic sensitivity function,  $\bar{\mathbf{S}}$ , is defined by:

$$\bar{S}_{ij} \triangleq \left. \frac{\partial \ln t_i(\mathbf{m})}{\partial \ln m_j} \right|_{\mathbf{m}_0} = \bar{S}_{ij}(\mathbf{m}_0). \quad (\text{A.23})$$

The  $\ln \mathbf{m}$  means the vector of the logarithms of the elements of  $\mathbf{m}$ , therefore  $\partial \ln \mathbf{m} = [\partial m_1/m_1 \ m_2/m_2 \ \dots \ m_M/m_M]$

The  $i$ th element of  $\bar{S}_{ij}$  is defined by:

$$\bar{S}_{ij} \triangleq \left. \frac{\partial t_i(\mathbf{m})/t_i}{\partial m_j/m_j} \right|_{\mathbf{m}_0} = S_{ij} \frac{m_{0j}}{t_{0i}}, \quad (\text{A.24})$$

where  $S_{ij}$  is the  $ij$ th element of absolute sensitivity function  $\mathbf{S}$  of Eq. (A.20). The  $i$ th element of the relative error of the system function is defined by:

$$\frac{\Delta t_i}{t_{0i}} \triangleq \sum_{j=1}^M S_{ij} \frac{\Delta m_j}{m_{0j}}, \quad (\text{A.25})$$

and the maximum Relative Error of the system function by

$$\left| \frac{\Delta t_i}{t_{0i}} \right| \triangleq \sum_{j=1}^M |S_{ij}| \frac{|\Delta m_j|}{m_{0j}}. \quad (\text{A.26})$$

There are also two ways to define a semirelative sensitivity function as follows.

The Upper-semirelative Logarithmic sensitivity function defined by:

$$\check{S}_{ij} \triangleq \left. \frac{\partial \ln t_i(\mathbf{m})}{\partial m_j} \right|_{\mathbf{m}_0}, \quad (\text{A.27})$$

with the components  $\check{S}_{ij}$  by

$$\check{S}_{ij} \triangleq \left. \frac{\partial t_i(\mathbf{m})/t_i}{\partial m_j} \right|_{\mathbf{m}_0} = \frac{1}{t_{0i}} S_{ij}. \quad (\text{A.28})$$

The Lower-semirelative Logarithmic sensitivity function defined by:

$$\hat{S}_{ij} \triangleq \left. \frac{\partial t_i(\mathbf{m})}{\partial \ln m_j} \right|_{\mathbf{m}_0}, \quad (\text{A.29})$$

and the components  $\hat{S}_{ij}$ , in terms of  $S_{ij}$ , by

$$\hat{S}_{ij} \triangleq \left. \frac{\partial t_i(\mathbf{m})}{\partial m_j/m_j} \right|_{\mathbf{m}_0} = m_{0j} S_{ij}. \quad (\text{A.30})$$

For this measure, the  $i$ th element of the relative error of the system function is defined in terms of  $S_{ij}$  by:

$$\Delta t_i \triangleq \sum_{j=1}^{j=M} S_{ij} \frac{\Delta m_j}{m_{0j}}, \quad (\text{A.31})$$

and the absolute error by

$$|\Delta t_i| \triangleq \sum_{j=1}^{j=M} |S_{ij}| \frac{|\Delta m_j|}{m_{0j}}. \quad (\text{A.32})$$

Due to the mathematical representation used for the sensitivity functions,  $S_{i,j}$ , and for the derivatives,  $G_{i,j}$ , we have the equality  $S_{i,j} = G_{i,j}$ , where the necessary functions  $G_{i,j}$  are given in Appendix C. Properties of the function  $G_{i,j}$  is given by Eq. (A.41).

## The CRSGM

As a simple description for completion of the text for the optimization fundamentals, it is desired with the Price method a solution of the global non-constrained nonlinear optimization problem, structured in the following form:  $\mathbf{min} \chi(\mathbf{m})$ ,  $\mathbf{m} \in R^M$ , where  $\chi : R^M \rightarrow R$  is a continuous function; that is, a minimum  $\chi(\mathbf{m})$  of the continuous function is searched, where the parameter vector  $\mathbf{m}$  (dimension  $M$ ) to be determined is defined in the  $R^M$  space. In this form,  $\mathbf{m}$  represents point-coordinates  $m_i$ , ( $i = 1, M$ ) in the continuous parameter space. The function object of minimizations is considered multimodal.

To initiate the process, a  $V$  search domain is defined through the specification of explicit constraints to each parameter. Next, at each iteration  $k$ , it is defined a predetermined quantity,  $N$ , of test points randomly chosen in  $V$  and consistent with the constraints (in case they are imposed) forming the set:

$$B_1^k = \left\{ \mathbf{m}_1^{(k)}, \mathbf{m}_2^{(k)}, \mathbf{m}_3^{(k)}, \dots, \mathbf{m}_N^{(k)} \right\}. \quad (\text{A.33})$$

The functional  $\chi(\mathbf{m})$  is evaluated at all  $N$  points, and the position and value of the function  $\chi(\mathbf{m})$  are saved in a matrix  $\mathbf{A}$  [ $N \times (M + 1)$ ].

At each iteration  $k$ , a new test point  $P$ ,  $\widehat{\mathbf{m}}^{(k)}$ , is calculated using a random sub-set  $B_2^{(k)}$  of  $B^{(k)}$  described in the form:

$$\widehat{\mathbf{m}}^{(k)} = \mathbf{c}^{(k)} - (\mathbf{m}_{20}^{(k)} - \mathbf{c}^{(k)}), \quad (\text{A.34})$$

being  $\mathbf{c}$  the centroid defined by:

$$c_j^{(k)} = \frac{1}{M} \sum_{i=1}^M m_{2i}^{(k)} \quad (j = 1, M). \quad (\text{A.35})$$

Next, a test is done if the point  $P$  satisfies the constraints, and if

$$\chi(\widehat{\mathbf{m}}^{(k)}) < \chi(\widehat{\mathbf{m}}_{\max}^{(k)}). \quad (\text{A.36})$$

In case these conditions are not satisfied, the process returns for new definitions. The probability that the points converge to the global minimum depends on the distribution, on the value of  $N$ , on the complexity of the functional, in the nature of constraints and in the choice of the test points.

## The GM

The Taylor series expansion of the function  $\mathbf{t}(x_m, h; \mathbf{m}_2)$ , in the neighborhood of  $\mathbf{t}(x_m, h; \mathbf{m}_1)$ , to the first order is written as an approximation ( $\cong$ ) as:

$$t_i(x_m, h; \mathbf{m}_2) \cong t_i(x_m, h; \mathbf{m}_1) + \sum_{j=1}^M \frac{\partial t_i}{\partial m_j}(x_m, h; \mathbf{m}_1) \Delta m_j, \quad (i = 1, N). \quad (\text{A.37})$$

The observed data is represented by  $t_i^{(\text{obs})}(x_m, h; \mathbf{m}_2 = \text{true})$ , and the predicted data by  $t_i^{(\text{pre})}(x_m, h; \mathbf{m}_1 = \text{model})$ . From these definitions, with  $\mathbf{m}_1 = \mathbf{m}$ , we can write Eq. (A.37) as:

$$t_i^{(\text{obs})}(x_m, h) - t_i^{(\text{pre})}(x_m, h; \mathbf{m}) = \sum_{j=1}^M \frac{\partial t_i^{(\text{pre})}}{\partial m_j}(x_m, h; \mathbf{m}) \Delta m_j, \quad (\text{A.38})$$

and in the matrix compact form

$$\Delta \mathbf{t}(x_m, h; \mathbf{m}) = \mathbf{G}(x_m, h; \mathbf{m}) \Delta \mathbf{m}. \quad (\text{A.39})$$

This equation represents a linearized form to obtain a solution to the nonlinear problem, where  $\Delta \mathbf{t}(x_m, h; \mathbf{m})$  is a column vector, ( $N \times 1$ ), that represents the data deviations;  $\Delta \mathbf{m}$  is a column vector, ( $M \times 1$ ), that represents the parameter deviations; and  $\mathbf{G}(x_m, h; \mathbf{m})$  is the problem matrix,

$(N \times M)$ , that has the data information along the columns, the parameter information along the lines, and the elements  $G_{i,j}$  are given by the partial derivatives of  $t(x_m, h; \mathbf{m})$  in the form:

$$G_{i,j} = \frac{\partial t_i^{(\text{pre})}(x_m, h; \mathbf{m})}{\partial m_j}, \quad (i = 1, N; j = 1, M) \quad (\text{A.40})$$

These partial derivatives are rather long, and they are used to represent the sensitivity functions with respect to the parameters.

The derivatives  $G = G(x_m, h; \mathbf{m})$ , described below, have a general form of the type:

$$G(x_m, h; \mathbf{m}) = \frac{a(\mathbf{m})(x_m - x_0) + b(\mathbf{m})(x_m - x_0)^2 + d(\mathbf{m})h^2}{t(x_m, x_0; \mathbf{m})}, \quad (\text{A.41})$$

that would rapidly decay with respect to  $t(x_m, h; \mathbf{m})$ , and increase with respect to the numerator function controlled by the coefficients,  $[a(\mathbf{m}), b(\mathbf{m}), d(\mathbf{m})]$ , and sign of the  $(x_m - x_0)^1$  factor.

The continuous partial derivative with respect to  $\alpha_0$ , and shown in Fig. A.10, is given by:

$$\frac{\partial t(x_m, h)}{\partial \alpha_0} = \frac{\frac{2 \cos \alpha_0 (x_m - x_0)}{v_0} \left( t_0 + \frac{2 \text{sen} \alpha_0 (x_m - x_0)}{v_0} \right) - \frac{2 t_0 \cos \alpha_0 \text{sen} \alpha_0}{v_0} \left( \frac{(x_m - x_0)^2}{R_N} + \frac{h^2}{R_{\text{NIP}}} \right)}{\sqrt{\left( t_0 + \frac{2 \text{sen} \alpha_0 (x_m - x_0)}{v_0} \right)^2 + \frac{2 t_0 \cos^2 \alpha_0}{v_0} \left( \frac{(x_m - x_0)^2}{R_N} + \frac{h^2}{R_{\text{NIP}}} \right)}}. \quad (\text{A.42})$$

The continuous partial derivative with respect to  $R_{\text{NIP}}$ , and shown in Fig. A.11, is given by:

$$\frac{\partial t(x_m, h)}{\partial R_{\text{NIP}}} = - \frac{\frac{t_0 h^2 \cos^2 \alpha_0}{v_0 R_{\text{NIP}}^2}}{\sqrt{\left( t_0 + \frac{2 \text{sen} \alpha_0 (x_m - x_0)}{v_0} \right)^2 + \frac{2 t_0 \cos^2 \alpha_0}{v_0} \left( \frac{(x_m - x_0)^2}{R_N} + \frac{h^2}{R_{\text{NIP}}} \right)}}. \quad (\text{A.43})$$

The continuous partial derivative with respect to  $R_N$ , and shown in Fig. A.12, is given by:

$$\frac{\partial t(x_m, h)}{\partial R_N} = - \frac{\frac{t_0 (x_m - x_0)^2 \cos^2 \alpha_0}{v_0 R_N^2}}{\sqrt{\left( t_0 + \frac{2 \text{sen} \alpha_0 (x_m - x_0)}{v_0} \right)^2 + \frac{2 t_0 \cos^2 \alpha_0}{v_0} \left( \frac{(x_m - x_0)^2}{R_N} + \frac{h^2}{R_{\text{NIP}}} \right)}}. \quad (\text{A.44})$$

The continuous partial derivative with respect to  $v_0$ , and shown in Fig. A.13, is given by:

$$\frac{\partial t(x_m, h)}{\partial v_0} = - \frac{\frac{2 \text{sen} \alpha_0 (x_m - x_0)}{v_0^2} \left( t_0 + \frac{2 \text{sen} \alpha_0 (x_m - x_0)}{v_0} \right) + \frac{t_0 \cos^2 \alpha_0}{v_0^2} \left( \frac{(x_m - x_0)^2}{R_N} + \frac{h^2}{R_{\text{NIP}}} \right)}{\sqrt{\left( t_0 + \frac{2 \text{sen} \alpha_0 (x_m - x_0)}{v_0} \right)^2 + \frac{2 t_0 \cos^2 \alpha_0}{v_0} \left( \frac{(x_m - x_0)^2}{R_N} + \frac{h^2}{R_{\text{NIP}}} \right)}}. \quad (\text{A.45})$$

From these partial derivatives, the quantities  $\bar{S}_{ij}(\mathbf{m}_0) = \frac{\partial \ln t_i(\mathbf{m}_0)}{\partial \ln m_{0j}} = \frac{m_{0j}}{t_{0i}} S_{ij}(\mathbf{m}_0)$  are calculated.

## Results

The calculation flow description of the computer program developed by Vieira and Leite (2009) is resumed as follows:

**01- Start**

**02-** Input: (1) Control parameters; (2) Model parameters; (3) Initial model parameters; (4) Inversion parameters.

**03-** Start iterations: Controlled Random Search Method.

**04-** End iterations: Controlled Random Search Method.

**05-** Start iterations: Gradient Method.

**06-** Calculation: Forward model.

**07-** Calculation: Curve fit measure, and test for ending the iterations.

**08-** Calculation: Derivatives of the CRS stack operator.

**09-** Calculation: Matrices  $\mathbf{G}$ ,  $\Delta\mathbf{d}$ ,  $\Delta\mathbf{m}$ .

**10-** Calculation: Parameter update.

**11-** Calculation: Convergence test.

**12-** Returns to 05.

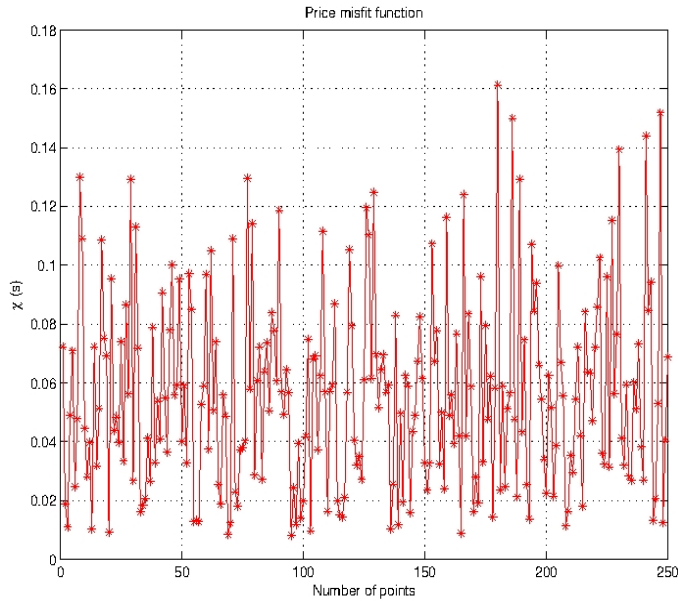
**13-** Calculation: Parameter Resolution matrix.

**14-** Calculation: Data Resolution matrix.

**15-** Calculation: Unit Covariance Unitary matrix.

The Price initial interval control parameters were set in the computer program to the following values. For  $v_0$  : 1400 – 1600 m/s, with the center value of 1500 m/s;  $R_{\text{NIP}}$  : 4500 to 5500 m, with the center value of 5000 m;  $R_{\text{N}}$  : –5500 to –4000 m, with center value of –5000 m; and  $\alpha_0$  :  $\pi/18$  to  $\pi/12$  rd, with center value of  $\pi/15$  rd. The parameter space has dimension 4, and the number of points in the parameter space were set to 200, with a tolerance of 0.01%. Fig. A.7 serves to exemplify the randomness of the misfit function  $\chi(\mathbf{m})$  as a result of the automatic random selection of  $\mathbf{m}$  for  $t_0 = 1.0$  s.

Figure A.7 – Price initial random misfit function.



Source: From autor

The GM inversion process were set to 20 iterations. The GM control parameters had the following initial values:  $v_0 = 1800$  m/s;  $R_{NIP} = 5700$  m;  $R_N = -4200$  m;  $\alpha_0 = \pi/10$  rd; the regularization factor  $\gamma = 1.0e - 7$ ; and  $t_0 = 1.0$  s.

Tab. A.1 presents the values obtained by the application of the CRSGM and GM methods, with the above control parameters, which shows agreement between the results, and to be a strong allied in the strategy for the 4 parameters search of the CRS forward model. We should make clear that the accuracy obtained depends on the inversion control parameters, and on the number of iterations. Since we are dealing with two independent methods, we intentionally chose for the independent solutions and, therefore, the values for CRSGM and GM were left close to the nominal values.

Table A.1 – Inversion values obtained by the CRSGM and GM optimization methods.

Parameter	Real	CRSGM	GM
$v_0$ (m/s)	1500	1459	1446
$R_{NIP}$ (m)	5000	5013	5112
$R_N$ (m)	-5000	-4910	-4800
$\alpha_0$ (radians)	0,2094	0,2019	0,2186

Tab. A.2 presents the Normalized Parameter Resolution ( $4 \times 4$ ) matrix of Eq. (A.17) that, should ideally have a unitary diagonal form, and shows a weak scatter in the off diagonal

elements. The correlation values in the  $\alpha_0$  columns are very small, (smaller than 0.0001), with respect to the other parameters, and they serve as a measure of relative parameter independence.

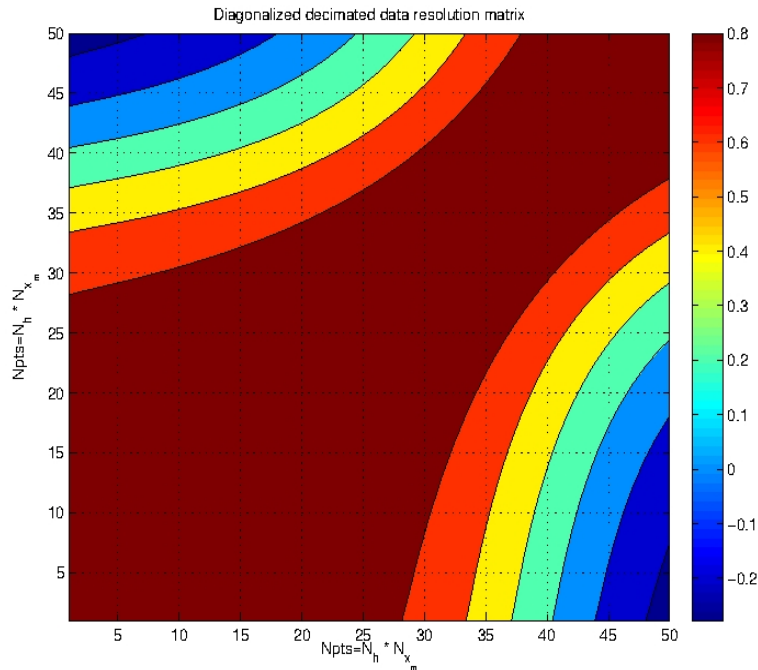
Table A.2 – Normalized Parameter Resolution matrix limited to 3 decimal places. Eq. (A.17).

$\mathbf{R}_p$	$v_0$	$R_{\text{NIP}}$	$R_{\text{N}}$	$\alpha_0$
$v_0$	1	0.287	-0.173	0.000
$R_{\text{NIP}}$	0.287	1	0.893	0.000
$R_{\text{N}}$	-0.173	0.893	1	0.000
$\alpha_0$	0.000	0.000	0.000	1

Source: From autor

Fig. A.8 shows the Normalized Decimated Data Resolution ( $50 \times 50$ ) matrix of Eq. (A.18). This matrix had originally dimensions ( $2500 \times 2500$ ), but was decimated for better plotting purpose, but conserved its original form and scale. This representation with contours is more convenient than as a table. This matrix should ideally have a unitary diagonal form, but shows a strong scatter of the off diagonal elements.

Figure A.8 – Data resolution matrix decimated by 50 points.



Source: From autor

Tab. A.3 presents the Normalized Unitary Parameter Covariance ( $4 \times 4$ ) matrix of Eq. (A.19), that should ideally have a unitary diagonal form, but shows a strong scatter of the off

diagonal elements. This representation in form of table is more convenient than as a figure with contours. The values shown correspond to a non-desirable strong correlation between the parameters, and means that by changing one parameter the others are also altered according to the sign as, for example, between  $R_N$  and  $R_{NIP}$  with  $\text{cov}_u = 0.999$ .

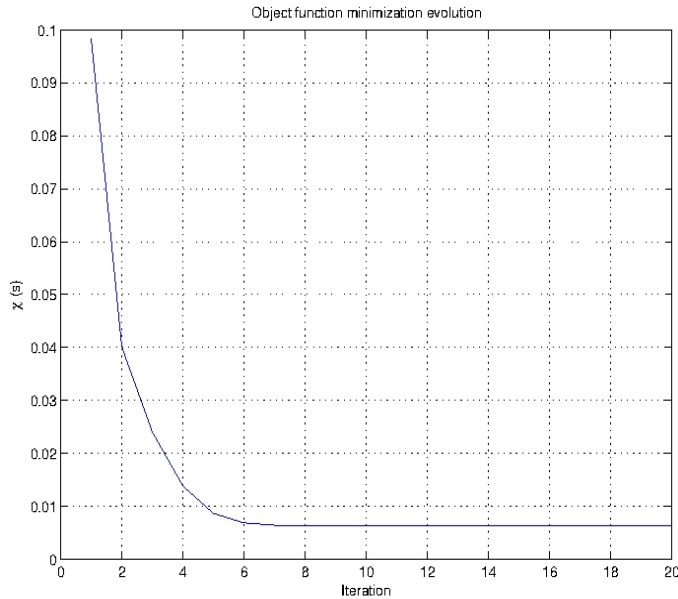
Table A.3 – Normalized Unitary Parameter Covariance matrix limited to 3 decimal places. Eq. (A.19).

$\text{cov}_u(\mathbf{m})$	$v_0$	$R_{NIP}$	$R_N$	$\alpha_0$
$v_0$	1	-0.832	-0.855	-0.362
$R_{NIP}$	-0.832	1	0.999	0.772
$R_N$	-0.855	0.999	1	0.750
$\alpha_0$	-0.362	0.772	0.750	1.0

Source: From autor

The maximum number of iterations in the GM method was limited to 20, and the evolution of the minimization object function is shown in Fig. A.9. It was established that the solution by the CRSGM was to be used as input to the GM method. But, for the above tables, they were obtained in independent experiments, to check for the convergence of the methods. Also, the Global method is only used to give the initial point in the parameter space for calculating the statistics based on the Local method. The experiment results show that a precise local point is not a decisive matter due to the linearity at the local minimum.

Figure A.9 – Evolution of the objective minimization function calculated in 20 iterations showing the stabilization of the process before the tenth iteration.



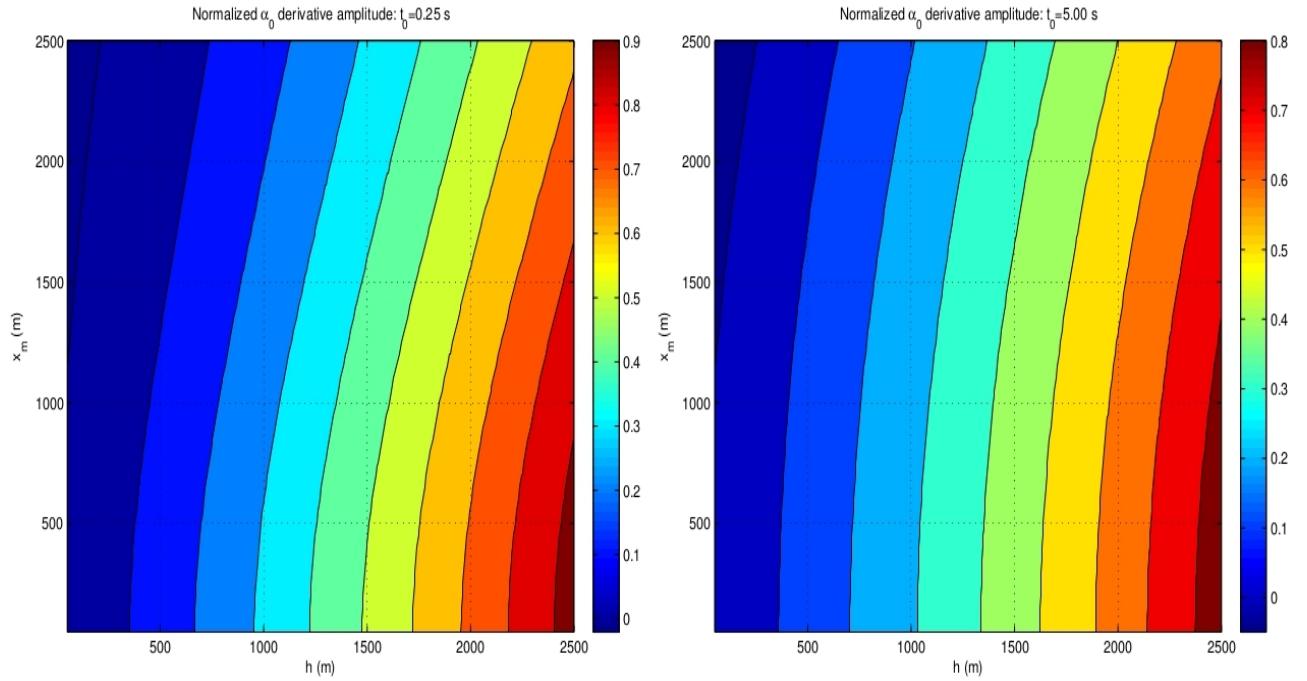
Source: From autor

The possible number of experiments with the sensitivity function  $\bar{\mathbf{S}}$ , Eq. (A.23), is theoretically equal to the number of points in a ZO section (time versus distance); therefore, it can be very large, and criteria must be used to select points for analysis. Examples are presented in Figs. A.10, A.11, A.12 and A.13, where the nominal values were  $v_0 = 1500$  m/s,  $R_{\text{NIP}} = 5000$  m,  $R_{\text{N}} = -5000$  m, and  $\alpha_0 = +(\pi/15)$  rad. The general chosen time points were  $t_{0i} = (0.25, 0.50, 1.00, 2.00, 2.50, 3.00, 4.00, 5.00)$  s, with selected values for each case.

Figs. A.10, A.11 and A.12 were calculated for only two values of  $t_{0i} = (0.25, 5.00)$ s, necessary to show because the function variation is very smooth.

Fig. A.10 is the simplest case, and involves the function  $(\alpha_0/t_0) * \partial t(x_m, h; \mathbf{m})/\partial \alpha_0$ , Eq. (A.42), and its relation to Eq. (A.9). The maps show a strong linear dependence with respect to the coordinates  $h$ , and a weak linear dependence with respect to the  $x_m$  coordinate; as a result, this parameter would be better determined along the  $x_m$  coordinate constrained to a  $h$  value. In the attribute search strategies, the Second Step solves for  $\alpha_0$ , as expressed by Eq. (A.9) for  $t = t(x_m, h = 0)$ .

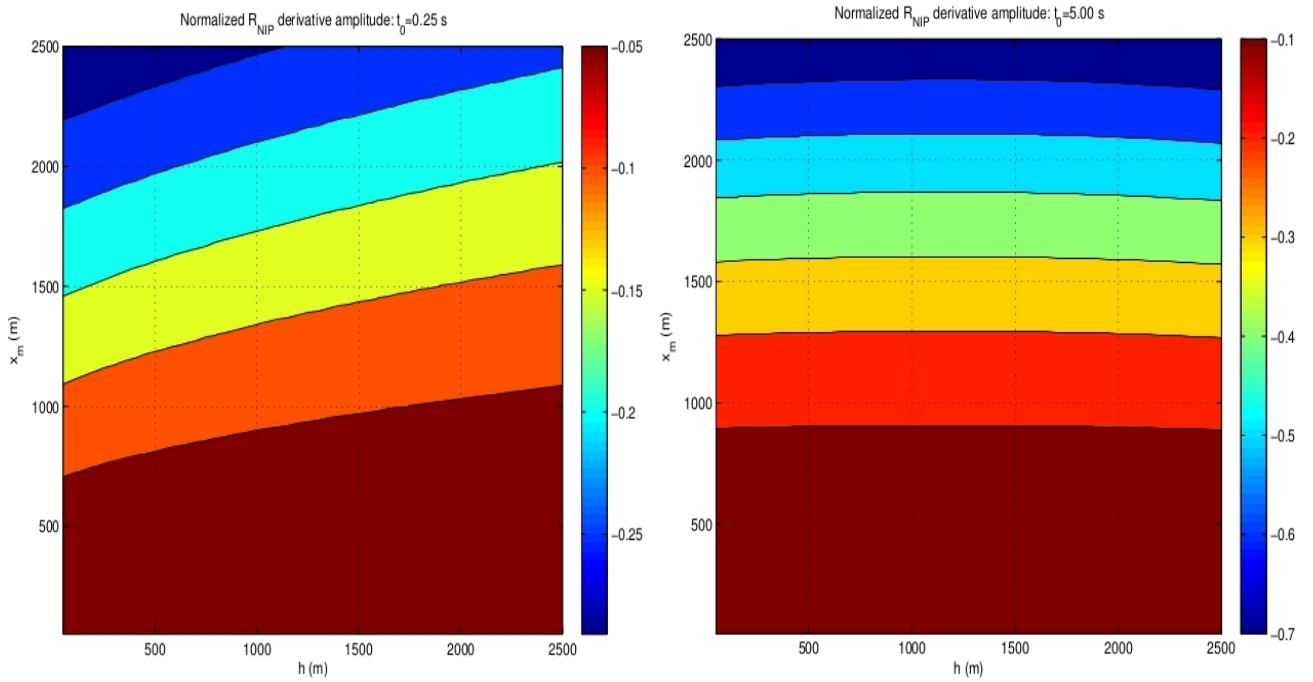
Figure A.10 – Contour maps of the normalized derivative  $(\alpha_0/t_0) * \partial t(x_m, h; \mathbf{m})/\partial \alpha_0$ . Figure positions: left,  $t_0 = 0.25$  s; right,  $t_0 = 5.00$  s.



Source: From autor

Fig. A.11 shows maps of the derivative  $(R_{\text{NIP}}/t_0) * \partial t(x_m, h; \mathbf{m})/\partial R_{\text{NIP}}$ , Eq. (A.43), and its relation to Eq. (A.7). The maps show a linear dependence with respect to  $x_m$ , and almost constant with respect to  $h$ , what makes this parameter less sensitive and stable along the  $h$  axis; as a result, this parameter would be better determined along the  $h$  coordinate constrained to a  $x_m$  value. In the attribute search strategies, a combination of the First and Second Steps solves for  $R_{\text{NIP}}$ , as expressed by Eq. (A.7) for  $t = t(h, x_m = 0)$ .

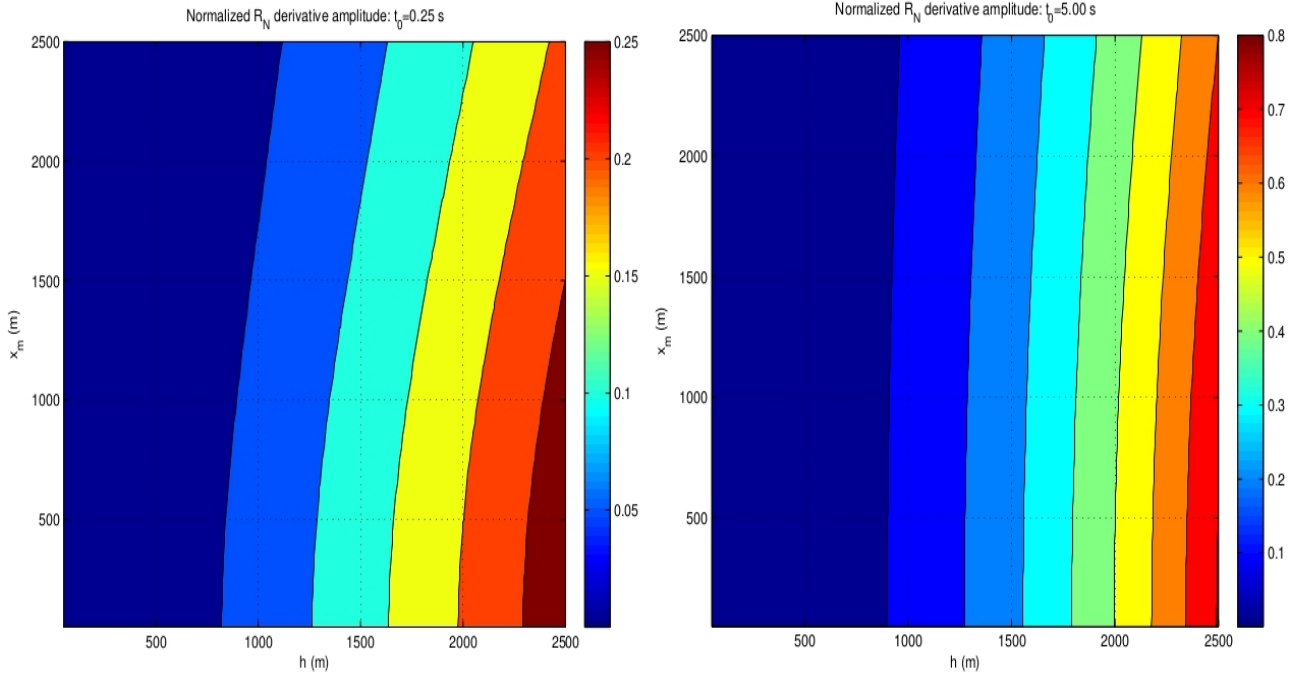
Figure A.11 – Contour maps of the normalized derivative  $(R_{\text{NIP}}/t_0) * \partial t(x_m, h; \mathbf{m}) / \partial R_{\text{NIP}}$ . Figure positions: left,  $t_0 = 0.25$  s; right,  $t_0 = 5.00$  s.



Source: From autor

Fig. A.12 shows maps of the derivative  $(R_{\text{N}}/t_0) * \partial t(x_m, h; \mathbf{m}) / \partial R_{\text{N}}$ , Eq. (A.44), and its relation to Eq. (A.10). The maps show a strong linear dependence with respect to the  $h$  coordinate, and almost constant with respect to the  $x_m$  coordinate; as a result, this parameter would be better determined along the  $x_m$  coordinate constrained to a  $h$  value. In the attribute search strategies, the Third Step solves for  $R_{\text{N}}$ , as expressed by Eq. (A.10) for  $t = t(x_m, h = 0)$ . This situation is opposite to the  $(R_{\text{NIP}}/t_0) * \partial t(x_m, h; \mathbf{m}) / \partial R_{\text{NIP}}$  case.

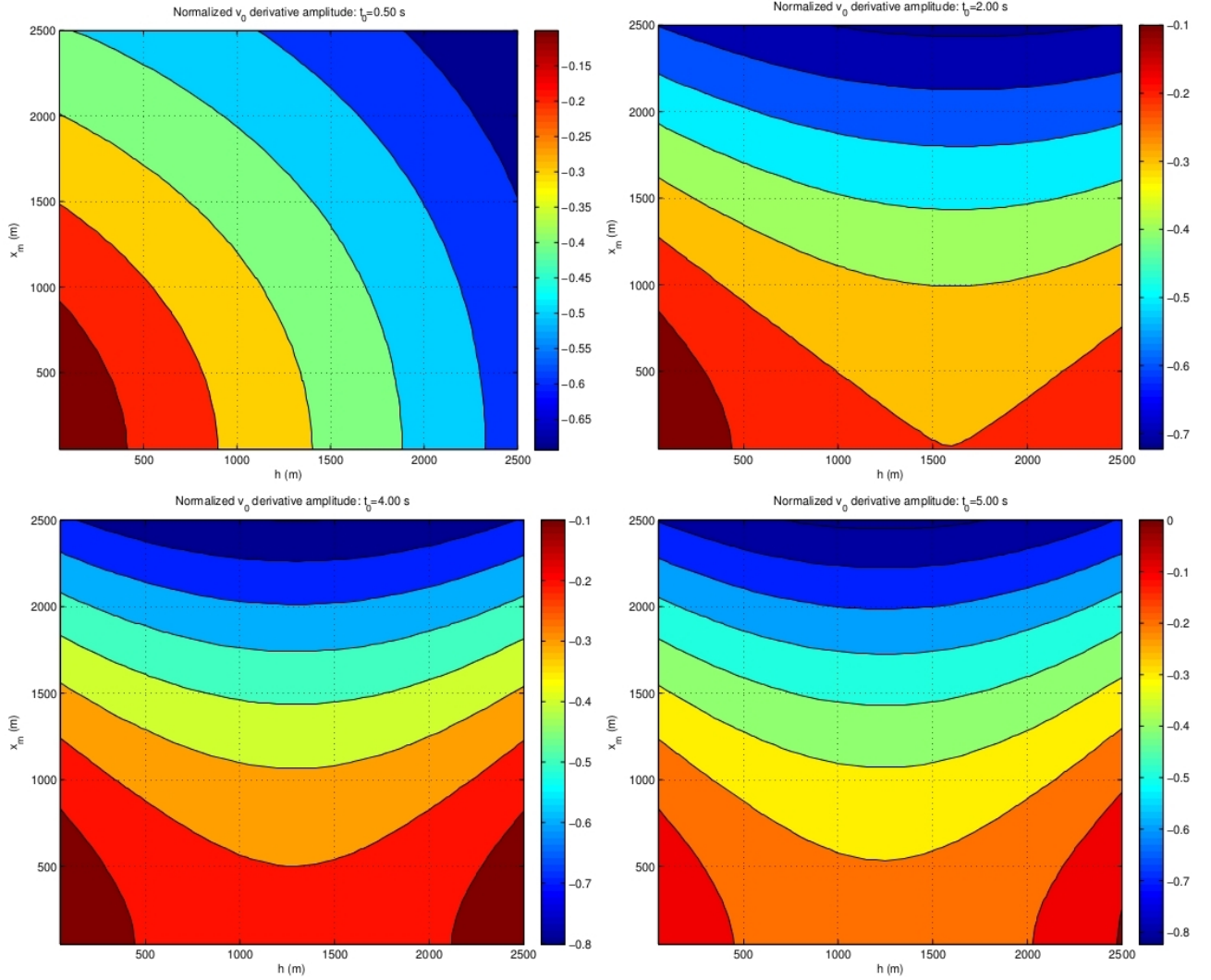
Figure A.12 – Contour maps of the normalized derivative  $(R_N/t_0) * \partial t(x_m, h; \mathbf{m})/\partial R_N$ . Fig. positions: left,  $t_0 = 0.25$  s; right,  $t_0 = 5.00$  s.



Source: From autor

Fig. A.13 displays the derivative  $(v_0/t_0) * \partial t(x_m, h; \mathbf{m})/\partial v_0$ , Eq. (A.45), and its relation to the constant value of  $v_0$ . The variation is still smooth, but faster than for the other three parameters ( $R_{NIP}$ ,  $R_N$  and  $\alpha_0$ ). The maps indicate a nonlinear variation with respect to the space coordinates ( $x_m$  and  $h$ ), without an ideal direction for  $v_0$  initial evaluation with respect to the nominal value of  $v_0 = 1500$  m/s positioned at the center of the figures. The maps indicate a very slow change with respect to higher  $t_{0i}$  values, and to be more complex for smaller  $t_{0i}$  values. Therefore, fixing the value of  $v_0$  in the CRS practice is a consistent constraint for the implementation and simplification of the data stack processing algorithm, with respect to the **S** analysis.

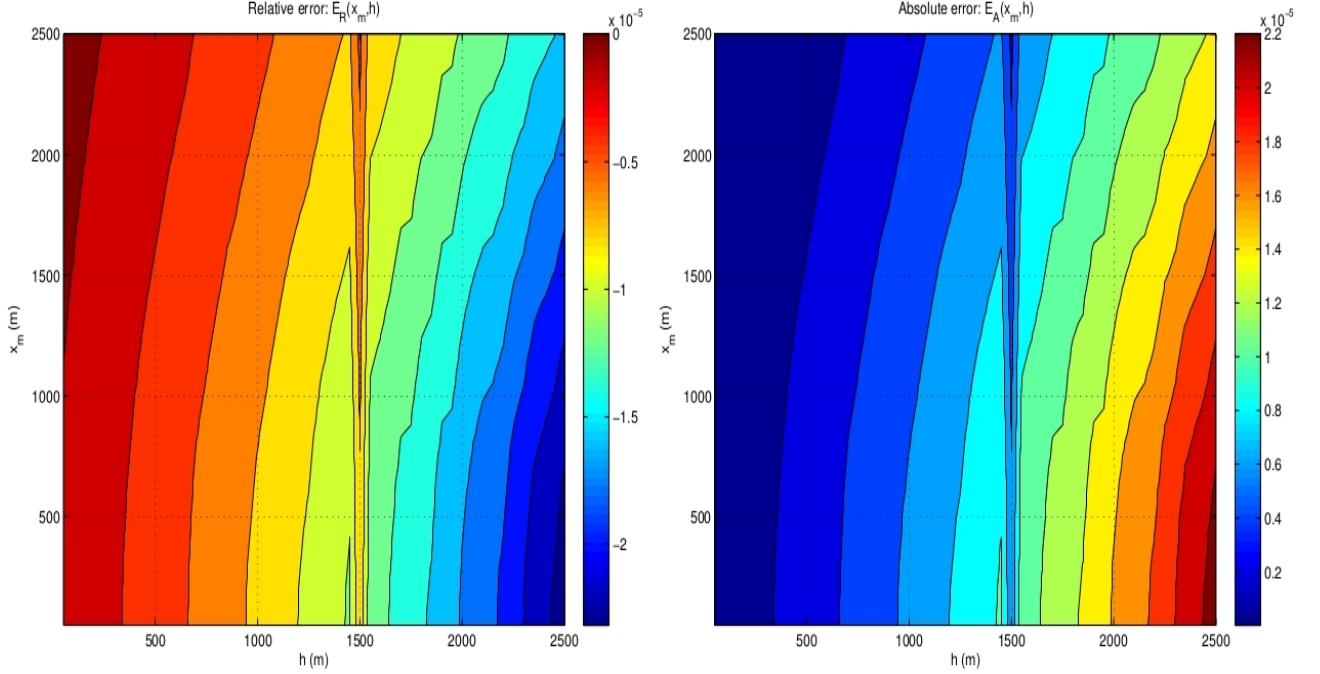
Figure A.13 – Contour maps of the normalized derivative  $(v_0/t_0) * \partial t(x_m, h; \mathbf{m})/\partial v_0$  for the nominal values  $v_0 = 1500$  m/s. Figure positions: top left,  $t_0 = 0.50$  s; top right,  $t_0 = 2.00$  s; bottom left,  $t_0 = 4.00$  s; bottom right,  $t_0 = 5.00$  s. From the experiments, the form varies very little after  $t_0 = 2$  s.



Source: From autor

Fig. A.14 are error functions calculated using Eq.s (A.12) and (A.13) of the adopted sensitivity measure,  $\bar{\mathbf{S}}$ . The maps show clearly and consistently a behavior of decreasing/increasing error with coordinates  $h$  and  $x_m$ , but mainly along the  $h$  axis, as a property of the hyperbolic operator (A.4). The elongated valleys of low values, along  $h = 1500$ m, coincide with the nominal values in Eqs. (A.12) and (A.13), that give minimum values for  $\Delta t_i$ .

Figure A.14 – Contour maps of the relative error calculated by Eq. (A.12) (left), and of the absolute error calculated by Eq. (A.13) (right), showing valleys of minimum around the nominal value at the center of figures.



Source: From autor

## Conclusions

We investigated the relationship between sensitivity functions for the CRS operator with respect to the parameters ( $v_0$ ,  $R_{NIP}$ ,  $R_N$  and  $\alpha_0$ ), and adopted the logarithm measure  $\bar{\mathbf{S}}$ . Then, we compared the  $\bar{\mathbf{S}}$  results with the attributes search strategies for ( $R_{NIP}$ ,  $R_N$  and  $\alpha_0$ ) that are based on physical-mathematical models for the construction of the CRS stack operator.

In the CRS stack,  $v_0$  is admitted as fixed, but it has a physical meaning as shown in Fig. A.2. In practical terms,  $v_0$  is represented by an average value taken along the geophone spread, and a sampling over the upper layers under the dominant wavelength window of the effective source pulse. The strategy for fixed  $v_0$  is consistent with the  $\bar{\mathbf{S}}$  analysis, due to the stronger variation of the  $v_0$  sensitivity function with respect to the space coordinates, as presented in Fig. A.13, where the main attention was called for.

The  $\mathbf{S}$  derivatives show some nonlinear behavior with respect to the spatial coordinates, ( $x_m$ ,  $h$ ), but complementary strategies for the parameter search were not here provided to establish the initial set of values  $(R_{NIP}, R_N, \alpha_0)^{(Ini)}$  to be used in the simultaneous optimization Step for obtaining  $(R_{NIP}, R_N, \alpha_0)^{(Opt)}$ .

For the parameter resolution, we have systematically concluded in the text that it is necessary a good start point for the optimization that searches simultaneously for the three parameters  $(R_{\text{NIP}}, R_{\text{N}}, \alpha_0)^{(\text{opt})}$  with  $v_0$  fixed. From the interpretation of the sensitivity functions, it is necessary to employ constraints as apriori conditions for the simultaneous parameter search.

The tests presented were performed for a fixed point  $P_0(x_0, t_0)$ . Another strategy would test for randomly chosen points along a trace,  $(t_0 = 0, t_{\text{total}})$ , and for any CMP.

Once established a form to represent the ambiguity and sensitivity of the  $t(x_m, h; \mathbf{m})$  function to its parameters, a next step would also be to repeat the experiment based on a form of modified fitting norm function.